

**Molecular electronic properties
of Porphyrin nanowires**

Neil Bennett

A thesis submitted to Cardiff University
for the degree Doctor of Philosophy

Nanophysics group,
School of Physics and Astronomy,
Cardiff University

Dec 2010

UMI Number: U575954

All rights reserved

INFORMATION TO ALL USERS

The quality of this reproduction is dependent upon the quality of the copy submitted.

In the unlikely event that the author did not send a complete manuscript and there are missing pages, these will be noted. Also, if material had to be removed, a note will indicate the deletion.



UMI U575954

Published by ProQuest LLC 2013. Copyright in the Dissertation held by the Author.
Microform Edition © ProQuest LLC.

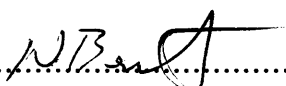
All rights reserved. This work is protected against
unauthorized copying under Title 17, United States Code.



ProQuest LLC
789 East Eisenhower Parkway
P.O. Box 1346
Ann Arbor, MI 48106-1346

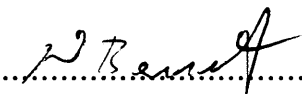
DECLARATION

This work has not previously been accepted in substance for any degree and is not concurrently submitted in candidature for any degree.

Signed  (candidate) Date 13/12/10


STATEMENT 1

This thesis is being submitted in partial fulfillment of the requirements for the degree of PhD

Signed  (candidate) Date 13/12/10

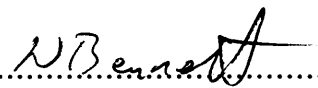
STATEMENT 2

This thesis is the result of my own independent work/investigation, except where otherwise stated. Other sources are acknowledged by explicit references.

Signed  (candidate) Date 13/12/10

STATEMENT 3

I hereby give consent for my thesis, if accepted, to be available for photocopying and for inter-library loan, and for the title and summary to be made available to outside organisations.

Signed  (candidate) Date 13/12/10

Abstract

We probe the electronic properties of conjugated porphyrin nanowires using the established current-versus distance $I(z)$ technique and by novel current-voltage (I-V) measurements. Initial test $I(z)$ measurements on nonanedithiol molecules in ultra high vacuum (UHV) revealed multiple conductance values over a wide range in general agreement with published data in ambient conditions and solvent environments. We find that the results are sensitive to the details of the sample preparation and there is evidence for some significantly lower conductance values than those previously reported suggesting a vacuum effect. The $I(z)$ technique is then applied to the porphyrin molecules to reveal a large spread in different conductance states, from $< 10^{-6} G_0$ up to $\sim 10^{-2} G_0$, indicating a range of possible configurations of the metal-molecule-metal junction.

Single porphyrin molecules and porphyrins isolated in a matrix of alkanethiols were probed by I-V spectroscopy. Repeated I-V measurements on individual molecules showed evidence of temporal fluctuations and changes of the coupling asymmetry in the molecular junctions. Analysis using the transition voltage spectroscopy technique revealed fluctuations in the voltage minimum V_m , which we suggest is due to the changing nature of the single molecule contact, and this provides estimates of the degree of contact asymmetry. Statistical analysis suggests more than one preferred value of V_m and a molecular energy level alignment to the Fermi energy of $E_F - \epsilon_{HOMO} < 0.4$ eV. The behaviour contrasts strongly with results from measurements over the alkanethiol matrix and over porphyrin monolayers, where such fluctuations are absent, in general agreement with previously reported studies. The results can be understood using a simple molecular model of coherent tunnelling and we conclude the electrical properties of single molecule junctions are highly sensitive to the microscopic details of the contacts and molecular conformations or configurations.

Acknowledgements

I would firstly like to thank my supervisors, Dr. Martin Elliott and Dr. J. Emyr Macdonald, for their continued advice and support in my personal development as a PhD student. Without their guidance and expertise this would not have been possible.

I would like to thank my peers in the Nanophysics research group for the mutual support, received knowledge and advice I have benefited from over the course of my research. I would particularly like to extend my thanks to Dr. Gengzhao Xu, who set a wonderful and inspiring example of a competent and effective researcher, and to Huw Thomas and Henje Simmonds for welcoming me to the group and for their continued friendship.

I would like to thank the group of Prof. Richard Nichols at the University of Liverpool for helpful discussions during our collaborative meetings and for giving me the opportunity to visit their lab to learn the experimental techniques and sample preparation methods used in this work. I would especially like to thank Wolfgang Haiss, Edmund Leary, and Gita Sedghi for giving their time and for helpful discussions. I would also like to thank the group of Prof. Harry Anderson at the University of Oxford for providing the Porphyrin molecules for the study and again for helpful discussions during the collaborative meetings.

Finally I would like to personally thank my friends, family and the staff at Cardiff student support services for their encouragement and support during difficult times and for helping me believe in myself and my abilities. Thank you all.

Symbols and acronyms

β	Decay constant in current versus distance relationship
BJ-STM	Break junction scanning tunnelling microscope. Variant of I(z)
C12, C16	Dodecanethiol, hexadecanethiol
DOS	Density of states
ε	Energy of molecular energy level
E_F	Fermi energy
ϕ	Barrier height in Simmons tunnelling model
F-N	Fowler – Nordheim
G	Conductance
G_0	Conductance quantum
Γ	Level broadening/coupling
η	Asymmetry parameter
I-V	Current versus voltage
I(s)	Special variant of I(z) – as distinct from BJ-STM
I(t)	Current versus time
I(z)	Current versus distance spectroscopy (general term)
HOMO	Highest occupied molecular orbital
LDOS	Local density of states
LUMO	Lowest unoccupied molecular orbital
MIGS	Metal-induced gap states
ML	Molecular energy level
MMM	Metal-molecule-metal
μ	Chemical potential

NDR	Negative differential resistance
SAM	Self assembled monolayer
SMC	Single molecule conductance
SPM	Scanning probe microscopy
STM	Scanning tunnelling microscopy
STS	Scanning tunnelling spectroscopy
$T(E)$	Transmission function
TVS	Transition voltage spectroscopy
UHV	Ultra-high vacuum
UPS	Ultraviolet photoelectron spectroscopy
V_m	Voltage minimum (transition voltage)
z	Vertical displacement (of probe tip)

Table of Contents

1	Introduction.....	1
1.1	Molecular electronics.....	1
1.2	Importance of scanning probe techniques.....	3
1.3	Thesis structure	4
2	Theoretical background.....	8
2.1	Introduction.....	8
2.2	Charge transport through nanoscale insulators.....	8
2.2.1	Conductance from transmission.....	8
2.2.2	Simmons model of tunnelling.....	9
2.2.3	Molecular energy level (ML) model.....	14
3	Experimental background.....	23
3.1	Introduction.....	23
3.2	Ultra high vacuum (UHV) facilities.....	23
3.2.1	Sample transfer and storage.....	24
3.2.2	Ion sputtering and sample annealing.....	24
3.3	Scanning probe microscopy.....	25
3.3.1	Scanning tunnelling microscopy (STM).....	25
	Atomic resolution - Si(111) 7×7.....	27
	STM for contacting single molecules.....	28
3.3.2	Scanning tunnelling spectroscopy (STS).....	30
	Current versus distance – I(z).....	30
	Current versus voltage – I(V).....	32
	Current as a function of time – I(t).....	32
3.4	Photoelectron spectroscopy.....	33
3.4.1	Ultraviolet photoelectron spectroscopy (UPS).....	34
3.4.2	Reduced work functions: Surface dipole.....	36

4 Single molecule conductance of nonanedithiol.....	38
4.1 Introduction.....	38
4.2 Alkanedithiols.....	38
4.3 I(z) technique.....	40
4.3.1 The development of I(z) for measuring SMC.....	41
4.3.2 Realising the I(z) measurement.....	44
4.3.3 Toy model of I(z) current plateaus.....	45
4.4 Results on bare Au single crystal.....	51
4.5 I(z) of nonanedithiol.....	55
4.5.1 Sample preparation	55
4.5.2 Current versus voltage.....	63
4.5.3 Lower coverage.....	66
I(z) results.....	69
4.5.4 Effect of surface roughness.....	71
4.5.5 High coverage sample – very slow curves.....	75
4.6 STM Break-junction	77
4.7 Discussion.....	79
5 Matrix isolated Porphyrin molecules.....	82
5.1 Introduction.....	82
5.2 Why study porphyrin molecules?.....	82
5.3 Matrix isolation.....	86
5.3.1 Sample preparation.....	88
5.4 Current voltage characteristics.....	92
5.4.1 Transition voltage spectroscopy.....	93
5.5 Results on isolated porphyrin molecules.....	99
5.5.1 Fluctuations and asymmetric response – examples, time series.....	99
5.5.2 Statistical distribution of V_m	102
5.5.3 Asymmetry in I-V (V_m).....	103
5.6 Result on Alkanethiol matrix.....	106

5.7 Fitting to the molecular model.....	107
5.8 Porphyrin self assembled monolayer.....	114
5.9 Discussion.....	117
6 Porphyrin single molecules.....	121
6.1 Introduction	121
6.2 Conductance by $I(z)$	123
6.2.1 Break-junction STM results.....	123
6.2.2 $I(s)$ method results.....	125
High resolution images.....	130
6.2.3 Conclusions from $I(z)$ experiments.....	131
6.3 I-V characteristics.....	133
6.3.1 Experimental approach.....	135
Time series of measurements.....	138
Expanding the model – multiple energy levels.....	146
Low temperature results.....	151
7 Summary and Conclusions.....	156
8 References.....	160
9 Appendix A. Results of numerical calculations.....	169
9.1 Molecular energy level model.....	169
9.1.1 Results - Varying coupling (energy level broadening) Γ	172
9.1.2 Results - Varying energy level offset ϵ	174
9.1.3 Results - Varying contact symmetry.....	176
9.1.4 Results – Varying temperature.....	179
9.1.5 V_m for Alkanes	182
9.1.6 Fitting to experimental data.....	182
9.2 Simmons model.....	185
9.2.1 Characteristics as a function of barrier height, ϵ	188
9.2.2 Characteristics as a function of barrier width, z	189
9.2.3 Versus effective mass.....	190

9.3 Summary/Discussion.....	190
10 Appendix B. Sample preparation.....	192
10.1 Au substrates.....	192
10.2 Molecular solutions.....	192
10.2.1 Alkanethiols/dithiols.....	192
10.2.2 Porphyrins	193
10.2.3 Mixed monolayers.....	193
10.3 STM tips.....	194
11 Appendix C.	195
11.1 UPS results	195
11.2 Voltage minimum analysis.....	196
11.3 Notes on statistical distributions.....	198
12 Appendix D. Example I-V data set.....	200

1 Introduction

1.1 Molecular electronics

The rapid progress in the development of electronics and computational devices has been one of the most defining features of the last century. The trend, coined Moore's law, for exponential growth in speed, processing power and computer memory has been possible due to the relentless downsizing of individual electronic components. This has been achieved by the paradigm shift from vacuum tube technology, to solid-state transistors, to integrated circuits, and by the continued improvement of fabrication techniques, such as lithography and etching. Advocates of Moore's law expect the trend to continue for another 15-20 years[1]. However, it is inevitable that continued downscaling should reach practical and financial limits in the near future.

Devices made by this "top-down" approach will eventually become so small that the statistical physics used to describe their behaviour will be inappropriate. There will also be power consumption and energy dissipation problems, as well as increased fabrication costs. In addition current techniques such as optical lithography are restricted (i.e. diffraction limited), so are not capable of achieving the required densities to reduce the scale of devices beyond hundreds of nanometres. It is these concerns that spur the interest in the electrical properties of molecules among researchers.

The idea that a molecule could act as a charge carrier and a functional electronic device was first suggested by Aviram and Ratner[2] when they showed that a molecule by virtue of a specific structure would act as a rectifying device if placed firmly between metal electrodes. If this idea of a single molecule device could be realised then electrical components could be shrunk to the nanometre scale. The appeal of the molecules is summarised by the following points: (1) Device size could feasibly be in the range 1 to 100 nm, (2) chemical interaction could be used for self

assembly of devices and circuit architecture (bottom-up instead of top-down), (3) the controlled synthesis of many complex molecules is possible on industrial scales already and (4) molecular systems could address problems that silicon electronics cannot broach, such as chemical sensing.

Since the birth of this “molecular electronics” field there have been some highly publicised experimental realisations of molecular devices, including memory devices and switching devices[3] and even molecular logic[4]. However much of this earlier work still incorporated large numbers of molecules and hence was not really making much progress toward the goal of nanoscale electronics. In addition some reported devices based on a few or single molecules suffered from poor characterisation and uncertainty about the actual mechanisms responsible for charge transfer[5].

So what questions need to be answered in molecular electronics? Charge transport in molecules is based on a few charge carriers at the most and the transport mechanisms are far removed from the statistical physics of bulk systems. Phenomena such as single electron tunnelling, hopping, and soliton or polaron motion must potentially be included in the picture of the movement of charge in molecular systems, and thus new paradigms for conduction in molecules are needed. There are also a number of unresolved issues relating to the actual measurement of molecular electronic properties. For example, to physically attach a molecule to metallic electrodes is not a trivial task. The physical dimensions of any single molecule are usually in the range of a few up to perhaps tens of nanometres. The fabrication of static electrodes with such small gaps between them is a challenge in itself, as are the determination of the interfacial coupling at molecule-electrode junction and the achievement of reproducible nano-gaps. Finally, for application to commercial products to be feasible the molecular devices must be stable over time and working temperature ranges, and the cost of industrial manufacture has to be economically attractive.

The clarification of interfacial electronic structure is a key element to understanding nanoelectronic devices[6], especially as metal/organic interfaces will be

important in wiring of devices. The optimisation of device performance depends both on the tuning of the interfacial energy levels between devices and electrodes, and the tuning of the molecular energy levels by chemical modification. Techniques that allow precise, quantitative determination of the properties of nanoscale objects, as a function of physical and chemical variables, are an important part of the molecular electronics drive.

1.2 Importance of scanning probe techniques

Scanning probe microscopy (SPM) techniques have quickly become an indispensable tool in this quest for good characterisation of individual nanoscale objects. The SPM principle is based on the interactions of a very sharp probing tip with the underlying sample surface. In particular the scanning tunnelling microscope (STM), with its ability to resolve individual atoms/molecules and its current sensing capability, has been an indispensable tool in studies of molecular electronic systems. One of the primary goals of molecular electronics is to simply attach an individual molecule between two nano-scale “crocodile clips” and probe its resistance; the means of scanning probe techniques provide an almost unrivalled capability to realise this end.

During the STM experiment the molecules can be imaged on a metal surface using an atomically sharp metallic probe. Regions of the sample surface or even individual molecules can then be targeted and the STM probe tip forced into intimate, but controlled, contact with the sample for a more detailed probing of the electronic properties. The sample surface and tip material can of course be tailored for the specific experiment.

It is expected that the precise nature of the experimental environment should have some effect on the molecular electronic properties. Such an effect could result simply from the differences between the effective through-space tunnelling barrier

(without the molecule) seen when comparing UHV, ambient and liquid environments. In addition the presence of atmospheric water and contaminations such as hydrocarbon molecules may affect the coupling between the molecule and electrode, or provide alternate conducting pathways, hence significantly altering the electronic properties. That the scanning probe techniques can operate in all these environments, and over a range of temperatures, is another illustration of the importance of these techniques.

What is often reported as being the single molecule conductance in any given experiment is more accurately the conductance of the metal-molecule-metal junction or ensemble. Microscopic differences in the atomic details of the metal-molecule contacts can greatly affect the overall electronic properties, but by using SPM techniques one can repeatedly probe the molecular junctions and gain an insight into the statistical or temporal nature of the electronic properties and variations therein.

Discrepancies between early results from different labs hold some clues to the important physical processes underlying the characteristics of such nanoscale conductors. The scope of earlier research was focussed on an issue of limited scientific importance, namely that in the low bias regime of tunnelling transport the molecule is merely an electron scatterer in the junction, like any dielectric material. However, the molecular orbitals provide elastic scattering (Landauer-Imry) channels that facilitate the current flow compared to the bare vacuum gap, and the electronic properties over a range of energies should reflect this. Thus it is of topical interest to extend the measurements on single molecules to higher energies, in particular to dynamically probe the current-voltage characteristics over a wide range of bias.

1.3 Thesis structure

We seek to measure the conductance of individual molecules, which, far from being classical conductors, are a few nanometres in size and have different electronic

structure compared to the equivalent bulk molecular solid, perhaps even acting more as a classical insulator than a conducting material. What happens when we reduce the dimensions of an insulating material to the scale of less than a few nanometres? This is the familiar problem of quantum mechanical tunnelling through a potential barrier, and is pertinent to our discussion in that it forms the basis of the operating principles of the microscopy techniques commonly employed to study nanometre-scale objects. In fact it is this phenomena that allows the scanning tunnelling microscope such precision control and the possibility of sub-angstrom resolution.

In addition one might expect that many molecular species would act as insulating (or semiconducting) materials and charge transport through molecules may well be described by such tunnelling phenomena (Figure 1.1). Thus in chapter 2 we first describe some elements of the theory of quantum mechanical tunnelling through finite potential barriers. This will form the basis for our understanding of the microscopy techniques employed as well as underpinning some of the theory describing charge transport in molecular systems.

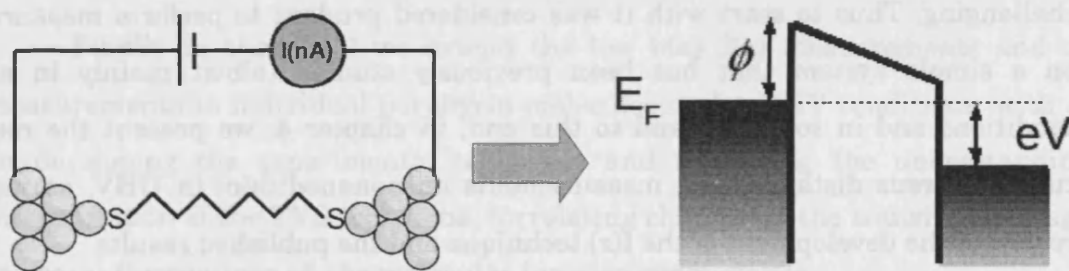


Figure 1.1. The problem of modelling the transport properties of a molecule connected to nanoscale electrodes is often treated as quantum mechanical tunnelling through a potential barrier of height ϕ , separating the electron reservoirs of the two metallic electrodes filled up to the Fermi energy E_F . Under an applied bias V the potential either side of the barrier is displaced and the barrier becomes trapezoidal, and eventually triangular, as V increases.

However the potential barrier picture of conduction through a molecule oversimplifies and removes information relating the specific molecular electronic states to the measured conductance. In this work we examine a relatively simple, and more realistic, model of molecular charge transport, based on transmission through a single, discrete molecular energy level (electron orbital) coupled to metallic electrodes. Together the concepts introduced here and the results of numerical calculations based on these models (see Appendix A) will form the basis for the discussion and interpretation of the experimental results.

The core theme running through this work is the use of STM based techniques to probe the electronic properties of single molecules, particularly under ultra-high vacuum (UHV) conditions. In chapter 3 we present a summary of the experimental and sample preparation techniques and facilities used in this work.

Prior to the commencement of this PhD project measurements of single molecule conductance (SMC) had never been attempted in our lab in Cardiff. In addition the majority of similar measurements performed by others have previously been done with the samples under ambient conditions or in a liquid/solvent environment, so we anticipated that performing such experiments in vacuum may be challenging. Thus to start with it was considered prudent to perform measurements on a simple system that has been previously studied (albeit mainly in ambient conditions and in solution), and to this end, in chapter 4, we present the results of current versus distance, $I(z)$, measurements on nonanedithiol in UHV, as well as a review of the development of the $I(z)$ technique and the published results .

We seek to understand charge transport through π -conjugated oligomers as this is central to the development of molecular electronic devices. Of particular importance are the current-voltage (I-V) characteristics of single molecules when contacted by nanoscale metallic electrodes, which in part are dictated by the energetic alignment between the molecular HOMO/LUMO levels and the Fermi level of the electrodes[7]. Measurements at fixed bias can be used to judge the single molecule conductance, and

low-bias I-V measurements are commonly used to determine the length dependence and effective contact resistance[8], [9], [10] of single molecules. However, wider range I-V characteristics provide a deeper insight into the transport properties over a range of energies[11].

As part of a larger collaborative research project with Richard Nichols' group in Liverpool and Harry Anderson's group in Oxford we investigate the electronic properties of porphyrin molecular wires and the motivation for this work and the results are presented in chapter 5 and chapter 6.

In chapter 5 we examine the I-V characteristics of individual thiol-tethered porphyrin molecules that have been isolated in an alkanethiol matrix. This is compared and contrasted to similar measurements on the alkanethiol monolayer as well as on self-assembled monolayers (SAMs) of the porphyrin molecules. A particular focus is on the analysis of the I-V curves in the framework of “transition voltage spectroscopy” (TVS), which characterises the I-V response in a single parameter, the so called “transition voltage”. At the time of writing the TVS technique and its interpretation is of topical interest as a tool in the characterisation of molecular conductors.

Finally in chapter 6 we extend the low bias $I(z)$ measurements and the I-V measurements to individual porphyrin molecules under UHV conditions, with a focus on developing the experimental technique and furthering the understanding and interpretation of the TVS technique, correlating changes in the transition voltage with temporal fluctuations of the molecular junction conductance.

2 Theoretical background

2.1 Introduction

In this chapter we outline the basic principles of conductance in nanoscale objects using Landauer's scattering formalism. This leads to important expressions describing the theoretical basis of quantum mechanical tunnelling through finite potential barriers. Appreciation of the tunnelling model is important as it not only underpins the operating principles of the scanning tunnelling microscope, but also as it forms a basis for understanding molecular conductance. The same scattering approach is also applied to a more realistic model for molecular systems and together the concepts introduced here and the results of numerical calculations based on these models (see Appendix A) will form the basis for the discussion and interpretation of the experimental results.

2.2 Charge transport through nanoscale insulators

2.2.1 Conductance from transmission

A widely adopted approach to modelling conductance in one-dimensional objects is to treat the system as a scattering problem. Thus the total current is determined by the transmission probability of the scattering object connected to two metallic electrodes. The consideration of conductance arising from the transmissive behaviour of the sample leads to the widely invoked general result[12] that the conductance, at a given energy, between two reservoirs of charge carriers

$$G = T_{av} N_c \left(\frac{2e^2}{h} \right), \quad (2.1)$$

where N_c is the number of channels mediating the current and T_{av} is the average transmission probability of the N_c channels. For a single channel with unity transmission the conductance is the well known conductance quantum $G_0 = 2e^2/h = 77.5 \mu\text{S}$. As a function of energy the current-voltage behaviour for a single one-dimensional channel is calculated from the Landauer formula:

$$I = \frac{2e}{h} \int_{-\infty}^{\infty} T(E) [f_1(E) - f_2(E)] dE \quad (2.2)$$

where $f_{1,2}(E) = [\exp((E - \mu_{1,2})/kT) + 1]^{-1}$ is the Fermi function, at temperature T , and chemical potential $\mu_1 = eV/2$ and $\mu_2 = -eV/2$, for the left and right electrodes respectively. The problem thus remains to define the transmission $T(E)$ for the system being modelled.

2.2.2 Simmons model of tunnelling

Charge transport in molecular systems is often approximated to quantum mechanical tunnelling through a rectangular potential barrier. In this model the regions either side of the barrier correspond to the metallic electrodes connected to either end of the molecule. At equilibrium and low temperature the electrode energy levels are occupied up to the Fermi energy E_F , or equivalently the chemical potential μ , of the metal (5.5 eV for Au). Without molecules or other dielectric material the vacuum tunnelling barrier in the gap between the electrodes corresponds to the metal work-function ϕ (approx. 4.7 eV for Au). For comparison with the experimental results symmetric electrodes ($\mu_1 = \mu_2 = E_F$ at 0 V) are assumed throughout the discussion. The molecule is then simply modelled as a rectangular potential barrier of height $\varepsilon = E_F + E_{\text{mol}}$ and width z (Figure 2.1). Under an applied bias V the chemical potentials of each electrode are shifted relative to one another; In analogy with our experimental set up μ_1 corresponds to the sample electrode and is fixed at 0 V and μ_2 is the STM tip

electrode and is raised by an amount eV . The applied potential eV is dropped linearly across the barrier and a tunnelling current flows in a given direction due to the greater tunnelling probability under the applied bias.

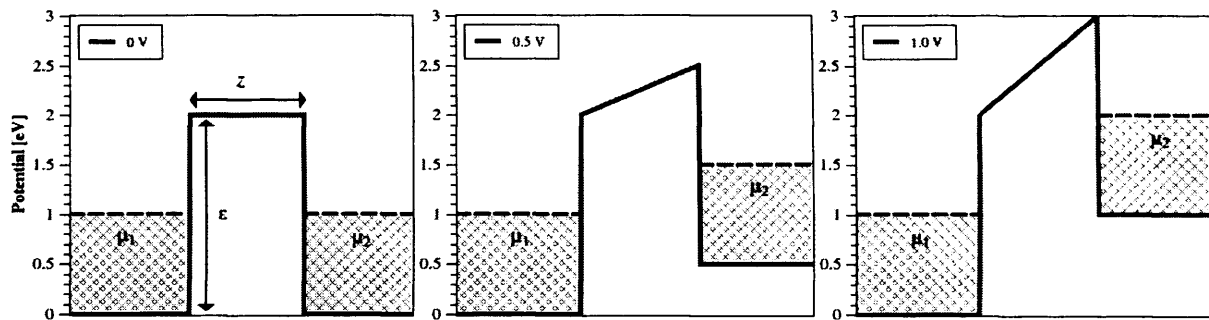


Figure 2.1. Rectangular potential barrier model of molecular conduction. The molecule is modelled as a potential barrier of height ϵ separating two metallic electrodes. The electrodes 1 and 2 are filled by electrons up to the chemical potential of each electrode μ_1 and μ_2 , equal to the Fermi energy E_F of the metal at zero bias. Under an applied bias μ_1 and μ_2 are driven out of equilibrium and current flows as the tunnelling probability in one direction increases relative to the other.

The tunnelling current versus bias is calculated numerically using the semi-classical (WKB) approximation for the transmission $T(E)$:

$$T(E_z) = \exp \left\{ -\frac{4\pi}{h} \int_{z_1}^{z_2} [2m(V(z) - E_z)]^{1/2} dz \right\} \quad (2.3)$$

where $E_z = mv_z^2/2$, the energy of the incident electron in the z direction, and $z_{1,2}$ are the limits of the barrier at the Fermi energy. The electrodes are assumed to have a continuous density of states. Using these approximations Simmons[13] developed full analytical descriptions of the tunnelling current behaviour for a general potential barrier of height ϕ between two infinite parallel plate electrodes. This gives separate expressions applicable at the limits of low ($eV \ll \phi$) and high bias ($eV > \phi$), but under

the assumptions made an expression cannot be written down covering the entire bias range. In the low bias regime, $V \approx 0$:

$$J = [3(2m\phi)^{1/2}/2 \cdot z](e/h)^2 V \cdot \exp[-(4\pi \cdot z/h)(2m\phi)^{1/2}] \quad , \quad (2.4)$$

i.e. the current at low bias can be seen to depend on V and z as:

$$I \propto V \cdot \exp\left(\frac{-2z\sqrt{2m\phi}}{\hbar}\right) \quad . \quad (2.5)$$

In the intermediate bias range, $eV < \phi$:

$$J = \frac{e}{2\pi\hbar z^2} \left(\left(\phi - \frac{eV}{2} \right) \exp\left[\frac{-4\pi z}{h} (2m)^{1/2} \left(\phi - \frac{eV}{2} \right)^{1/2} \right] - \left(\phi + \frac{eV}{2} \right) \exp\left[\frac{-4\pi z}{h} (2m)^{1/2} \left(\phi + \frac{eV}{2} \right)^{1/2} \right] \right) \quad . \quad (2.6)$$

Simmons showed that using a polynomial expansion in $V/(2\phi)$ this may be written as:

$$I \approx G_{(V=0)}(V + C V^3 + P V^5 + \dots) \quad , \quad (2.7)$$

which, if we ignore the fifth order term, we may write [11]:

$$\frac{I}{V} \approx G_{(V=0)}(1 + C V^2) \quad . \quad (2.8)$$

Thus over the low bias region the plot of I/V versus V is approximately quadratic and we may fit the curve to equation (2.8) to obtain the equilibrium integral conductance G (at $V=0V$).

At high bias, the field emission or so called Fowler-Nordheim (F-N) regime, $eV > \phi$:

$$I \propto V^2 \exp\left(-\frac{4z\sqrt{2m\phi^3}}{3\hbar q V}\right); \quad (2.9)$$

This can be linearised and written as:

$$\ln\left(\frac{I}{V^2}\right) \propto -\frac{4z\sqrt{2m\phi^3}}{3\hbar q} \left(\frac{1}{V}\right). \quad (2.10)$$

In this regime a plot of $\ln(I/V^2)$ vs $1/V$, sometimes called a F-N plot, gives a straight line with negative slope proportional to $z \cdot \phi^{3/2}$. Reformulating the low bias expression (2.4) in the same way gives:

$$\ln \frac{I}{V^2} \propto \ln\left(\frac{1}{V}\right) - \frac{2z\sqrt{2m\phi}}{\hbar}, \quad (2.11)$$

giving logarithmic growth on the F-N plot, and hence we can clearly distinguish low-bias conduction from field emission.

A weak temperature dependence arises in any version of the scattering model through the Fermi function $f(E)$ (demonstrated for the molecular model below in Appendix A). However for typical barrier heights and at low bias the effect is negligible and coherent tunnelling is generally regarded as a temperature independent process.

Previously we defined the height of the tunnelling barrier in the form $\varepsilon = E_F + E_{\text{mol}}$ for a particular reason. In the molecule energy level model presented below the relevant parameter is the offset, E_{HOMO} or E_{LUMO} , of the nearest molecular orbital from the Fermi energy of the electrodes. Thus for consistency it is useful to define the barrier height as being equal to E_F plus some offset and in some studies[14] the barrier height extracted from fits to the Simmons model is interpreted as being a direct measurement of $E_{\text{HOMO/LUMO}}$.

Figure 2.2 and Figure 2.3 show examples of the transmission and I-V curves numerically calculated using the Landauer formalism based on the rectangular

barrier model. Figure 2.2 shows a change in tunnelling at fixed barrier height for a small change in barrier width and Figure 2.3 at fixed barrier width with a change in barrier height. Further results of the numerical calculations are given in Appendix A.

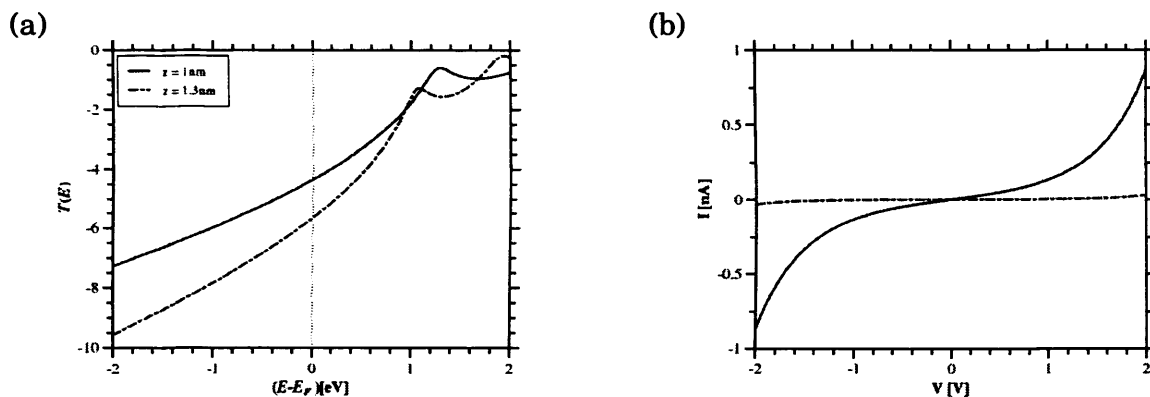


Figure 2.2. Results of numerical calculations for a rectangular potential barrier showing (a) the transmission and (b) the resultant I-V curve for a barrier of height 2 eV and width 1 nm (solid line) or width 1.3nm (dot-dash line)

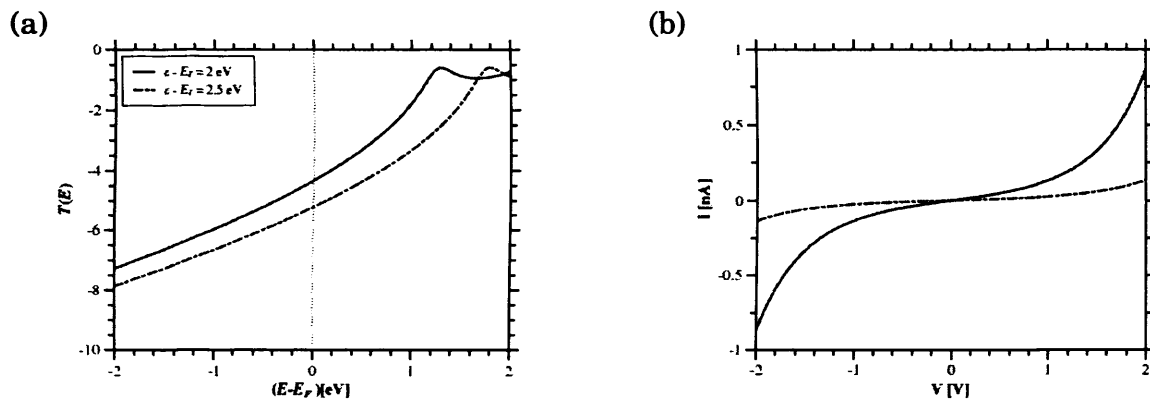


Figure 2.3. (a) transmission and (b) I-V curve for a barrier of width 1 nm and height 2 eV (solid line) or height 2.5 eV (dot-dash line)

It might be expected that certain molecules could act as an insulating material (or very large band-gap semiconductor). However it is not obvious how the parameters of the Simmons model, ϕ and z , would correspond to the real physical properties of the molecule[15]; the rectangular potential profile is unlikely to be a realistic

approximation to the potential distribution in a molecule and the barrier height therefore tells us nothing about the molecular electronic structure (molecular orbitals). There is also growing evidence that the Simmons relations are not generally capable of describing the experimental results on molecular systems [11][15][16][17][18][19][20][21][22]. Instead we use a more realistic approximation to the molecular transmission derived directly from consideration of the molecular electronic orbitals.

2.2.3 Molecular energy level (ML) model

Molecules are comprised of atoms bonded together by the interaction and hybridisation of electron orbitals. To a first approximation the electronic orbitals, wavefunctions, of the molecule can be considered as a linear combination of atomic orbitals (LCAO). Thus the shape and extent of the electron wavefunctions depends greatly on the molecular structure, the nature of the bonds and their orientation. Of particular interest in the design of conducting molecular devices is the degree of conjugation of the electron orbitals.

The term conjugation refers to a delocalisation of electronic wavefunctions due to the overlap and subsequent hybridisation of nearby molecular orbitals. This is seen typically in unsaturated systems such as alkenes (Figure 2.4 b), which are classically considered to be comprised of alternating single and double bonds along the carbon backbone. The electron orbitals of the adjacent C atoms form three hybrid sp^2 orbitals, linear combinations of atomic s and p orbitals. The sp^2 orbitals form the strong, localised σ bond between the atoms and the remaining p orbitals of adjacent C atoms overlap to form delocalised π bonds. The physical extent of the electron wavefunction in the π bond is thus large and facilitates charge transport across the molecule. This is in contrast to the sp^3 hybridisation in saturated alkanes (Figure 2.4 a) forming only σ bonds and hence highly localised electron wavefunctions.

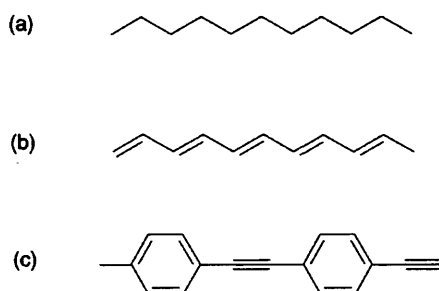


Figure 2.4. (a) Alkane, (b) alkene and (c) linked benzene rings. Tomfohr *et al* [23] calculated the complex band structure for the infinitely extended versions of these molecules.

The ground state occupancy of the electron orbitals defines the highest occupied molecular orbital (HOMO) and the lowest unoccupied molecular orbital (LUMO), analogous to the valence and conduction bands respectively in inorganic semiconductors; the HOMO – LUMO gap being the molecular equivalent of the semiconductor band gap. Considering a particle-in-a-box approximation of the band structure we expect the HOMO – LUMO gap to be large (possibly insulator-like) for non-conjugated molecules, and much smaller for more highly conjugated molecules. Indeed the calculated band gap of the infinitely extended alkane chain (Figure 2.4 a) is ~ 10 eV, compared with that for the infinite alkene (Figure 2.4 b) ~ 1.9 eV and linked benzene rings (Figure 2.4 c) ~ 2.1 eV [23].

Upon physically coupling a molecule to metallic electrodes we in fact couple the electronic states of the molecule to the states of the metal surface. The energetic position of the molecular orbitals relative to the Fermi energy of the electrodes is particularly important and, returning to the semiconductor analogy, the offset of HOMO/LUMO from electrode Fermi level is equivalent to the Schottky barrier height at metal-semiconductor interfaces. It must also be appreciated that the interface energetics, adsorption geometry of a molecule on a metal surface, and the orientation and configuration of the molecule will variously affect the extent of the molecular wavefunctions, their overlap with states of the electrode, and also their alignment relative to E_F .

To realise a strong and stable coupling of metal electrodes to the target molecules chemists typically add functional end groups to the molecule to facilitate direct bonding of the molecule to the metal electrodes. A common example of this is to add thiol (-SH) end-groups to the end of the molecule, which allows strong covalent bonding to Au electrodes. An important point to note is that the S atom at the end of the molecule must change somehow the molecular electronic wavefunctions, especially as the orbitals of the end-group are now hybridised with the metal surface states. The effect on the electronic structure induced by the bonding to the metal is analogous to the metal induced gap states (MIGS) of metal-semiconductor interfaces.

At relatively low bias voltage transport through a molecule will be dominated by the closest molecular level to E_F . Thus we attempt to model charge transport through a single molecule by considering the case of a single molecular energy level (ML), the conducting *channel*, coupled to two metallic electrodes, the electron *reservoirs*. In a one-dimensional model the molecular channel is a discrete quantised energy level ε of the molecule, with a density of states (DOS) that corresponds to a delta function. In contrast the contacts are considered as having a continuous DOS, the familiar sea-of-electrons picture. The effect of coupling to the metallic electrodes is to broaden the energy level into a continuous DOS. The simplistic view is that, upon coupling of the molecular energy level to the contacts, some of the state is effectively “lost” as it spreads into the contact. Equivalently some of the energy states of the electrodes are also “lost” as they spread into the molecular channel. Thus the channel DOS suffers a loss at fixed energy, whilst experiencing a gain over a range of energies and hence the original discrete energy level is broadened through the coupling to the contacts.

This can be more fully understood by considering the density of states of the molecular channel and of the contacts [24]. The electrode is an electron reservoir with a dense, almost continuous, set of energy levels ε . Initially the molecular channel is not coupled to the reservoir and is a single discrete energy level ε (Figure 2.5 a). The expressions for the DOS in each are:

$$\begin{aligned} \text{In the reservoir } D_r(E) &= \sum_r \delta(E - \varepsilon_r) \\ \text{and in the channel } D_c(E) &= \delta(E - \varepsilon_c) . \end{aligned} \quad (2.12)$$

It is the local density of states (LDOS) in the channel itself that will govern charge transport through the channel. Upon coupling of the channel to the contacts the electrode state wavefunctions will have some spatial overlap with the channel state. The LDOS in the coupled channel is thus given by weighting each of the reservoir states by the fraction of its squared wavefunction that resides in the channel, $\psi(d)$:

$$D(d; E) = \sum_r |\psi_r(d)|^2 \delta(E - \varepsilon_r) \quad (2.13)$$

States in the contacts close to the channel will be weighted more strongly and hence the result is a broadened line-shape of the channel LDOS as illustrated in Figure 2.5.

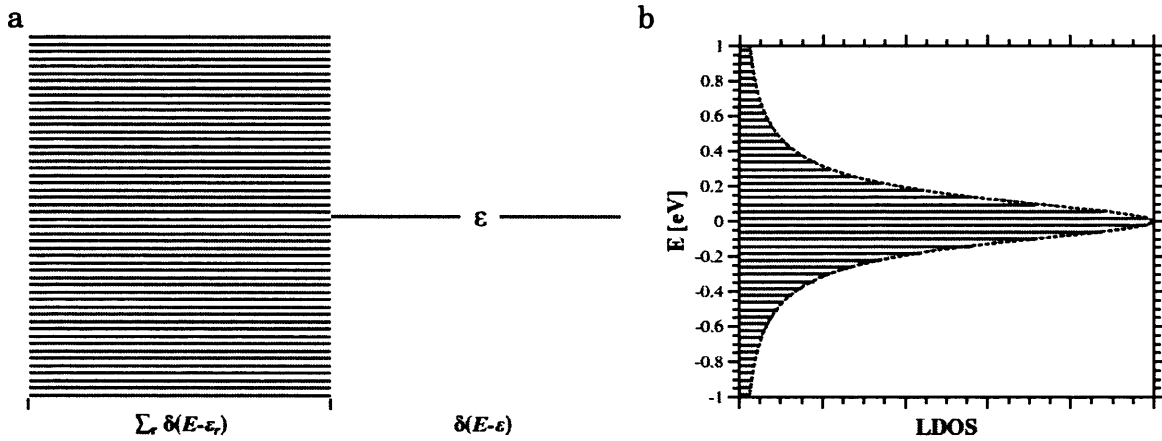


Figure 2.5. (a) The discrete molecular energy level, ε , is coupled to the dense set of contact states, ε_r . (b) As the discrete energy level is coupled to the contacts it is broadened into an almost continuous local density of states.

Returning to the simplified approximation of the contacts having a continuous density of states, we define the broadened channel by its energy, ε , and an additional parameter which describes the total broadening due to the coupling. The shape of the broadened energy level is then most simply approximated by a Lorentzian such that the LDOS in the channel is:

$$D_c(E) = \frac{\Gamma/2\pi}{(\Gamma/2)^2 + (E - \varepsilon)^2} \quad , \quad (2.14)$$

at a given energy E , where ε is the position of the energy level ($\varepsilon_{\text{LUMO}}$ or $\varepsilon_{\text{HOMO}}$ as previously defined) and Γ is the total broadening of the level due to coupling to the contacts, the sum of the individual contributions Γ_1 from the sample electrode and Γ_2 from the tip electrode [18][24]. The transmission is thus written down as:

$$T(E) = \frac{\eta(1-\eta)\Gamma^2}{\Gamma^2/4 + (E - \varepsilon)^2} \quad . \quad (2.15)$$

The parameter $\eta = \Gamma_1/\Gamma = (1 - \Gamma_2/\Gamma)$ defines the asymmetry of the coupling, i.e. $\eta = 0.5$ denotes symmetric coupling. We make the reasonable ansatz that under applied bias V the energy shift of the molecular level (with respect to the sample electrode, or ground) is $(1-\eta)V$. Thus in the case of no coupling to the tip, $\eta = 1$, the potential in the molecular channel is that of the sample electrode and the voltage is dropped entirely at the tip contact; at $\eta = 0.5$ half the voltage is dropped at each contact. (Strictly speaking the potential in the molecular channel will be affected by the transfer of electrons into the channel, which in turn affects the density of states and hence the transmission, therefore a self-consistent solution to the potential is needed; this is beyond the scope of the current work). The I-V relationship is then calculated from the Landauer formula as previously outlined.

Figure 2.6 and Figure 2.7 show examples of the transmission and I-V curves numerically calculated using the Landauer formalism based on the ML model. Figure

2.6 shows the effect of a shift in the energy level offset ($\varepsilon - E_F$) at fixed coupling, and Figure 2.7 shows the effect of changing the coupling at fixed energy level offset. Further results of the numerical calculations are given in Appendix A.

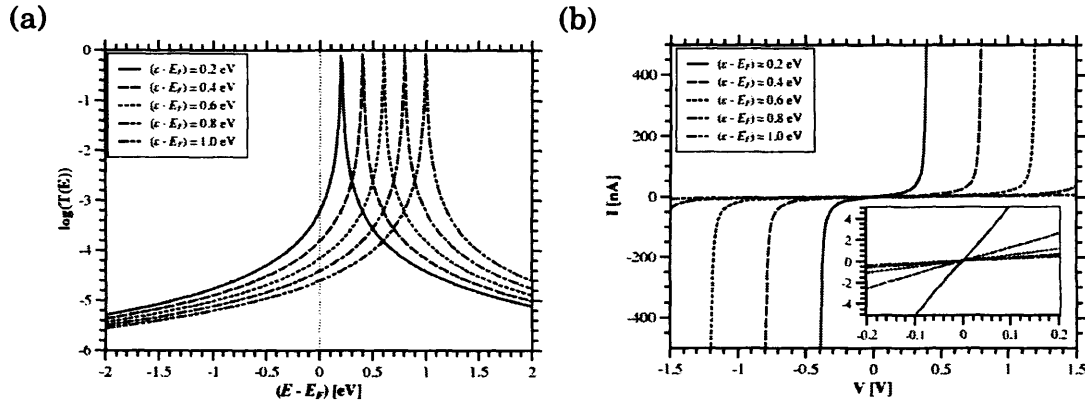


Figure 2.6. Results of numerical calculations based on the molecular energy level model. (a) transmission and (b) the resultant I-V curves for varying energy level offset ($\varepsilon - E_F$) (see legend) and fixed coupling ($\Gamma = 0.01$ eV).

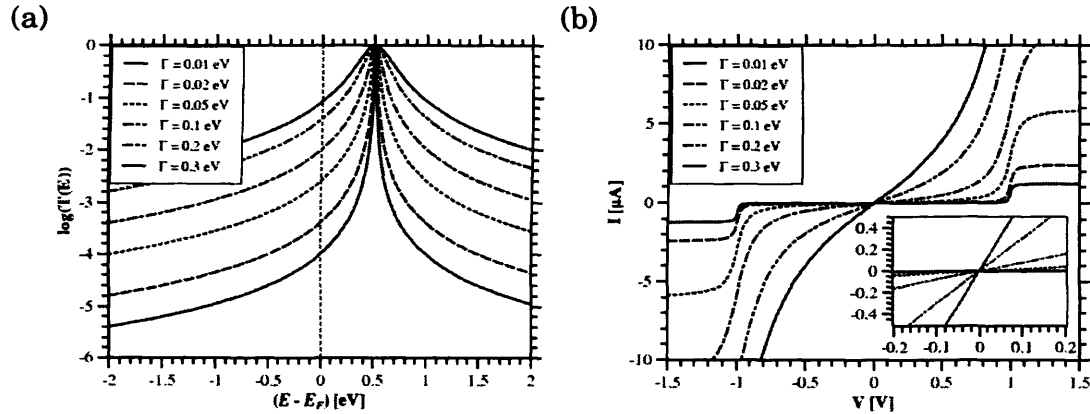


Figure 2.7. (a) transmission and (b) I-V curves for varying coupling (see legend) and fixed energy level offset ($\varepsilon - E_F = 0.5$ eV).

Before we use this ML model, we must discuss and appreciate its limitations. We have made several assumptions to arrive at this simplified view of molecular conductance. We have assumed a single broadened energy level with a given line-shape. A more realistic model of $T(E)$ must at least include higher energy levels, above

and below E_F , especially in the case of highly conjugated molecules where the HOMO/LUMO levels may be accessible at relatively low bias voltage. It is also probable that the broadening and energetic alignment of the molecular orbitals will depend slightly on the applied bias voltage, thus in a realistic model $T(E) \Rightarrow T(E; V)$. Also, as previously discussed, $T(E)$ is likely to be highly dependent on the microscopic details of the metal-molecule-metal junction and this is something which will be evident in our experimental results.

Much of the theoretical research into molecular charge transport is focussed on calculations of the correct DOS, and hence $T(E)$, for a given molecule. A common approach used is density functional theory (DFT), in which quantum mechanical calculations are performed using approximations to the density functional instead of attempting to solve the N -electron Schrödinger equation. The DFT approach is successful in computing the equilibrium density of states [25][26], thus gives a more accurate description of $T(E)$, but due to the ground-state nature of this treatment the full current-voltage characteristic is nevertheless still only qualitatively accurate. Finally we must acknowledge that this transmission approach is but one view of charge transport mechanisms in molecular systems.

Experimental evidence from studies of molecular conductance suggest that transport in many molecular systems is indeed consistent with the coherent scattering/tunnelling models, that is to say that conductance decreases exponentially with molecular length and is temperature independent. However other charge transport mechanisms can be proposed and may act in parallel. One such scheme is the hopping mode of charge transport.

In this mechanism charge transport is via a multi-stage “hopping” of charge carriers between sites on the molecule that allow some localisation of excess charge. A characteristic of hopping transport is that the process is thermally assisted; the hopping rate and, hence conductance, is increased with temperature. In addition the conductance is linearly dependent on molecular length, in contrast to the exponential

length dependence of barrier tunnelling. This mechanism can be particularly important through longer molecules, where the probability of direct tunnelling is very low, and recent experiments on a homologous series of conjugated oligomers suggests that the two mechanisms operate in parallel [20] with the hopping contribution becoming significant only in the longer molecules.

Additionally there is evidence that in some molecular systems, or metal-molecule systems, charge transport is dominated by electron-electron interactions e.g. exhibiting single electron tunnelling (SET) (or Coulomb blockade)[27][28], or Kondo resonances[29]. SET is considered to occur in special instances where the charging energy of the molecular channel is greater than either k_bT or Γ , and experimentally SET is characterised by staircase like I-V characteristics and specific gate-electrode dependence resulting in typical “Coulomb-diamond” plots. Incorporation of electron-electron interactions into the model requires a more sophisticated treatment, although the results obtained in this thesis are not generally suggestive of this behaviour for the molecular systems studied.

It is clear that the assumption of one simple model will not be adequate to describe charge transport in all molecular systems, nevertheless the ML model contains much of the necessary physics needed to understand published results on many molecular systems as well as the results presented herein. Needless to say the theoretical modelling of molecular electronic properties constitutes a large amount of the research effort in this field.

In summary we have outlined the principles of conductance in nanoscale objects from a transmission point of view. Current voltage characteristics can be calculated for transport through the scattering channel if the energy dependent transmission function can be written down. This approach leads to the well known approximate analytical expressions for the current through a rectangular potential barrier and numerical calculations can also be performed. We also discussed a molecular model of

charge transport based on considerations of molecular orbital wavefunctions. The same transmission approach can be used to calculate current voltage characteristics for a molecular energy level coupled to metallic electrodes.

3 Experimental background

3.1 Introduction

In the previous chapter we outlined the basic theory underpinning the tunnelling/scattering models of charge transport in nanoscale objects, and also forming the foundations of the operating principles of the microscopy techniques employed in molecular electronics research. In this chapter we present a summary of the experimental and sample preparation techniques and facilities used in this work. Briefly details of the ultra high vacuum equipment are given; more comprehensive descriptions of vacuum principles, equipment and procedures can be found in numerous published texts on the subject. The principles and modes of operation of the scanning tunnelling microscope are presented (see also Chapter 2). Finally the principles of photoelectron spectroscopy are outlined.

3.2 Ultra high vacuum (UHV) facilities

Much of the experiments performed in this thesis have been done under ultra high vacuum (UHV) conditions. The Omicron[30] UHV system (Figure 3.1) houses a variable temperature scanning probe microscope as well as an Ar^+ ion source for sputtering and X-ray and ultraviolet sources and electron detector for photoemission experiments. Samples can be kept under UHV conditions, at typically 10^{-9} to 10^{-10} mbar, for the duration of an experiment and longer. This enables us to minimise the contamination and oxidation of the sample from atmospheric gases, especially H_2O , and to explore the possible effects of performing a measurement in vacuum compared to ambient conditions. The system can be routinely baked to ensure good vacuum conditions are maintained.

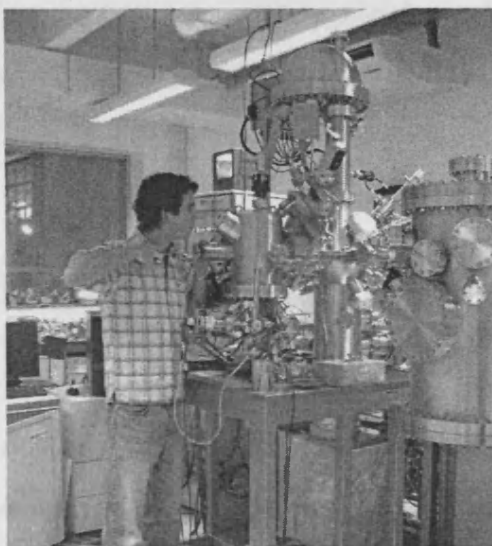


Figure 3.1. Omicron UHV system in use.

3.2.1 Sample transfer and storage

Samples for analysis are introduced to the UHV system via a loading chamber which is then sealed and pumped for several hours to achieve a low pressure. The sample is then transferred to the main chamber which is maintained at UHV. The sample may be manipulated and transferred within the UHV system by using a system of externally controlled transfer arms and manipulator stages.

3.2.2 Ion sputtering and sample annealing

For preparation of clean and crystalline metal surfaces, e.g. Au(111), in-situ sputtering and annealing is used. An argon ion source is used to remove the surface layers of e.g. a Au single crystal, by exposing the sample to a beam of high energy ions for a period of time. Subsequently the sample is annealed by passing a current through a polyboron-nitride heating element built into the sample manipulator. The sputtering and annealing process is often repeated for several cycles to achieve an atomically flat, clean crystal surface.

3.3 Scanning probe microscopy

The term scanning probe microscopy refers to a class of microscopy in which imaging at sub-wavelength resolution is achieved via the interaction between a sharp probe and the sample being studied. The archetypal SPM experiment involves raster scanning the probe over the sample surface to build up a three dimensional image of a small area, i.e. two spatial dimensions (x,y) plus a third dimension, which is some physical parameter that depends on the type of experiment and is characteristic of the interaction between the tip and sample. The scanning tunnelling microscope is but one example of such an instrument, but its ability to combine atomic/molecular resolution imaging with current sensing abilities makes it an ideal technique to explore molecular electronic properties.

3.3.1 Scanning tunnelling microscopy (STM)

The scanning tunnelling microscope was invented in 1982 by Binnig and Rohrer[31] at IBM Zurich and, due to its unprecedented ability to resolve the atomic structure of flat conducting surfaces and manipulate individual surface atoms, would go on to win them the Nobel prize in physics in 1986. STM was the first example of a scanning probe microscope and its basic elements and operating principles are common to all the variants that have followed. The microscope exploits the quantum mechanical tunnelling effect to achieve surface sensitive probing with picometre precision.

A sharp metallic tip, etched or cut from a metal wire, acts as the probe. The tip is brought close to a conductive surface under d.c. bias and the gap between the tip and sample acts as a potential barrier to charge transport. The transmission through the barrier depends on both the height and width of the barrier, as in the Simmons

model of tunnelling (see Chapter 2). If the tip-sample separation is sufficiently small (less than a few nanometres) a tunnelling current can be measured in the range of pico-amps up to several hundred nano-amps, depending on the precise separation of the tip and sample.

The tunnelling current is approximately exponentially dependent on the barrier width, therefore the measured current is a highly sensitive indicator of the tip-sample separation. In addition by using a sharp probing tip the tunnelling barrier will be confined to the very end atoms at the apex of the tip, further enhancing the sensitivity of the current to vertical and lateral displacements of the tip relative to the sample surface. To map the tip-sample interaction the probe is typically raster scanned across the sample surface using piezoelectric motors to build up an image, one line at a time. In the constant-height mode the tip vertical displacement is fixed and an image of the spatial variation over the sample surface of the tunnelling current is obtained. This is of limited use and is also restricted to very flat surfaces due to the high sensitivity of the current to even very small changes in tip sample separation. Instead more commonly used is the constant-current mode of operation.

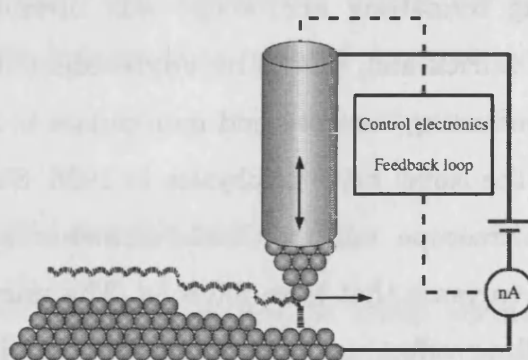


Figure 3.2. Cartoon representation of the STM experiment. In close contact a tunnelling current I_t flows between the biased tip and the sample. A feedback loop regulates the height z by applying a voltage to the z -piezo motor that depends on the magnitude of the measured current.

In this mode a feedback loop is used to keep the tunnelling current constant at all times by varying the probe vertical displacement (z) using the z -piezo motor, as the probe is scanned (Figure 3.2). This current value is known as the setpoint current. The feedback response is proportional to the current magnitude, thus the tip sample distance can be closely controlled and the sample topography can be mapped. It must be noted that to a good approximation the tunnelling current at fixed bias depends on the density of the available sample states at that energy (and hence STM is limited to the study of conductors). Thus the sample “topography” being imaged is better described as a surface of constant density-of-states, i.e. it is a convolution of the electronic and topographic properties of the sample surface.

For experiments in UHV the microscope is an Omicron VT-AFM model [30]. The microscope is equipped with two current amplifiers limited to 3.3 nA (low current amplifier) and 330 nA (high current amplifier); the tip-sample bias is variable in the range ± 10 V. The sample temperature may be varied in situ by He cooling down to a minimum of ~ 40 K, or heating using sample plates with inbuilt heating elements. For other experiments we use a Veeco multimode III SPM [32], keep in a home-made glove-box under flowing N_2 to reduce the ambient humidity. In both microscopes the STM tip electrode is biased, while the sample is kept at ground.

Atomic resolution - Si(111) 7×7

As a standard test for good operation of the STM in UHV we perform imaging experiments of the Si(111) 7×7 reconstructed surface. UHV is particularly important in this test to prevent oxidation and contamination of the freshly prepared Si surface. The sample surface is prepared from silicon wafer with native oxide by slowly degassing and annealing under vacuum followed by flash annealing to remove the oxide layer. Figure 3.3 shows that atomic resolution of the 7×7 surface reconstruction can be achieved as well as illustrating surface defects where individual atoms are missing.

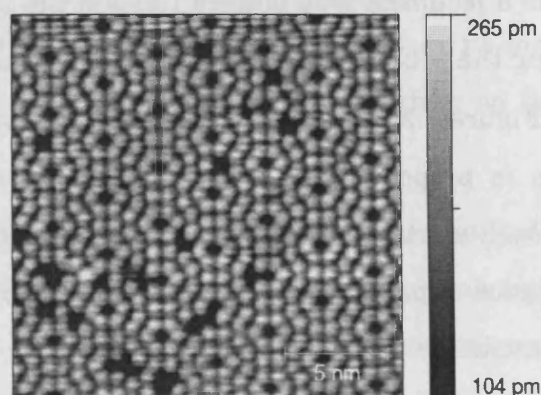


Figure 3.3. STM image of Si(111) 7X7 reconstructed surface; bias = 1.8 V, setpoint = 0.2nA, etched W tip.

STM for contacting single molecules

In experiments on single molecules the STM can be used to provide the nanoscale contacts needed to wire a molecule into an electrical circuit. Figure 3.4 shows a cartoon illustration of the typical STM based single molecule conductance experiment. The molecule of interest is attached at one end to the sample surface and at the other end to the STM tip. The STM spectroscopy techniques outlined below can then be used to probe the properties of this wired-up molecule.

To form a strong contact to the electrodes the molecules of interest are usually synthesised with particular end groups that bind chemically to the metal of the tip and sample surface. The molecules are then dispersed over the metal surface (in this thesis all molecules are deposited from a solution phase) and the STM tip can be brought down close to the surface in an attempt to form a metal-molecule-metal (MMM) junction. If the molecule can attach to both the tip and substrate simultaneously it has effectively become a component in an electrical circuit.

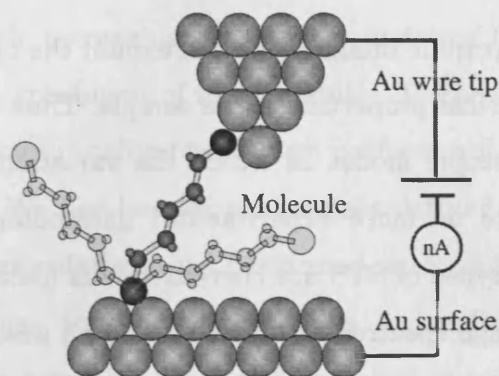


Figure 3.4. Cartoon illustration of a typical experiment to probe the electronic properties of a single molecule using the STM.

The chemical attachment of the molecule to the metal electrodes could be realised in a number of ways, however there are several of factors to consider before choosing a particular method and we must also consider the choice of electrode material. In our experiments, as in the majority of the published work, we use Au as the tip and substrate metal for several reasons. Firstly Au is relatively inert and thus will not oxidise easily when exposed to ambient conditions. Secondly it is desirable to use the same metal for both the tip and substrate so that the electrical properties of the MMM junction are not affected by chemical asymmetry of the electrodes. Au can easily be cut or etched to form sharp probing tips and for the substrate, flat, crystalline surfaces with large terraces can easily be formed by a number of methods. Finally, Au has the added advantage that it binds strongly to sulphur and thus a -thiol (-SH) group added to a molecule is a simple way to facilitate strong chemical binding to the Au electrodes. This reasoning has steered the course of experiments since the beginning of research into single molecule electronics and forms the basis of our experimental approach, although more recently it has been shown that other functional groups can provide effective binding to Au electrodes, some of which perhaps provide a more reliable contact than the Au-S bond [10][33].

3.3.2 Scanning tunnelling spectroscopy (STS)

Beyond topographic imaging one can exploit the operating principles of the STM to explore the electrical properties of the sample. Thus the STM can be operated in a number of spectroscopic modes in which the variation in the tunnelling current is recorded whilst one or more experimental parameters are varied. The two most common and basic types of STS are current versus distance spectroscopy – $I(z)$ – and current versus voltage spectroscopy – $I(V)$; we shall describe these modes of operation below.

Current versus distance – $I(z)$

In $I(z)$ spectroscopy the tunnelling current is monitored as the tip-sample distance is varied at fixed bias voltage. The tunnelling theory presented in chapter 2 predicts an exponential dependence of the tunnelling current versus distance, with current density

$$J = [3(2m_e\phi)^{1/2}/2 \cdot z](e/h)^2 V \cdot \exp[-(4\pi \cdot z/h)(2m_e\phi)^{1/2}] \quad . \quad (3.1)$$

Typically we define a parameter,

$$\beta_s = (4\pi/h)(2m_e\phi)^{1/2} \quad , \quad (3.2)$$

and we see that the exponential term dominates, so the current at a given bias varies approximately exponentially with the tip sample distance, viz. $I \propto \exp(-\beta \cdot z)$, i.e. for Au $\phi = 4.7$ eV which gives $\beta = 22.2 \text{ nm}^{-1}$.

Thus the parameter β (in units of \AA^{-1} or nm^{-1}) is the slope of the $\ln(I)$ versus z curve and is often used to characterise the tunnelling barrier. At high bias (F-N) the equivalent expression is:

$$\beta_{FN} = \frac{8\pi\sqrt{2m_e}}{3e \cdot h \cdot V} \phi^{3/2} \quad . \quad (3.3)$$

Over a clean metal surface the resulting curve is the expected exponential decrease in current with increasing tip sample distance (see Figure 3.5; also see chapter 4 for a thorough treatment of these results). To check the expected results for Au based on the Simmons tunnelling model, we perform full numerical calculations of the $I(z)$ characteristics. We use barrier parameters defined for Au electrodes with a bare vacuum gap. The calculations are performed with and without the inclusion of the effect of image forces on the potential (see Appendix A). A linear fit to the calculated $\ln(I)$ versus z curve confirms the expected exponential decay and gives a decay parameter $\beta = 22.2 \text{ nm}^{-1}$ (or 20.3 nm^{-1} for the near exponential fit with the image potential included).

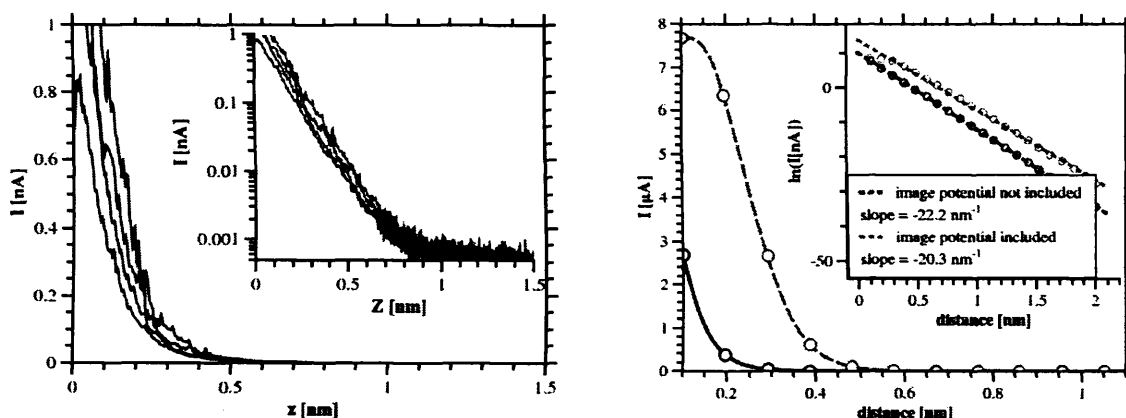


Figure 3.5. (Left) Example of 4 successive $I(z)$ measurements showing the exponential decay of the tunnelling current versus distance over a Au(111) single crystal surface with a Au STM tip; the inset shows the same curves on a semi-log plot. (Right) Results of numerical calculations based on the Simmons tunnelling model. Barrier parameters: $E_F = 5.5 \text{ eV}$, $\phi = 4.7 \text{ eV}$ and bias = 100mV for Au electrodes. Results with (grey) and without (black) the inclusion of the image potential. Inset shows linear fits to the $\ln(I)$ versus distance curve.

With β on the order of 20 nm^{-1} at any given current an atomic scale fluctuation of e.g. 1 \AA will see the current change by a factor of $\exp(2) = 7.39$. In addition the previously reported features in $I(z)$ curves due the presence of molecules may typically span more than one order of magnitude in current, in a single measurement. Thus for both these reasons it is natural and useful to visualise the $I(z)$ curve on a semi-log scale.

Current versus voltage – $I(V)$

In $I(V)$ spectroscopy the tunnelling current is monitored as the bias voltage between the tip and sample is varied. In the Simmons formalism approximate analytical expressions for high, low and intermediate bias ranges can be written (these are presented in chapter 2), and we may also easily do full numerical calculations based on realistic transmission models to compare with the experimental results.

Current as a function of time – $I(t)$

This is conceptually the simplest form of spectroscopy mode. When operated in the typical imaging mode the tunnelling current can be monitored and recorded, however the feedback loop continuously regulates the tip-sample distance to keep the current constant, and thus the current channel does not contain any useful information except to serve as an error signal. In contrast as a spectroscopy mode the tunnelling current can be sampled for a given period of time with the feedback loop switched off. So the tunnelling current is simply recorded as a function of time, with the probe held at a fixed position (i.e. in the absence of feedback) and at fixed bias voltage. This method enables us to monitor any fluctuation in the tunnelling current that may be the result of spontaneous changes in the microscopic details of the tip or sample electrodes or indeed the medium between them. Figure 3.6 shows some examples of $I(t)$ measurements; fluctuations and discrete jumps in the current (plotted here as conductance = I/V) may occur over time. Using lock-in techniques to simultaneously record the differential conductance and filter random noise, we see that the dI/dV signal closely follows the $I(t)$ signal. Thus the fluctuations and jumps in the tunnelling current cannot be explained by random noise, but instead represent real changes in the tunnelling conditions. In particular the discrete jumps in $I(t)$ signals in the presence of molecules are thought to be caused by molecular attachment/detachment events or configuration switching of an attached molecule[34].

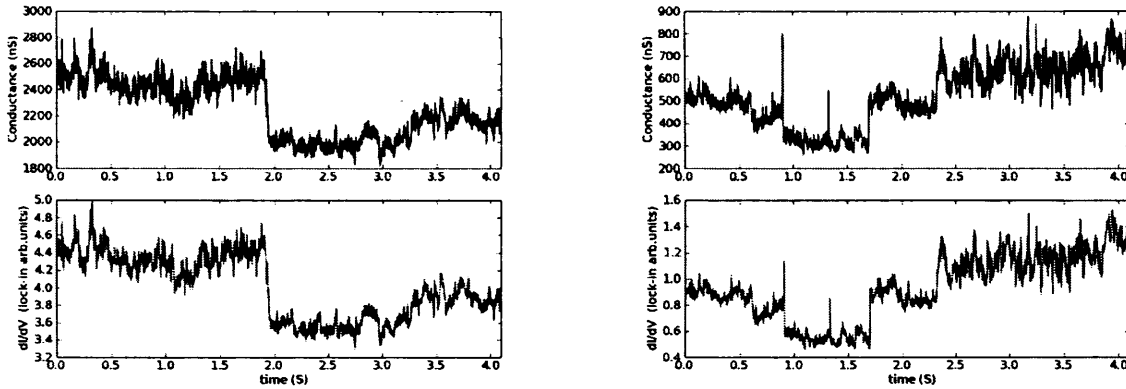


Figure 3.6. Conductance (I/V) and lock-in (dI/dV) versus time measured over a sample of porphyrin dimer molecules on Au (measured in parallel to the results shown in chapter 6)

3.4 Photoelectron spectroscopy

Photoelectron spectroscopy (PES) refers to a class of surface sensitive techniques to probe the electron band structure of a sample using electromagnetic radiation. In a typical experiment a monochromatic beam of electromagnetic radiation is incident upon the sample and an electron detector is scanned to measure the energy distribution of the emitted electrons. Using a helium source at He(I) resonance of $h\nu = 21.22$ eV an ultraviolet photoelectron spectroscopy (UPS) experiment measures the energy of electrons excited from the upper electron orbitals. Using a twin anode source the X-ray photoelectron spectroscopy (XPS) experiment is done using either a Mg $K\alpha$ (1253.6 eV) resonance or an Al $K\alpha$ (1486.6 eV) resonance to excite the core electrons. The kinetic energy of an emitted photon in each type of experiment is directly related to the binding energy of the electron in the solid state due to the monochromatic excitation.

3.4.1 Ultraviolet photoelectron spectroscopy (UPS)

Consider the energy levels of electrons in an atom and recall that the levels (atomic orbitals) are discrete and quantised and that the spacing between adjacent energy levels decreases with increasing energy. Core electrons in a molecule or bulk solid are still confined to localised atomic orbitals and therefore the energy spectrum of such core electrons as obtained by XPS is highly element specific, showing well defined peaks which can often be identified as coming from a specific element by comparing with library values. In contrast the upper electron orbitals interact to form hybridised (sometimes delocalised) molecular orbitals, so these are energy levels of the entire molecule. A few useful definitions are required to enable further discussion (Figure 3.7): The separation of the highest occupied molecular orbital (HOMO) from the vacuum level is called the gas phase ionisation potential (I_g) and that of the lowest unoccupied molecular orbital (LUMO) from the vacuum level is the electron affinity (A_g). The work function (Φ) is defined, as in a metal, as the separation of the Fermi level and the vacuum level. A and I of the molecular solid differ from the single molecule values due to a multi-electronic effect in which polarisation of molecular charge helps stabilise ions and thereby reduce the ionization potential. I and Φ can be determined by UPS measurements (Figure 3.7(b)), thus UPS experiments can provide information regarding charge transfer and/or dipole formation at the metal-molecule contact[35].

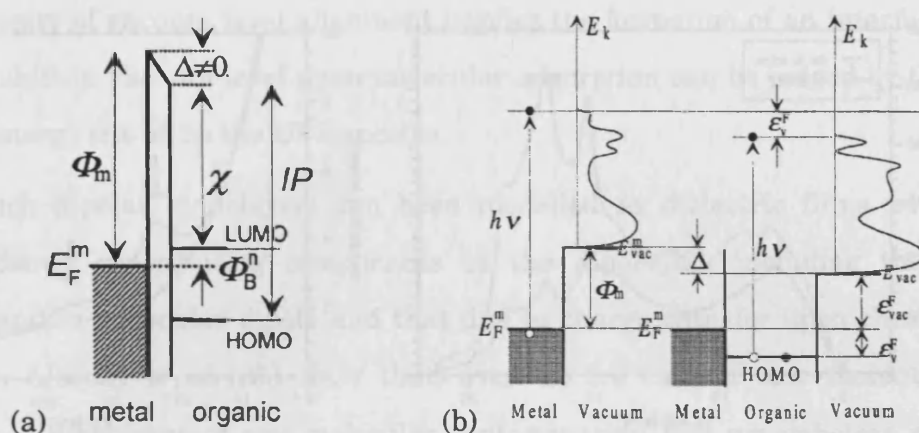


Figure 3.7. (a) Electronic structure at the organic-metal interface (the electron affinity is labelled χ here). (b) Cartoon UPS spectra (shown side-on) of a metal surface (left) and then the same metal surface with an organic layer (right). Comparison of the two spectra yields information on the vacuum level shift $\Delta = E_{vac}^m - E_{vac}$, the difference, ϵ_v^F , between the metal Fermi level (E_F^m) and the HOMO and the difference ϵ_{vac}^F between ϵ_v^F and E_{vac} . Reprinted from [35]

Figure 3.8 shows the UPS spectrum of both bare Au and Au with Ni-octaethylporphyrin molecules. Without the molecules the spectrum reflects the valence band structure of the Au surface; with the addition of the porphyrin molecules the peaks from the Au surface are somewhat attenuated by the molecular layer and additional peaks appear (black arrows) that are related to the energy levels (orbitals) of the molecule. In the following section we will further discuss some of the key points relating to surface/interface energetics (gathered from UPS literature), as is pertinent to our understanding of molecular electronics, although the UPS technique itself will not be used extensively in this work.

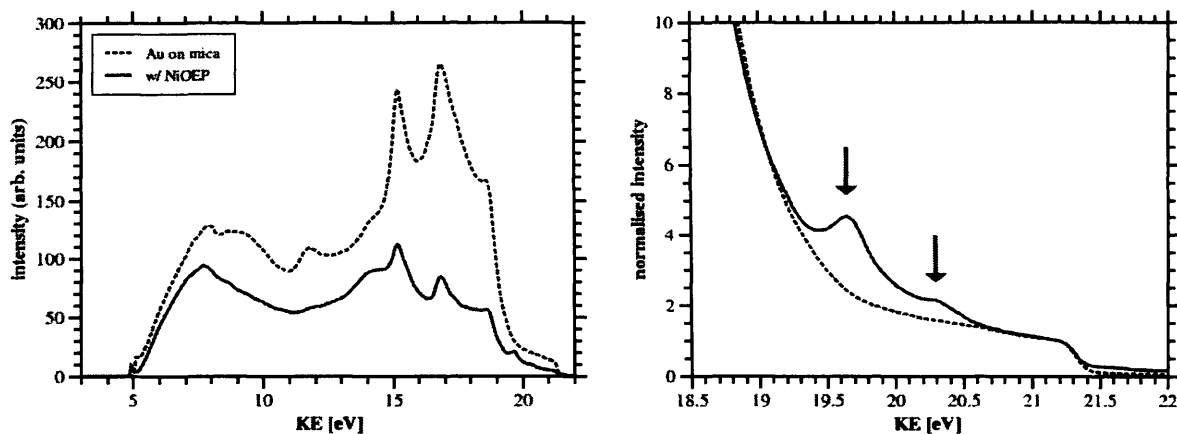


Figure 3.8. UPS spectrum of bare Au (solid line) and of Ni-octaethylporphyrin molecules on Au.

3.4.2 Reduced work functions: Surface dipole

It is common to consider the vacuum energy level of an electron as being the energy of the electron removed from a solid and placed at an infinite distance away; this is an invariant reference energy. However, the effective vacuum level of the electron we measure in a PES experiment is the energy just outside the solid surface and is influenced by the potential at the surface. This vacuum level may differ for different solid surfaces and is in fact the origin of the well known work function variations between different crystal faces of the same metal. When we create an interface between two solids these vacuum levels must align, hence there is a relative shift in the energy levels of the materials. Thus the energetic distance between an orbital in an adsorbate molecule and the Fermi level of the metal surface will depend on the interface energetics.

In analogy with bulk semiconducting materials Fermi level alignment between the metal surface and the molecular layer is possible by band bending. However this requires a sufficiently thick molecular layer to accommodate the associated charge transfer, so in general Fermi level alignment is unlikely to be achieved in molecular monolayers (either those intentionally deposited or layers of contaminants). Instead

the necessity of vacuum level alignment implies the formation of an interfacial dipole [6]. The shift in vacuum level upon molecular adsorption can be judged by the shift of the low energy cut-off in the UPS spectra.

Such dipolar monolayers can be modelled as dielectric films with several independently contributing components to the dipole[36], including the intrinsic surface and/or molecular dipole and that due to charge transfer upon chemisorption. However, Alloway *et al* [37] show that, even in the case of zero molecular dipole moment, a monolayer of *any* molecular contamination will nevertheless modify the effective work function of the Au surface by shifting the vacuum level, illustrated by the case of physisorbed, nonpolar Xe atoms where the work function is reduced by around ~0.5 eV.

To illustrate the case of chemisorption Ito *et al* [38] showed a work function reduction of ~0.45 eV when the non-polar, non-bonding hexadecane molecule was deposited on Au(111); in contrast the work function reduction for hexadecanethiol was ~0.9 eV. Finally, Zangmeister *et al*[39] observed the vacuum level shift for isocyanide and thiol linked molecules as a function of metal work function and posit that the electrostatics of the interface region plays a more important role in energy level alignment than does the local density of states of the molecule and electrodes. Thus the details of the metal-molecule linkage determine the rigid shift of the molecular energy levels relative to the Fermi energy, but the shape of the I-V characteristic is dominated by the availability of levels near E_F (see the ML model, Appendix A).

4 Single molecule conductance of nonanedithiol

4.1 Introduction

This chapter is intended as an introduction to the STM based techniques for measuring the conductance of single molecules. Most importantly this chapter provides a basis for understanding and interpreting the results of experiments on porphyrin molecular wires, as presented in chapters 5 and 6. The experimental results presented in this chapter serve primarily to illustrate the techniques and to build a knowledge and experience base to guide the main experiments on the porphyrin molecules.

Herein we review the literature surrounding the development of the current versus distance, $I(z)$, experimental technique and discuss the current state of understanding of the results from these measurements. We show that the results of the $I(z)$ method are consistent with the molecular energy level model of charge transport previously outlined in chapter 2. We finally present measurements on nonanedithiol molecules in ultra high vacuum, for comparison with published results in air and solvent environments.

4.2 Alkanedithiols

The most widely studied molecular system in the field of single molecule electronics is the family of α,ω -alkanedithiol molecules. Alkane chains are the simplest organic molecules that can be studied, the chemical synthesis is facile and the compounds are commercially available. This family of molecules consists of a chain of n singly bonded carbon atoms, the alkane chain (familiar to the reader as those common petrochemicals methane, ethane, propane, butane, etc.), with a terminal -thiol (SH) group at each end of the molecule (hence “ α,ω ”), as illustrated in Figure 4.1. The

thiol group provides chemical bonding to the Au electrodes, typically via automatic deprotonation of the -SH to form an alkanethiolate[40] and then subsequent formation of a strong Au-S covalent bond[41]. Molecules with a single thiol group, alkanethiols, have been shown to form well ordered monolayers on Au(111) surfaces [42], hence these and similar molecules have been used variously to effectively tune the work function of a metal surface[37], to protect [43] and functionalise [44] metallic nanoparticles and to form a host matrix in which to isolate other molecules[45]. The S ... S length L in nm of a linear alkane(di)thiol molecule with n CH₂ groups is given by the empirical equation[46][47]:

$$L = (1,2) \times 0.25 + 0.127n \quad . \quad (4.1)$$

An alkane chain is considered to be nominally insulating as the HOMO-LUMO gap is large at ~8 eV[48]. Given this fact the mechanism of charge transport through an alkane molecule is expected to be quantum mechanical tunnelling through a potential barrier. The characteristics of this tunnelling barrier must be related to the length of the molecule and the alignment of the electrode Fermi energy in the HOMO-LUMO gap of the molecule. Chemists can easily synthesise a range of alkanedithiol molecules with different lengths by simply changing the number of carbon atoms, and, at least in this particular chemical system, this change does not greatly affect the molecular orbitals; the HOMO-LUMO gap is virtually constant with increasing chain length[36]. These facts have made it possible to examine systematically the length dependence of conduction over a homologous series of molecules[48][49][9][22][50].

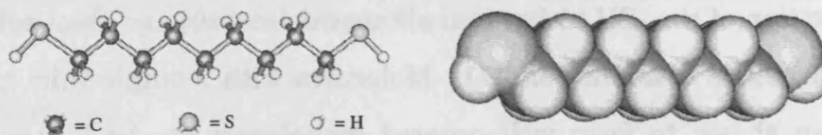


Figure 4.1. Structure of 1,9-Nonanedithiol (1,9-Dimercaptononane; $\text{HSC}_9\text{H}_{18}\text{SH}$). (left) Ball and stick diagram and (right) space filling diagram.

Thus by choosing to study at least one alkanedithiol molecule we will prove in principle that the experiments can be performed under vacuum conditions; we will be able to compare the results to published results for the same molecules in ambient conditions; we will also be able to compare and contrast the results from the alkanedithiol molecules with what we see with the porphyrin molecules. After some consultation with the group in Liverpool we chose to study 1,9-nonanedithiol (1,9-Dimercaptononane; $\text{HSC}_9\text{H}_{18}\text{SH}$) as a suitably intermediate molecule in the alkanedithiol series; the molecule is neither too long nor too short to prove experimentally challenging and the expected conductance[9] is well within the range of measurable current, over a range of bias voltage. (In retrospect it may have been better to study 1,8-octanedithiol or 1,10-decanedithiol as there is more published data on these molecules). In this chapter we focus on the $I(z)$ technique for measuring single molecule conductance.

4.3 $I(z)$ technique

As previously introduced (chapter 3) $I(z)$ is a general term for experiments in which the current (I) versus the relative separation (z) of the electrodes is measured. In the presence of molecules on the metal surface this spectroscopy technique can show departures from the exponential decay normally seen over the clean metal surface, in

the form of distinct plateaus in the tunnelling current. These plateaus are ascribed to conduction through a molecule that is attached at either end to the tip and surface. Figure 4.2 shows an example of an $I(z)$ curve exhibiting this plateau behaviour for a sample of another alkanedithiol molecule, 1,5-pentanedithiol, on a Au(111) single-crystal surface.

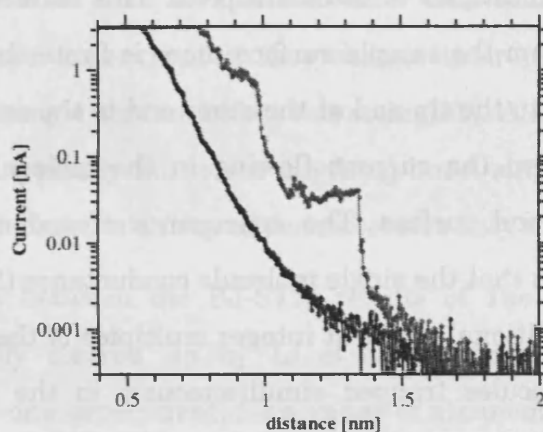


Figure 4.2. Example of the $I(z)$ technique. Two typical curves in the presence of pentanedithiol molecule on Au single crystal.

4.3.1 The development of $I(z)$ for measuring SMC

The first version of this $I(z)$ technique for measuring single molecule conductance was introduced by Xu (in the group of Nongjian Tao, Arizona)[51] in what we shall call the breakjunction STM (BJ-STM) method. Xu drove the Au STM tip into and out of contact with a Au surface in a solvent environment containing the molecules of interest. It was shown for 4,4'-bipyridine and several alkanedithiol molecules that plateaus in the tunnelling current often appeared at certain values. At high currents plateaus are seen at multiples of $G_0 = 2e^2/h$, the quantum of conductance, but these are also seen in the absence of molecules. These plateaus are interpreted as the stepwise decrease in conductance, upon stretching, of the metallic

wire which is formed after mechanical contact of the tip with the metal substrate. This wire eventually breaks and the current should decay exponentially as the tip is retracted further.

In the presence of molecules, however, additional plateaus often appear at lower currents. Xu analysed the statistical distribution of these plateau currents and saw that a peak in the histogram appeared at a given current value, as well as smaller peaks at integer multiples of the main peak. This feature is interpreted thus: as the tip is retracted from the sample surface there is finite chance that a molecule will be bound at one end to the tip and at the other end to the sample surface. The plateau in the current is then the current flowing in the molecular “wire” bridging the gap between the tip and surface. The appearance of a distinct peak in the statistical distribution shows that the single molecule conductance (SMC) is well defined and the appearance of additional peaks at integer multiples of the lowest value corresponds to 1, 2, 3, etc. molecules trapped simultaneously in the tunnelling gap. This is an interesting observation as it is not obvious that currents through simultaneously contacted molecules should add linearly; some interaction between molecules and effects of quantum interference could have resulted in a more *complex* addition of currents.

Haiss *et al* (Richard Nichols’ group, Liverpool) [52][53] performed similar experiments in which the STM tip is brought to a high setpoint, but not into contact with the metal surface, before retracting and measuring the current versus distance. This is known as the $I(s)$ technique to distinguish it from the BJ-STM experiment and is notably different because the probing Au tip is not regularly deformed and Au wires are not drawn out from the sample surface when the tip is retracted (see cartoon in Figure 4.3). Similar plateaus in the current are seen and peaks in the statistical distribution also suggest integer multiples of a given conductance due to the attachment of multiple molecules in the tip-sample gap.

However, despite the qualitative similarity of the Nichols group results to those of Tao, the exact values of SMC for a given molecule were not in agreement, e.g. for octanedithiol Tao measured a conductance of 19.6 ± 1 nS compared to Nichols' value of 0.99 ± 0.07 nS. Tao's group subsequently reported that, after careful inspection of the data, there was in fact a second group of conductance peaks, about 5 times lower than the first[54], i.e. a given alkanedithiol has two conductance states, high and low, in this experiment. Haiss *et al* were also able to show that some of the higher current values appeared in their experiment if they change their procedure and purposely crash the tip into the sample surface before retracting[53]. Alongside this the group of Venkataraman[10][55] typically fail to see anything but a single broad peak resulting from their BJ-STM experiments on any of the molecules they study.

The discrepancy between the BJ-STM results of Tao and the $I(s)$ results of Nichols was eventually cleared up by Li *et al*[9] who observed three separate conductance groups in one experiment, for a range of alkanedithiol molecules ($n = 5 - 10$). These three conductance groups are in agreement with the two values reported by Tao and the lower value reported by the Liverpool group. Haiss and co-workers[22] have subsequently been successful in measuring all three conductance values for the alkanedithiols, as well as other molecules, by careful adjustment of the experimental procedure and sample preparation. In a recent work[56] they were able to show that the relative frequency of occurrence of the low, medium and high (A, B, C) conductance groups depends on the details of the junction formation and the surface roughness. In brief the C conductance group dominates in rough junctions, such as those formed in BJ-STM or at Au atomic steps, and the A group dominates when the roughness is low, e.g. when the molecule is in the middle of a large, flat area of a Au terrace. Rough and stepped surfaces will provide higher coordination of the molecular binding groups to the metal electrodes, thus the mechanism for increased conductance is an increased coupling of the molecule to the electrodes at more highly coordinated sites.

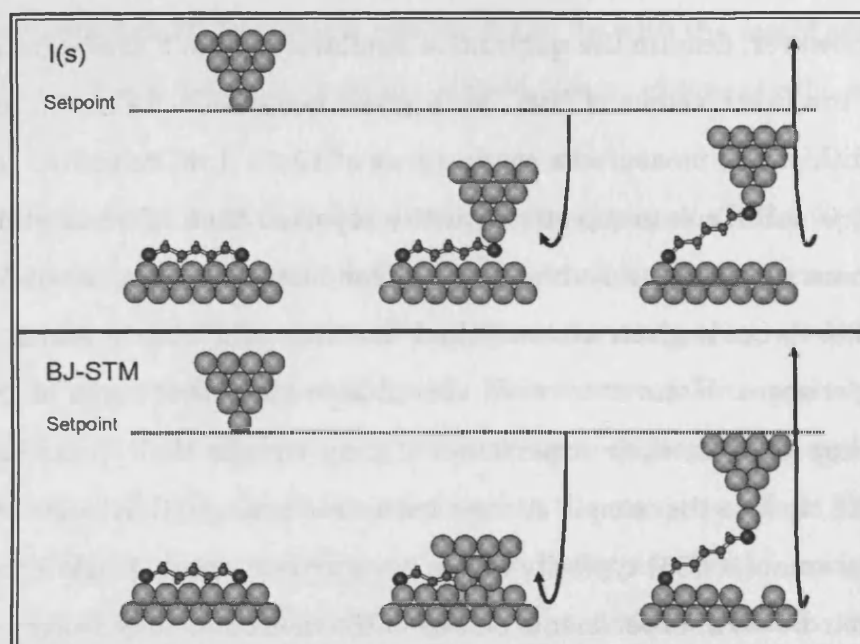


Figure 4.3. Cartoon representation of the $I(s)$ and breakjunction STM techniques. (a) The $I(s)$ technique is realised by approaching the tip by a given distance and retracting before contact with the metal surface is made. (b) In the BJ-STM experiment the tip is driven further forward before retraction, so as to contact the metal surface; subsequently the tip and surface are deformed and metallic wires may be drawn out. In the presence of molecules in both cases a MMM junction may be formed.

4.3.2 Realising the $I(z)$ measurement

We explore both approaches to measuring the single molecule conductance of the nonanedithiol molecule and we implement the two techniques using the following procedure: (a) The tip is put into feedback at a low setpoint with a given bias, e.g. 100pA setpoint at 100mV. We cannot tell the exact tip-sample distance based on the tunnelling current, instead the z scale is measured relative to the feedback position and this defines $z = 0$ nm on our distance scale (b) Feedback is switched off and the tip is moved toward the sample by a fixed distance (c) The tip is then retracted and the tunnelling current is measured as a function of the distance. This process is repeated, e.g. 100 times, at one position (x,y) on the sample surface, before moving to another location.

For the $I(s)$ method the approach distance is adjusted ad hoc during some initial tests to find the nearest approach without crashing the tip into the surface. Correct tuning of this approach distance results in fairly reproducible $I(z)$ curves (Figure 4.4 a); each trace follows a similar exponential decay, except where plateaus appear, and the curves generally pass through the setpoint value at $z = 0$ nm (although the current goes beyond the saturation limit of the amplifier we nevertheless estimate that the current at the closest approach is of the order of $5 \times 10^{-3} G_0$, therefore we are far from making contact with the surface). In contrast in the BJ-STM experiment the approach is set to be sufficiently large as to cause the tip to crash upon each approach (Figure 4.4 b). As the tip and surface are deformed upon contact and retraction the effective tip-sample distance is changed each time a measurement is made and the resultant current traces do not overlay or pass through the setpoint at $z = 0$ nm.

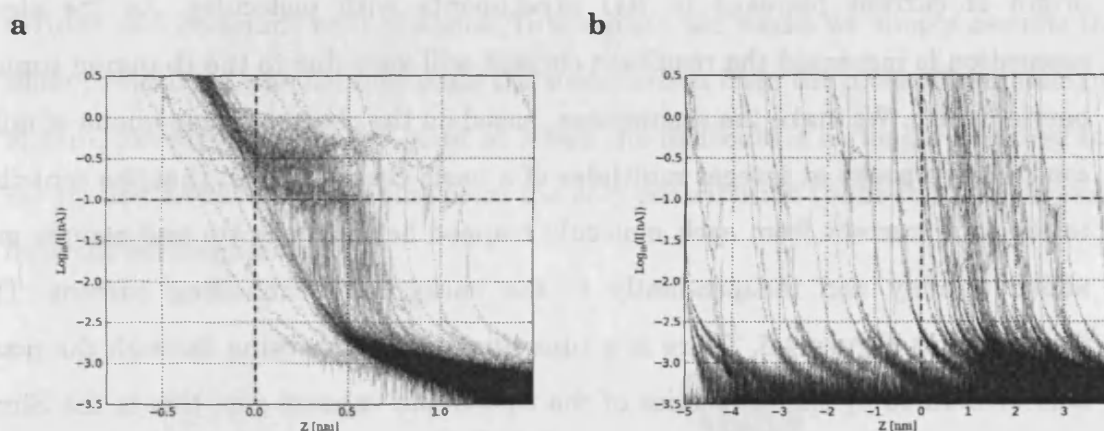


Figure 4.4. (a) $I(s)$ method and (b) Breakjunction STM example data sets. The dashed lines indicate the feedback current and z position.

4.3.3 Toy model of $I(z)$ current plateaus

Before we see the results of our own experiments we first seek to understand why we should expect to see such plateaus in $I(z)$ curves in the presence of molecules. The molecule is attached to both the tip and surface by strong chemical bonds[54] and

thus one end of the molecule is lifted away from the surface as the tip is retracted (see Figure 4.5). We consider that the total measurable current is a combination of the direct through-space-tunnelling background current, i.e. that which would exist in the equivalent bare tip-sample gap, and a separate contribution to the current which is mediated somehow by the molecule itself (see the molecular energy level (ML) model in chapter 2). At some point the tip-sample distance will become too great for the molecule to continue straddling the tip-sample gap and the metal-molecule-metal junction will break. At this point the contribution from the molecule will change abruptly.

We find that the main features reported in such experiments can be qualitatively described by using a combination of our ML model and the Simmons tunnelling model. This contains all the necessary physics needed to understand the origin of current plateaus in $I(z)$ experiments with molecules. As the electrode separation is increased the resultant current will vary due to the changing tunnelling barrier width. We make the assumption, based on the observed phenomena of multiple conductance peaks at integer multiples of a basic current value, that the contribution to the total current from each molecule trapped between the tip and sample may be added linearly and independently to the background tunnelling current. This is illustrated in Figure 4.5. There is a tunnelling current passing through the potential barrier defined by the properties of the tip-sample vacuum gap; this is the Simmons model barrier and forms one conducting “channel”. Added to this is the contribution due to conduction through the molecule itself; this is a second channel conducting in parallel to the first.

Thus we propose a model in which we calculate separately the transmission probability as a function of distance through the rectangular potential barrier, T_{Sim} , and that through the molecule, T_{mol} . The total transmission probability is an average of the two multiplied by the number of channels (in this case equivalent to the sum of two transmissions, without any relative weighting of the molecular contribution) and

the current is calculated using the Landauer formula, i.e. the resulting total conductance is:

$$G = \frac{2e^2}{h} \cdot 2 \cdot \frac{(T_{\text{Simm}} + T_{\text{mol}})}{2} \quad (4.2)$$

For the molecular contribution we use the ML model previously outlined (chapter 2; although in fact we see that we need only assume that the current through the attached molecule is constant to reproduce qualitatively similar results, regardless of the actual model assumed for the molecular conduction). We assume that the molecule is attached to both the tip and sample with equal coupling and that the coupling strength and energy relative to E_F of the LUMO/HOMO being modelled are both well defined and invariant with distance. To complete the model we simply assume that at some point along the distance scale the contribution from the molecule suddenly drops to zero, corresponding to the point at which the molecule is no longer attached to both the tip and surface. Beyond this point the only contribution to the total transmission is from the rectangular barrier.

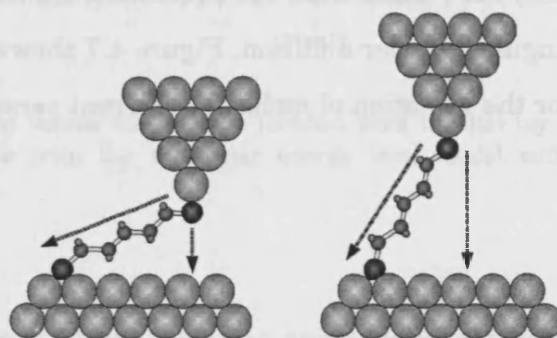


Figure 4.5. In the $I(z)$ toy model two separate contributions to the total current are considered. Firstly direct tunnelling between tip and surface occurs as in a bare vacuum gap. The magnitude of this tunnelling current depends on the tip-sample separation. Additionally some charge transport is mediated by the attached molecule. The resulting current is the sum of these two contributions.

Figure 4.6 Shows the result of calculations based on this model with the following parameters: For the metallic electrodes and vacuum gap the Fermi level from band bottom, $\mu = 5.5$ eV, and the height of the rectangular barrier $\phi = \mu + 2.0$ eV and for the molecular contribution to the current the offset of molecular orbital, $\varepsilon = \mu + 1.0$ eV, the coupling symmetry, $\eta = 0.5$ and the coupling strength (broadening) $\Gamma = 0.1$ eV. The barrier width is varied from 0.1 nm to 2.0 nm, at 100mV bias and the molecular contribution is removed half way. We also assume a non zero current of 1 pA at infinite z to model the lower limit of the current amplifier.

It can be clearly seen that the model reproduces qualitatively the appearance of a plateau in the tunnelling current. Figure 4.6 also shows the total transmission $T(E)$ (black, dashed) at two points along the curve with the contributions T_{Simm} (black) and T_{mol} (grey). The thin shaded band is the bias window over which the transmission has been integrated, (a) corresponds to the transmission at $z = 0.1475$ nm and (b) at $z = 1.05$ nm, just before the plateau ends. Thus it can be seen that in this simple model the exponentially decreasing transmission through the potential barrier may simply become vanishingly small compared to the assumed constant contribution from the well coupled molecule, and hence a plateau appears. This implies that the value of the current plateau and its behaviour with bias and parameters of the molecular energy level are identical to the results from the equivalent molecular energy level calculation without the rectangular barrier addition. Figure 4.7 shows that the two models do give the same result for the variation of molecular current versus bias voltage.

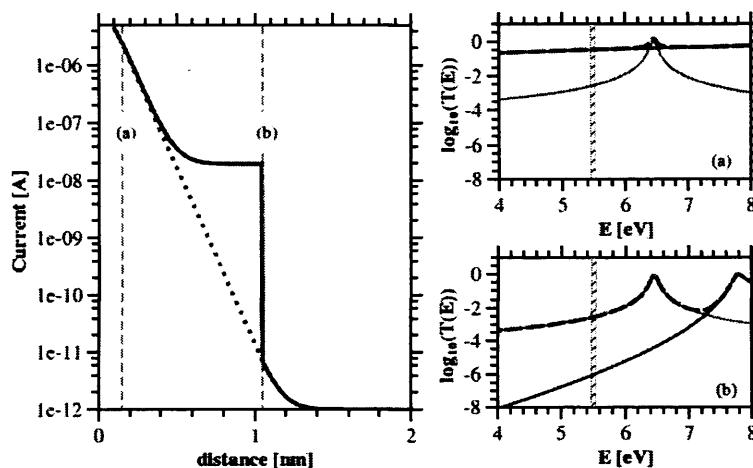


Figure 4.6. Toy model of current plateaus in molecular junctions. (left) current versus distance curve, (right) transmission at points (a) and (b) for model with Simmons barrier height $\phi = \mu + 2.0$ eV and a molecular orbital, $\varepsilon = \mu + 1.0$ eV.

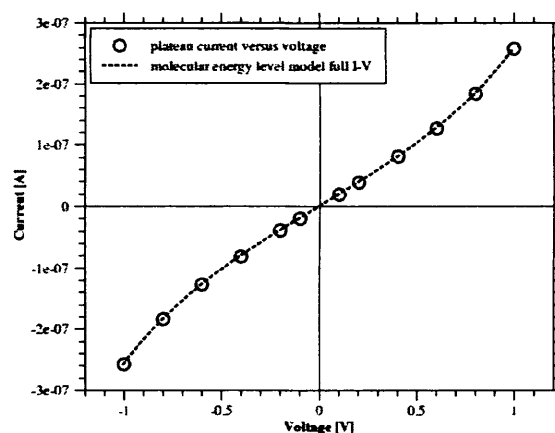


Figure 4.7. Plateau current versus bias voltage (circles) from the $I(z)$ toy model. Also shown (dashed line) is the full I-V curve from the molecular energy level model without the Simmons barrier contribution.

It has been proposed[9][56] that the appearance of different conductance groups in the $I(z)$ experiments is the result of varying the coupling strength (level broadening) of the molecular level. Thus we consider this effect by varying Γ over a wide range from 0.1 eV to 0.00625 eV and it was noted that plateau current scales with Γ

following a quadratic dependence. Thus when the energetic alignment of the molecular energy level with the Fermi level of the electrodes is fixed and well defined we are still able to affect the molecular conductance by changing the coupling strength. In this model a factor of 2 increase (decrease) in the coupling strength gives a factor of 4 increase (decrease) in the molecular current.

The appearance of peaks at integer multiples of a given current value can easily be accounted for in the transmission picture of molecular conductance. A more general expression than (4.2) for N molecules in the tunnelling gap would be:

$$G_N = \frac{2e^2}{h} \cdot (N+1) \cdot \frac{(T_{Sim} + N \cdot T_{mol})}{N+1} \quad (4.3)$$

So the ratio of the conductance through N molecules in the tunnelling gap to that through a single molecule is:

$$\frac{G_n}{G_1} = \frac{T_{Sim} + N \cdot T_{mol}}{T_{Sim} + T_{mol}} \quad (4.4)$$

However, as we have seen in the calculated transmission versus distance, T_{Sim} becomes vanishingly small at large z , i.e. $T_{mol} \gg T_{sim}$ and:

$$\frac{G_n}{G_1} \approx N \quad (4.5)$$

Thus the conductance as judged by the current plateau through N molecules should be a factor of N greater than that through one molecule, as is experimentally observed. We check this in our numerical model by simply scaling T_{mol} by integer factors. The

contribution from the molecular energy level to the total transmission was varied as 25%, 50%, 75% and 100% and the plateau current scales as integer multiples of the lowest (25%) curve.

4.4 Results on bare Au single crystal

We first check to see the behaviour of the $I(z)$ curves over the bare Au surface and to confirm that such plateaus do not form except in the presence of molecules. We prepare the atomically flat Au surface from a solid crystal by repeated cycles of Ar^+ ion sputtering and annealing in vacuum. Figure 4.8 shows an STM image of the clean Au single crystal surface in UHV system. In the image large flat areas of crystalline Au can be seen with mono-atomic steps separating the terraces (see figure caption).

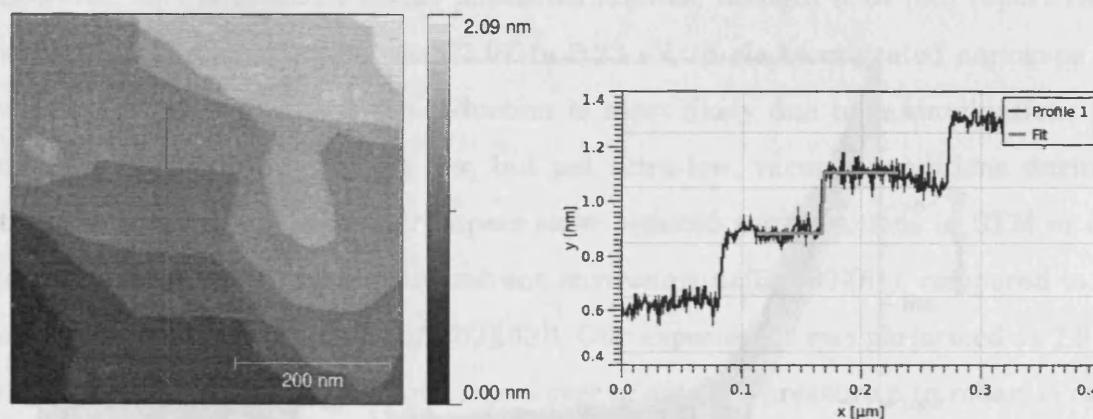


Figure 4.8. STM image of the Au single crystal surface. The profile section shows the monatomic steps separating the terraces, the fitted step (grey line) having height = 0.222 ± 0.034 nm in agreement with the expected step height of ~ 0.24 nm [57]

$I(z)$ curves were measured starting from either 1nA setpoint or 20nA setpoint, at 100mV bias. The result is qualitatively as expected and is illustrated below in Figure 4.9 with a data set of 100 curves measured sequentially at the same spot on the

sample. The result is an exponential curve (linear as seen on the semi-log plot) without any plateaus or significant fluctuations or deviations, but the curves level out at a finite value at large z due to the limited sensitivity of the current amplifier. Figure 4.9 also shows a histogram of the $\log_{10}(I)$ values (abscissa on the vertical axis; the number of counts is normalised by the total number of data points), showing no obvious peak in the distribution except at low current values corresponding to the low end limit of the amplifier.

Taking the logarithm of the current is a particularly prudent step in analysing these curves as we can easily see the linear behaviour, but moreover we are able to judge whether there are any significant features in the traces over the full current range. The histogram of $\log_{10}(I)$ in the absence of plateaus or any other departures from the exponential decay is thus flat and featureless. This is important to note as we will later plot similar histograms for data sets where molecular plateaus are evident.

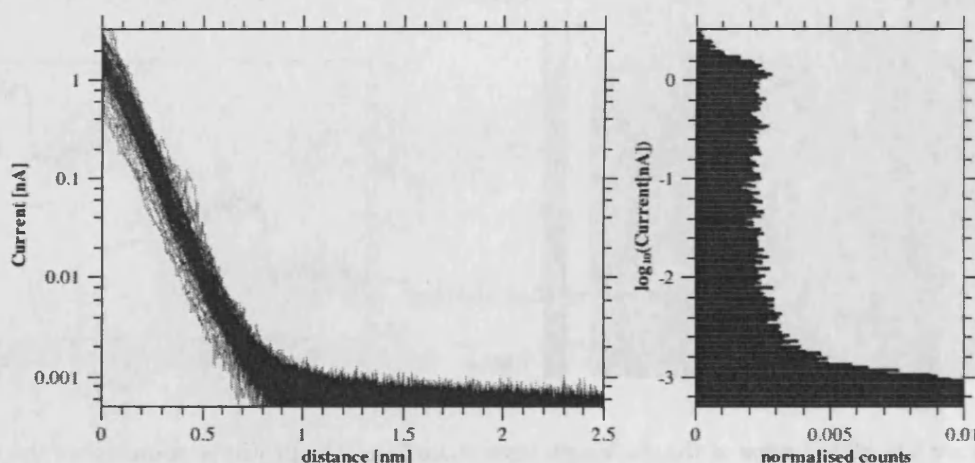


Figure 4.9. (left) 100 $I(z)$ curves over the bare Au(111) single crystal. (right) histogram of the measured current (150 bins).

To characterise the exponential decay we fit the $I(z)$ curve to a function of the form $I = A \cdot \exp(-\beta \cdot Z) + I_0$ and this gives an average decay parameter $\beta \sim 11.2 \pm 0.03$

nm^{-1} (from results using high current amplifier/high setpoint) $\beta \sim 14.7 \pm 1.7 \text{ nm}^{-1}$ (from low current amplifier/low setpoint). This fitting is more sensitive to the higher current values and does not allow for possible changes in the decay parameter, i.e. $\beta \equiv \beta(z)$. As an alternative we can determine the decay parameter from the slope of the $\ln(I)$ versus z curve and the curve can be broken into short sections, thus the slope at different z (or I) values can be evaluated. This approach is expanded on more in chapter 5, but for now we quote the result of this analysis as giving an estimate for the average slope as $\beta = 11.4 \pm 0.03$ ($\sigma = 5.1$) nm^{-1} (high setpoint curves) and $\beta = 9.65 \pm 0.02$ ($\sigma = 3.33$) nm^{-1} (low setpoint curves).

The expected decay over clean bare Au is $\beta \sim 22 \text{ nm}^{-1}$, so our value is significantly lower than predicted. From the definition of β (see chapter 3) this gives a reduced work function estimate of the gold surface of between $\phi = 0.89$ and 1.2 eV . However, this is consistent with published studies; Mangin *et al* [58] report reduced work functions, ranging between 3.97 to 0.23 eV , in electromigrated nanogaps of Au wires. They conclude that the reduction is most likely due to contaminations of the metallic electrodes due to the low, but not ultra-low, vacuum conditions during the electromigration process (other papers show reduced workfunctions in STM or break-junction experiments in air and solvent environments[59][60][61], compared to those obtained in ultraclean conditions[62][63]). Our experiment was performed at $1.9 \times 10^{-9} \text{ mbar}$. The time for formation of a monolayer of air, at a pressure p in mbar, is roughly given by the monolayer-time[64]:

$$t_{\text{mono}} = \frac{3.6 \times 10^{-6} \text{ mbar}}{p} \text{ [s]} \quad (4.6)$$

At 10^{-9} mbar a monolayer is formed in about 1 hour, thus we cannot consider the Au single crystal to be uncontaminated in this experiment and a somewhat reduced work function is expected. At least part of this reduction can be accounted for by the

interfacial dipole that will be formed by any layer of molecules (see chapter 3). In the case of physisorbed, nonpolar molecules a vacuum level shift of ~ 0.5 eV is expected[36], but we did not perform XPS measurements on this sample, so we are left to speculate on the exact nature of the contaminations.

Hydrogen from the stainless steel is the main source of degassing in a baked UHV system. However, in an *unbaked* system, due to its somewhat high desorption energy, adsorbed H_2O is slow to remove by pumping alone and is the major contributor to the pressure by degassing[64]. The pressure of $\sim 1.9 \times 10^{-9}$ mbar in this experiment is an order of magnitude higher than the typical pressure in the freshly baked UHV system, suggesting that a significant amount of adsorbed H_2O may be present on the sample. The dipole moment of water is 1.8 D and based on the results of Alloway *et al*[37] this suggests that adsorbed water could give a vacuum level shift in excess of 1 eV. It is also possible that the unknown geometry of the tip may account for some of the reduction in the barrier height as the crystal structure of the tip is irregular and may exhibit non-homogeneous work function.

Careful preparation of the Au surface at lower base pressure should result in an uncontaminated sample surface. However our experiments with molecules on Au involve ex situ sample preparation, thus some contamination of the Au surface by atmospheric species, particularly H_2O , is nevertheless inevitable. Thus this result is interesting but not of great importance to our study.

4.5 I(z) of nonanedithiol

We now turn our attention to the results of the I(z) experiments on samples of nonanedithiol on the Au crystal surface.

4.5.1 Sample preparation

Our sample preparation is similar to that employed by Richard Nichols' group in Liverpool. We present here the general outline of the sample preparation; specific details of importance appear in the text as necessary. Toluene, methanol, ethanol and hydrochloric acid were purchased from Sigma-Aldrich and used as received without any further purification. Au wire, 0.25mm was purchased from Goodfellow Cambridge Limited. All glassware was cleaned by ultra-sonic treatment with acetone and isopropanol. The Au single crystal was prepared by repeated (at least 3) cycles of Ar⁺ ion sputtering and annealing in UHV. A solution of the analyte molecule is prepared at a given concentration in an appropriate solvent (e.g. 5×10^{-5} M in toluene). The clean Au substrate is removed from UHV and immediately immersed in the mixed solution. The sample is then left in the solution for a short time (e.g. 15 seconds), removed, then rinsed in fresh solvent to remove any unbound/physisorbed molecules and finally dried in flowing nitrogen for about 1 minute. The sample is then mounted on a sample plate and introduced to the vacuum chamber. STM tips were made from Au wire by electrochemical etching in HCl/ethanol (1:1) following the procedure of Ren *et al*[65]. Ideally we would have liked to deposit molecules directly onto the Au surface in vacuum, which, with the facilities available, would involve evaporation of solid material by direct heating. As nonanedithiol is liquid at room temperature it is not possible to deposit in situ under UHV conditions.

Following the success of Li and co-workers[9] we prepare the sample from a solution of nonanedithiol at 0.1mM in methanol and the sample is immersed for 2 minutes in the solution. The concentration and immersion time are both relatively

high compared to the typical treatment prescribed by the Liverpool group, thus we consider this sample to have a “high” coverage of nonanedithiol molecules. Figure 4.10 shows an STM topographic image of the Au single crystal surface treated with nonanedithiol; in 4.10(a) we can clearly see the terraces of the underlying Au surface. The etched Au tips were typically not capable of molecular or atomic resolution imaging, but in Figure 4.10(b) we can at least clearly see evidence of pits on the Au surface. These pits are caused by the etching effect on the Au surface of the thiol molecules in the solution phase[41].

Figure 4.11 shows some typical example $I(z)$ curves for this sample. We operate in the $I(s)$ mode with the STM tip biased at 0.1V and the typical duration of each curve is ~ 0.25 s, corresponding to a tip retraction rate of ~ 9 nm s^{-1} . In the two panels the first curve (furthest left) shows no plateau in the exponential decay. The other curves in each panel show the next 3 measurements in the repeated sequence of sampling. Each curve shows a distinct departure from the exponential decay; the curves are offset along the z axis for clarity.

Clearly there are some fluctuations in the measured current, the plateaus are not perfectly flat or single valued. Thus it is common to perform a statistical analysis of the data to determine the most frequent value(s) of the current plateaus and hence we define the SMC. Figure 4.12 shows a data set of 100 $I(z)$ curves; in the left-hand plot all 100 curves are overlaid and the right plot is a histogram of all the current values, taken as $\log(I)$, from the set of 100 curves. We compare this to the result on bare Au (Figure 4.9) and we see that there are some clear peaks in the distribution of $\log(I)$ corresponding to the values of the current plateaus.

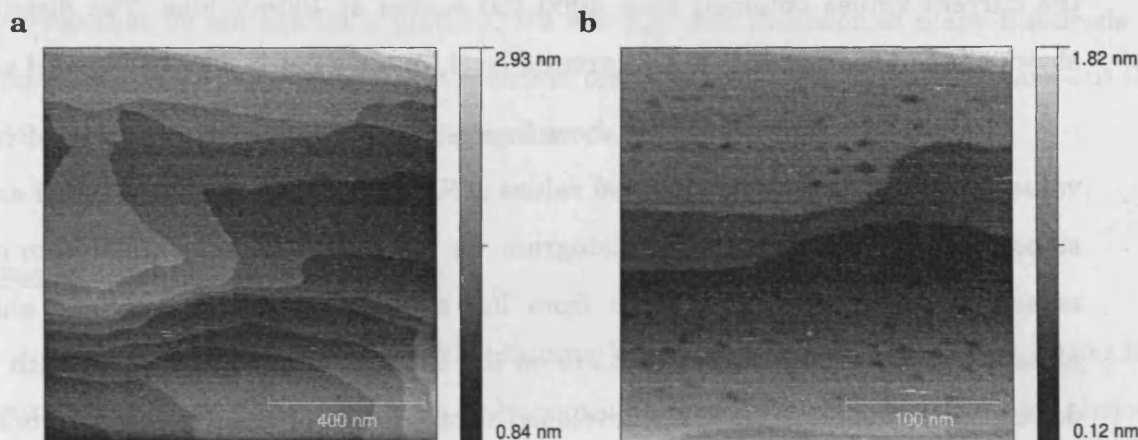


Figure 4.10. STM images. 20 pA 100mV, Au etched tip. Etched Au tips are often incapable of achieving molecular resolution although this is not a prerequisite to getting spectroscopic measurements. (a) The underlying Au terraces can be seen (b) etch pits due to the monolayer formation are visible

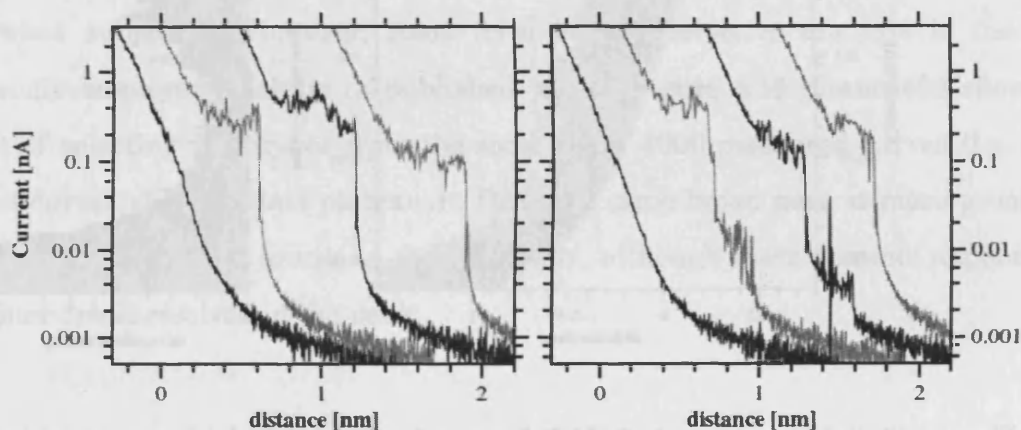


Figure 4.11. Typical $I(z)$ curves for high coverage of nonanedithiol on Au; 100mV.

Typically the statistics of the current plateaus are built from many thousands of repeat measurements. The experimental plan is as follows: collect 200 $I(z)$ curves at an arbitrary location on the sample surface; move to new part of the sample and repeat until we have several thousands of curves; repeat to get data at different bias voltages, e.g. -0.3 to +0.3 V in steps of 0.1 V. Figure 4.13 shows the statistical distribution of all

the current values obtained from 4000 $I(z)$ curves at 100mV bias. The distribution shows a broad peak above the background level, roughly marked by the shaded area.

Published results typically show finer structure in the distribution of current values corresponding to well defined values of SMC, although some additional analysis steps are usually taken. In the histogram we count the current values from *all* the measured curves, including those from $I(z)$ curves that are smooth and show no plateau and also those curves that are on the contrary particularly noisy, with poorly defined plateaus, etc. We have developed three modes of analysis to determine the statistical nature of the current plateaus and these are summarised below.

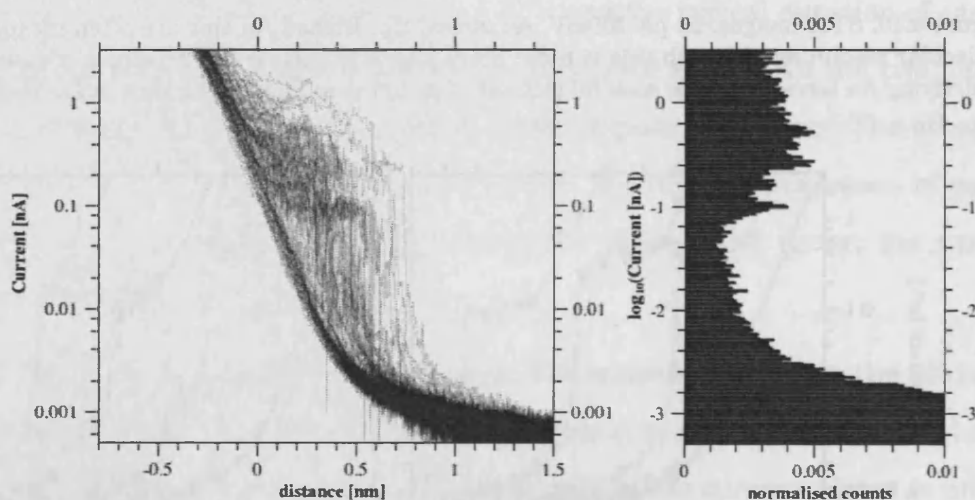


Figure 4.12. (left) one data set of 100 $I(z)$ curves for nonanedithiol on Au. (right) histogram of the measured current

All-data histogram

This is the simplest analysis that can be performed to elucidate the statistical behaviour of the current plateau values (as demonstrated in Figure 4.12 and Figure 4.13). None of the $I(z)$ curves have been excluded in this analysis, so the histogram also contains contributions to the background tunnelling current distribution from those

curves that do not exhibit a plateau. We will see that inclusion of many hundreds or thousands of curves without data selection tends to somewhat obscure or wash-out the details of the plateaus from the histogram.

Selected traces

Thus a commonly employed technique is to manually select a subset of the $I(z)$ curves, such that the histogram only contains data from curves exhibiting obvious plateaus. The benefit is that it reduces the background counts in the histogram and in some cases additional peaks in the distribution appear, which were previously obscured by the heightened background counts. The major caveat here is that human judgement is involved in selecting the data, so there is a risk that the results will be somewhat subjective. However, some form of this selective analysis is the most commonly employed analysis in published works. Figure 4.15 (lower-left) shows the result of selecting 738 traces from the total set of 4000 measured curves (i.e. about 18% of curves show distinct plateaus) . Here the same broad peak is more prominent against the background counts in the histogram, although there does not appear to be any finer detail resolved in the peak.

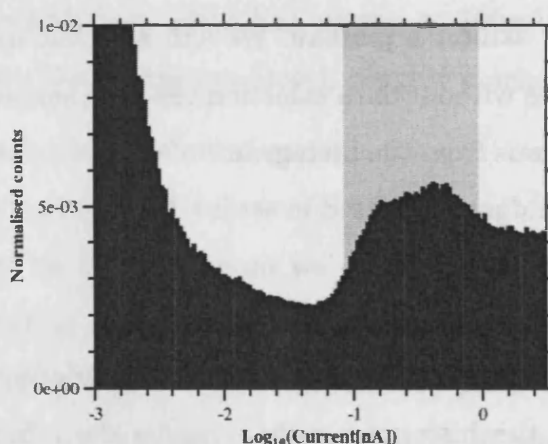


Figure 4.13. Statistical distribution of all the current values from 4000 $I(z)$ curves at 100mV. The shaded area is a guide for the eye to highlight the position and spread of the peak in the distribution.

Automated analysis – Gradient analysis

There are obvious benefits to rejecting some of the data, so we have additionally explored a more sophisticated and objective approach and have hence developed an automated analysis based on simple mathematical selection criteria. The simplest way to distinguish the plateau regions of the $I(z)$ curve is to consider the local slope of the curve. In the form of $\log(I)$ versus V the standard exponential decay will have a finite negative gradient, but plateaus in the curve will have a slope close to zero. To perform this analysis we use a Savitsky-Golay filter[66] in two stages: first we perform signal smoothing with third order polynomials, the advantage of the SG filter being that it preserves the signal's main features better than, for example, moving average techniques which tend to squash maxima and minima and distort the width of features in the signal. Secondly the SG filter can be used for calculation of the local derivative of the smoothed signal, this time based on first order polynomials to simply extract the local linear gradient. For each curve we can thus simply select those individual data points that lie in a region of the curve that is flat, that is to say where the local gradient is close to zero within some adjustable limits. The only other

parameter that affects the results of this analysis is the number of data points over which the smoothing and derivative calculation is performed. Figure 4.14 demonstrates the gradient analysis on two example $I(z)$ curves; the sections marked by the grey vertical dashes correspond to a smoothed derivative below a chosen threshold (0.001 in the arbitrary unit used here) and only these data points are to be included in the analysis.

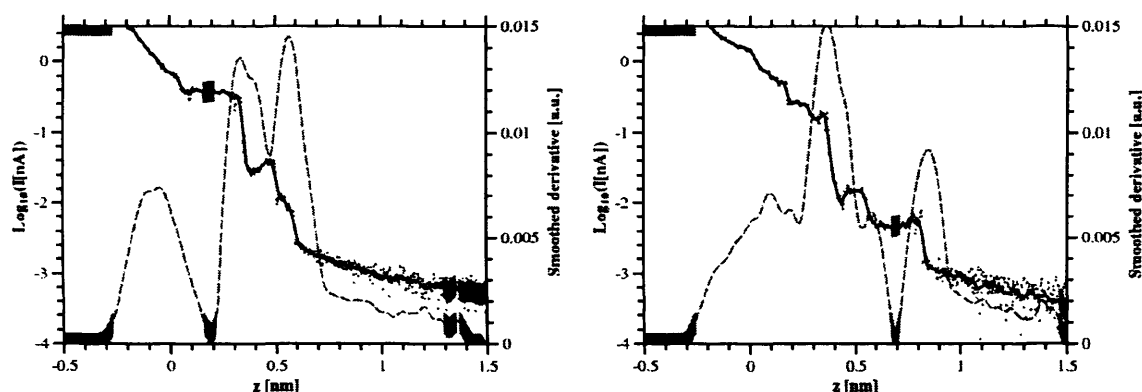


Figure 4.14. Automated gradient analysis; two example curves. In each panel raw data is shown by dots, the smoothed $I(z)$ curve is the solid line, the smoothed derivative is the dashed grey line and the sections where the smoothed derivative is low (<0.001) are marked on each curve by grey vertical dashes.

The results of this analysis on all 4000 curves are shown in Figure 4.15 (upper-right) and are similar to those of the manual selection. In general we see that the selection and automated analysis methods enhance the peak in the histogram relative to the background. We judge the average peak position from the three plots by Gaussian fit to be at 0.284 nA corresponding to a conductance of 2.84 ± 0.05 nS, but with a large uncertainty (standard deviation) of $\sigma = 2.41$ nS (the results of all the experiments in the chapter are summarised in Table 1). Based on observations in similar published data it is possible that the broadness of the peak is due to a

combination of separate peaks from multiples of a given current value (1, 2, 3, etc. molecules). However, in this data set, for nonanedithiol at 100mV, we do not see any convincing evidence of there being several well defined conductance peaks, instead only a single broad peak is identifiable. It may be that the fluctuations or noise in the individual plateaus is too large to give well defined peaks that can be resolved as such. An alternative explanation is that this is a genuine difference between our results in vacuum compared to the published results in air or solvent, i.e. that the SMC is poorly defined in vacuum. This is unlikely, however, as Fujihira, Nishikawa and co-workers[67][68] have already successfully shown well defined conductance peaks for another alkanedithiol, viz. 1,6-hexanedithiol, in UHV. Figure 4.15 also shows some example curves and the dashed line marks the average peak position and standard deviation of the peak.

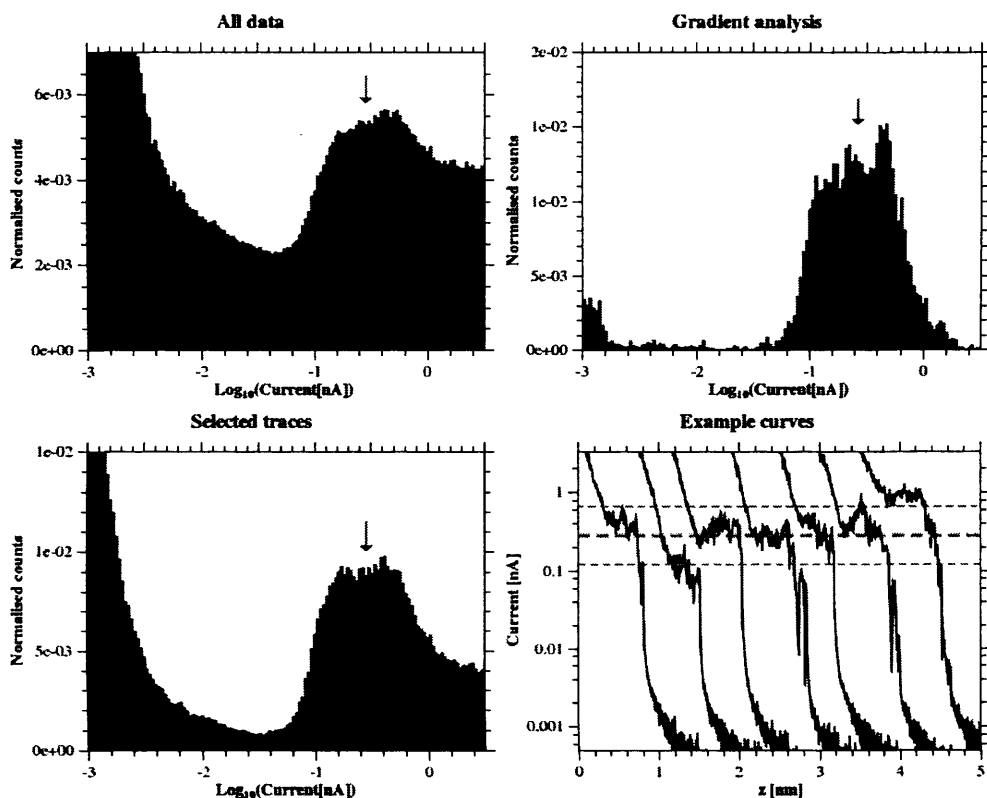


Figure 4.15. Statistical distributions of the current in $I(z)$ curves for nonanedithiol at high coverage on Au, 100mV. (top left) All data, 4000 curves; (top right) gradient analysis of all curves; (bottom left) 738 selected traces (~18%). The peak positions judged by a Gaussian fit to the data are marked by the arrows. The mean peak is 2.84 ± 0.05 ($\sigma = 2.41$) nS. (bottom right) Example $I(z)$ curves; the dashed lines show the average peak position and the width (standard deviation) of the peak.

4.5.2 Current versus voltage

The peak in the current histogram shifts with bias voltage (tested between -0.3 to +0.3 V) and analysis of the statistical distribution shows qualitatively similar distributions. Evaluating the peak current at each bias value enables us to build a current versus voltage (I-V) curve to more fully describe the SMC over the low bias range. Figure 4.16 shows the current peak, I , and the integral conductance, I/V , versus V . The resulting I-V curve is non-linear, thus the low bias conductance is not constant over this range. Due to the large HOMO-LUMO gap of the alkane chain it is often

assumed that transport through an alkane molecule can be approximated by tunnelling through a large potential barrier ~ 4 eV high, thus we would expect the resulting I-V curve to be approximately linear at low bias; the curvature seen here suggests a much lower barrier height is in effect. However, the I-V curve has been built up from separate measurements at fixed bias and is based on broad peaks in the distribution of current plateaus. A direct, dynamic measurement over a wider bias range would more reliably describe the I-V characteristics of the molecular junction (and it is this approach that we use to study the porphyrin molecular wires).

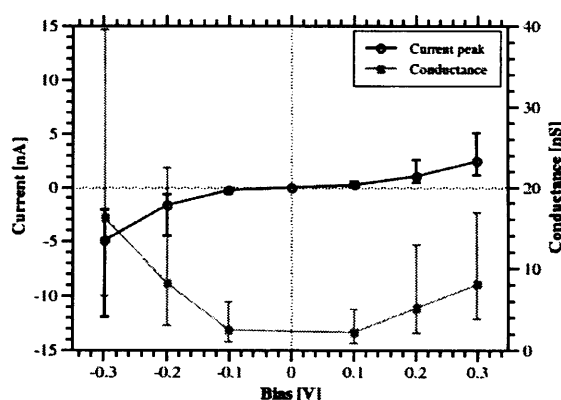


Figure 4.16. I-V curve for nonanedithiol based on the peak conductance from the statistical distribution of $I(z)$ curves.

Occasionally there are well defined current plateaus at much lower current than suggested by the peak in the statistical distribution. However the occurrence of these plateaus is too infrequent to add significant weight to the histogram of all the 4000 curves (Figure 4.15). One particular data set of 100 curves showed several examples of these low current plateaus, as illustrated in Figure 4.17. Some plateaus are clearly evident at a current about one order of magnitude lower than the peak in the previous histograms. However, as can be seen in the histograms, these plateaus do not give a

strong peak in the distribution of just these 100 curves. A peak at low current does appear when we select just the 7 curves showing low plateaus, thus we are left to conclude that these low current plateaus are statistically insignificant in this experiment.

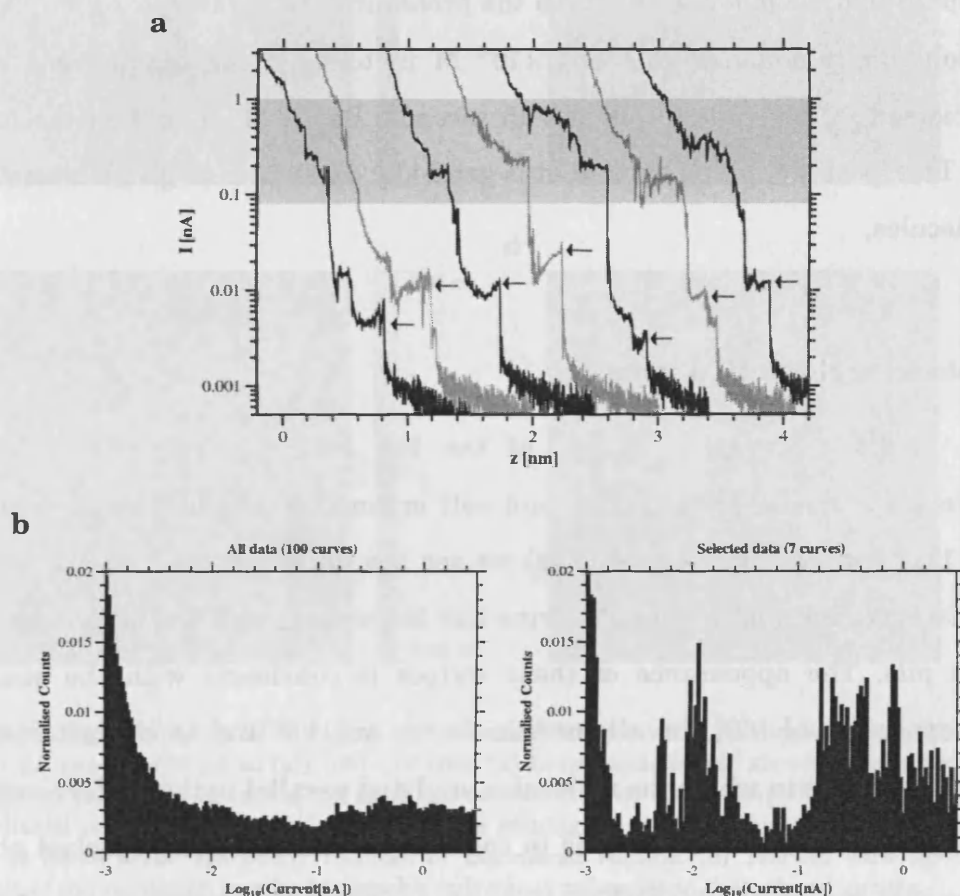


Figure 4.17. (a) $I(z)$ curves exhibiting low current plateaus. The shaded area marks the peak region seen in the previous histograms; the plateaus marked with arrows are clearly outside this region, about an order of magnitude lower. (b) The I - V curves come from one data set of 100 curves, for which we show the all-data histogram (left) and the histogram for the 7 selected curves shown in (a) (right).

4.5.3 Lower coverage

The results thus far from the previous experiment have failed to show distinct peaks or evidence of the different conductance groups reported by other researchers. We decide to repeat the experiment again at 100mV, but with different sample preparation. We followed this time the procedure of the Liverpool group and prepared a solution of nonanedithiol at 5×10^{-5} M in toluene; the sample was subsequently immersed in the solution for just 15 seconds. Based on private correspondence with the Liverpool group this treatment is generally considered to give a low coverage of the molecules.

Molecular resolution imaging

STM topographic images of the low coverage sample reveal evidence of molecular monolayer formation and self organisation into distinct domains on the Au(111) surface. In Figure 4.18 (a) we see the underlying terraces of the Au crystal surface, zooming in (b) reveals stripe-like features as well as the previously observed etch pits. The appearance of these stripes is consistent with the observations of Kobayashi *et al* [69] for alkanedithiols on Au(111) and is characteristic of a low coverage phase in which the molecules are lying parallel to the surface, with both thiol groups bound to the Au. This is in contrast to a more densely packed phase at high coverage, but it is clear that even at so-called low coverage the Au surface is nevertheless well covered with molecules.

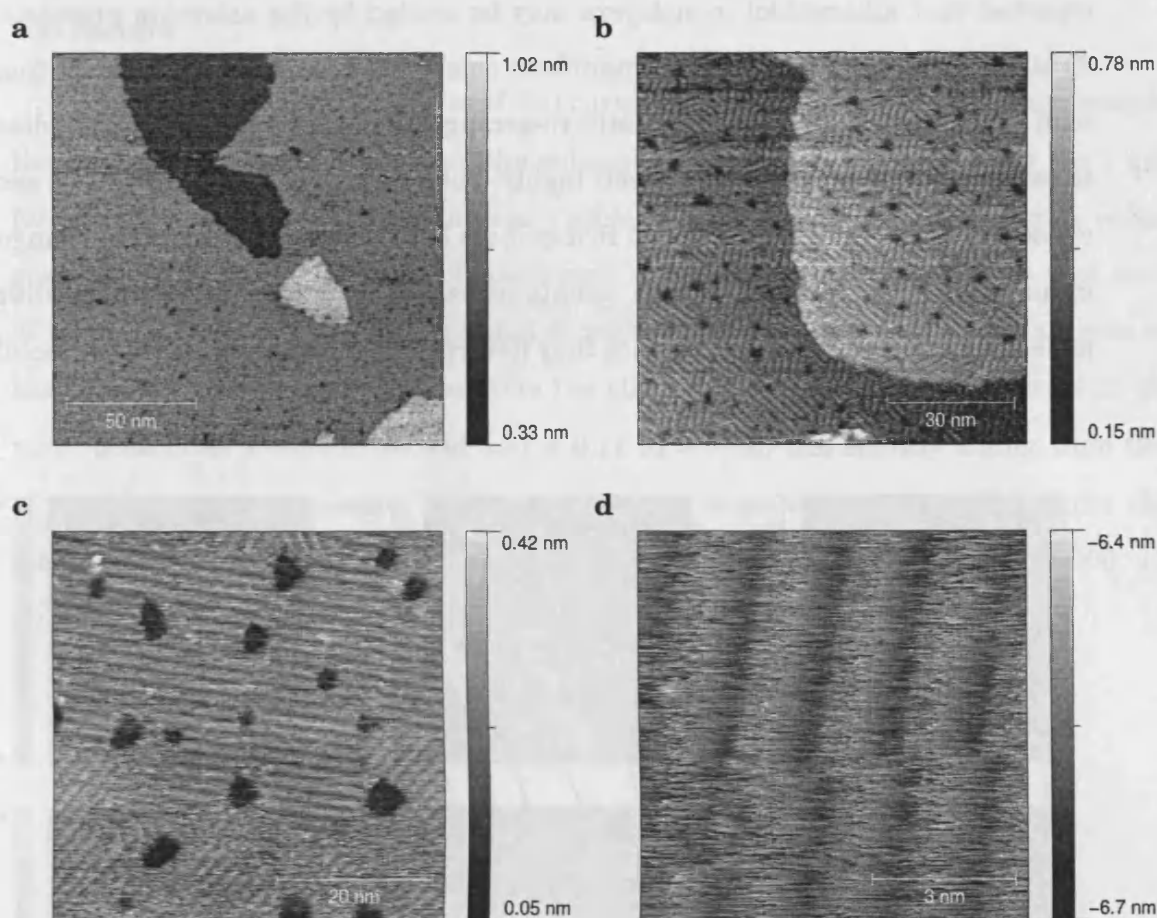


Figure 4.18. High resolution STM images of the nonanedithiol covered Au single crystal. Au etched wire tip, at 1 pA sepont (30 pA in (a)), 100 mV bias. (a) Large scale image showing three terraces of the substrate Au crystal (b) Reducing the scan size reveals ordered stripe shaped regions composed of the nonanedithiol molecules. Pits are seen due to the etching effect of the thiol molecules in the solution phase. (c) Some areas are poorly resolved or disordered regions. (d) The Au wire tip is generally incapable of the resolution required to resolve individual molecules in the ordered stripes.

The mean spacing of the stripes is 1.65 ± 0.04 nm consistent with the molecular length of 1.643 nm from (4.1), which is again consistent with similar measurements by Kobayashi, supporting the idea that the molecules are lying down on the surface. In a sequence of images repeatedly taken over the same area (Figure 4.19) we observed that the direction of the stripes may change whilst scanning. It has previously been

reported that alkanethiol monolayers may be eroded by the scanning process of the STM tip itself[41], [70], but this manifests chiefly as a removal of material from the scan area instead of the more subtle re-arrangement seen here. (These studies also show that the underlying Au is itself highly mobile at room temperature). In addition we do not have enough evidence to firmly state here whether or not these changes are induced by the scanning or are spontaneous; we simply observe that while the molecules are ordered on the surface they nevertheless enjoy some degree of mobility.

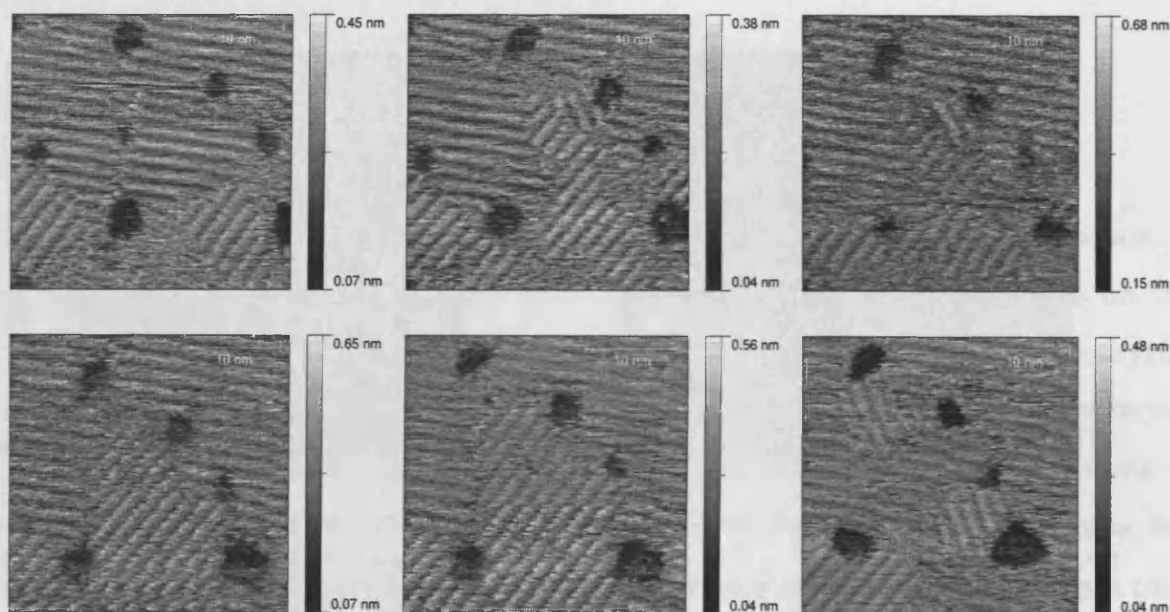


Figure 4.19. A sequence of STM images of the striped phase of nonanedithiol on Au(111). The images are a time sequence from top-left to top-right then bottom-left to bottom-right. Some of the groups of similarly orientated stripes can be seen to change direction between images.

I(z) results

Figure 4.20 shows examples of $I(z)$ curves measured on the low coverage sample; the first curves shows no plateau, the subsequent ones are displaced along the z axis for clarity. There are distinct plateaus visible in these curves and the current values span approximately two orders of magnitude. Of particular interest we note that some of these plateaus are at a current that is much lower than the previous peak seen on the high coverage sample. Judged from the statistical distributions in Figure 4.21 the main peak gives a conductance of 3.21 ± 0.17 ($\sigma = 2.38$) nS, slightly higher than that of the high coverage sample, but considering the large variance in both results this difference does not seem to be significant. We selected 518 curves from 6000, i.e. approximately 9% exhibit well defined plateaus.

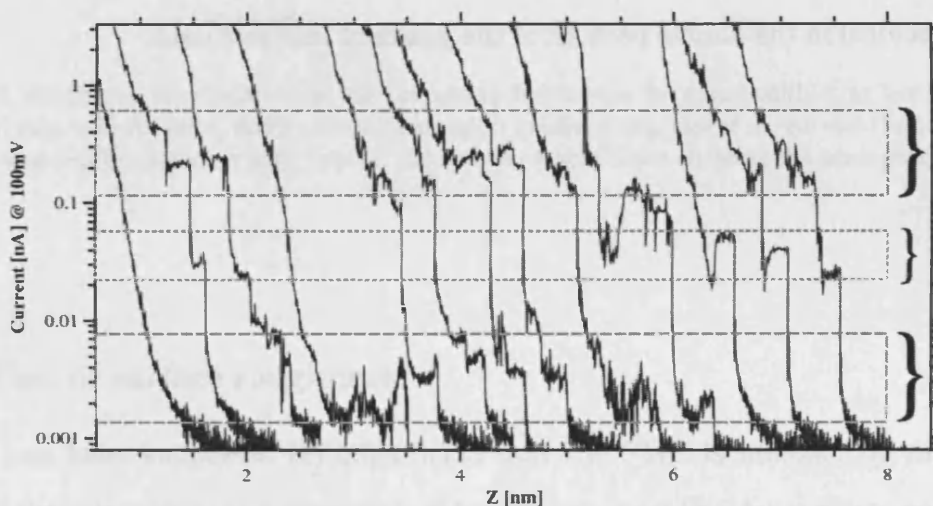


Figure 4.20. Typical $I(z)$ curves for nonanedithiol on Au, at low coverage, 100mV. The marked regions show the approximate current ranges where plateaus are seen giving peaks in the histogram.

There are clearly also some other peaks in the distribution when we take only the manually selected curves as well as when we employ the automated analysis (we

reiterate that the automated analysis is simply an alternative method of selecting/rejecting data points for inclusion in the histogram). Thus these peaks were previously obscured by the background counts in the all-data histogram, but we know that they do represent real current plateaus as we can see these in the individual $I(z)$ curves.

The results of the gradient analysis show some well defined peaks, especially at the lower end of the current range, with some evidence of the multiple peaks (multiple molecules) behaviour visible. The two lowest peaks are well described by a fit of two Gaussian peaks at fixed separation corresponding to a factor of two (red curve) giving a SMC of 0.0193 ± 0.0002 ($\sigma = 0.0038$) nS. Another smaller peak appears at 0.321 ± 0.003 ($\sigma = 0.065$) nS (green curve; a fit to the main peak is also shown in blue). In the histogram of the selected curves we also see evidence of the lowest conductance group with a peak at ~ 0.04 nS (grey dashed arrow) corresponding to the second peak ($N = 2$ molecules) in the double peak fit of the gradient analysis data.

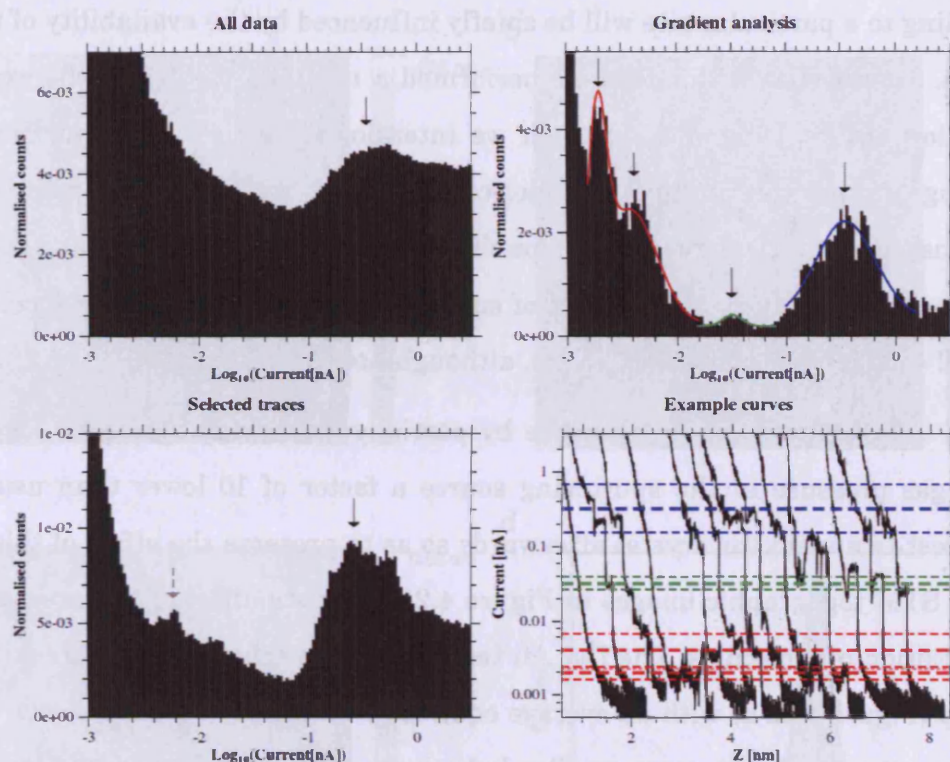


Figure 4.21. Statistical distributions of the current in $I(z)$ curves for nonanedithiol at low coverage on Au, 100mV. (top left) All data, 6000 curves; (top right) gradient analysis of all curves; (bottom left) 518 selected traces ($\sim 9\%$); (bottom right) Typical $I(z)$ curves, dashed lines showing the peak positions.

4.5.4 Effect of surface roughness

It has been suggested [9][53][71][72] that the SMC is affected by the specific details of the adsorption site geometry of the molecule on the Au surface, particularly whether it is bound atop a Au atom, in a bridging site between two atoms or in a three-fold hollow site. Molecules bound in these different geometries give rise to different values of SMC and we would expect that the statistical weighting of those different conductance groups reported by Li *et al*[9] will depend on the relative probability of a molecule to bind at a given site. Given that these adsorption geometries are energetically almost equally favourable[71] the relative probability of

binding to a particular site will be chiefly influenced by the availability of the different sites. To investigate this idea we performed a modified version of the experiment on the low coverage sample, in which we intentionally roughen the surface to effect a change in the availability of under-coordinated sites at step edges. As previously discussed, in a more recent publication Haiss *et al*[56] have performed a comprehensive study of the effect of surface roughness and junction formation on the SMC conductance of alkanedithiols, although not in vacuum.

We create a rougher surface by partially sputtering the clean Au crystal with the gas pressure in the sputtering source a factor of 10 lower than usual. We then neglect to anneal the crystal afterwards so as to preserve the effect of this sputtering. The STM topographic images in Figure 4.22 show the effect of this treatment prior to deposition of molecules. The flat Au terraces are now marked by pits one atomic layer deep (Figure 4.22 d) with an average equivalent radius of ~2.1 nm. Closer inspection of these pits also shows some smaller holes presumably another atomic layer deep. The edges of these pits are equivalent to step edges of the conventionally prepared surface, but with high areal density.

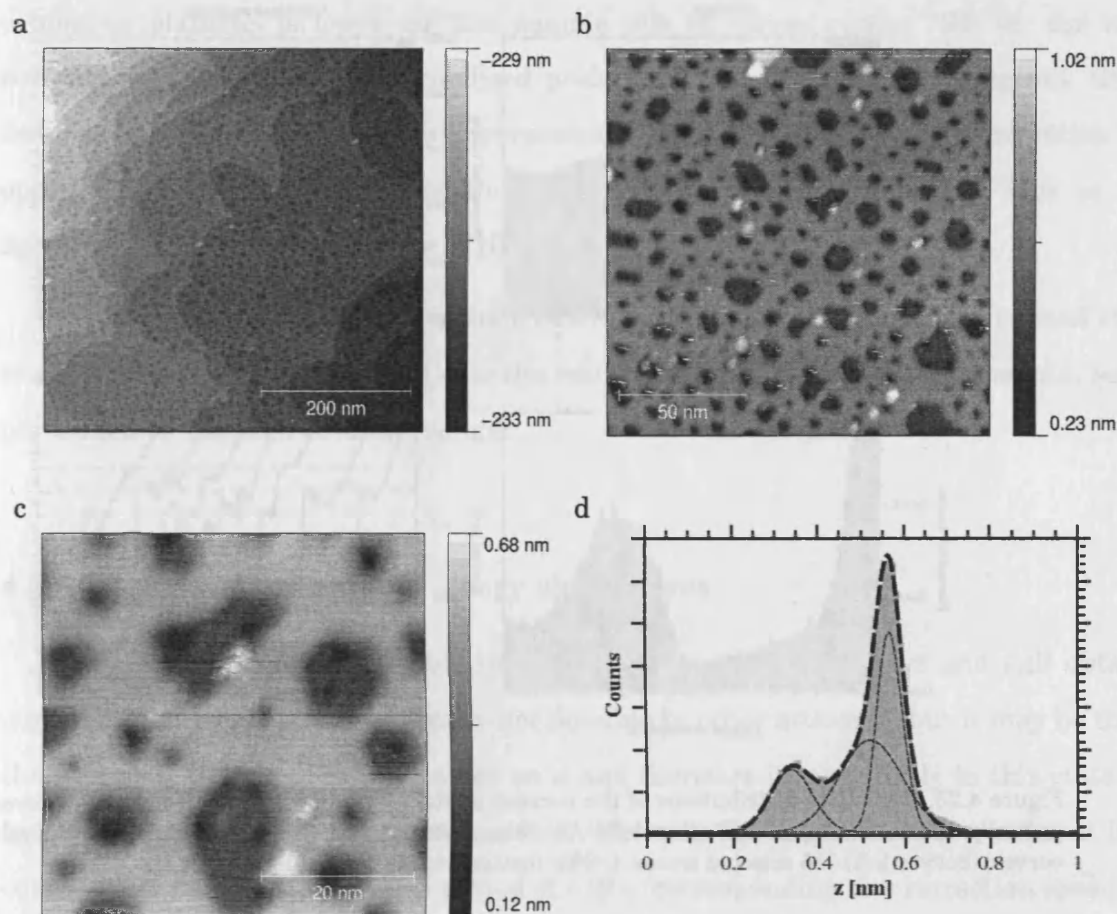


Figure 4.22. STM topography images of the partially sputtered Au surface before deposition of nonanedithiol molecules. (d) The depth of the pits judged from the distribution of z is 0.230 ± 0.003 nm.

Nonanedithiol molecules were deposited on to the partially sputtered sample with the same concentration and immersion time as the previous low coverage sample. The $I(z)$ experiment was subsequently repeated to gather 5400 curves at 100mV and the resulting statistics are shown in Figure 4.23. We selected 315 curves from 5400, i.e. approximately 6% exhibit well defined plateaus.

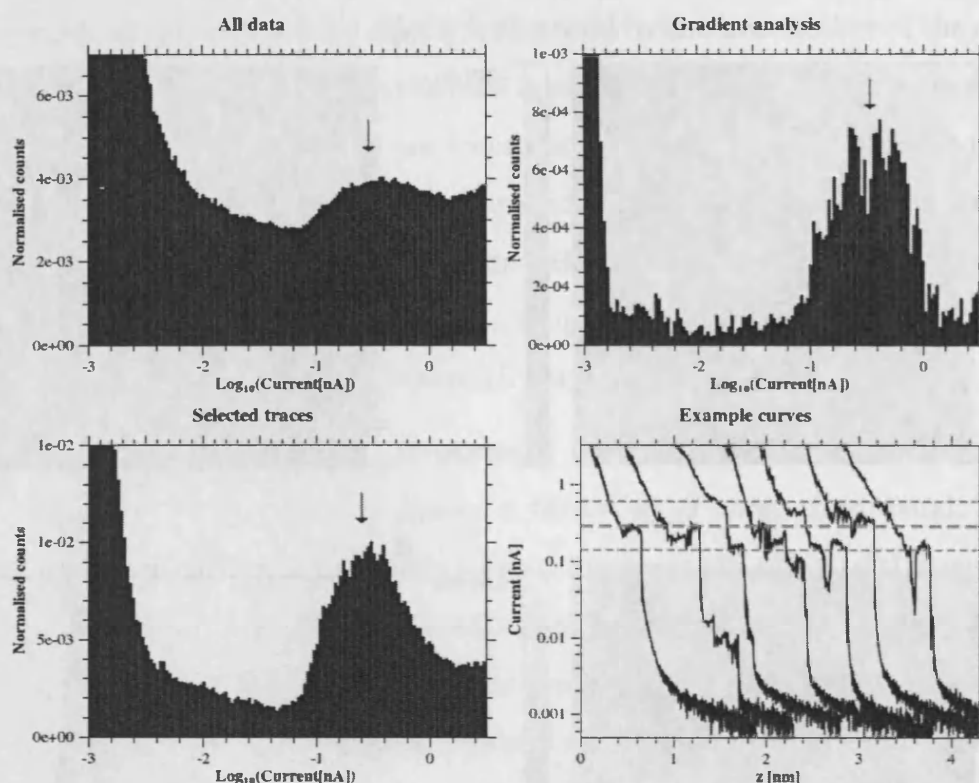


Figure 4.23. Statistical distributions of the current in $I(z)$ curves for nonanedithiol at low coverage on partially sputtered Au, 100mV. (top left) All data, 5400 curves; (top right) gradient analysis of all curves; (bottom left) 315 selected traces (~6%); (bottom right) Typical $I(z)$ curves

The statistical distribution resembles that of the high coverage sample. One broad peak is visible and is enhanced relative to the background by the selection process and gradient analysis. The peak conductance as judged by Gaussian fit to each distribution is 2.88 ± 0.15 ($\sigma = 2.13$) nS in agreement with the high coverage data. There is no evidence of significant features at the lower end of the current range.

This result suggests that the increase in surface roughness, by increasing the areal density of step edges, has enhanced the relative probability of forming high current plateaus, such that these dominate the statistics; conversely, but to similar effect, it may be that it has actually suppressed the formation of the low current plateaus, such that only high current plateaus remain. The percentage of curves

exhibiting plateaus is lower for this sample (6% of curves versus 9% for the low coverage sample), as is the normalised peak height in the all-data histogram, thus favouring the interpretation of a suppression of the low current plateau formation as opposed to an enhancement of the high current plateau frequency. This is in agreement with the observations of Haiss *et al.*

For completeness we now include below the results of $I(z)$ curves performed at a much slower retraction rate and also the results of BJ-STM type measurements, both performed on the high coverage sample.

4.5.5 High coverage sample – very slow curves

Occasionally it was possible to perform a very slow $I(z)$ curve and still obtain current plateaus. This was generally not possible in other attempts, but it may be that the well used tip has many molecules on it and therefore is more likely in this state to be able to make long lasting plateaus often. Whatever the reason, we observed that $I(z)$ curves could be drawn out over a period of ~ 10 s (corresponding to a retraction speed of ~ 0.2 nm s⁻¹) compared to the previously presented curves with a duration of ~ 0.25 s.

Figure 4.24 shows some examples of these slow $I(z)$ curves (displaced along the z axis for clarity) demonstrating that current plateaus can last for several seconds. It is also interesting to note that there are some jumps and fluctuations in the current plateaus, suggesting that some changes in the microscopic details of the contacts or the molecular configuration can take place without breaking the molecular junction. Huang *et al* [73] have shown that at these slow retraction speeds the breakdown of the molecular junction is due to spontaneous bond breaking (rather than forced breaking by pulling), so these fluctuations are not thought to be effected by the applied force of the retracting tip. It is notable that there is again a large variance in the statistical data (Figure 4.25); the SMC from these slow $I(z)$ curves is 2.06 ± 0.04 ($\sigma = 1.26$) nS

and 72 curves out of 200 (36%) showed current plateaus. However the peak in the distribution is well defined and it is evident that this variance is due to the aforementioned fluctuations in the otherwise stable current plateaus.

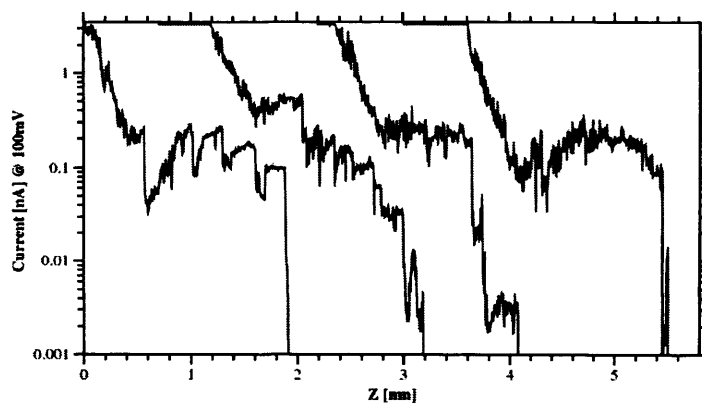


Figure 4.24. Slow $I(z)$ curves on the high coverage sample of nonanedithiol on Au, 100mV.

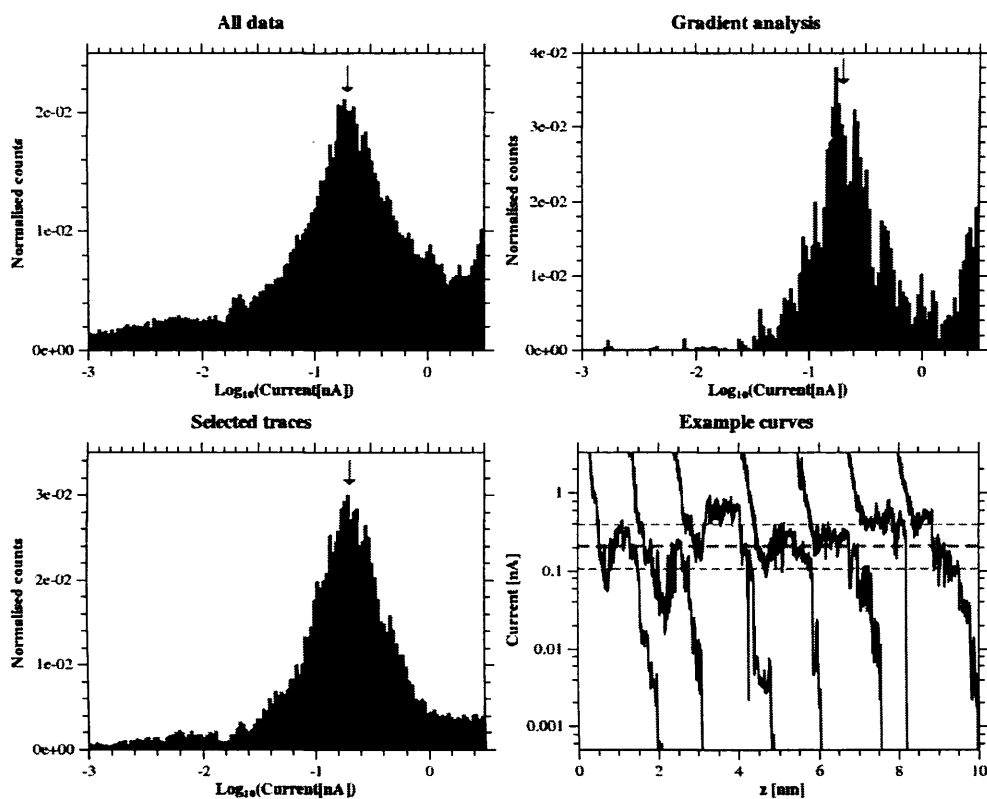


Figure 4.25. Statistical distributions of the current in slow $I(z)$ curves for nonanedithiol at high coverage on Au, 100mV. (top left) All data, 200 curves; (top right) gradient analysis of all curves; (bottom left) 72 selected traces ($\sim 36\%$); (bottom right) Example $I(z)$ curves

4.6 STM Break-junction

In addition to the $I(s)$ style method we perform $I(z)$ measurements in the BJ-STM mode, on the high coverage sample at 100mV. Figure 4.26 shows example $I(z)$ curves exhibiting plateaus in the current. The peak in the statistical distribution (Figure 4.26) gives a SMC of 2.09 ± 0.05 ($\sigma = 0.94$) nS ; 140 curves out of 4200 ($\sim 3\%$) showed plateaus. The value of SMC is in agreement with the data from the slow $I(z)$ curves, but both these experiments give a slightly lower value than the estimates from the other experiments. There is again no evidence of current plateaus at the lower end of the current range, in agreement with the $I(s)$ results on the same sample. The

variance of the SMC in the BJ-STM experiment is markedly lower than the previous experiments. The ramping distance and number of sampled data points in the BJ-STM experiment is larger, but this cannot account for the smaller variance. In fact the overall retraction speed ($\sim 7 \text{ nm s}^{-1}$) is slower than that used in the I(s) style measurements, so should allow more time for fluctuations in the junction during the retraction cycle.

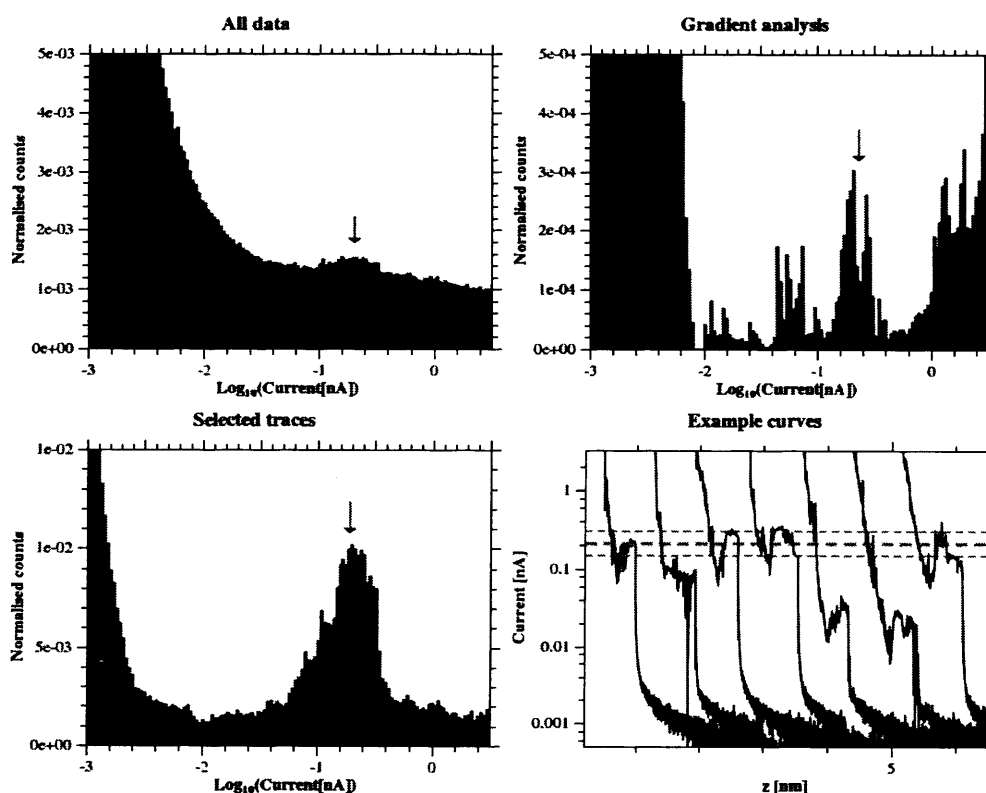


Figure 4.26. Statistical distributions of the current in breakjunction -STM style I(z) curves for nonanedithiol at high coverage on Au, 100mV. (top left) All data, 4200 curves; (top right) gradient analysis of all curves; (bottom left) 140 selected traces ($\sim 3\%$); (bottom right) Example I(z) curves

The results of all the I(z) measurements nonanedithiol are summarised in Table 1 below.

Experimental method	Sample Environment	Single molecule conductance (nS) (figure in brackets is the standard deviation of the peak, σ)		
		Ultra low	Low(A)	Medium(B) /High(C)
High coverage	UHV			2.84 ($\sigma = 2.41$)
Low coverage		0.019 ($\sigma = 0.004$)	0.32 ($\sigma = 0.07$)	3.21 ($\sigma = 2.38$)
Rough surface				2.88 ($\sigma = 2.13$)
BJ-STM				2.06 ($\sigma = 1.26$)
Slow retraction				2.09 ($\sigma = 0.94$)

Table 1. Summary of results in this chapter for the SMC of nonanedithiol by I(z) methods

4.7 Discussion

The most common observation in all the data sets in our study is a broad peak in the range of 1.4 to 3.2 nS, the overall mean value of SMC from this main peak being at 2.616 ± 0.092 ($\sigma = 1.824$) nS. Table 2 summarises a review of conductance values for nonanedithiol and similar molecules from published studies. This main peak in our data is in reasonable agreement with the Medium (group B) conductance reported by other groups. On the low coverage sample we also see a statistically significant number of additional lower current plateaus. A small number of these are in approximate agreement with the Low conductance (A) group reported by others, but most are much lower suggesting a fourth ultra-low group. This is possibly consistent with the observations of Fujihira, Nishikawa and co-workers[67][68] for hexanedithiol in vacuum, where a significantly lower value for the A group was reported compared to other studies in ambient conditions or under solution. This suggests there may be

some effect of the vacuum on the low conductance state (or that noise prevents detection of such low plateaus in liquid), but the mechanism is unknown.

For the main conductance peak there is no clear evidence of well defined separate peaks at multiples of a given conductance. However, the width of this main peak suggests that it could actually be several overlapping peaks due to contributions from multiple molecules in parallel. In published studies the ratio between the B and C group conductance of alkanedithiols is typically between ~ 3 and ~ 5 [9][22][54][56][74]. Data from the most comprehensive systematic study by Haiss *et al* [22] shows empirical evidence that this ratio is most likely a factor of 4, independent of molecular length (in the ML model this could be accounted for by a doubling of the total coupling, Γ). (The ratio between A and B is more widely varying and depends strongly on molecular length.) Thus we may have expected a high conductance group (the C group) for nonanedithiol with SMC between ~ 5 nS and ~ 10 nS. Such is the breadth of the main peak that it is possible this C group is present in our data and it is the combination of the plateaus from both the B and C group that form the broad distribution seen here. However, as we cannot resolve distinct sub-peaks within this broader peak we cannot draw any firm conclusion.

In summary we have reviewed the $I(z)$ technique for the measurement of single molecule conductance and we have shown that the appearance of plateaus in the tunnelling current is consistent with the molecular model of charge transport. We have measured the single molecule conductance of nonanedithiol under UHV conditions, finding general agreement with previously reported values for the Medium (B) and High (C) conductance groups in air and solvent environments. Low current plateaus expected for the A conductance group were relatively infrequent except in the case of the low surface coverage, but the majority of the lower current plateaus are about an order of magnitude lower than published results.

Source	Experimental method	Sample Environment	Single molecule conductance (nS) (quoted error is the standard deviation of the peak)			
			Ultra low	Low(A)	Medium(B)	High(C)
Haiss <i>et al</i> [2004] [53]	I(s)	Ambient Solvent		0.51 ± 0.07 0.51 ± 0.06	-	-
Cui <i>et al</i> [2002] [75] ^a	C-AFM ^b	Solvent		0.58 ± 0.01	-	-
Li <i>et al</i> [2008] [9]	I(s)	Solvent		0.47 ± 0.03	2.0 ± 0.2	9.9 ± 0.9 ($\sim 5.0 \times B$)
Haiss <i>et al</i> [2009] [22] [56]	I(s) / BJ-STM	Ambient (and N ₂)		0.44 ± 0.09	1.8 ± 0.4	6.0 ± 1.2 ($\sim 3.3 \times B$)
This thesis		UHV	0.019 ± 0.004	0.32 ± 0.07	2.62 ± 1.8	
Morita and Lindsay [2007] [74] ^a	C-AFM ^b	Solvent		-	1.6 ± 0.4	4.9 ± 1.3 ($\sim 3 \times B$)
	BJ-STM	Solvent		-	1.1 ± 0.3	5.8 ± 1.6 ($\sim 5.3 \times B$)
Li <i>et al</i> [2006] [54] ^a	BJ-STM	Solvent		-	1.4 ± 0.3	6.2 ± 1.2 ($\sim 4.4 \times B$)
Xu <i>et al</i> [2003] [51] ^a	BJ-STM	Solvent		-	-	7.1 ± 0.7
Haiss <i>et al</i> [2006] [34]	I(t) ^c	Ambient		~ 0.40 to 2.4 depending on setpoint		
Haiss <i>et al</i> [2006] [76]	I(t) ^c	Ambient		0.52 ± 0.09 (at 20°C) to 2.90 ± 0.4 (at 67°C)		
Martín <i>et al</i> [2008] [50] ^{a,d}	I(s)	Ambient		0.27 ± 0.18	-	-
Venkataraman <i>et al</i> [2006] [10] ^{a,c}	BJ-STM	Ambient		-	1.0 ± 0.1	-

Table 2. Summary of published values for the conductance of nonanedithiol. ^a Calculated value based on the trend of conductance versus molecular length. ^b Contact mode atomic force microscopy; probe is brought into contact with matrix-isolated molecules, on Au surface, capped by Au nanoparticles. ^c alternative to I(s). ^d carboxylic-acid terminated alkanes. ^e amine terminated alkanes

5 Matrix isolated Porphyrin molecules

5.1 Introduction

In the previous chapter we introduced a common method of characterising the low bias conductance of single metal-molecule-metal junctions by the $I(z)$ method. This technique was applied to a known system, nonanedithiol, under ultra high vacuum conditions. In this chapter we introduce the motivation behind a study of porphyrin molecular wires and the $I(z)$ technique is subsequently applied to the porphyrins in chapter 6. However in this section we present the current-voltage (I-V) characteristics of porphyrin molecules isolated in a matrix of alkanethiol molecules. We introduce the transition voltage spectroscopy analysis technique and apply this to the I-V measurements, finding that the transition voltage is dependent on the microscopic details of the molecular junction and the molecule itself. The findings are explained in the context of the molecular energy level model.

5.2 Why study porphyrin molecules?

Porphyrins are an important group of naturally occurring chemical compounds, most notably for their biological significance in haemoglobin, chlorophyll and Vitamin B₁₂. All porphyrin chemicals contain the same central macrocycle, porphine, consisting of four pyrrolic subunits linked by four methine bridges (Figure 5.1 a). A great range of changes to this basis can be made by addition of side-chains at the “meso” and “ β ” points or by substitution of the metallic central atom, M (Figure 5.1 b). Almost all metals can form complexes with the porphyrin on a 1:1 basis, although the valency of the metal determines the residual charge and some metals form 2:1 [77]. These changes do not adversely affect the chemical stability, which is perhaps why porphyrin derivatives are so ubiquitous.

For molecular electronic applications the idea of molecular-wires (Mws) is of great interest. Molecular wires would provide not only charge transport over nanometre distances, but also important functionality, possibly incorporating charge storage, current rectification, logic or switching abilities. Porphyrins based Mws are of interest as candidates for molecular electronic devices for a number of reasons. Firstly, the synthesis of porphyrin oligomers has a well established methodology within chemistry laboratories, so chemical structure can easily be used as a variable in electrical studies (Figure 5.2). The oligomers are also highly π -conjugated, therefore fulfilling a prerequisite for good conduction. The aforementioned stability is beneficial and extends to high temperatures and over time also. The metal cation M can be a wide range of different elements, so along with peripheral substitutions this allows a certain amount of tuning of the electrical properties. Porphyrins also display strong non-linear optical activity [78] and redox activity, giving porphyrin devices scope for optical switching and chemical modulation.

While measurements on molecular wires have to-date yielded a variety of interesting transport properties, the mechanisms of electron transport in single molecular wires are not well understood. This is why a comprehensive study of one type of system would be beneficial to the molecular electronics community. By measuring the properties of porphyrin molecular wires as a function of length, temperature and chemistry the results obtained will not only go toward characterising one system, but also this should provide important information to help resolve outstanding issues in molecular wire physics in general. This is the motivation for the porphyrin project as a whole.

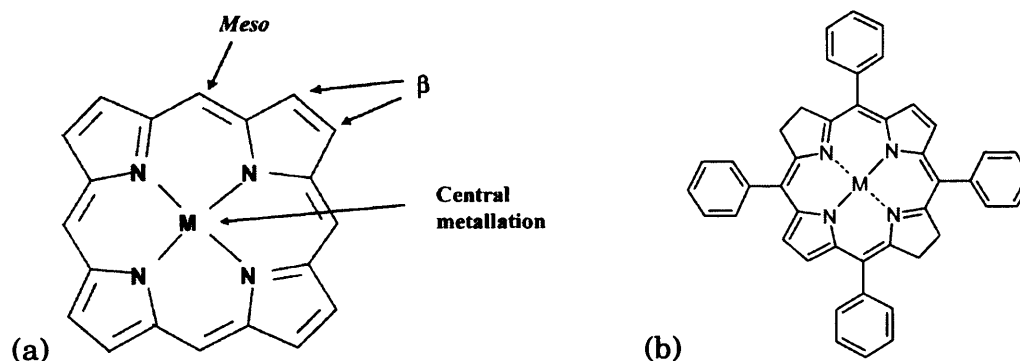


Figure 5.1. (a) structural diagram of the porphyrin macrocycle. Molecules classed as porphyrins are those composed of the porphyrin macrocycle with additional molecular groups located at the “Meso” (meso-linked) and/or “β” (β-linked) positions. The “M” can be a number of different elements e.g. 2H, Zn, Fe, Co, Cu, Ag, Cd, Hg, etc. (b) shows a (metal) tetraphenylporphyrin (M-TPP) with the four phenyl groups meso-linked to the macrocycle. Reprinted from [78].

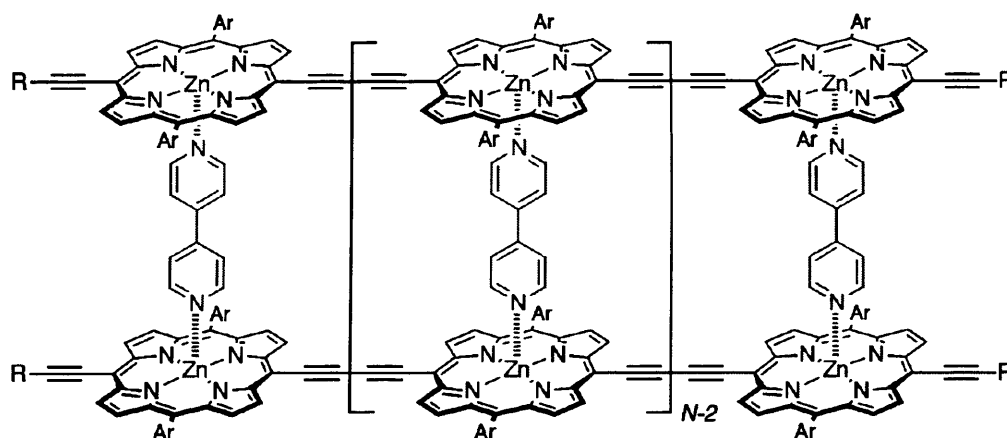


Figure 5.2. Some more sophisticated architectures can be created by chemists, including meso-linking macrocycles to create porphyrin nanowires. The side chains and end groups can also be tailored and there is scope to organise the wires into the “ladder” structure as shown in the figure, where two nanowires are linked out of the plane of the macrocycle, by a pyridine ligand coordinated to the central metallisation site.

The porphyrin molecules we study are part of a homologous series of oligomers (Figure 5.3) synthesised by Harry Anderson's group in Oxford and recently examined by Richard Nichols' group in Liverpool (Sedghi et al [16]). The molecules bear terminal thioacetates at both ends for bonding to gold substrates and to help ensure good chemisorbed contact to an STM tip used to measure the I-V characteristics. In the

study published by Sedghi et al the SMC of the porphyrins was measured for the series of oligomers up to $n = 3$ and the variation of the conductance, G , versus molecular length, l , can be fitted by an exponential decay function of the form $G \propto \exp(-\beta l)$, typical of tunnelling transport. The porphyrins were found to have an ultra-low attenuation parameter $\beta < 0.4 \text{ nm}^{-1}$, cf. typically larger values for members of the alkanedithiol series: 4.2 to 7.3 nm^{-1} in ref. [56], 7.9 nm^{-1} in ref. [79], 7.5 nm^{-1} in ref. [9]. The values for the alkanedithiol are in good agreement with predictions based on a non-resonant tunnelling model of transport [23], thus the ultra-low value reported by Sedghi et al suggests a mechanism other than pure tunnelling may be involved in charge transport in the porphyrin system, or at least the effective barrier height in a Simmons-type model is very low. The single molecule conductance measurements are performed at a fixed low/intermediate bias value and it is therefore of great interest to also examine their higher-bias behaviour in the form of current-voltage (I-V) characteristics.

Thus in the experiments presented in this chapter we investigate the I-V characteristics of the porphyrin molecules, using two different approaches for comparison. We first isolate individual porphyrin molecules in a host matrix of alkanethiols. This allows us to target single molecules for I-V measurements and the principles are described in more detail below. In parallel to this the properties of the hosting alkanethiol matrix can be explicitly probed for comparison. In a separate experiment we also prepare self assembled monolayers (SAMs) of the porphyrins only and perform similar measurements on these samples for direct comparison with the results on the isolated porphyrins. Samples of both the porphyrin monomer ($n=1$) and porphyrin dimer ($n=2$) are prepared. We present a detailed study of the I-V characteristics of these samples, including the time dependence and statistics of the extracted physical parameters.

5.3 Matrix isolation

One approach to address individual conjugated molecules is to isolate the target molecule, the porphyrin, at low concentration, in a hosting matrix of alkanethiol molecules. This is known as the matrix isolated (MI) method [45] (see Figure 5.4). The MI method is based on the principles that a) alkanethiols form ordered monolayers on Au [42], thus can act as a structured matrix for inserting other molecules, and b) the large HOMO – LUMO gap of the alkanethiol (~8 eV [48]) means that there are no molecular energy levels related to the matrix material within a few eV of the Fermi energy, thus this ensures negligible interaction between the electronic states of the inserted molecules (assuming a small HOMO – LUMO gap, desirable for conducting molecules) and the host matrix. The strong interaction between the Au substrate and thiol terminal group, along with the packing effect of the alkanethiol molecules at saturation coverage, forces the porphyrin molecules into an upright or tilted configuration with respect to the Au surface, rather than flat lying. This allows us to target the isolated porphyrin molecules with the STM tip and measure the I-V characteristics of the tip-molecule-substrate junction.

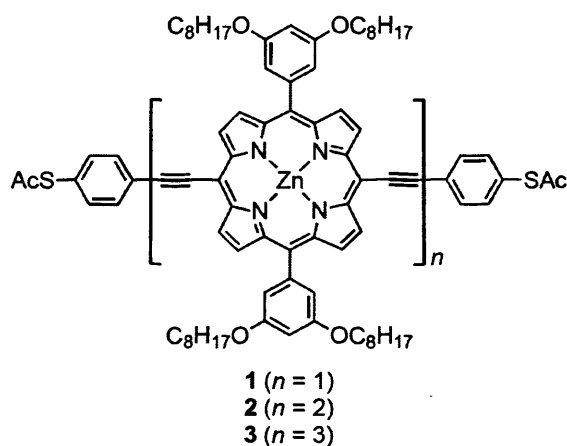


Figure 5.3. General structure of the porphyrin derived oligomer series used in the study (see the supporting information from ref. [16] for details of the chemical synthesis). Acetyl protected thiol groups provide chemical contact to the Au surface and STM tip. The octyloxy side groups aid solubility.

We prepared a mixed monolayer of porphyrin dimer ($n = 2$) molecules and hexadecanethiol (C16) molecules (see *Sample preparation* box for details). STM constant current topography images[32] (using an etched Au wire tip with typically 100pA setpoint and -1V bias) of matrix-isolated samples are shown in Figure 5.5. Flat regions on the Au terraces are occupied by the C16 matrix, whilst the pits seen over the surface are caused by the etching effect on the Au surface of the thiol molecules in the solution phase[41]. The raised spots (absent in samples prepared from solutions of the C16 molecule only) correspond to one, or a few, inserted porphyrin molecule(s). This is supported by the known size of the molecules (3.82 nm long) and statistics from a large number of these spots, which show areas measuring typically $6 \times 3 \text{ nm}^2$. Additionally, separate experiments (see chapter 6) on porphyrin molecules deposited on Au surfaces, with piperidine ligands to prevent a lying down phase, show an average molecular separation of **3.9 nm**. Thus we can be sure that these raised spots are indeed the porphyrin molecules and importantly, these raised spots have very different I-V characteristics to the surrounding matrix.

5.3.1 Sample preparation

Mixed monolayers (MI)

We prepare the molecular layers on Au/mica substrates, purchased from Phasis Sàrl, Switzerland and sputtered and annealed in UHV before use. Porphyrin molecules were isolated in an alkanethiol matrix using the one-step matrix insolation method[45] for mixed monolayer samples. Fresh solutions of alkanethiol and porphyrin were prepared both at 5×10^{-5} M in toluene, then mixed together at a ratio of 100:1 (alkanethiol to porphyrin) by volume. The mixed solution was then placed in a nitrogen filled glovebox (<0.05% oxygen, and less than 5% humidity). A freshly sputtered and annealed Au/Mica substrate was removed from UHV and immediately immersed in the mixed solution. The sample was left to incubate in the solution overnight then rinsed in toluene for 1 minute, to remove any unbound/physisorbed molecules, and dried in flowing nitrogen for about 1 minute. Electrical contact to the sample was made using a small amount of conductive silver paint. STM tips were made from Au wire by electrochemical etching in HCl/ethanol (1:1)[65]. STM experiments were performed using a commercial instrument[32] operating inside a glovebox under constant nitrogen flow to reduce the ambient humidity.

Porphyrin SAM

For comparison with the results of experiments on the MI porphyrins a self assembled monolayer (SAM) of the porphyrin molecules only was formed, on an atomically flat Au surface, from solutions in toluene at 5×10^{-5} M. The authors take advice from Sedghi et al[16] and use piperidine as an axially binding ligand to help facilitate a standing-up configuration of the molecules, although this is not thought to influence the electronic properties of the molecule, as the current is expected to flow between the two thiol end groups bound to the electrodes, via the porphyrin macrocycle, but by-passing the central zinc atom[80]. A fresh solution of the porphyrin dimer was prepared at 5×10^{-5} M in toluene, and piperidine ligand was added to give a ratio of piperidine to porphyrin greater than 5:1 to ensure all porphyrin molecules are coordinated to two axially binding ligands. The solution was then placed in a nitrogen filled glovebox (<0.05% oxygen, and less than 5% humidity). A freshly sputtered and annealed Au/Mica substrate was removed from UHV and immediately immersed in the mixed solution. The sample was left to incubate in the solution for several days then rinsed in toluene to remove any unbound/physisorbed molecules and excess piperidine, and dried in flowing nitrogen for about 1 minute.

The observed apparent, average, height of the spots above the surrounding matrix is 0.61 ± 0.04 nm. Assuming that the molecules in the alkanethiol matrix are tilted by 30° to the normal and the porphyrins are upright, we would expect the height difference to be ~ 1.84 nm; this apparent height difference is due to their higher conductivity and in a barrier tunnelling model this can be used to estimate β_m for the inserted molecule [81]:

$$\beta_m = [\beta_{alkane} h_{alkane} - \alpha(\Delta STM - \Delta h)] / h_m \quad . \quad (5.1)$$

This calculation assumes that the decay constant of air $\alpha = 23 \text{ nm}^{-1}$ and β for the alkane matrix is 12 nm^{-1} ; h_m and h_{alkane} are the heights of the inserted molecule and tilted alkane molecules respectively, Δh is the difference between the two and ΔSTM is the measured apparent height difference. Thus this gives an estimate of β for the inserted porphyrin dimer at $\sim 8.6 \pm 0.1 \text{ nm}^{-1}$. With the tip bias at -1 V we assume field emission and this corresponds to an effective work function of $\phi \sim 0.51 \pm 0.02 \text{ eV}$ ($\sim 0.68 \pm 0.02 \text{ eV}$ if we assume direct tunnelling; from the definition of β , see chapter 3). This is an indication of the interfacial dipole at the Au-porphyrin interface, *not* the molecular energy levels/orbitals. We also studied the porphyrin monomer ($n = 1$) isolated in a matrix of the shorter dodecanethiol (C12) molecule. The sample preparation was the same as above and the STM images were qualitatively similar. Apparent height analysis on the porphyrin monomer inserted into a matrix of dodecanethiol gives $\beta \sim 8.0 \pm 0.5 \text{ nm}^{-1}$ corresponding to an effective work function of $\phi \sim 0.46 \pm 0.06 \text{ eV}$, indicating that the dipole formed at the porphyrin-Au interface is comparable for the dimer and monomer.

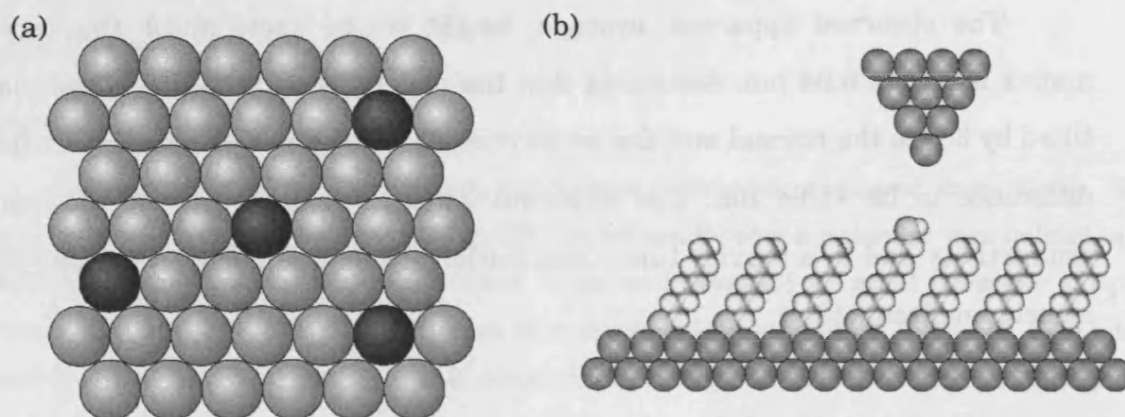


Figure 5.4. Cartoon representations of the matrix isolation method. (a) In this view from above of the mixed molecular monolayer the target molecule (black) is isolated in a matrix of host molecules (grey). The host molecules, at relatively high concentration, form an ordered monolayer and the target molecules, introduced at relatively low concentration, are incorporated as isolated molecules in the host matrix. (b) the isolated molecules can be individually targeted by the probing STM tip.

Complementary to the apparent height measurements of the MI porphyrins we estimate β from the $I(z)$ dependence over the monolayer samples. Figure 5.6 shows the STM image of the porphyrin dimer monolayer. It is thought that at such high coverage of the porphyrins many molecules are interacting with the Au tip as it scans across the surface and this usually prevents high resolution imaging, as is the case in this example. Some examples of the $I(z)$ characteristics are shown in Figure 5.7. We use the Savitsky-Golay filter[66] to calculate the smoothed derivative of $\ln(I)$ versus z at each point in the curve. We then split the curve into sections based on the current values and plot the distribution of the slope for each of the sections to see how it changes with current. The curve of $\ln(I)$ versus z is typically non-linear (see Figure 5.7) and is therefore uncharacteristic of tunnelling through a Simmons-type barrier. Figure 5.7 (b) shows how the average slope decreases with increasing current (decreasing tip-sample distance). It has been shown[82] that such a change in slope can be the result of the STM tip penetrating the molecular monolayer and hence effecting a change in the apparent tunnelling barrier height. We suggest that this change is the result of making the transition from Simmons-type tunnelling at large z to direct coupling of

the molecule at small z . When the tip is far away from the molecular monolayer conduction is initially by through-space tunnelling with a barrier height determined by the effective, surface work function. Subsequently, as the tip contacts the monolayer, the molecules are coupled directly to the STM tip and hence transmission is through molecular energy levels with through-space tunnelling in parallel. The coupling to the molecule will increase with further tip approach, thus current continues to increase as z reduces, but the slope is not necessarily the same as at large z .

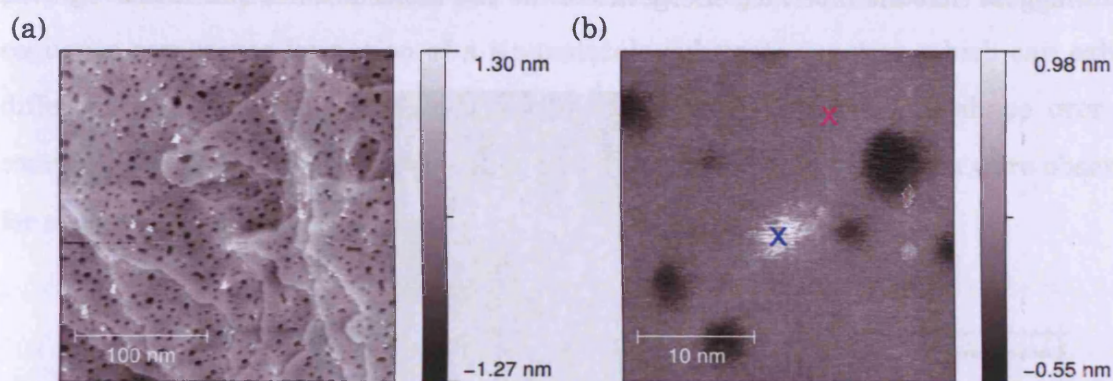


Figure 5.5. (a,b) STM constant current topography image (100 pA setpoint, -1V bias) of Au/mica covered by a mixed monolayer of the porphyrin dimer and C16, imaged by Au etched wire tip. Raised spots in STM images show the spatial confinement of individual, or small groups of, porphyrin molecules. The flat regions between the pits and raised spots are occupied by the C16 matrix. (b) Smaller scale image illustrating the procedure for targeting the isolated molecules. The STM tip is thus positioned over the porphyrin molecule, e.g. at the position marked by the blue X, or alternatively over the matrix (magenta X).

For the porphyrin dimer SAM in N_2 , at -100mV the slope at the low current range gives $\beta = 6.40 \pm 0.17$ ($\sigma = 4.11$) nm^{-1} , which gives an estimate of the barrier height in the Simmons model of $\phi = 0.390 \pm 0.020$ (0.501) eV. At high currents the curve flattens off with an average slope = -0.966 ± 0.036 nm^{-1} which would give $\phi = 8.89$ meV. Such a low barrier height is again uncharacteristic of Simmons-type tunnelling behaviour. Similarly for the porphyrin monomer SAM at low current $\beta = 6.93 \pm 0.13$ ($\sigma = 3.20$) nm^{-1} giving $\phi = 0.458 \pm 0.018$ (0.423) eV; at high current the

slope = $-0.426 \pm 0.025 \text{ nm}^{-1}$ which would give $\phi = 1.73 \text{ meV}$. These estimated tunnelling barrier heights are similar to those taken from the apparent height analysis, although in that case ϕ is lower for the monomer compared to the dimer. The full $I(z)$ characteristic is ultimately more instructive than the apparent height analysis and is a better probe of the low bias characteristics. The conclusion from this analysis is simply that the charge transport through the porphyrins is not well described by tunnelling through a rectangular barrier, as we anticipated from Sedghi's previous results, but the estimated barrier heights for the porphyrin monomer and dimer suggest that the interface energetics of the two molecules are quantitatively similar.

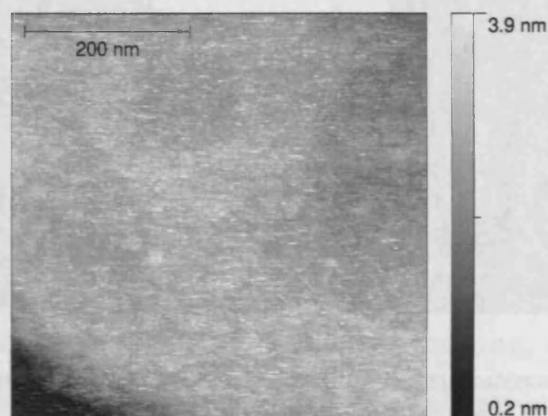


Figure 5.6. STM image of the self-assembled monolayer of Porphyrin dimer on Au/mica (100 pA setpoint, -1V bias).

5.4 Current voltage characteristics

To explore the electrical properties of the porphyrin molecule over a range of energies we perform I-V spectroscopy above the isolated porphyrin molecules, in particular aiming to form a contact between the STM tip and an individual molecule. To perform I-V spectroscopy on the isolated molecules we perform a "measurement sequence" as follows: (i) place the tip over one of the molecules (with 20 mV bias and 100 pA setpoint) (ii) turn off feedback (iii) commence a series of ~ 200 I-V curves

(typically from -1.5 to +1.5 V and back again at a rate of 14 Hz) (iv) re-establish feedback in between each curve. (The feedback setpoint value chosen corresponds to an overall tunnelling conductance of 5 nS, which, based on the typical 2 nS conductance of the molecules found by Sedghi *et al*[16], is sufficiently high to ensure a good chemisorbed contact of the STM tip with the exposed sulphur of the porphyrin molecule). This sequence thus repeatedly samples the I-V characteristic as the tip-molecule junction evolves due to changes in the molecular configuration and possible lateral or vertical drift of the tip. I-V characteristics are shown both above the porphyrin molecules and over the C16 matrix (Figure 5.8). Each measurement sequence represents formation of a tip-molecule-substrate junction which can exhibit different I-V behaviour and which can fluctuate in magnitude and shape over the course of the sequence. Both symmetric and asymmetric type I-V curves were observed for the porphyrin molecule.

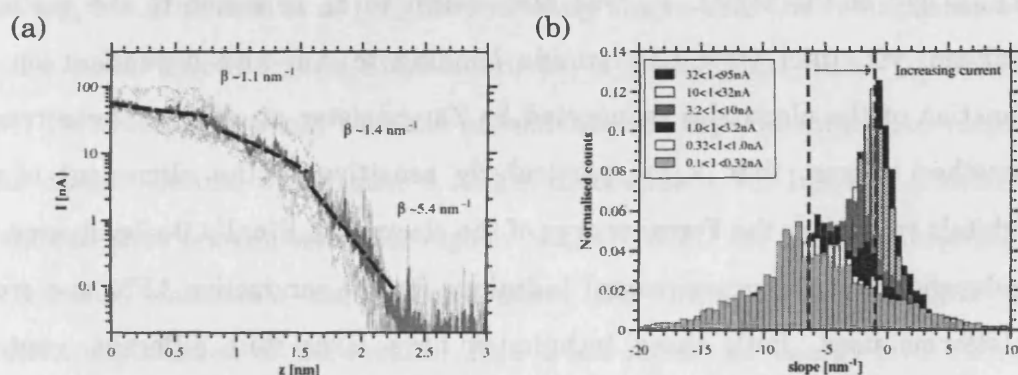


Figure 5.7. $I(z)$ curves above the porphyrin dimer monolayer. (a) The average (dark grey) of 5 individual measurements (light grey) is shown, with linear fits over three sections to demonstrate the change in slope. (b) distribution of the smoothed derivative of $\ln(I)$ versus z for different current ranges.

5.4.1 Transition voltage spectroscopy

One way of analysing such I-V characteristics is through transition voltage spectroscopy (TVS), first introduced by Beebe *et al* [14], [17], in which a plot of $\ln(I/V^2)$ versus $1/V$ (known as a Fowler-Nordheim or F-N plot) shows a minimum at a

particular voltage V_m . This voltage (the so called transition voltage) was assumed to be equal to the height ϕ of the equivalent rectangular tunnelling barrier between metal and molecule, since a comparison with the commonly-employed Simmons tunnelling model of molecular conductance shows that the F-N plot has opposite slopes in the limit of $eV \gg \phi$ and $eV \ll \phi$. The F-N plot for the I-V curves in Figure 5.8 is shown below in Figure 5.9; the transition effect can be clearly seen in the curves over the porphyrin molecules.

For a series of similar molecules showing extended conjugation Beebe showed that V_m scaled approximately linearly with the $E_F - E_{HOMO}$ gap of the molecule (from UPS measurements), and also inversely with molecular length (within a homologous series; the HOMO-LUMO gap is known to decrease with molecular length in conjugated systems). Additionally for a series of alkanethiol molecules V_m was found to be invariant with length (within error), in agreement with the virtually constant $E_F - E_{HOMO}$ gap of the series. V_m was also shown to be sensitive to the metal-molecule linkage, viz. thiol versus isocyanide bonding to Au, and dependent on the work function of the electrodes (supported by Zangmeister et al[39]). These results taken together suggest that V_m is particularly sensitive to the alignment of molecular orbitals relative to the Fermi energy of the electrodes. Finally Beebe showed that V_m is independent of the experimental technique for the conductive AFM and crossed-wire platforms used. Both these techniques have large, but different, contact areas, facilitating contact to large numbers of molecules simultaneously and thus cannot be regarded as single-molecule experiments.

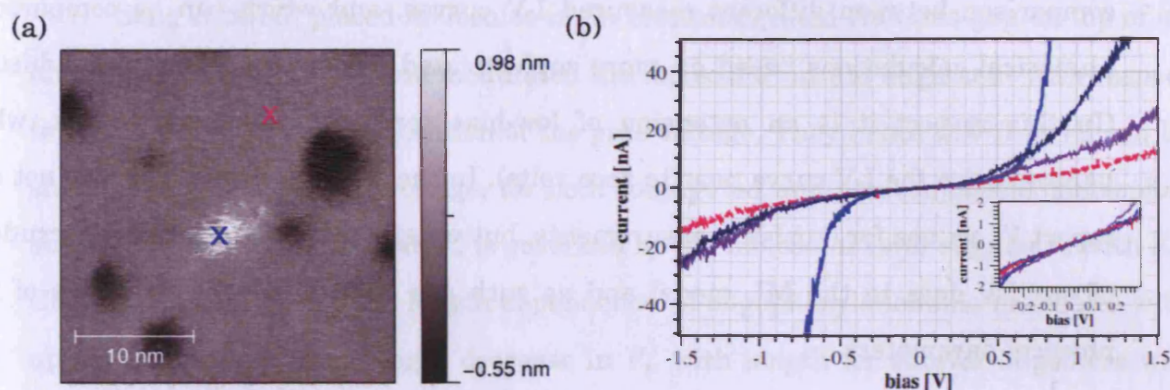


Figure 5.8. (a) STM constant current topography image of an isolate porphyrin molecule, as shown in Figure 5.5. The STM tip is positioned (central, blue X) over a porphyrin molecule or (magenta X) over the matrix to take a series of I-V curves. (b) Representative I-V curves, without averaging, one taken over the hexadecanethiol matrix (magenta dashed line) and three over an inserted porphyrin molecule (solid lines). Inset: low bias range, (± 300 mV shown). Feedback settings: -20 mV, 100 pA (equivalent to $0.2 \text{ G}\Omega$ or 5 nS); Au etched tip.

The results of Beebe were interpreted in the Simmons barrier model of tunnelling, but Huisman *et al* [18] have recently shown that the relationship between V_m and ϕ which follows from a Simmons model is more subtle, with V_m in fact scaling as $\sqrt{\phi/z}$. This result contrasts with the aforementioned experimental observations [14], [17] for alkane chains, which have a length-independent V_m . Instead, Huisman *et al* [18] showed that transmission through a single HOMO (or LUMO) molecular level (with certain reasonable assumptions about the level broadening) gave a more consistent explanation of the results. This is the molecular energy level (ML) model outlined in chapter 2. In this case, the difference between the Fermi energy of the Au contacts and the nearest molecular level (typically HOMO) governs the measured V_m . The model, however, fails to account for the discrepancy between $E_F - E_{HOMO}$, as measured by UPS, and V_m ; the difference is especially acute for the case of the alkanethiols where $V_m \sim 1.23 \pm 0.04 \text{ V}$ whilst $E_F - E_{HOMO}$ is expected to be of the order $\sim 4 \text{ eV}$ depending on the exact Fermi level alignment in the HOMO-LUMO gap.

Irrespective of the underlying physics governing the value of V_m it gives an extremely useful parameter which can be used to make straightforward quantitative



comparison between different measured I-V curves, and which can be compared to numerical calculations based on more sophisticated models of molecular conduction. (In this respect it is an extension of low-bias conductance measurements, which parameterise the I-V curve near to zero volts). In the analysis that follows we not only report V_m values for our I-V measurements, but we are also able to produce a crude fit of our I-V data to the ML model and as such are able to extract estimates of real physical parameters.

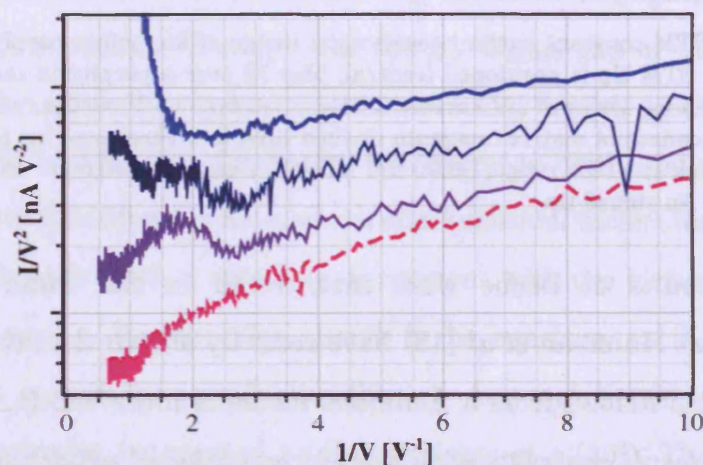


Figure 5.9. F-N plot for the same data in Figure 5.8 (positive bias only, offset and scaled for clarity) plotted as I/V^2 versus $1/V$.

TVS has become a popular tool in studies of molecular electronic properties and we shall now review some of the other recent findings. Wang *et al*[83] reported different V_m for SAMs of alkanethiols C8, C10 and C12 under high loading force of the AFM cantilever; V_m values as low as 0.4 V were measured for C8, in marked contrast to Beebe's result. V_m was found to be dependent on the loading force and we extrapolate their data to find that $V_m \sim 1.0$ to 1.1 V at zero applied force, in approximate agreement with Beebe *et al*. Song *et al*[84] measured I-V for alkanethiol (C8, C12 and C16) SAMs in nanowells and reported only direct tunnelling (i.e. no V_m within the ± 1 V window) in 87.8 % of the devices, but 6.5% did show a transition below 1 V.

Song *et al*[85] placed molecules in an electromigrated Au nano-gap on top of an aluminium gate electrode and modulated the molecular orbital alignment with respect to the Fermi energy by application of the gate voltage. They hence saw that V_m can be shifted linearly with gate voltage, for both conjugated and non-conjugated molecules, supporting the assertion that V_m is governed by the molecular level alignment with E_F . Choi *et al*[20] examined the length dependence of oligophenyleneimine molecules with up to 10 repeat units. A slight decrease in V_m with length for shorter oligomers was seen, in agreement with a barrier height decrease expected from the trend in oxidation potentials. (The longer molecules show no such continuation of the trend, and other indications suggest that the transport mechanism, in the longer oligomers, is distinctly different to that in the shorter chains.)

Pakoulev *et al* [21] measured V_m for MI molecules of 2-[4-(2- mercaptoethyl)-phenyl]ethanethiol and saw a increase in V_m from ~ 0.7 to ~ 2.4 V with increasing temperature from 15 K to 294 K. Such temperature dependence suggests that the rectangular barrier tunnelling model is not appropriate for this molecule, nevertheless the authors pursue the analysis based on this model and propose a modified barrier shape, which includes a temperature dependent injection barrier, to account for it. In light of Huisman's results this model seems somewhat naïve. However in the simple molecular model such a strong temperature dependence is not expected (see Appendix A), thus this result points to a more complicated mechanism of charge transport than assumed.

Related to our study, Noguchi *et al* [86] measured V_m for a single porphyrin molecule in an electromigrated break junction, at low temperature. Both symmetric and asymmetric I-V curves were reportedly measured, but only the symmetric curves were considered in the analysis of V_m and a single average value of V_m was quoted for the cobalt ($V_m = 0.19$ V) and free-base porphyrins ($V_m = 0.34$ V) used. This compares to

the estimated barrier heights, from UPS, of $E_F - E_{HOMO} = 1.9$ eV and 1.7 eV for the cobalt and free-base porphyrins respectively.

An important set of results was presented by Mangin *et al*[58] for Au electromigrated nano-gaps. The authors studied nominally clean devices, but nevertheless found I-V curves which exhibited a $V_m < 0.5$ V. The I-V curves were fitted by the results of numerical calculations based on the WKB model and this gave estimates of the asymmetric barrier heights of the left and right electrodes in the range ~0.2 to 1.6 eV (much lower than the ~4.7 eV expected work function of Au; see previous discussion in chapter 4).

More recently two further papers have been published regarding the modelling and interpretation of the TVS results. Araidai *et al* [15] perform *ab initio* calculations to determine the transport through a single phenyl-thiol molecule between Au electrodes. They reproduce qualitatively the appearance of V_m in the I-V characteristic and note that the value of V_m is just less than the peak position, in eV, of the HOMO level relative to E_F . Seemingly unaware of the work of Huisman they nevertheless use the same ML model as that in [18] to investigate the factors influencing V_m in the simple molecular model and reach the same conclusions. The *ab initio* calculations of the potential profile in the molecule show that the molecular junction in no way resembles the rectangular barrier so often invoked. In addition the profile is not significantly perturbed by the applied bias, again in direct contrast to the changing barrier shape in the conventional model.

Chen *et al*[19] expand on the model of Huisman and assume a linear dependence of the HOMO level position on the applied bias scaled by the asymmetry factor η ($= 0.5$ corresponds to a perfectly symmetric junction); this is the same approach that we have used, independently, in our model. The authors used DFT calculations to determine η and V_m for some of the molecules previously studied by Beebe and showed that $(|E_F - \epsilon_{\text{molecule}}|)/V_m$ scales linearly with η (seemingly

independent of $\epsilon_{\text{molecule}}$). For the molecules considered, even when modelling a highly asymmetric STM configuration, η was never larger than ~ 0.7 .

5.5 Results on isolated porphyrin molecules

As previously illustrated we are able to see the transition voltage phenomenon in our data for the MI porphyrin molecules. We find that the asymmetry in some of the I-V curves is also reflected as an asymmetry in the values at positive (V_m^+) and negative bias (V_m^-). In addition fluctuations in the series of I-V curves manifest as fluctuations in V_m over time, for any given measurement sequence. To quantify this effect, and also gain an insight into the statistical distribution of V_m , the voltage minimum is extracted for each *individual* curve in the sequence, *without* taking an average over several curves. After more than 50 measurement sequences on the isolated dimer molecules over 10,000 I-V curves were acquired (and more than 30,000 curves were taken for the MI monomer molecule). The minimum point is automatically determined by first smoothing the curve, then finding the minimum in $\log(I/V^2)$ and finally fitting a parabola near the minimum to be sure to get the correct local minimum (see Appendix C). Due to noise in individual traces V_m is not always well defined, and around 30% of the I-V curves were rejected from the final analysis.

5.5.1 Fluctuations and asymmetric response – examples, time series

Two examples of the fluctuation of V_m over the course of a measurement are shown in Figure 5.10 for the MI dimer. The first series, Figure 5.10 (a) positive and negative bias, shows a sequence where the tunnelling characteristic is consistent over the course of the measurement (i.e. each I-V curve is of similar shape and magnitude for >200 I-V curves, labeled 1), with $V_m \sim 0.35$ V for both positive and negative bias.

After a certain point, however, V_m changes rather abruptly to a value of ~ 1.3 V in region 2. Series (b) shows a more dynamic junction behaviour in which V_m is seen to fluctuate and is also not always equivalent for positive and negative bias. In all cases, the measurement sequence terminates with a higher V_m value and overall I-V characteristic similar to that seen over the C16 matrix. For this reason, detailed I-V curves were also recorded over the surrounding C16 matrix (and C12 matrix for the monomer sample) and yielded measurable values of V_m (as previously reported for pure alkanethiol SAMs[17], [83]). However, the I-V characteristic is typically asymmetric over the alkanethiol matrix, and measurement sequences show little evidence of fluctuations in V_m , in contrast to those seen over the porphyrin molecule. The typical value of V_m measured directly above the C16 matrix is similar to the final values seen in Figure 5.10, strongly suggesting that over the course of a sequence the lateral drift rate is enough to move the tip away from the porphyrin molecule and over the surrounding matrix[87]. The results on the alkanethiols are discussed further below.

In measurement over the inserted porphyrin molecule, lateral drift means that the exact tip-molecule contact configuration will not remain constant over a long period and the measurement, therefore, necessarily samples different tip-molecule configurations. Several studies have shown that, for a given thiol-terminated molecule on Au, distinctly different transport characteristics are possible depending variously on the precise details of the absorption geometry[71][88][89][90], coordination of the terminal group with the electrode atoms[9][91], molecular conformation[92][93], tilt angle[34][94], or the molecular orientation and packing[95]. It is thus probable that the fluctuations in V_m are caused by change in the configuration at the Au-thiol contact which determines the charge transport via the nanoscale contact.

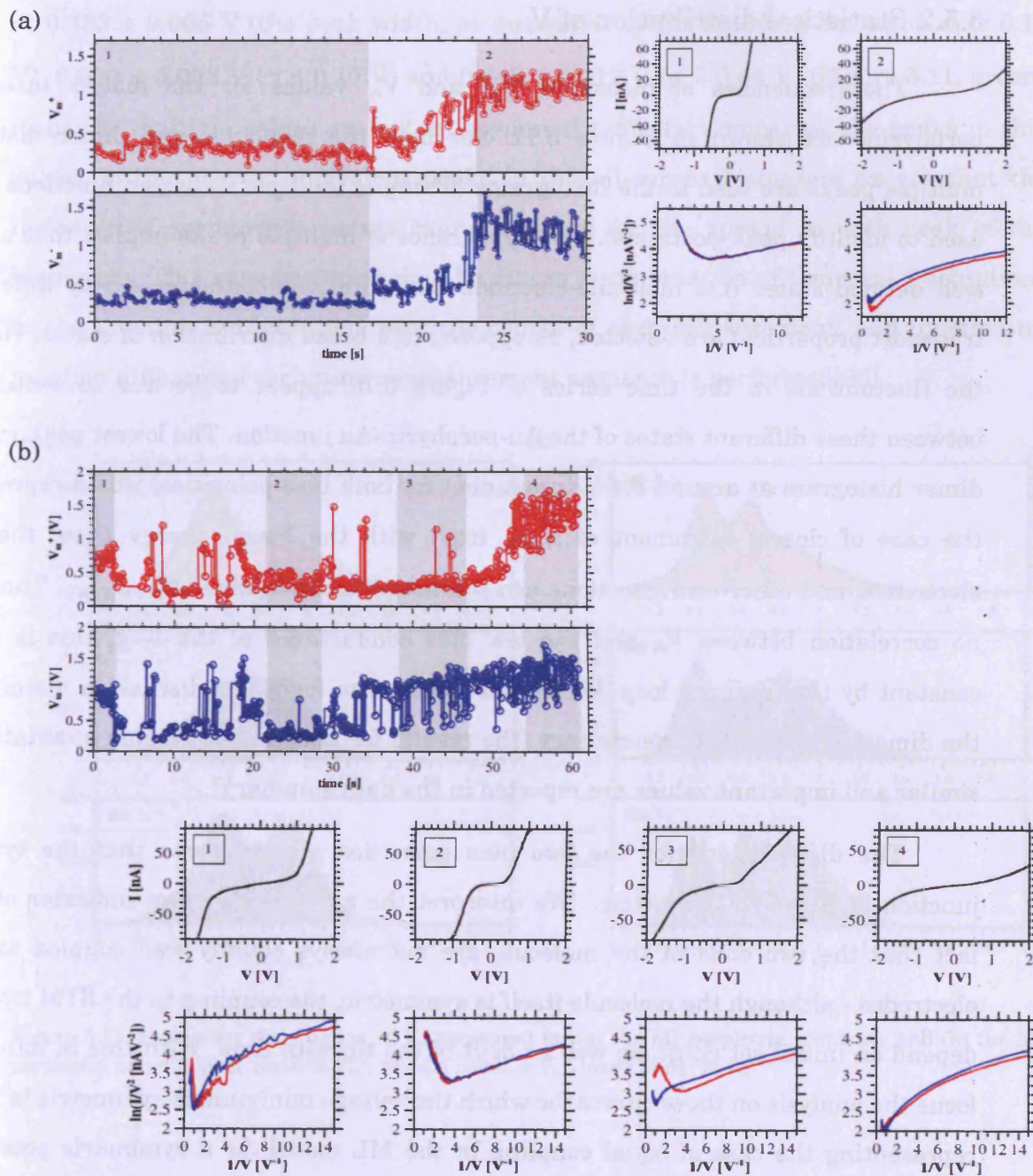


Figure 5.10. Two examples time series (a) and (b) of V_m from repeat measurements over the MI porphyrin dimer molecule. Also shown for each is the average I-V curve and corresponding F-N plot for each of the shaded, numbered regions.

5.5.2 Statistical distribution of V_m

The frequencies of measured V_m^+ and V_m^- values for the matrix inserted porphyrins are shown in Figure 5.11. For both the monomer and dimer distinct multiple peaks are seen in the histograms (fitting of multiple Gaussian functions was used to identify peak positions). The appearance of multiple peaks implies that a few well defined states (i.e. molecule-electrode configurations characterised by different transport properties) are detected, as opposed to a broad distribution of states. Hence the fluctuations in the time series of Figure 5.10 appear to be due to switching between these different states of the Au-porphyrin-Au junction. The lowest peak in the dimer histogram at around 0.4 V (prominent for both bias polarities) would represent the case of closest alignment of ϵ_{HOMO} (say) with the Fermi energy E_F of the Au electrodes, and other configurations are characterised by a larger $E_F - \epsilon_{HOMO}$. There is no correlation between V_m and the low bias conductance of the I-Vs; this is held constant by the feedback loop. We herein continue to focus our discussion mainly on the dimer for the sake of consistency (the results for the monomer being qualitatively similar and important values are reported in the data summary).

The distributions for the two bias polarities also suggests that the typical junction is slightly asymmetric. We interpret the asymmetry as an indicator of the fact that the two ends of the molecule are not always equally well coupled to the electrodes - although the molecule itself is symmetric, the coupling to the STM tip will depend on initial set point, as well as drift of the tip with time. With this in mind we focus the analysis on those curves for which the voltage minimum is symmetric in bias, representing the case of equal coupling in the ML model (or a symmetric potential barrier in the Simmons model of tunnelling). In this experiment approximately 18% of the I-V curves measured showed V_m^+ equal to V_m^- to within $\pm 10\%$, and we use this criterion to define and select the symmetric curves for analysis. The resultant histogram of V_m^{sym} for this subset of the measured I-V curves also shows several peaks

at 0.383 ± 0.005 V (the peak width, as measured by the standard deviation σ , is 0.16 V), 0.630 ± 0.003 V ($\sigma = 0.10$ V) and 0.849 ± 0.012 V ($\sigma = 0.44$ V) (Figure 5.11, green) (thus the multiple values are not an asymmetry effect). Comparing the peaks in this subset to the nearest equivalent peaks in the all-curves histogram we see that the inclusion of asymmetric curves cannot account for the spread in each peak of the histogram. This variance must then be due to a combination of temporal fluctuations in the junction configuration, over the course of each measurement, and junction-to-junction differences each time a measurement sequence is performed[96].

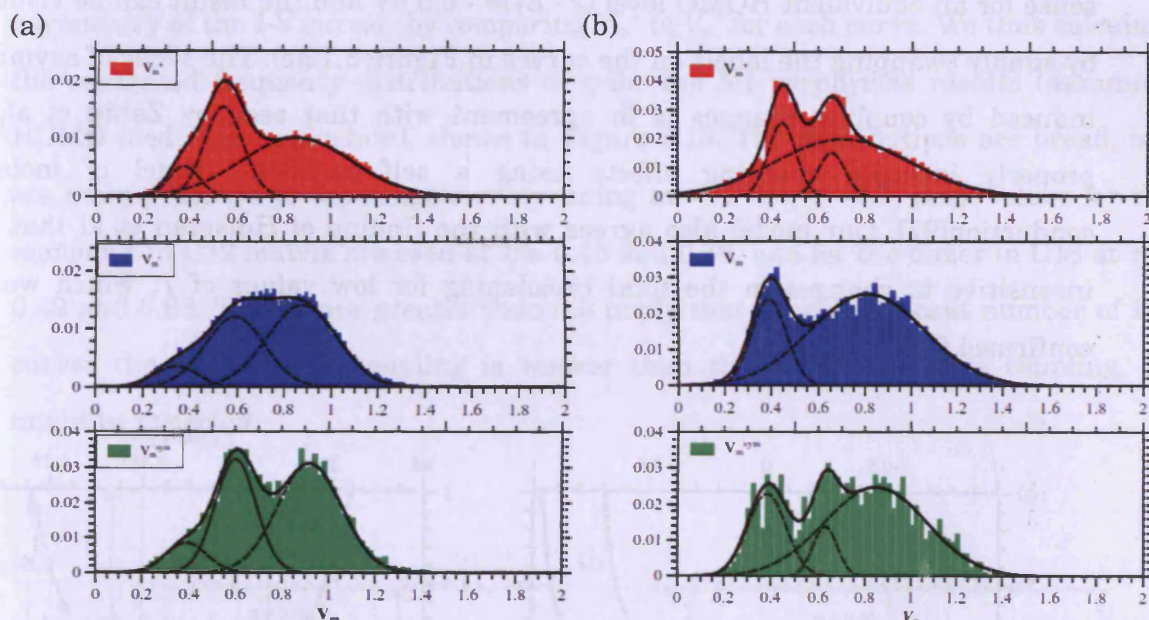


Figure 5.11. Frequency distribution of V_m measured for (a) the MI porphyrin monomer and (b) the MI porphyrin dimer. Upper panel is V_m^+ , middle panel is V_m^- , lower panel is V_m^{sym} .

5.5.3 Asymmetry in I-V (V_m)

The asymmetry in many of the I-V curves is thought to be produced by unequal coupling at the two electrodes. To examine this effect and aid our discussion we use the ML model[24] to simulate the I-V characteristics. We examine the I-V

characteristics for a LUMO level at $\varepsilon - E_F = 0.5$ eV. We fix the broadening contribution from the sample electrode Γ_1 to 5 meV, while the tip-molecule coupling strength is varied by altering the broadening term at the tip, Γ_2 . Example I-V curves in Figure 5.12(a) show that varying the coupling at one electrode does indeed give asymmetric characteristics, reducing the current at positive bias for weaker coupling at the tip if the conduction is LUMO mediated. The effect of the asymmetry on V_m (Figure 5.12(b)) is to increase V_m^+ and decrease V_m^- , with increasing η (a symmetric response is seen for the case of equal coupling at the two electrodes). The symmetry is in the opposite sense for an equivalent HOMO level ($\varepsilon - E_F = -0.5$ eV and the result can be visualised by simply swapping the labels on the curves in Figure 5.12(c). The sense of asymmetry induced by coupling changes is in agreement with that seen by Zahid et al, who properly included charging effects using a self-consistent model of molecular conduction[97]. Our model also agrees with the finding of Huisman et al that V_m is insensitive to changes in the total broadening for low values of Γ , which we have confirmed for $\Gamma < 0.1$ eV.

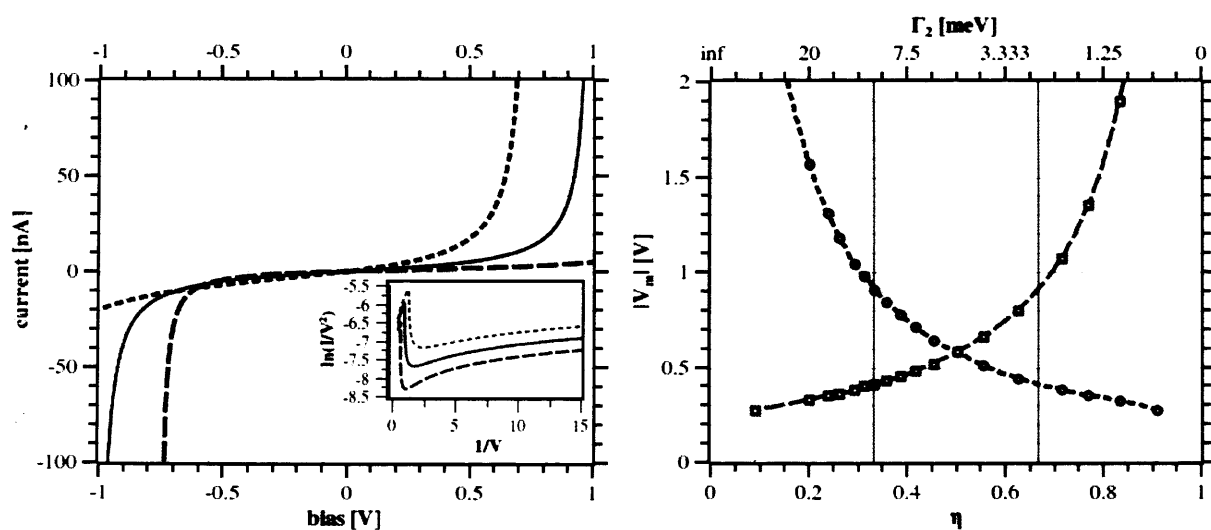


Figure 5.12. (a) Modelled I-V characteristics for a LUMO at energy $\varepsilon - E_F = 0.5$ eV ($E_F = 5.5$ eV) and fixed substrate-molecule coupling parameter $\Gamma_1 = 5$ meV, for three tip-molecule coupling values Γ_2 of 5 meV (solid black line, $\eta = 0.5$), 2 meV (dashed black line, $\eta = 0.667$) and 10 meV (dotted black line, $\eta = 0.333$). Inset: Corresponding positive-bias V_m plots. (b) $|V_m|$ versus $\eta = \Gamma_1 / (\Gamma_1 + \Gamma_2)$ the grey squares is V_m^+ , the black circles is V_m^- (the result for an equivalent HOMO level is given by swapping these labels).

It is interesting to note that for a given molecule, whether tunnelling is mediated by a HOMO or LUMO level, variation in the relative coupling strengths can produce bias asymmetry in V_m in either sense (i.e. $V_m^- < V_m^+$ and vice versa), simply depending on whether the biased electrode is more or less well-coupled to the molecule than the grounded electrode. Thus a study of V_m versus controllably varied coupling strength could identify HOMO mediated transport from the asymmetry.

The results of the calculations also show that $\log_{10}(V_m^+ / V_m^-)$, for any given curve, scales directly with the asymmetry parameter η , thus we can characterise the asymmetry of the I-V curves by comparing V_m^+ to V_m^- for each curve. We thus calculate the estimated frequency distributions of η for the MI porphyrins results (assuming HOMO mediated conduction), shown in Figure 5.13. The distributions are broad, but are mainly limited to the range corresponding to $\sim 0.3 < \eta < \sim 0.7$; peak values for the monomer in C12 matrix are seen at $\eta = 0.48$ and 0.59 , and for the dimer in C16 at $\eta = 0.49$ and 0.68 . The values greater than 0.5 imply that for a significant number of I-V curves the tip-molecule coupling is weaker than the surface-molecule coupling, as might be expected.

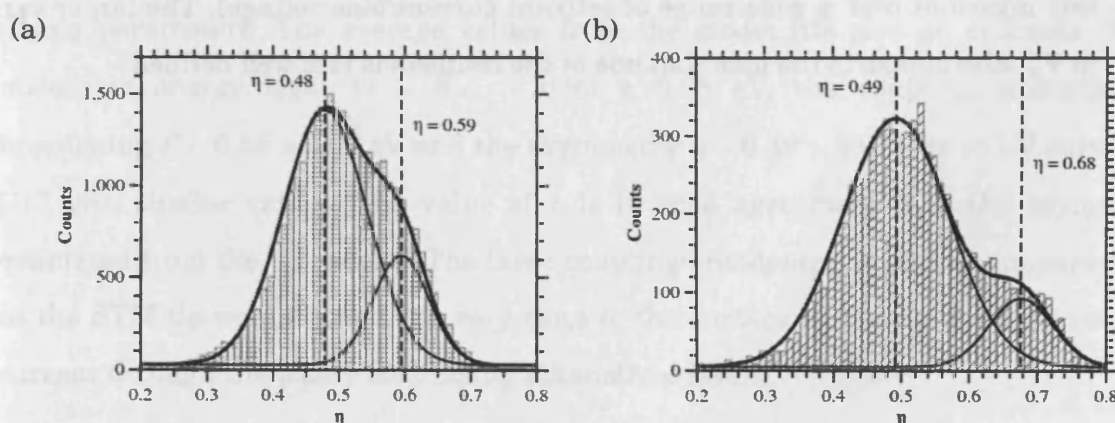


Figure 5.13. Frequency distribution of the asymmetry parameter estimated from $\log_{10}(V_m^+ / V_m^-)$ for (a) the MI porphyrin monomer and (b) the MI porphyrin dimer. Also shown is a Gaussian fit to the data.

5.6 Result on Alkanethiol matrix

Figure 5.14 shows the average I-V characteristic and F-N plot for a set of measurements (112 curves) over the C16 matrix. Also shown is the frequency distribution of V_m^+ and V_m^- for all the measured curves. Unlike the porphyrin, the C16 molecule has a single thiol end group, which is chemisorbed to the Au sample surface, and the exposed methyl end is only physisorbed at the probing STM tip[98]. The chemisorbed -thiol end is thus expected to be more strongly coupled to the electrodes than the physisorbed -methyl end. Non-equal coupling will lead to asymmetric V_m statistics. Indeed, the distributions of V_m for all the I-V curves measured over the alkanethiol matrix (Figure 5.21) show a single peak asymmetric in bias, with $V_m^+ = 1.380 \pm 0.015$ V ($\sigma = 0.31$ V) and $V_m^- = 1.220 \pm 0.007$ V ($\sigma = 0.15$ V). This compares with a value of 1.15 ± 0.11 V (for positive bias) reported by Beebe et al[17] but our observation that $V_m^+ > V_m^-$ is in contrast to results[14] on other molecules. We estimate that $\eta \sim 0.47$ (assuming HOMO mediated tunnelling), which indicates that the STM tip contact is in fact slightly better coupled. Wang et al[83] find that for alkanethiol SAMs V_m depends on the loading force of the probing tip on the molecular layer, so a direct comparison may not be valid (although results for the C12 matrix show that V_m was invariant over a wide range of setpoint current/bias voltage). The larger variance in V_m^+ also supports the idea that one of the contacts is less well defined.

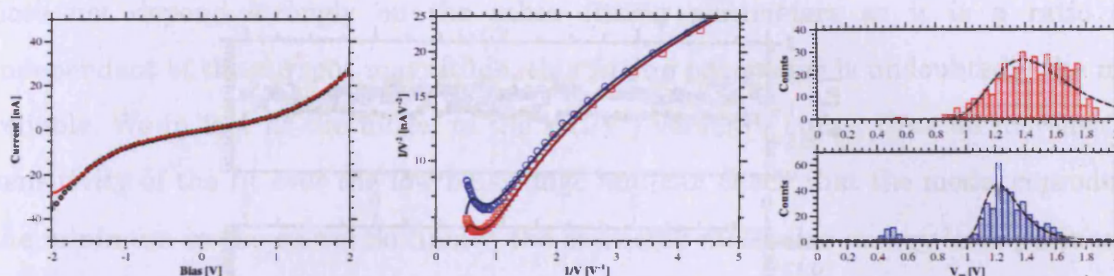


Figure 5.14. (left) average I-V curve from one set of measurements over the C16 matrix (open circles, from 112 individual curves). (Centre) the FN-plot shows the voltage minimum for positive (red squares) and negative (blue circles) bias. In both plots a reasonable fit to the ML model (solid line) is also shown. (Right) histogram of V_m for all 410 curves measured. Positive bias Gumbel fit, peak = 1.38 ± 0.016 V, ($\sigma = 0.314$), Negative bias Gumbel fit, peak = 1.22 ± 0.007 V, ($\sigma = 0.146$)

5.7 Fitting to the molecular model

Also shown in Figure 5.14 is a reasonable fit of the numerical result from the ML model to the average I-V curve (we assumed HOMO transport and optimise the fit by least-squares method, see Appendix A). Figure 5.15 shows the time series for the batch of 112 I-V curves with the results of fits to the ML model for each curve given alongside $V_m^{+/-}$. There is a small amount of variation in V_m and this is reflected in the fitting parameters. The average values from the model fits give an estimate of the molecular energy level $|\varepsilon - E_F| \sim 0.90 \pm 0.05$ eV, the coupling strength/level broadening $\Gamma \sim 0.55 \pm 0.03$ eV and the asymmetry $\eta \sim 0.48 \pm 0.01$; fits to I-V curves for C12 give similar values. The value of η is in good agreement with the asymmetry estimated from the V_m results. The large coupling/broadening is perhaps unsurprising as the STM tip would have to be very close to the surface to achieve the high setpoint current through the poorly conducting alkanethiol layer.

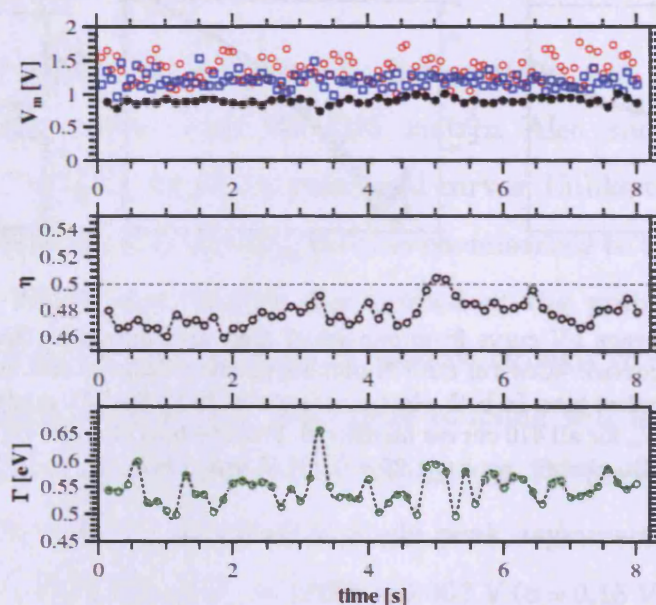


Figure 5.15. Time series of parameters from 112 I-V curves over C16 matrix; red circles V_m^+ , blue squares V_m^- . Also shown are estimated parameters from fits to the ML model (pairs of I-Vs are averaged to give 56 fitted curves); black filled circles is $|\epsilon_{HOMO} - E_F|$, open circles is the asymmetry parameter η , green circles is the total coupling Γ .

However, the results of fits to this model must be treated with caution. The calculations assume a single, broadened energy level that is shifted in energy proportionally with the applied bias (scaled by η). In reality the associated transmission spectrum will contain other molecular levels, affecting the higher voltage range of the I-V curve and the energetic shifting and relative intensity of the transmission peaks may change in a more subtle way with the applied bias than is currently assumed. In addition the necessary scaling of the calculated current to match the known low-bias conductance (governed by the setpoint/bias) is itself dependent on Γ , as the broadening affects the magnitude of $T(E)$ near E_F (see Appendix A). The value of Γ is thus only likely to be a rough order-of-magnitude estimate and may be systematically overestimated, as an over-broadened level could in part compensate for the missing transmission peaks at higher energies. Conversely η

does not depend strongly on the other fitting parameters as it is a ratio and independent of the current magnitude; this fitting parameter is undoubtedly the most reliable. We in fact fit the model to the $\ln(I/V^2)$ versus V curve, thus we increase the sensitivity of the fit over the low bias range and can check that the model reproduces the minimum in the curve. So finally, the extracted molecular energy level position $|\varepsilon - E_F|$ is expected to be a reasonable approximation of the true energetic alignment of the nearest molecular orbital (although it may be underestimated if Γ is anomalously large).

With these considerations in mind we attempt to fit to a few example data-sets from the MI porphyrin dimer. Figure 5.16 shows fits to the ML model for the time-series previously presented in Figure 5.10(a). In the first section **1** the I-Vs are approximately symmetric, and $V_m^+ \approx V_m^- \approx |\varepsilon - E_F|$. In **2** the fits indicate a more asymmetric I-V curve with an increase in $|\varepsilon - E_F|$ mirroring the increased V_m . The coupling strength also appears to increase, which is unsurprising: an increase in $|\varepsilon - E_F|$ will decrease $T(E=E_F)$ and reduce the current, hence this must be compensated for by an increase of Γ to maintain the current setpoint. Figure 5.17 (a), (b) and (c) show fits to three sub-sets of data for the MI dimer with consistent, asymmetric I-V characteristics. The single level model is able to provide an approximate fit to I-V curves exhibiting different degrees of asymmetry and with different energetic alignment. The asymmetry from the fit results is again in good agreement with the estimate from $V_m^{+/-}$ and supports the idea that in (a) and (c) the tip-molecule coupling is weaker than the coupling to the surface electrode, i.e. the tip is not making a particularly good contact to the molecule. The different $|\varepsilon - E_F|$ in (a) and (b) again support the idea that the multiple values of V_m are not simply an artefact of asymmetry induced by a fluctuating weak contact; the energetic alignment/ dominant transmission peak is truly different, independent of the coupling. Finally it can be seen in (c) that the model is not adequate to capture all of the I-V behaviour and in this case a good fit over the entire energy range was not possible.

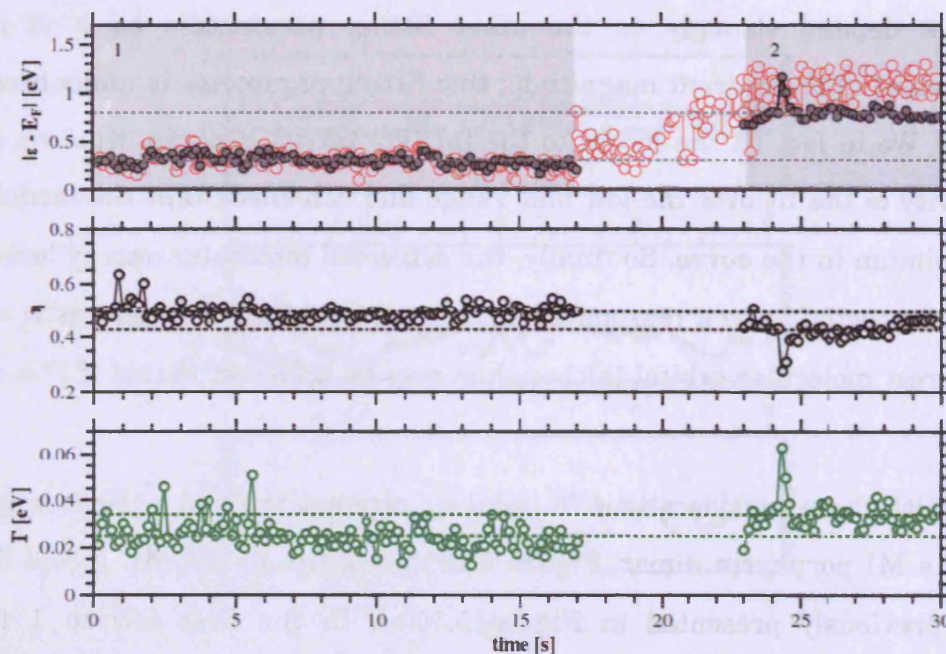
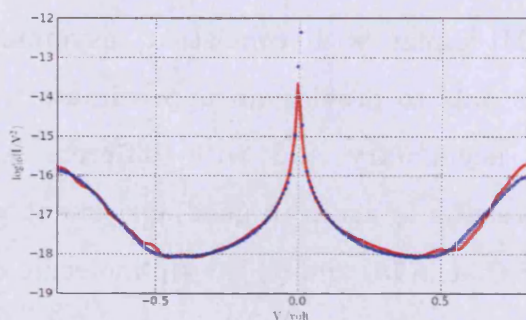
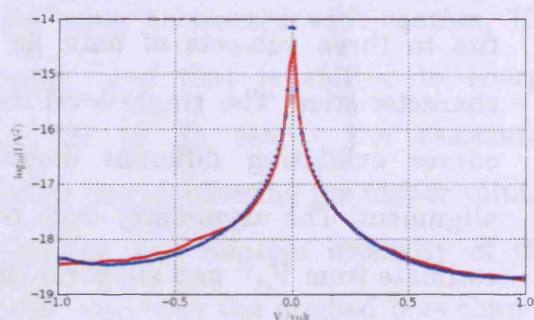


Figure 5.16. ML model fit results for the time-series previously presented in Figure 5.10(a). Red open circles in the top panel show V_m^+ in [V]. Below example fits (blue dots) of individual I-V curves (red line) from the two regions 1 and 2.



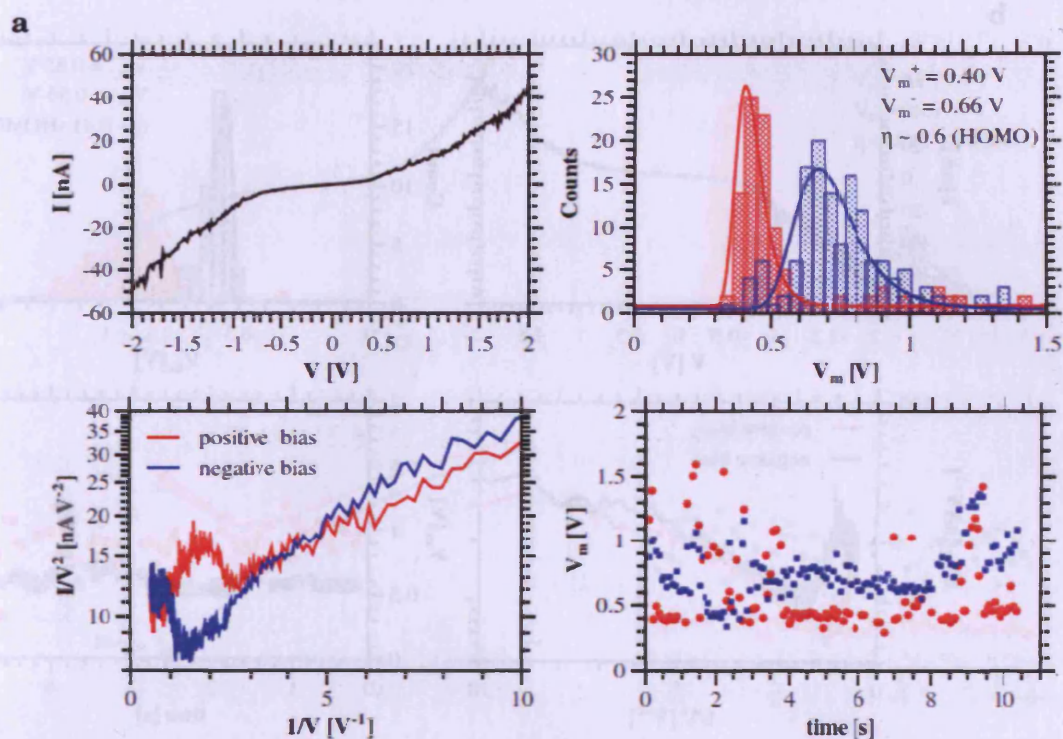
ML model fit (1)

- Average fit parameters:
- $|\varepsilon - E_F| = 0.31 \pm 0.05$ eV
- $\Gamma = 0.025 \pm 0.006$ eV
- $\eta = 0.49 \pm 0.03$



ML model fit (2)

- Average fit parameters:
- $|\varepsilon - E_F| = 0.80 \pm 0.08$ eV
- $\Gamma = 0.034 \pm 0.006$ eV
- $\eta = 0.43 \pm 0.04$



ML model fit

- Average fit parameters:
- $|\mathcal{E} - E_F| = 0.37 \pm 0.14$ eV
- $\Gamma = 0.24 \pm 0.13$ eV
- $\eta = 0.57 \pm 0.06$

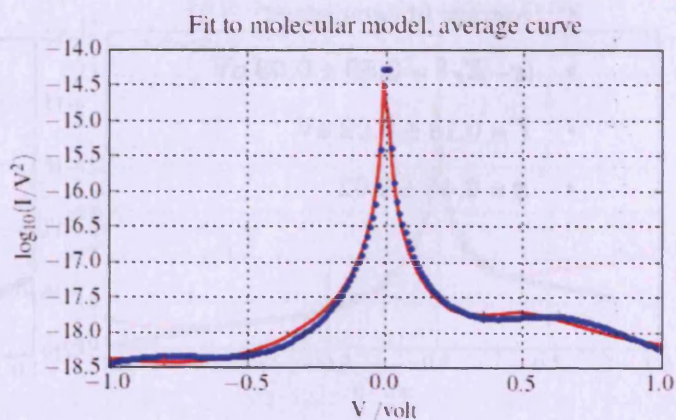
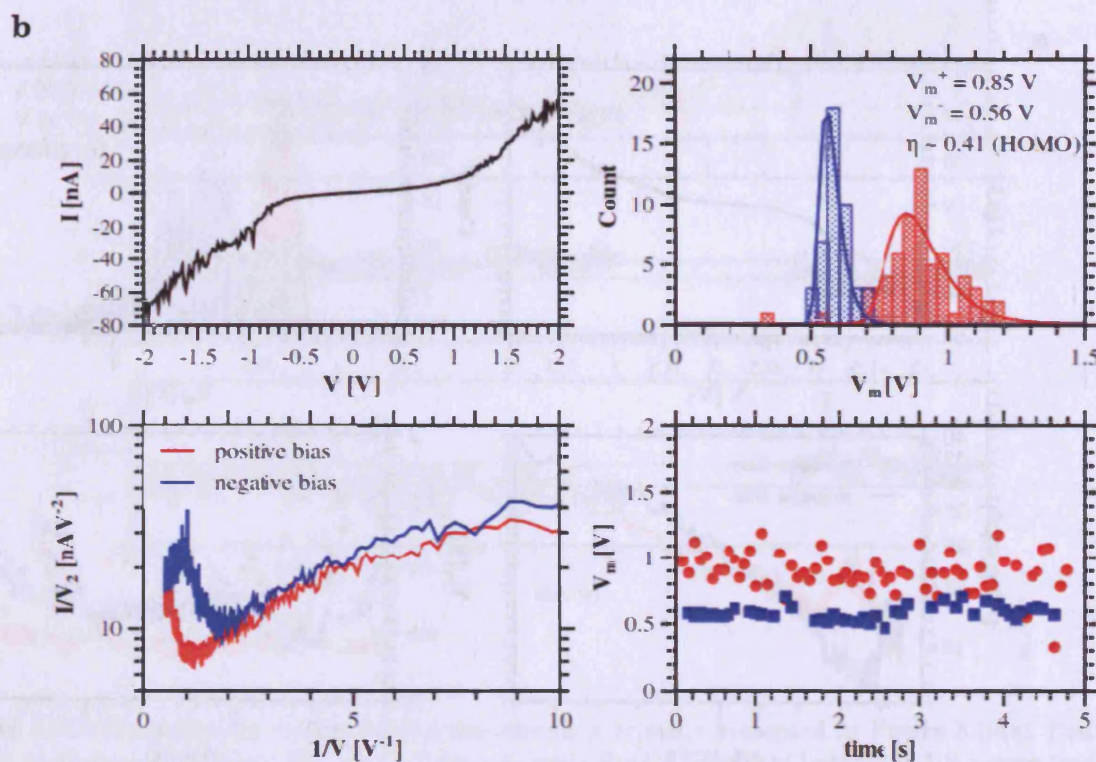
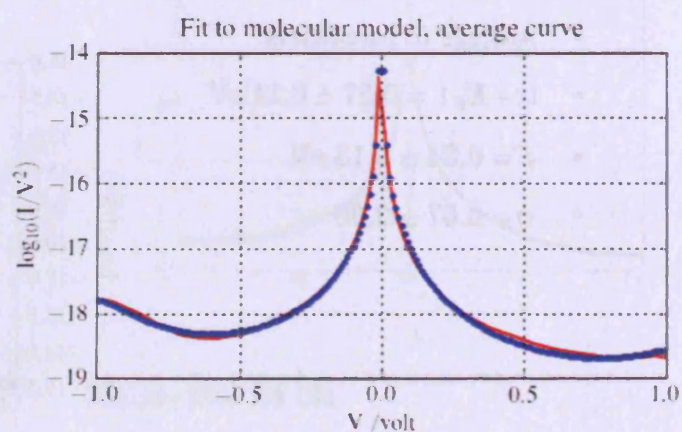


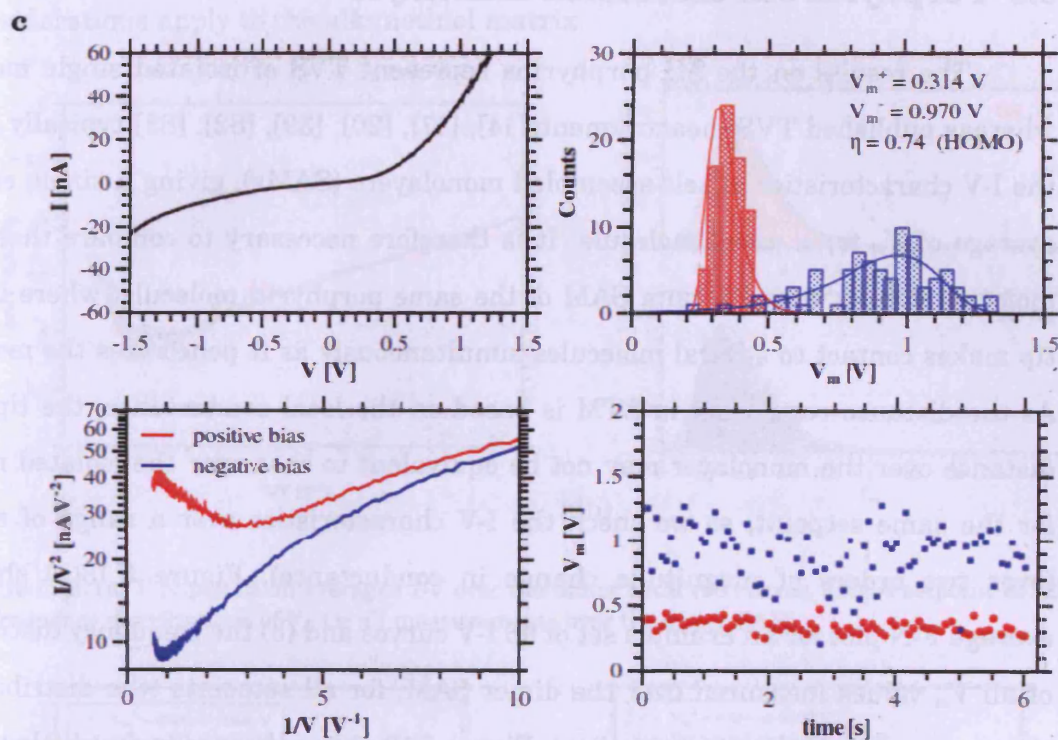
Figure 5.17. Examples of measurement sequences resulting in asymmetric I-V characteristics (continued on following pages). In each figure a), b) and c) a representative I-V curve is shown (top left) with the corresponding F-N plot (bottom left), the statistical distribution of V_m^+ and V_m^- (top right) and the associated time series (bottom right). For each sequence the ML fit (blue dots) to the average IV (FN) curve (red line) is shown and the average fitting parameters are the reported for the fits to the individual curves.



ML model fit

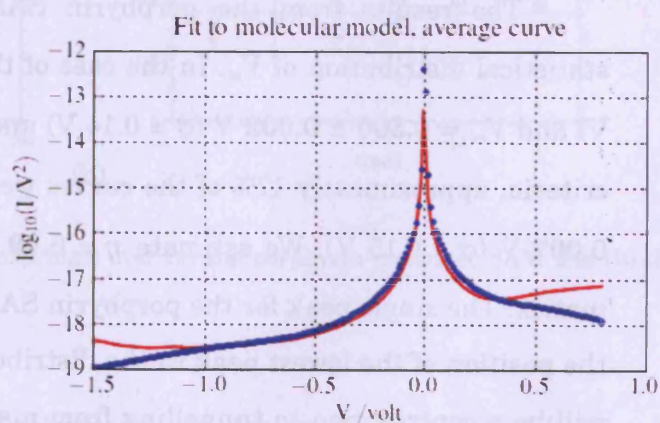
- Average fit parameters:
- $|\mathcal{E} - E_F| = 0.59 \pm 0.03$ eV
- $\Gamma = 0.18 \pm 0.02$ eV
- $\eta = 0.45 \pm 0.02$





ML model fit

- Average fit parameters:
- $|\varepsilon - E_F| = 0.36 \pm 0.02$ eV
- $\Gamma = 0.25 \pm 0.05$ eV
- $\eta = 0.62 \pm 0.10$



5.8 Porphyrin self assembled monolayer

The results on the MI porphyrins represent TVS of isolated single molecules, whereas published TVS measurements[14], [17], [20], [39], [82], [83] typically focus on the I-V characteristics of self-assembled monolayers (SAMs), giving a single ensemble average of V_m for a given molecule. It is therefore necessary to compare these single molecule results with I-V on a SAM of the same porphyrin molecule, where the STM tip makes contact to several molecules simultaneously as it penetrates the monolayer. As the distance regulation in STM is based on the local conductance, the tip-sample distance over the monolayer may not be equivalent to that over the isolated molecule for the same setpoint, so we check the I-V characteristics over a range of setpoints (over two orders of magnitude change in conductance). Figure 5.18(a) shows the average F-N plot for an example set of 96 I-V curves and (b) the frequency distributions of all V_m values measured over the dimer SAM, for all setpoints (the distribution for the monomer is qualitatively similar). Figure 5.19 shows there is in-fact little variation in the V_m values as a function of conductance.

The results from the porphyrin SAM sample reveal a single peak in the statistical distribution of V_m . In the case of the dimer $V_m^+ = 0.340 \pm 0.002$ V ($\sigma = 0.14$ V) and $V_m^- = 0.300 \pm 0.002$ V ($\sigma = 0.14$ V) and, using the previously defined symmetry criteria, approximately 17% of the curves were symmetric in V_m , with $V_m^{sym} = 0.340 \pm 0.007$ V ($\sigma = 0.15$ V). We estimate $\eta = 0.49$, similar to the result for the alkanethiol matrix. The single peak for the porphyrin SAM is thus in approximate agreement with the position of the lowest peak in the distribution for the MI porphyrin. Because there will be a contribution to tunnelling from many molecules in parallel in this case, the probability is high that at least one molecule will be well contacted to both the tip and sample and hence will have the smallest possible $E_F - \epsilon_{HOMO}$. Transport will be dominated by such molecules (as they have higher conductance) leading to the peak for

the SAM to be close to the lowest peak seen in the single-molecule case. Similar considerations apply to the alkanethiol matrix.

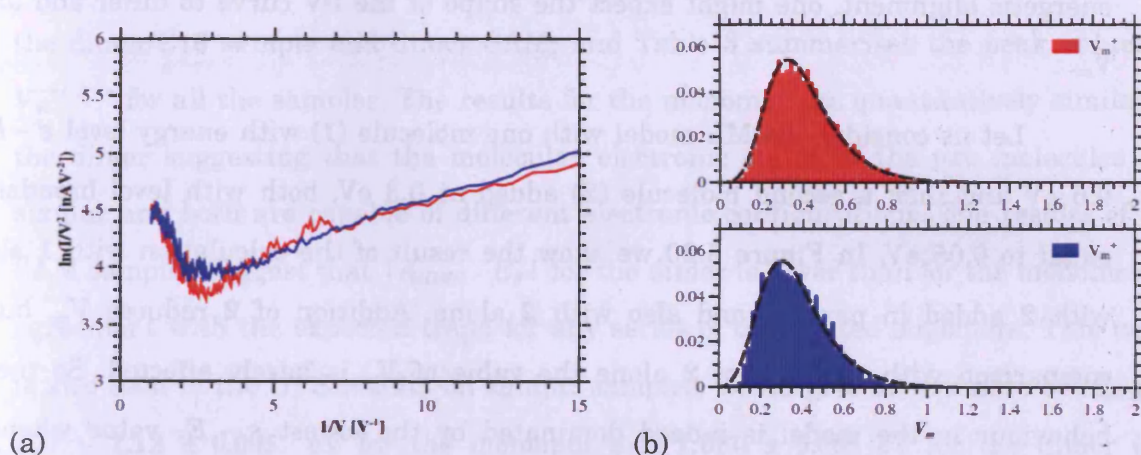


Figure 5.18. (a) F-N plot of an averaged I-V over the dimer SAM (96 curves, 100pA setpoint at -20mV). (b) frequency distributions of V_m for all measurements over the dimer SAM.

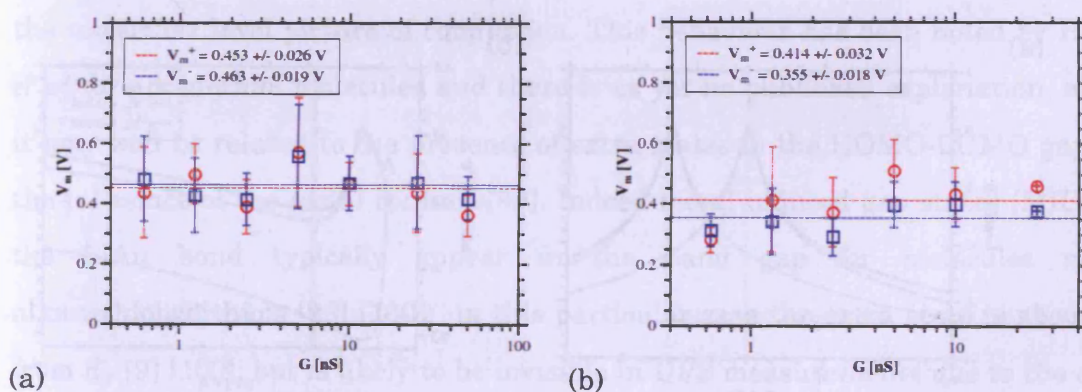


Figure 5.19. V_m versus conductance (=setpoint/bias) over (a) the porphyrin monomer SAM and (b) the dimer SAM.

This argument also helps us understand why the multiple values of V_m^{sym} seen for the MI porphyrins cannot be interpreted simply as the formation of multiple molecular contacts. Existing single molecule conductance studies where one, two and three molecules are routinely trapped between STM electrodes show that they conduct in parallel. Increasing the number of molecules in the junction simply increases the

magnitude of the current, leaving the *shape* of the I-V curve (and hence the value of V_m) unaffected. But if two *non-identical* molecules are in the gap, each with *different* energetic alignment, one might expect the shape of the I-V curve to differ and affect V_m .

Let us consider the ML model with one molecule (**1**) with energy level $\varepsilon - E_F = 0.6$ eV and then a second molecule (**2**) added at 0.3 eV, both with level broadening equal to 0.05 eV. In Figure 5.20 we show the result of the calculation with **1** alone, with **2** added in parallel and also with **2** alone. Addition of **2** reduces V_m , but in comparison with the case of **2** alone the value of V_m is barely affected. So the V_m behaviour in the model is indeed dominated by the lowest $\varepsilon - E_F$ value whenever several molecules are in parallel.

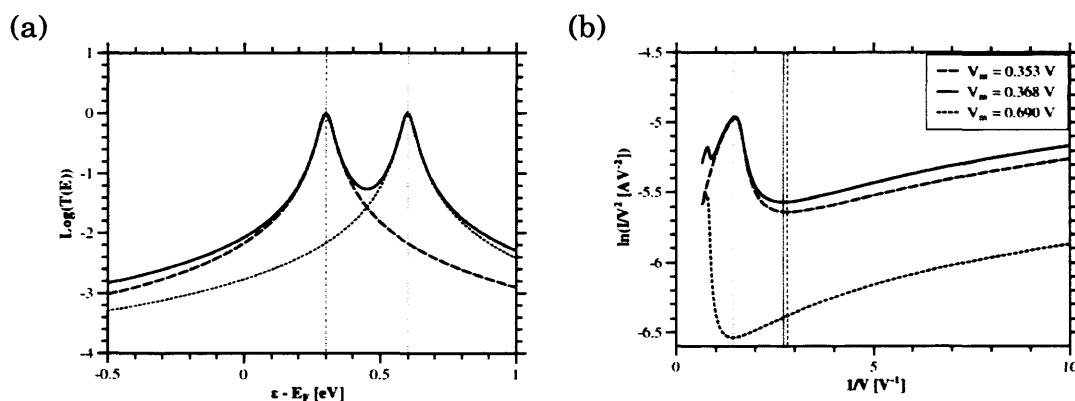


Figure 5.20. (a) $T(E)$ for one molecule at $|\varepsilon - E_F| = 0.3$ eV (dashed line) or $|\varepsilon - E_F| = 0.6$ eV (dotted line) and $T(E)$ for both in parallel (solid line). (b) Fowler-Nordheim plot showing the V_m for the three cases in (a).

5.9 Discussion

Figure 5.21 compares the frequency distributions for all the measurements on the dimer/C16 sample and dimer SAM, and Table 3 summarises the peak values of $V_m^{+/-/sym}$ for all the samples. The results for the monomer are quantitatively similar to the dimer suggesting that the molecular electronic states of the two molecules are similar and both are capable of different electronic configurations. The results of the SAM samples suggest that $|\epsilon_{HOMO} - E_F|$ for the dimer is lower than for the monomer, in agreement with the expected trend for any series of conjugated oligomers. This trend is also seen in the UPS results on similar samples, which give an estimate of $|\epsilon_{HOMO} - E_F| \sim 1.12 \pm 0.005$ eV for the monomer and 1.080 ± 0.005 eV for the dimer (see Appendix C).

The UPS results are obviously much larger than V_m and not in agreement with the molecular level picture of conduction. This behaviour has been noted by Huisman *et al* for alkanethiol molecules and there is as yet no published explanation, although it may well be related to the presence of extra states in the HOMO-LUMO gap due to the influence of the metal contacts[99]. Indeed metal induced gap states (MIGS) from the S-Au bond typically appear in the band gap for molecules such as alkanethiols/dithiols [23] [100]; in this particular case the extra state is about ~ 1 eV from E_F [9] [100], but is likely to be invisible in UPS measurements due to the absence of a top electrical contact [101]. These MIGS would greatly influence the I-V characteristics (as seen in our calculations in Figure 5.20) and we confirm this in the alkanedithiol case by integrating the $T(E)$ curve calculated by Li *et al*[9] for alkanedithiols to find $V_m \sim 1.2$ eV, corresponding to the energy of the sulphur state (see Appendix A). Thus the molecular level measured in UPS measurements is not the same level being probed in TVS. However, it can at least be noted that the discrepancy is in general agreement with that reported for other conjugated molecules[14], where V_m is seen to scale directly with $|\epsilon_{HOMO} - E_F|$ (see Figure 5.22).

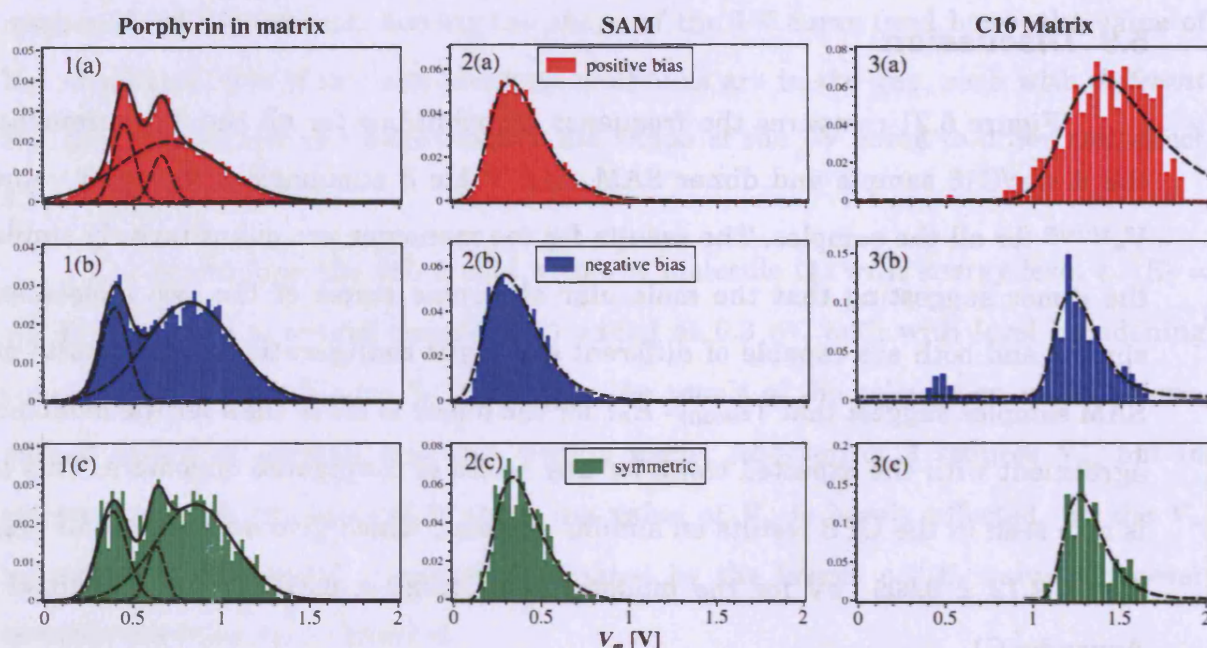


Figure 5.21. Normalised frequency distributions of V_m extracted from individual I-V curves taken over (1) the matrix inserted porphyrin dimer, (2) the self-assembled monolayer of the porphyrin molecule and (3) the C16 matrix itself. V_m is presented for positive (a) and negative (b) bias only, plus those I-V curves that are symmetric in V_m (c). A sum of multiple Gaussian functions (dashed lines) yield a good fit (solid) to 1(a – c). Skewed single Gumbel distribution functions (dashed) were fitted to 2(a – c) and 3(a – c).

	(1) porphyrin in matrix		(2) porphyrin SAM		(3) alkanethiol matrix	
	Monomer in C12	Dimer in C16	Monomer	Dimer	C12	C16
(a)	0.38 ± 0.010 (0.07)	0.45 ± 0.001 (0.12)	0.38 ± 0.001 (0.08)	0.34 ± 0.002 (0.14)	1.19 ± 0.005 (0.20)	1.38 ± 0.015 (0.31)
V_m^+	0.55 ± 0.004 (0.08)	0.66 ± 0.001 (0.11)				
	0.86 ± 0.008 (0.24)	0.71 ± 0.007 (0.58)				
(b)	0.34 ± 0.022 (0.09)	0.39 ± 0.002 (0.15)	0.37 ± 0.002 (0.09)	0.30 ± 0.002 (0.14)	0.99 ± 0.004 (0.16)	1.22 ± 0.007 (0.15)
V_m^-	0.59 ± 0.010 (0.13)					
	0.88 ± 0.016 (0.15)	0.82 ± 0.006 (0.49)	$(\eta = 0.49)$	$(\eta = 0.47)$	$(\eta = 0.46)$	$(\eta = 0.47)$
(c)	0.39 ± 0.028 (0.09)	0.38 ± 0.005 (0.16)	0.39 ± 0.001 (0.14)	0.34 ± 0.007 (0.15)	1.13 ± 0.008 (0.16)	1.27 ± 0.014 (0.14)
V_m^{sym}	0.60 ± 0.006 (0.09)	0.63 ± 0.003 (0.10)				
	0.92 ± 0.005 (0.14)	0.85 ± 0.01 (0.44)				

Figure in brackets is the standard deviation of the distribution, extracted from the fitting parameters of the Gaussian or Gumbel distribution as appropriate.

Table 3: Summary of the V_m values for each sample.

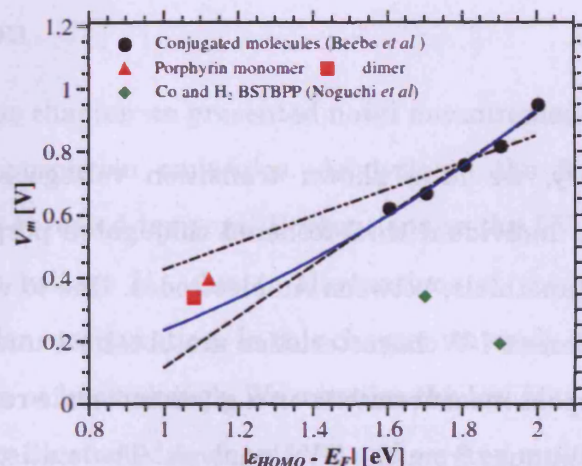


Figure 5.22. V_m versus $|\epsilon_{HOMO} - E_F|$. Data from Beebe et al[14] for several conjugated molecules is shown (black circles) as well as our result for the porphyrin dimer SAM (red square) and monomer SAM (red triangle). Fits to Beebe's data are also shown; (dashed line) Linear fit, (dot-dash line) linear fit through the origin and (solid line) quadratic fit through the origin. (Green diamonds) Noguchi et al[86] on Co and H₂ tetraphenyl porphyrin derivatives.

As a final note of discussion it is known that the acetylene bonds in the porphyrin oligomer can rotate affecting the degree of conjugation, but this is unlikely to account for the observed fluctuations in V_m . According to Kocherzhenko *et al* [102] the energy barrier to rotation at ~ 35 meV is comparable to $k_B T$ at room temperature, and the rotation time is on the order of a nanosecond. We expect a Boltzmann distribution of rotational conformations and, on the time scale accessible in this experiment, we are thus measuring thermally averaged transport properties. Although the rotation could be quenched by preparation of a ligand-porphyrin complex, e.g. with DABCO, the associated aggregation effect is unlikely to leave isolated molecules and would be indistinguishable from the monolayer formation. However, it would be interesting to synthesise variants of the porphyrin molecule, in which the twist angle is controlled by substituent groups that sterically hinder the rotation; this has already been shown to affect the conductance of amine-linked biphenyl derivatives[92] and

could have an affect on V_m . Also, given the nonlinear optical properties of some porphyrin molecules, it would be interesting to see what effect in-situ irradiation might have on V_m .

In summary, we have shown transition voltage spectroscopy results from measurements on individual thiol-tethered conjugated porphyrin molecules, isolated in a matrix of alkanethiols, between Au electrodes. Due to variations in the molecular configuration different I-V characteristics are obtained under identical experimental conditions and repeat measurements on a given molecule reveal temporal fluctuations in the voltage minimum from the TVS analysis. The statistical distribution of the V_m values reveals multiple peaks corresponding to the different transport characteristics of the various molecular configurations. In contrast, parallel conduction through multiple molecules in a self assembled monolayer results in a single, low V_m value in qualitative agreement with other studies on molecular SAMs. The voltage minimum is thus seen to be sensitive to the details of the nanoscale contact and is not defined by a single value for the porphyrin molecules studied. Finally, by performing simple numerical calculations based on a realistic model of molecular conduction, we have been able to show that bias asymmetry and variation in the value of V_m can be accounted for by changes in the relative degree of coupling of the two ends of the molecule to the nanoscale contacts. We have performed rudimentary fits of the model to the experimental data and extracted estimates of real physical properties of the molecular systems.

6 Porphyrin single molecules

6.1 Introduction

In the previous chapter we presented novel measurements of I-V characteristics on matrix-isolated porphyrin molecules. Analysis in the framework of transition voltage spectroscopy revealed temporal fluctuations in the I-V characteristics and the extracted transition voltage V_m , due to fluctuations of the metal-molecule contact geometry or molecular configuration. In this chapter we study the porphyrin molecules in ultra high vacuum at low coverage. We measure the low bias conductance by the $I(z)$ technique, previously illustrated in chapter 4, and we find multiple conductance peaks corresponding to different molecular geometries/configurations. I-V measurements on the same samples reveal stochastic formation and fluctuations of the metal-molecule-metal junction. Changes in V_m and the low bias conductance are compared and the observations are found to be consistent with the molecular energy level model.

The porphyrin molecules synthesised by Harry Anderson's group in Oxford were a completely unknown system at the start of this study, but results have since been published by the Liverpool group and ourselves on this molecular series. Sedghi et al [16] used the $I(z)$ spectroscopy technique to measure the single molecule conductance of the first three members of the oligomer series (as well as an $n = 0$ compound without the porphyrin macrocycle repeat unit) and reported a remarkably low rate of decrease in conductance versus molecular length (their data for the monomer and dimer molecules is summarised in Table 4). The trend of conductance versus molecular length in many molecular systems [8][22][33][50][92][103] has been shown to follow an exponential decay, i.e. $G \propto \exp(-\beta l)$, typical of what would be expected in a non-resonant model of molecular conduction. However in certain conjugated systems [16][20][104][105] the characteristic β parameter is significantly lower than would be

expected in a tunnelling model and within the experimental error the conductance versus length trend can equally be described by a linear fit, suggestive of a hopping mechanism of charge transport.

Number of porphyrin rings	Conductance by $I(z)$ [nS]	Estimated $E_F - E_{HOMO}$ [eV]
$n = 1$	2.1 ± 0.3 (= $2.71 \times 10^{-5} G_0$)	0.96
$n = 2$	1.2 ± 0.3 (= $1.55 \times 10^{-5} G_0$)	0.90

Table 4. Summary of results from Sedghi et al[16]

In parallel to the efforts of the Liverpool group we have studied the porphyrin molecules using STM techniques based in UHV, as previously employed to study the conductance of nonanedithiol (chapter 4). We characterise the single molecule conductance of the low coverage porphyrin monolayers using the $I(z)$ technique in vacuum. In addition we perform I-V measurements on the same samples without re-establishing feedback in between measurements. This enables us to maintain the metal-molecule-metal junction over a series of repeat measurements and preserve information about conductance changes due to molecular attachment/detachment events. We can then analyse the I-V in the transition voltage spectroscopy framework and compared this to the previously reported results on the matrix-isolated porphyrins and porphyrin monolayers in ambient conditions (chapter 5). All experiments were performed in UHV at a base pressure of $\sim 3 \times 10^{-10}$ mbar.

6.2 Conductance by $I(z)$

We prepare the sample almost identically to the porphyrin high-coverage monolayer described in chapter 5, except we immerse the Au substrate in the solution for ~ 15 seconds only, thus achieving a low coverage phase of the molecules. We

gathered a finite series of measurements of the porphyrin monomer by BJ-STM and I(s) methods (as previously discussed in chapter 4 these were until recently regarded as competing techniques that gave different results, thus a comparison was prudent) and additional measurements also of the dimer by I(z).

The experimental procedures for implementing the BJ-STM and I(s) experiments are identical to the methods described in chapter 4 for measurements on nonanedithiol.

6.2.1 Break-junction STM results

Figure 6.1 shows some examples of the BJ-STM I(z) curves exhibiting plateaus, for a sample of the porphyrin monomer on Au (100mV bias). In the BJ-STM experiments we prepared the porphyrin sample with and without the piperidine ligands for comparison (see [16] and chapter 5). In both cases clear plateaus are seen in the I(z) curves over a wide range of conductance values, but the histogram of all data (Figure 6.2; 3600 curves without piperidine, 3700 with piperidine) shows no clear peaks. We perform the selection analysis previously employed on the nonanedithiol data, leaving ~2% of the curves from the data without piperidine and ~8% of the curves from the data with piperidine. The histogram in each case shows several, not very well defined, peaks. We comment on the I(z) curves themselves simply to note that by visual inspection, during the selection process, the plateaus were typically short and not as well defined as the plateaus from the I(s) experiment (results shown below).

The results with and without the piperidine ligand are qualitatively similar and the peaks in the distribution give molecular conductance values in the range ~ 0.7 nS up to ~2200 nS, with adjacent peaks being separated by a ratio of at least 3. We consider that given the spread of the measured conductance values and the short length plateaus there is insufficient data to detect a significant difference between the

experiment with and without the piperidine. However it does suggest that the addition of piperidine does not have a great influence on the molecular conduction, consistent with observations of the Liverpool group[16]. What is certainly significant is the observation of plateaus at a conductance as high as $\sim 3 \times 10^{-2} G_0$. This is about 3 orders of magnitude larger than those seen by Sedghi et al.

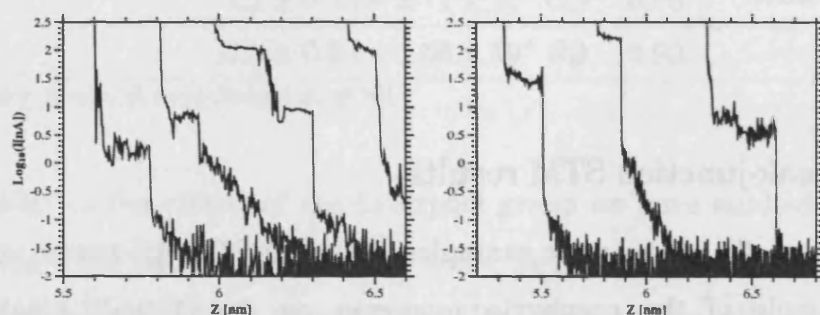


Figure 6.1. Monomer BJ-STM without ligand (left) and with ligand (right)

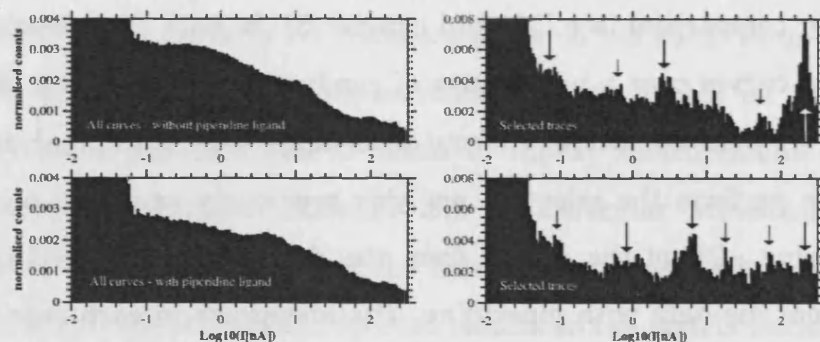


Figure 6.2. BJ-STM histogram results. Top without piperidine, bottom with piperidine

6.2.2 I(s) method results

We continue the I(s) style experiments on the porphyrin molecules using the piperidine ligand for consistency with the published results by Sedghi et al. Figure 6.3 shows some example I(z) curves for the porphyrin monomer with piperidine on Au

(100mV bias). Plateaus are again seen over a wide range of current values and are generally more clearly defined than the results of the BJ-STM experiments.

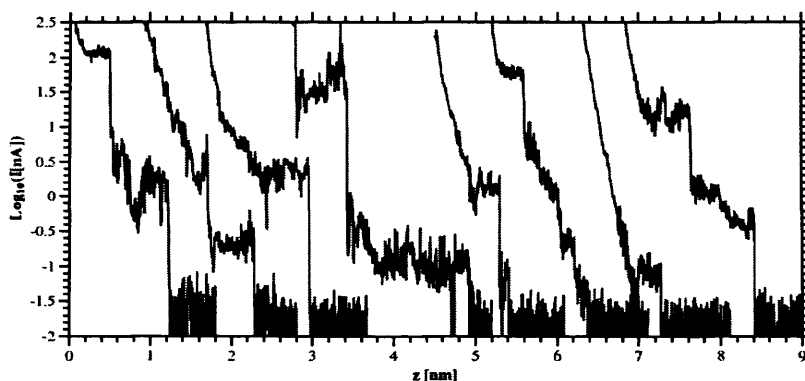


Figure 6.3. Monomer $I(z)$; example curves, displaced in z for clarity.

The results of the $I(z)$ experiments on the porphyrin monomer using the low current amplifier and high current amplifier are shown in figures 6.4 and 6.5 respectively. The low current results show several peaks suggestive of integer multiples of some given values (due to one, two, three, etc. molecules in parallel). Three conductance groups with two or three multiple peaks are identified (indicated by arrows in the figure) and this gives SMC values of:

- 0.0374 ± 0.0011 nS, $(4.83 \times 10^{-7} G_0)$
- 0.159 ± 0.003 nS, $(2.05 \times 10^{-6} G_0)$
- 1.29 ± 0.01 nS. $(1.66 \times 10^{-5} G_0)$

The conductance values are summarised graphically and compared to the results of Sedghi et al in Figure 6.10 below; interestingly in our measurements we see evidence for conductance values both higher and lower than those previously published. Experiments using the high current amplifier reveal five broad peaks in the histogram of selected curves. The peaks are centred on SMC conductance values of

- 2.07 ± 0.03 ($\sigma = 1.02$) nS, $(2.67 \times 10^{-5} G_0)$
- 20.0 ± 0.6 ($\sigma = 5.5$) nS, $(2.58 \times 10^{-4} G_0)$
- 94.6 ± 2.5 ($\sigma = 25.0$) nS, $(1.22 \times 10^{-3} G_0)$
- 347 ± 11 ($\sigma = 70$) nS and $(4.48 \times 10^{-3} G_0)$
- $1,280 \pm 30$ ($\sigma = 220$) nS. $(1.65 \times 10^{-2} G_0)$

Thus similar to the BJ-STM results we see a statistically significant number of $I(z)$ curves with a plateau $\sim 1.7 \times 10^{-2} G_0$. The ratios of the conductance of adjacent peaks in the distribution are (lowest to highest) 9.7, 4.7, 3.7 and 3.7, thus none of these peaks is an integer multiple of another lower peak. (We note that the lowest peak in this data set is equivalent to the highest peak seen in the low current data set above, although there is some discrepancy between the exact peak position; each peak here probably contains contributions from multiple molecules and thus the peak position is skewed, i.e. it is a weighted average of one, two, three, etc. molecules, hence the mismatch with the low current data). These peaks therefore represent five different conductance groups, cf. the three conductance groups reported for alkanedithiol molecules (see chapter 4). And although we can clearly distinguish the five individual peaks they are each fairly broad, as can be seen by the standard deviations σ , consistent with the idea that each represents a different conductance group and contains contributions from one, two, three, etc. molecules in each group.

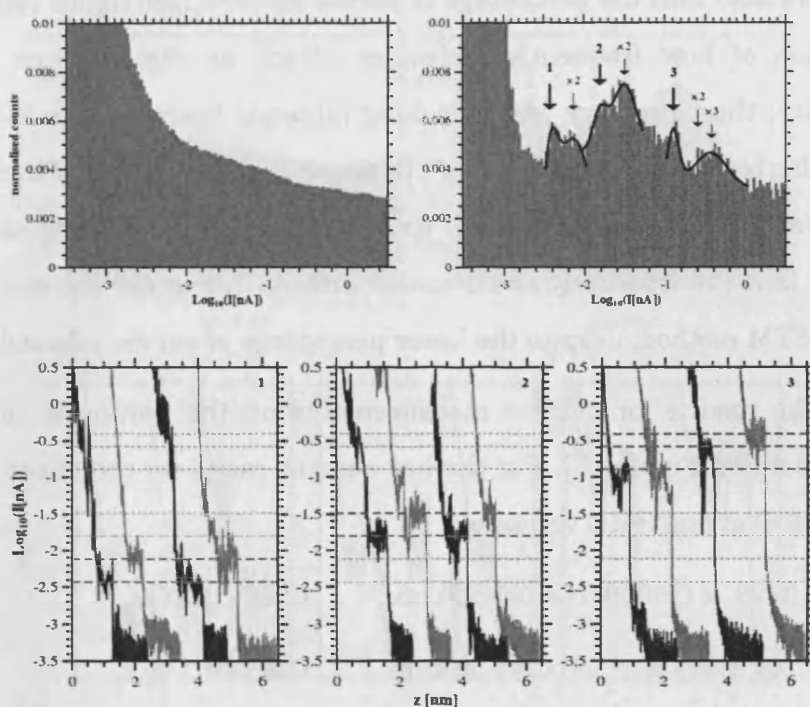


Figure 6.4. Porphyrin monomer $I(z)$ histograms (low amplifier). (left) all data, 7200 curves total; (right) selected curves, 363 selected ~ 5%. The grey lines show the results of separate Gaussian fits to each conductance group.

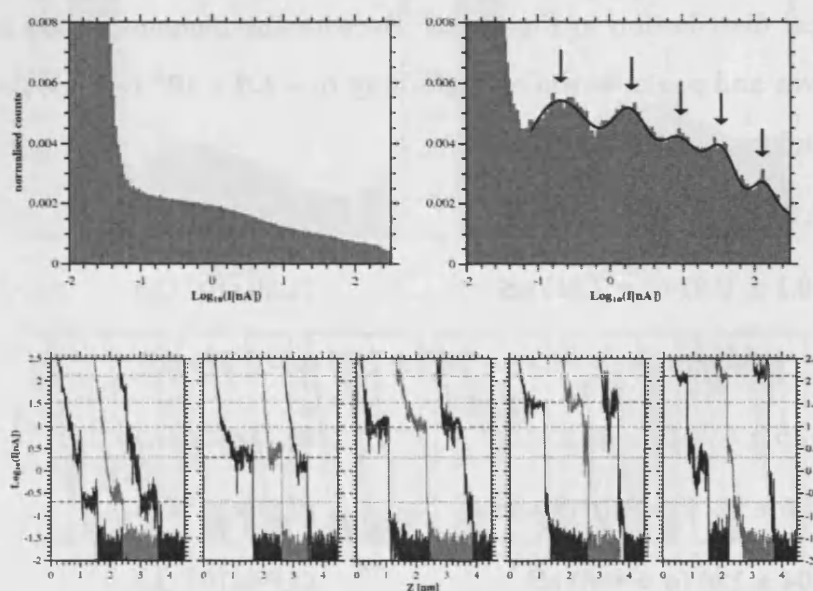


Figure 6.5. Porphyrin Monomer $I(z)$ histograms (high amplifier). (left) all data, 23800 curves total; (right) selected curves, 637 curves selected ~ 3%.

We note that the percentage of curves selected (see figure captions) is not a good indication of how frequently molecules attach as the selection procedure is very subjective; the more very “good” looking plateaus there are the more likely we are to reject shorter, less distinct looking plateaus, and a high rate of molecular attachment also gives a large number of noisy $I(z)$ curves which must be rejected. Thus we would remark that the frequency of molecular attachment in the $I(s)$ method is higher than the BJ-STM method, despite the lower percentage of curves selected.

The results for similar measurements on the porphyrin dimer are shown in Figure 6.6 and Figure 6.7. For the low current range we see peaks in the distribution (Figure 6.6) giving SMC values of:

- 0.0229 ± 0.0008 ($\sigma = 0.0122$) nS, ($2.95 \times 10^{-7} G_0$)
- 0.144 ± 0.005 ($\sigma = 0.088$) nS, ($1.86 \times 10^{-6} G_0$)
- 1.45 ± 0.04 ($\sigma = 1.44$) nS ($1.87 \times 10^{-5} G_0$)

The data set for the porphyrin dimer using the high current amplifier gives the statistical distribution in Figure 6.7. As with the monomer there are plateaus in the $I(z)$ curves and peaks in the histogram up to $\sim 1.0 \times 10^{-2} G_0$. The peaks are centred on SMC conductance values of

- 3.18 ± 0.14 ($\sigma = 2.60$) nS, ($4.10 \times 10^{-5} G_0$)
- 10.1 ± 0.81 ($\sigma = 2.81$) nS ($1.30 \times 10^{-4} G_0$)
 - (and a peak at $\sim 2 \times i = 22.5 \pm 1.88$ ($\sigma = 9.07$) nS),
- 67.6 ± 4.04 ($\sigma = 33.0$) nS ($8.72 \times 10^{-4} G_0$)
- 225 ± 22 ($\sigma = 98$) nS and ($2.90 \times 10^{-3} G_0$)
- 804 ± 120 ($\sigma = 466$) nS. ($1.04 \times 10^{-2} G_0$)

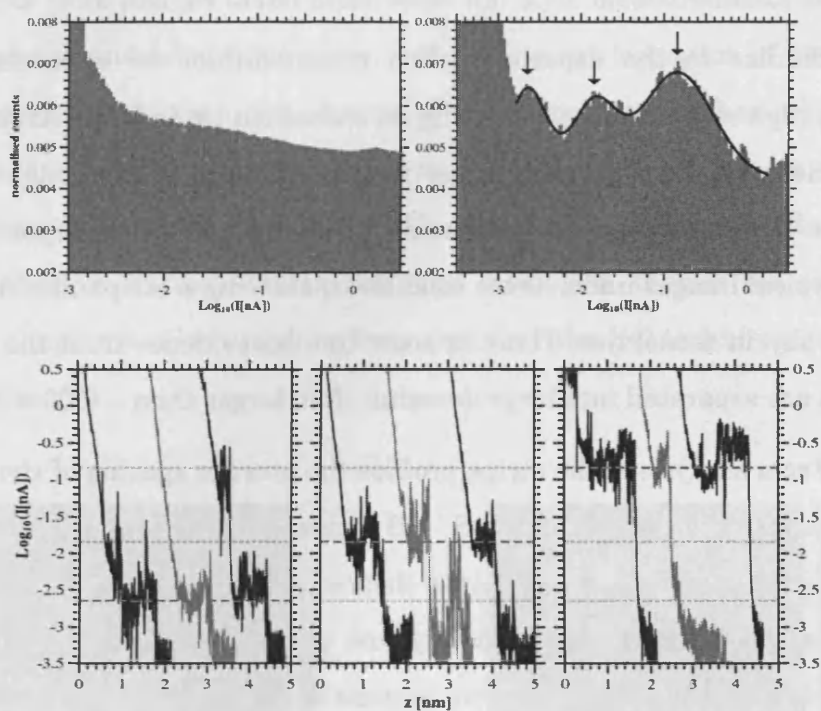


Figure 6.6. Porphyrin dimer $I(z)$ histograms (low amplifier), (left) all data, 27600 curves total; (right) selected curves, 660 selected ~ 2.4%

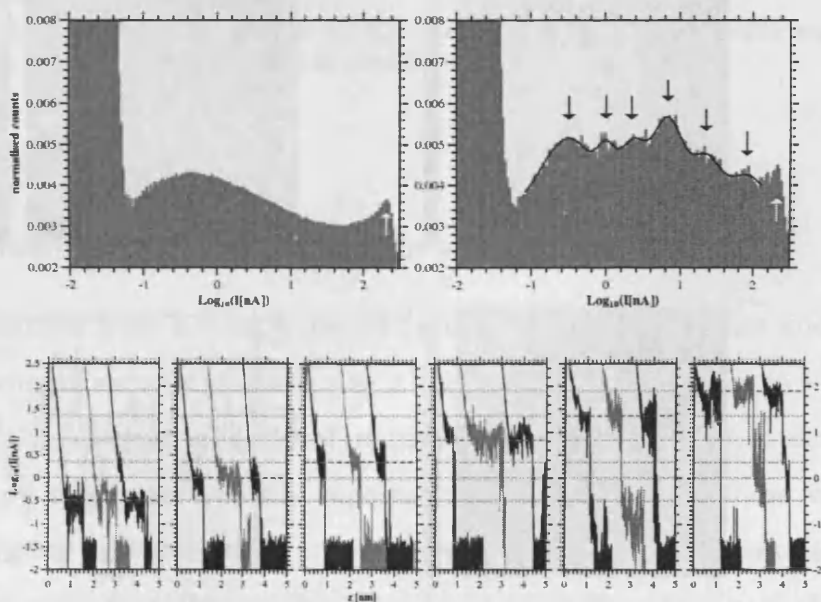


Figure 6.7. Porphyrin dimer $I(z)$ histograms (high amplifier), (left) all data, 32800 curves total; (right) selected curves, 735 selected ~2.2 %

High resolution images

Similar to the experiments on nonanedithiol we were occasionally able to achieve high resolution images using an etched Au tip in UHV. At the beginning of the experiment on the porphyrin dimer we were able to achieve high resolution images and see the self-organised structure of the molecular monolayer. Figure 6.8 shows some typical images under these conditions, showing a stripe-like ordered structure to the porphyrin monolayer. There is some limited evidence from the images that these regions are separated into large domains often larger than $\sim (100 \times 100) \text{ nm}^2$.

From analysis of the stripe profiles the average spacing of stripes is $3.90 \pm 0.145 \text{ nm}$, compared to the calculated S ... S distance for the dimer of 3.82 nm . We cannot resolve any details along the stripes themselves. The sample preparation procedure is empirically known to give relatively low coverage (see also the previous result for nonanedithiol, chapter 4), thus we assume a low density of porphyrin molecules, and conclude that the molecules are flat-lying with respect to the surface.

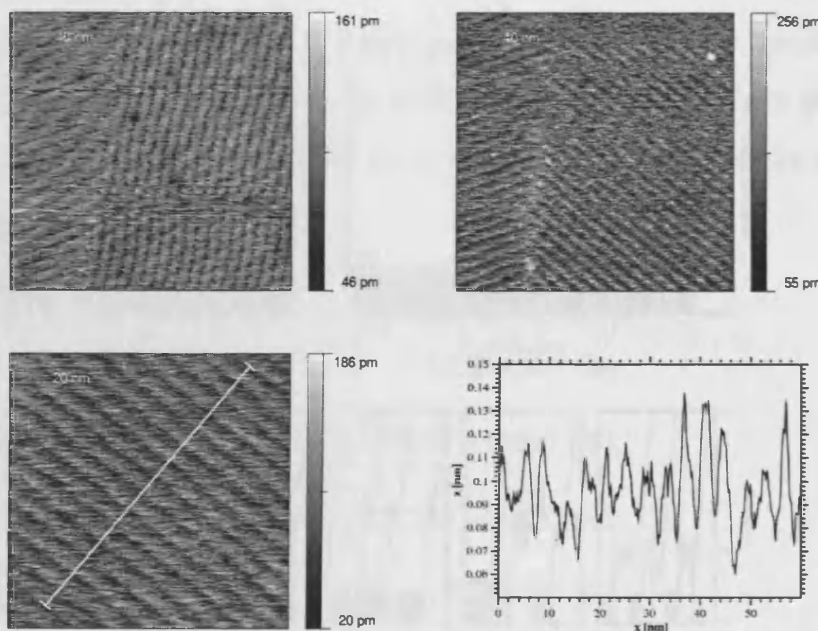


Figure 6.8. Porphyrin dimer at low coverage imaged by STM under UHV (setpoint = 30pA, bias = 0.8 V). Striped regions show ordering in the porphyrin monolayer and the average spacing from line profiles was determined to be $\sim 3.90 \text{ nm}$.

Evidence from images taken after some I(s) style measurements shows that the repeated approach and retract sequence, and subsequent formation of metal-molecule-metal junctions, causes some disturbance of the immediate surface area. As seen in Figure 6.9 a hole in the surface was formed during I(s). In the time it took (~8 minutes) to image the same area several times the hole disappeared due to the high mobility of the Au surface atoms and the molecules themselves (as previously discussed in chapter 4). So it is clear from this that the I(s) technique is not entirely non-destructive.

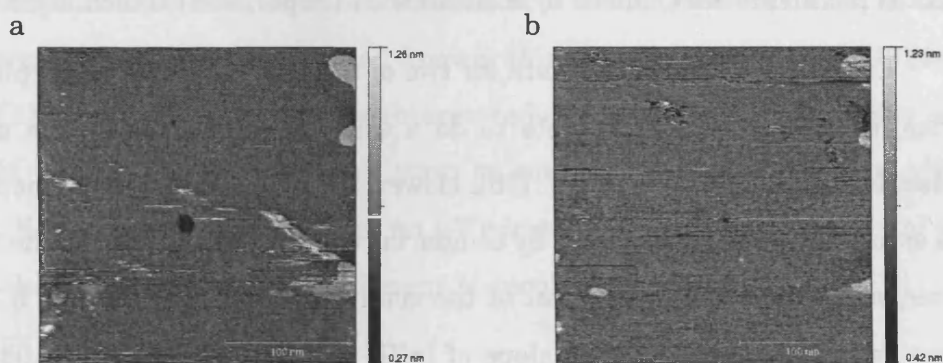


Figure 6.9. (a) Appearance of a hole in the surface after I(s) measurements (b) after repeated scanning of the same area for ~ 8 minutes the hole has almost disappeared.

6.2.3 Conclusions from I(z) experiments

In summary from I(z) experiments on the porphyrin monomer and dimer there is clear evidence of current plateaus over a wide range of current (up to $\sim 10^{-2} G_0$ and as low as $< 10^{-6} G_0$), showing evidence of multiple conductance groups; interestingly there are more than the three typically reported for alkanedithiols. These values span a range both higher and lower than previously published data for the same molecules in air. This indicates that the porphyrin molecules are therefore capable of multiple stable contact configurations/geometries. The high conductance values are comparable

to values measured for Au-benzenedithiol-Au junctions [106][107][108][109], which also show a wide spread in conductance and evidence of multiple conductance groups.

Currently unpublished data from Liverpool for an equivalent porphyrin molecule with a *pyridine* end-group shows the existence of three conductance groups, similar to published results for the alkanedithiols. It is unclear why there appears to be more than three conductance groups in our data, but we can clearly show examples of the current plateaus corresponding to these peaks. In addition we did not see similarly high conductance values in the experiments on nonanedithiol, thus this effect is not an artefact caused by a difference in experimental technique.

Currently we only have data for two of the molecules in the porphyrin oligomer series, therefore we are not able to do a full analysis of the length dependence of molecular conductance as in ref. [16]. However if we assume an exponential decay we can estimate the decay constant by comparing conductance peaks for the monomer and dimer, and check this for several of the conductance groups (Figure 6.10). Based on these assumptions the average slope of $\ln(G)$ versus S...S length is $0.030 \pm 0.013 \text{ \AA}^{-1}$, compared to $0.04 \pm 0.006 \text{ \AA}^{-1}$ measured by Sedghi et al. To confirm this trend we would need to measure the conductance of the $n=0$ compound and the porphyrin trimer.

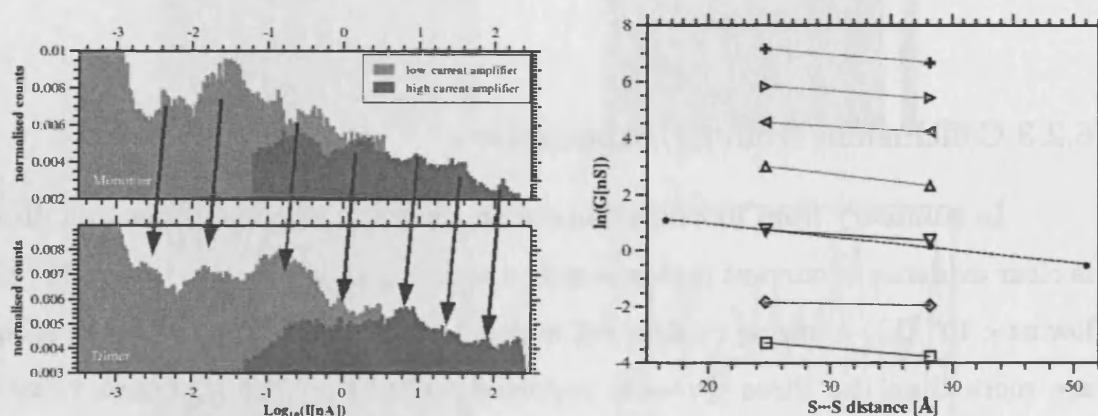


Figure 6.10. Comparison of conductance group peaks for the porphyrin monomer (S...S length = 24.7 \AA) and porphyrin dimer (S...S length = 38.2 \AA) (open symbols). (filled circles/dashed line) results from Sedghi et al [16]

6.3 I-V characteristics

We performed initial I-V tests, in UHV, on nonanedithiol and the porphyrin molecules on similar low coverage samples as used for the $I(z)$ experiments. The tip is kept in feedback at a given setpoint, i.e. 0.5 nA, at -600mV bias, and the feedback loop is re-established in between each individual I-V measurement. It could be seen that many of the I-V curves showed stochastic jumps in the current during the measurements; Figure 6.11 shows some examples of this effect. Similar observations can be made at fixed bias, and this fluctuation of the current over time, at fixed z and in the presence of molecules, is well known; this is Haiss' $I(t)$ method [16][34][50][53][56][76][110][111]. These jumps are interpreted as molecules spontaneously contacting the STM tip, changing its contact state or configuration, and hence modifying the current. Seeing these current jumps on I-V curves opens up the possibility of gathering full I-V characteristics for these different molecular states.

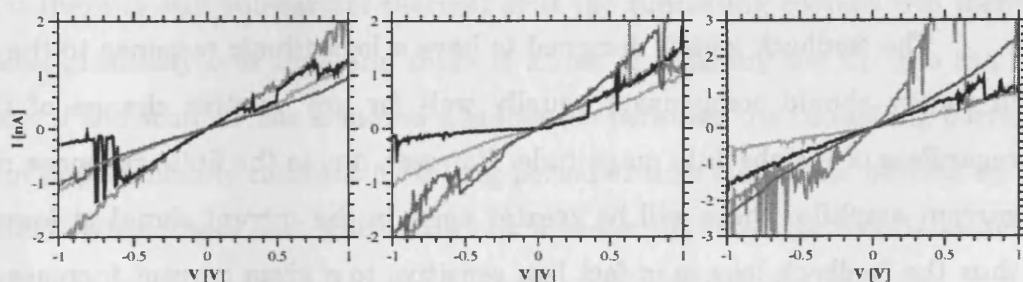


Figure 6.11. preliminary I-Vs over nonanedithiol, from 0.5 nA setpoint at -600mV bias. Each curve is ~ 1 second in duration.

Indeed if we overlay a few I-V curves it sometimes appears that jumps occur between two or more well defined levels, but taking a larger data set washes-out any details about these levels; there are no distinct groupings of I-V curves of different magnitude or shape. This is perhaps unsurprising as in between each individual

measurement feedback is re-established; the tip-sample distance is adjusted to compensate for any jump in the current, thus any change in the molecule contact geometry of configuration may be disrupted, and it is therefore difficult to directly compare one I-V curve to another.

Ideally we would like to be able to hold the tip-molecule-surface junction in any one of these contact states/configurations for a length of time and repeatedly probe the full I-V characteristics. We have previously seen in chapter 5 that the I-V behaviour of matrix isolated porphyrin molecules shows some interesting fluctuations in the asymmetry and energy level alignment, as judged by transition voltage spectroscopy. However in that experiment the feedback loop was also re-established in between each I-V, thus conductance jumps/fluctuations were not observed. (The thermal drift in the Veeco instrument is too large to operate without feedback; the tip is likely to drift away from or crash in to the surface if the distance is not regulated). In that case any disruption to the fluctuating junction/contact was minimised by using a very low bias (-20 mV) at feedback; we explain this further below as it may not be immediately obvious to the reader why this should help.

The feedback loop is designed to have a logarithmic response to the current, so in theory should compensate equally well for any relative change of the current regardless of the absolute magnitude. However, due to the finite response range of the current amplifier there will be greater noise in the current signal at lower currents, thus the feedback loop is in-fact less sensitive to a given current increase at -20 mV, where the current is low, compared to -600 mV. In addition, in any tunnelling model, the current typically has an exponential dependence on bias but is approximately linear near zero volts. The range of this quasi-linear region depends on the tunnelling barrier/molecular properties. Thus it can be clearly seen that the current will be less sensitive to changes in the barrier height/molecular configuration at low bias. Feeding-back at low bias voltage allows the experimenter to maintain the approximate tip-sample distance whilst also allowing some fluctuation in the barrier/molecular properties.

With the current setpoint maintained the results from the matrix isolated porphyrins suggest that fluctuations in V_m are not correlated to changes in junction conductance. However it seems counter intuitive that a change in the molecular configuration or contact, that effects a change in the I-V characteristic, would not in turn alter the conductance. The major caveat in the previous experiments is that any changes in the conductance are compensated for by changing the tip-sample distance, so to fully address this issue we adopt the experimental approach outlined below.

6.3.1 Experimental approach

We use the same low coverage sample as used in $I(z)$ experiments on the *Porphyrin dimer* (with piperidine ligand). We commence topographic imaging and continue for some time simply imaging whilst the microscope scanning assembly warms up and achieves a steady operational temperature. This can be tested by monitoring the tunnelling current at a fixed location whilst deactivating the feedback loop; if there is still substantial thermal drift the tunnelling current will increase or decrease gradually over time and there is a risk of crashing the tip into the sample surface; if the scanner has achieved a stable temperature the tunnelling current will remain approximately constant for a long period of time (tested for periods up to ~30 minutes). When these low drift conditions are met the feedback loop is switched off and I-V curves are continuously recorded without re-establishing feedback.

The conductance of the measured I-V curves is free to fluctuate and does not simply reflect the current setpoint. More importantly the tip-sample distance is held constant so the interpretation of the jumps in conductance is no longer complicated by the fluctuating tip-sample distance, and hence represents an augmentation of the tunnelling junction by the fluctuating molecular contact or configuration. We may then analyse the time series of conductance from the individual I-V curves and compare this to the transition voltage behaviour.

Figure 6.12 shows a short section from a series of I-V measurements; the equilibrium conductance G (judged by parabolic fit to the low bias range) versus time shows sudden jumps and the I-V curves in the shaded regions (1-4) are shown below. At each jump the conductance increases/decreases by around an order of magnitude, which is substantially more than would be expected if the number of molecules in the tunnelling gap simply increased from one to two, or from two to three, etc.

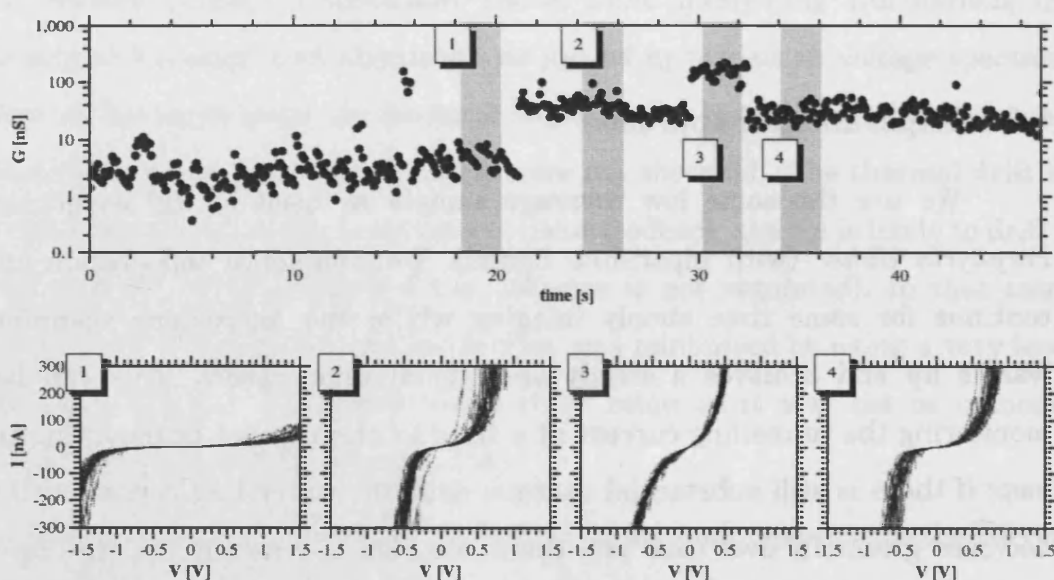


Figure 6.12. (top) Example time series of conductance G from repeated I-V measurements. (bottom) The I-V curves in the shaded regions 1-4 are shown.

We measured 21 separate data sets at room temperature, giving a total of 31000 I-V curves initialised from a setpoint current of 100 pA at 20 mV bias. In addition we performed similar measurements at low temperature (~ 57 K), gathering 37200 curves from a setpoint current of 500 pA, at 100 mV bias, and 32800 curves from 10 pA, at 100 mV bias. In all cases the resulting I-V curves vary not only in magnitude, but also in shape, and can be loosely categorised as (approximately) symmetric curves, asymmetric curves and curves displaying negative differential resistance (NDR).

Figure 6.13 shows some examples of I-V curves that are approximately symmetric, although this description is used loosely as the curves are clearly not exactly symmetric. In fact most of the I-V curves fall into this category and many display some asymmetric features and departures from the typical sigmoidal-shape I-V curves of simple barrier tunnelling. These features may be signs of resonant tunnelling through molecular energy levels. We can judge the absolute symmetry by the ratio of current at positive and negative bias. The distribution of $\log_{10}(I_{+1V}/I_{-1V})$ for all the I-V curves is well described by a Lorentzian centred around zero and with a width that indicates that the typical ratio I_{+1V}/I_{-1V} (or I_{-1V}/I_{+1V}) is less than about three (for the three curves shown in Figure 6.13 the ratios at ± 1 V are: (+/-) 3.9, (-/+) 2.4 and (-/+) 1.7 respectively). In contrast a small number of curves ($< 0.05\%$ of all curves at room temperature and $< 2\%$ at 57K) show highly rectifying characteristics with the example curves in Figure 6.14 giving a current ratio at ± 1 V of (+/-) 84, (-/+) 41 and (+/-) 96.

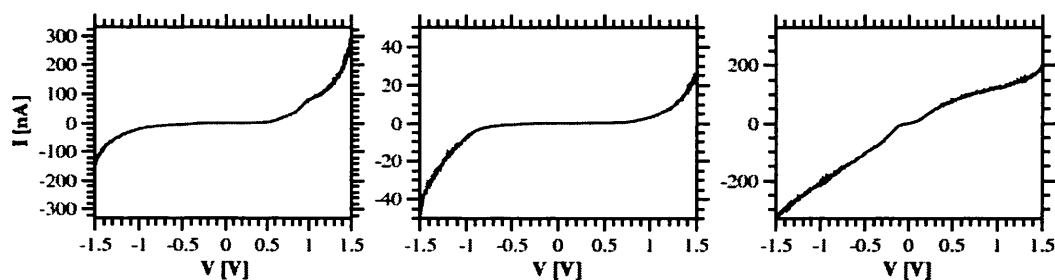


Figure 6.13. Examples of approximately symmetric I-V curves

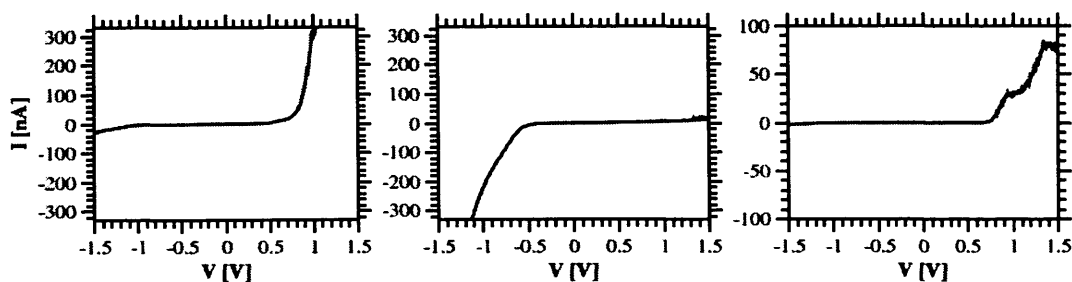


Figure 6.14. Examples of highly asymmetric I-V curves

A small proportion of the I-V curves display NDR, that is a clear drop in the absolute current with increasing voltage (Figure 6.15). The occurrence of this type of characteristic is more frequent in the low temperature data sets with $\sim 0.8\%$ of curves showing the feature, compared to $\sim 0.2\%$ at room temperature.

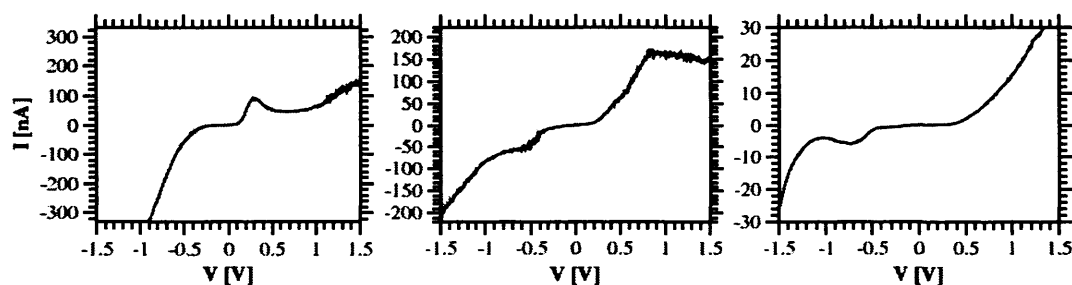


Figure 6.15. Examples of I-V curves showing negative differential resistance

Time series of measurements

Each series of I-V measurements consists of several hundreds or thousands of repeat measurements and there is a rich variety of different curves resulting from the molecular fluctuations. As an example Appendix D shows thumbnail images for all the I-V curves in one data set of 4200 repeat measurements, but it is difficult to concisely

present this time series in a single figure. We can, however, extract certain parameters from the I-V curves and analyse the time dependence. Figure 6.16 shows several examples of the time dependence of the equilibrium conductance G for a given set of I-V measurements, each initialised from the same setpoint current/bias, equivalent to 5 nS. (Some time passes between switching the feedback loop off and commencing the series of measurements, thus a jump in the current away from the setpoint may have already occurred and the first value of G in the series does not necessarily reflect the setpoint.) There are clear jumps between well defined conductance levels in each example and the total range of the conductance fluctuations is over several orders of magnitude. In all cases the current neither monotonically increases nor decreases over time, confirming that the vertical drift is low and that a gradual extension or contraction of the atomic structure of the tip or surface is not generally responsible for the conductance changes.

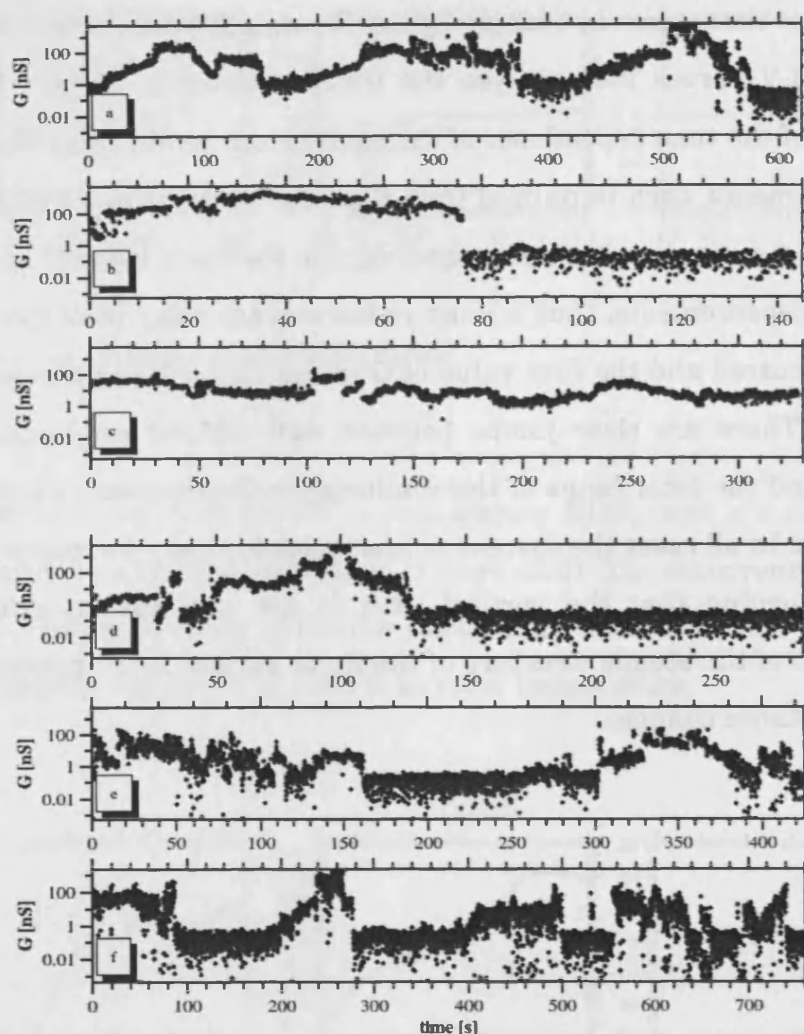


Figure 6.16. Examples of equilibrium conductance G versus time from several series' of repeated I-V measurements without feedback.

Under the low drift conditions the tip-sample distance is effectively constant and the jumps in the conductance correspond to some change in the tunnelling gap, e.g. attachment of a molecule to the tip; movement of the molecule in the tunnelling gap; lateral drift of the tip and an associated height change; rearrangement of the tip or surface Au atoms, giving an effective height change. Tests on the bare Au surface show that similar jumps in the current are rarely seen in the absence of molecules, indicating that the jumps in this experiment are indeed a molecular feature. Figure

6.17 shows the frequency distribution of conductance values taken from the six time series' of I-V measurements in Figure 6.16. There are several distinct peaks in the distribution of $\log_{10}(G)$ and other data sets show similar behaviour.

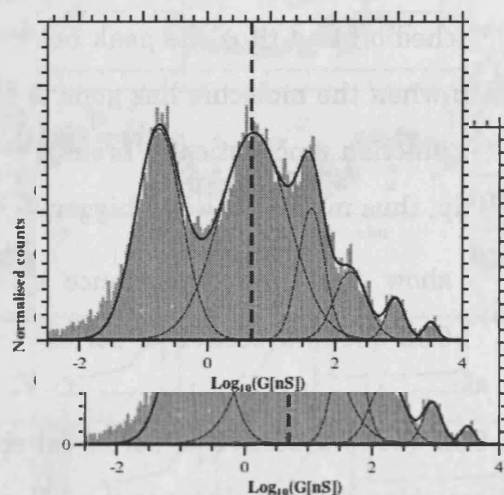


Figure 6.17. Frequency distribution of conductance from the 6 time series shown in Figure 6.16. The dashed line indicates the setpoint equivalent conductance. Also shown is a fit to the data by multiple Gaussian peaks.

A fit of 6 Gaussian peaks to the distribution gives peak values at 0.176 nS, **5.40 nS**, 42.9 nS, 176 nS, 893 nS and 3190 nS (a span of $\sim 2 \times 10^{-6} G_0$ to $\sim 4 \times 10^{-2} G_0$) (ratios between the peaks: 31, 7.9, 4.1, 5.1, 3.6); the peak at ~ 5 nS corresponds to the setpoint. The peaks cannot be interpreted in the same manner as the $I(z)$ results as the experimental technique here does not result in the molecule being lifted up in the tunnelling gap. Instead the tunnelling gap width is nominally constant and the molecule may explore different conformations or contact geometries allowed by the fixed tip-sample gap. Nevertheless the distribution of conductance values is strikingly similar to those measured by $I(z)$ (Figure 6.5 and Figure 6.7); both experiments suggest several possible well defined states of the molecular junction, that cannot simply be explained as one, two, three molecules, etc. Both experiments also show conductance values as high as $\sim 10^{-2} G_0$ are possible in the molecular junction, and even

in the I-V experiments the fixed tunnelling gap precludes the explanation that such high conductance values are the result of a background through-space tunnelling in parallel to the molecular conduction.

It is unclear why there is a peak in the conductance histogram below the setpoint. It could imply that there is often a molecule attached to the tip before the feedback loop is switched off and thus the peak below the setpoint is the conductance of the tunnelling gap when the molecule has gone away. Alternatively it could be that when the molecular junction stochastically breaks the molecule removes a Au atom from the end of the tip, thus making the gap bigger, reducing the current.

We can also show the time dependence of V_m alongside the conductance fluctuations. Figure 6.18 shows a section of series (a) shown in Figure 6.16, with G , V_m^+ and V_m^- versus time. Also shown below are the I-V curves and corresponding F-N plots taken from the positions labelled 1 to 7 marked by the dashed grey lines. In this example it can be seen that there are some changes in G and $V_m^{+/-}$ but there is no obvious correlation between the two parameters. At some points, however, it appears that a sudden change in G is accompanied by a sudden change in V_m .

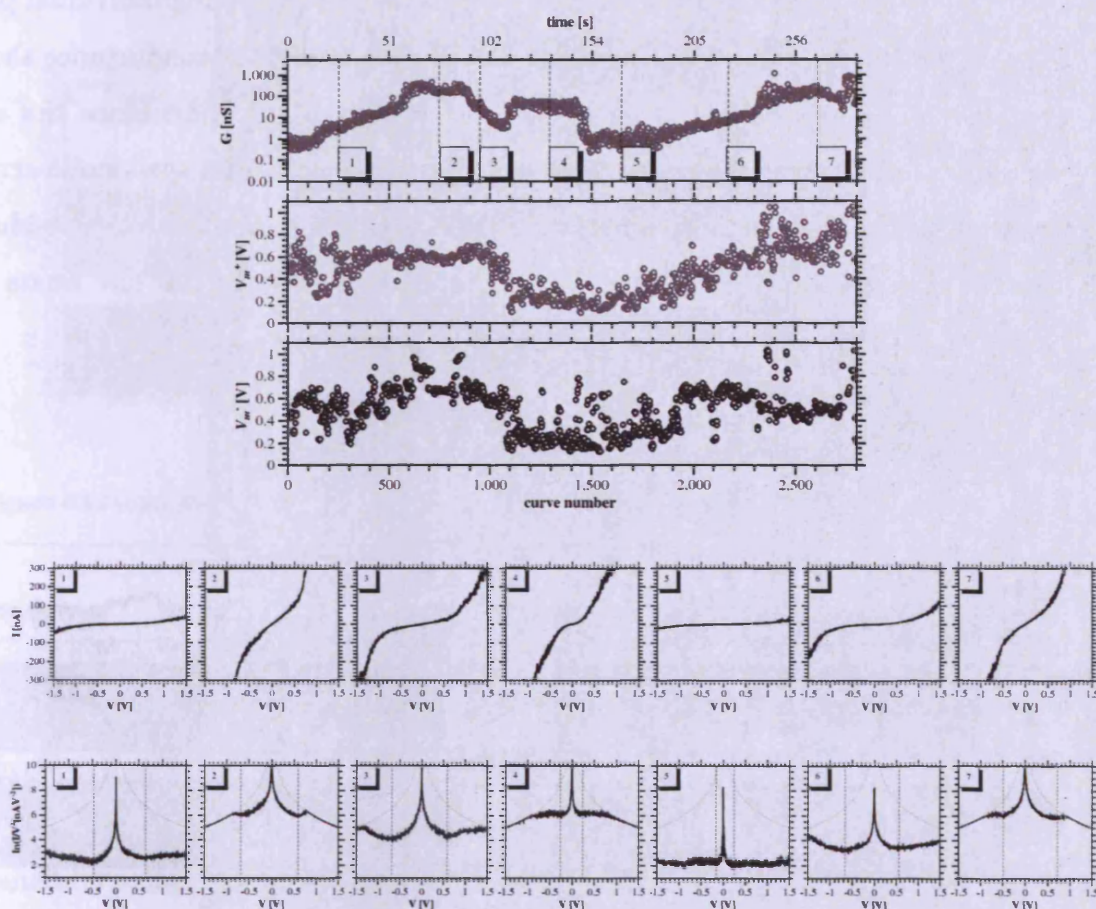


Figure 6.18. Example time series (c.f. fig 6.16 a) with G and V_m . At each of the points in the series marked 1 to 7 the I-V curve and corresponding F-N plot (shown as $\ln(I/V^2)$ versus V) is also shown, with V_m marked by dashed vertical lines. The curved, dashed, grey line shows the saturation limit of the current amplifier.

To help us visualise the changes in the I-V curves in each of the series (a – f) we generate a colour contour plot of $\ln(I/V^2)$, versus curve number on the abscissa and bias voltage on the ordinate axis (Figure 6.19 a – f). The colour in the plots indicates the magnitude of $\ln(I/V^2)$ after each curve has been scaled by G to aid comparison of the *shape* of the I-V curve; blue indicates low values of $\ln(I/V^2)$ and a black line is overlaid to show the absolute position of the minimum point; this is V_m . Where the current exceeds the measurable limit (i.e. saturates the current amplifier) $\ln(I/V^2)$ is set to an arbitrary high value and appears as block red.

From the visualisation of the time series and checking individual plots we see that, for the analysis of V_m , curves at very high and very low conductance should be excluded from the analysis. This is because at very high conductance the current amplifier is saturated even at low bias and this may introduce a systematic error into the analysis, where V_m simply reflects the point of saturation. At very low conductance there is a large amount of noise when the current is near the low limits of the amplifier and thus the minimum is often not well defined.

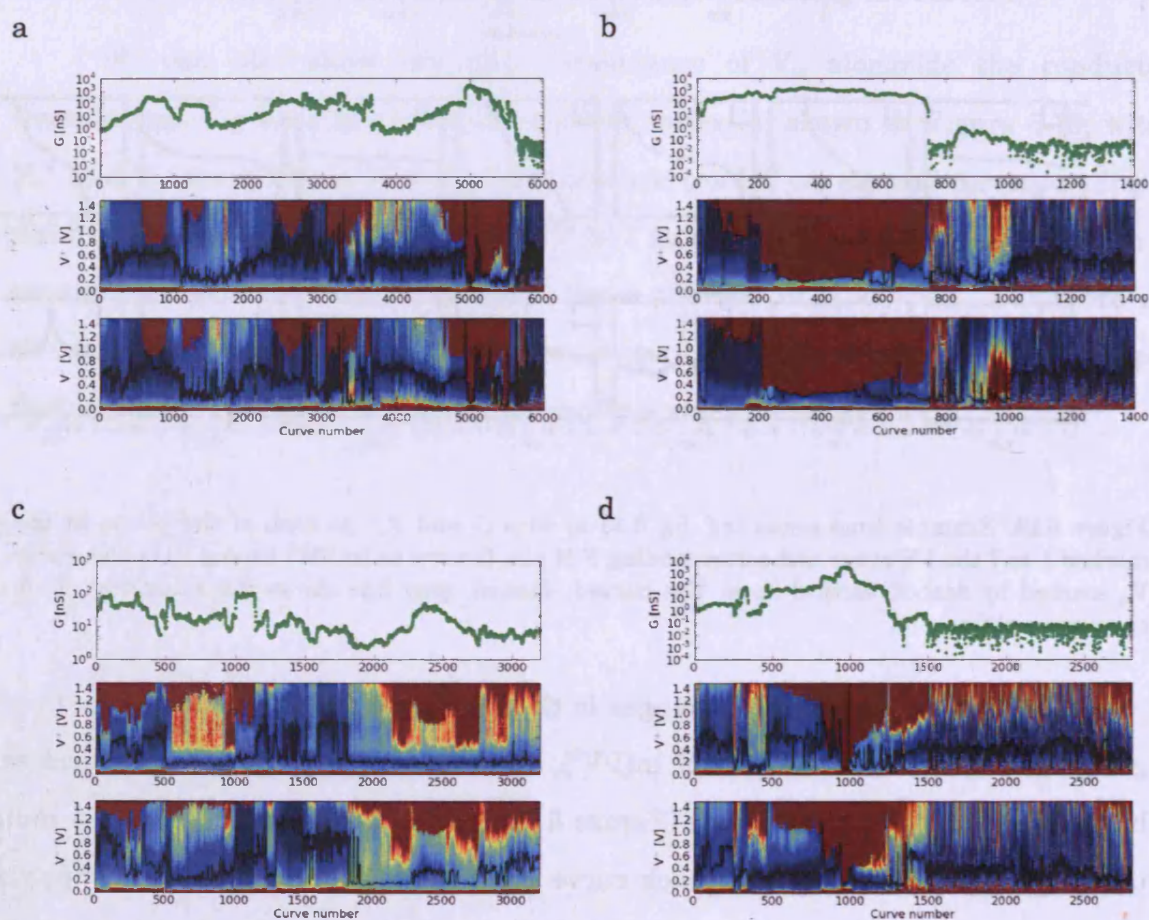


Figure 6.19. Colour contour plot visualisation of the I-V time series' previously shown in Figure 6.16. In each series the lower two panels show $\ln(I/V^2)$ as a colour intensity (scaled by G to aid comparison, blue for low values, red for high) versus curve number on the abscissa and bias voltage on the ordinate axis. A black line is overlaid on the colour plots to indicate the absolute minimum V_m .

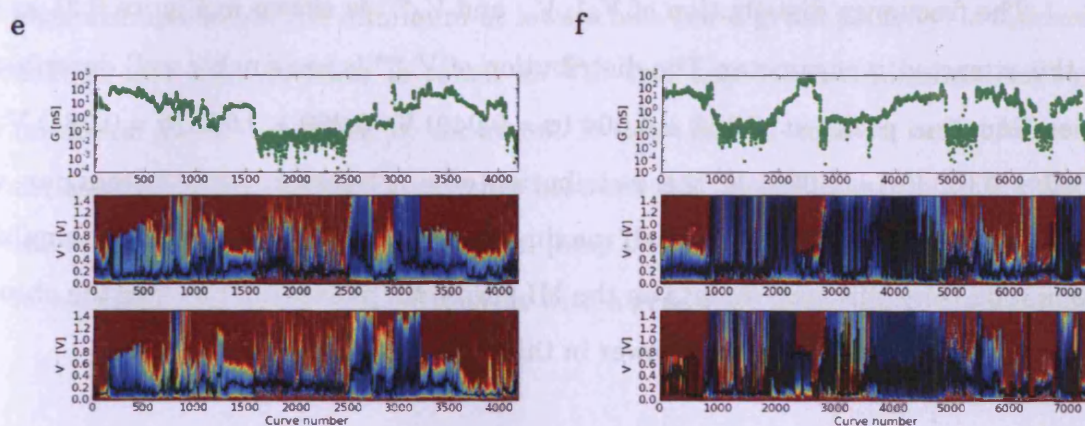
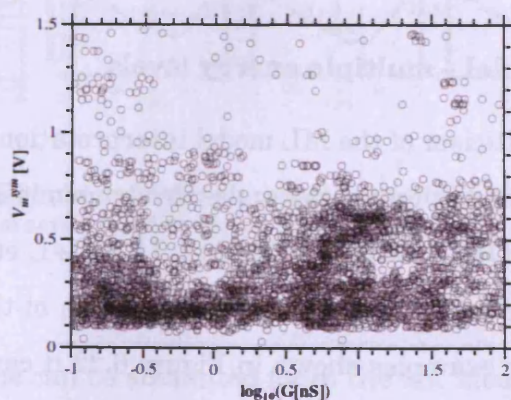


Figure 6.19 (continued).

Figure 6.20 shows the scatter of V_m^{sym} (as defined previously in chapter 5) versus G , in the region considered appropriate for the V_m analysis. From this, and the inspection of each time series, there appears to be no correlation between the voltage minimum and the equilibrium conductance. To re-iterate a previous point, it can be generally remarked that a jump in the conductance is *often* accompanied by a change in V_m , but this is not *always* the case and there is certainly no monotonic dependence of V_m on G . Some specific examples of the evolution of the I-V characteristics are considered in the further discussion below.

Figure 6.20. Scatter plot of V_m^{sym} versus G for all I-V curves at room temperature

The frequency distribution of V_m^+ , V_m^- and V_m^{sym} is shown in Figure 6.21 as well as the extracted η parameter. The distribution of V_m^{sym} is reasonably well described by three Gaussian peaks at 0.158 ± 0.004 ($\sigma = 0.040$) V, 0.269 ± 0.051 ($\sigma = 0.084$) V and 0.557 ± 0.021 ($\sigma = 0.096$) V; the distribution of η is approximately Lorentzian with mode at 0.49 and half width at half maximum of 0.21. This is qualitatively similar to the results from the experiments on the MI porphyrin molecules, however the absolute value of the voltage minimum is lower in this case.

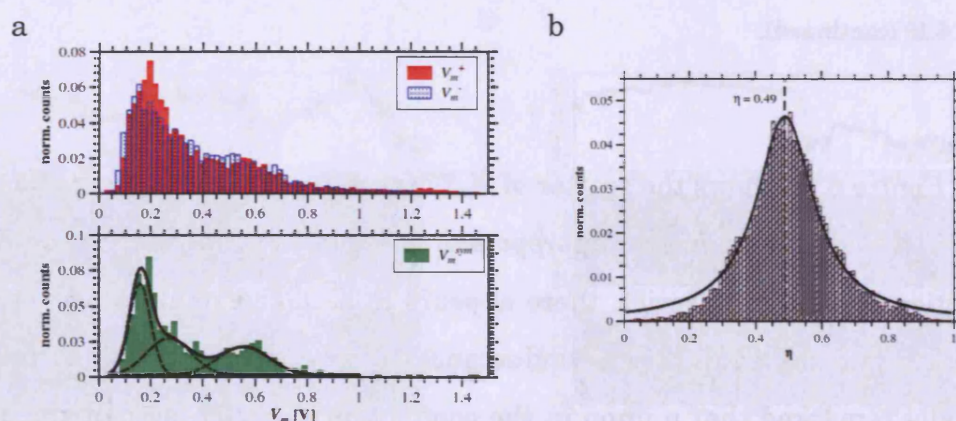


Figure 6.21. (a) Frequency distribution of V_m^+ , V_m^- and V_m^{sym} for all I-V curves at room temperature. (b) distribution of η

Expanding the model – multiple energy levels

An obvious criticism of the ML model interpretation of the TVS results is that a more realistic approximation for the molecular transmission must incorporate higher energy levels, e.g. HOMO, LUMO, HOMO+1, LUMO+1, etc. This fact is evident when we examine many of the I-V curves and the evolution of the characteristics over time. As illustrated by the examples shown in Figure 6.22 it can often be seen that there is more than one minimum present (in the positive bias half of the curve, say), or that there are changes in the slope suggestive of two broad minima merged together. In

each example below the minimum at lowest bias (for a given polarity) is marked by the dashed line (this is what is taken as V_m) and any second minimum or suggested minimum point is marked by an arrow. It can then be seen in each of the example series that at some point V_m switches between the two values. In both 6.22(a) and (b) the conductance increases by a sudden jump, but while in (a) V_m^+ decreases, in (b) V_m^+ is seen to *increase*. In (c) V_m^+ decreases with a gradually decreasing conductance.

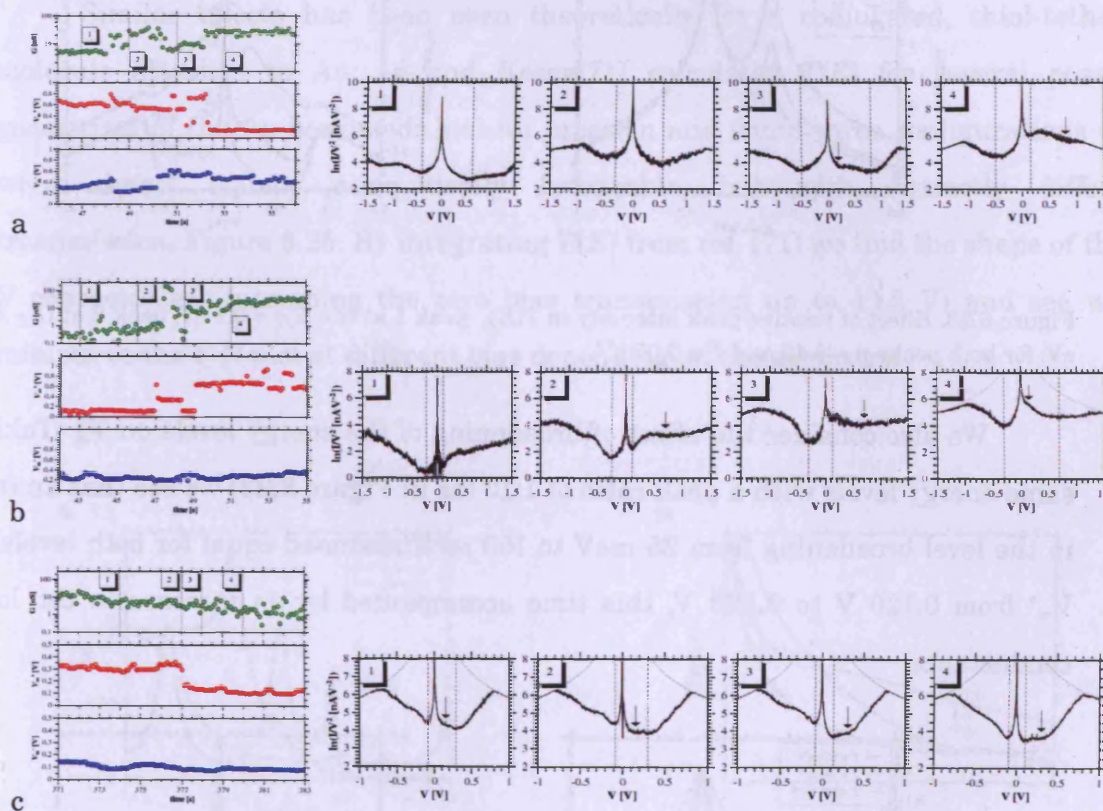


Figure 6.22. Examples of F-N plots exhibiting a change in minimum point and double minima, taken (a) from series 6.16c, (b) from series 6.16d and (c) from series 6.16e

Such observations can be accounted for in the ML model if we consider the effect of a more complex $T(E)$ on the model results. We consider below a model with two levels (LUMO, LUMO-1) that are not well separated; level 1 at $(\epsilon - E_F) = 0.1$ eV and

level **2** at $(\varepsilon - E_F) = 0.4$ eV. In a realistic model of $T(E)$ it should be appreciated that the relative magnitude of each peak may not be identical. Figure 6.23 shows the effect of decreasing the transmission of level 1 relative to level **2**. For these overlapping transmission peaks, at a given level broadening ($\Gamma = 0.05$ eV for both), a decrease in the peak height of the first level effects an increase of V_m^+ from 0.120 V to 0.465 V. This is accompanied by a *decrease* in the low bias conductance.

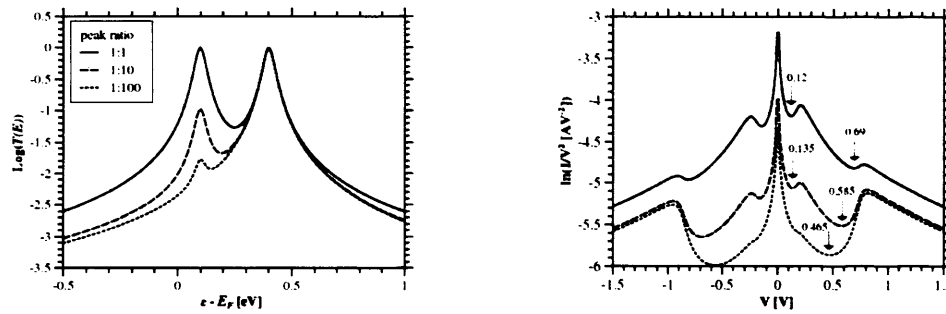


Figure 6.23. Effect of relative peak intensity in $T(E)$, peak **1** at $(\varepsilon - E_F) = 0.1$ eV, peak **2** at $(\varepsilon - E_F) = 0.4$ eV; for both peaks $\eta = 0.46$ and $\Gamma = 0.05$ eV.

We also consider the effect of broadening of the energy levels on V_m . Taking the same energy levels with a peak ratio of 1:10 (as in Figure 6.23) we see that an increase in the level broadening from 25 meV to 100 meV (assumed equal for both levels) shifts V_m^+ from 0.120 V to 0.563 V, this time accompanied by an *increase* in the low bias conductance.

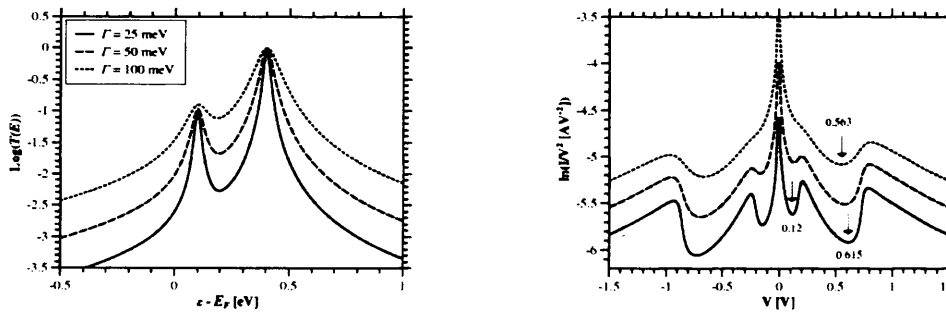


Figure 6.24. double peak; effect of broadening peak **1** at $(\varepsilon - E_F) = 0.1$ eV, peak **2** at $(\varepsilon - E_F) = 0.4$ eV, $\eta = 0.46$.

Far from merely being toy-illustrations of the complexity of the V_m interpretation, we consider that both these mechanisms for changes in V_m are realistic possibilities, i.e. a contact/configuration change that affects $T(E)$ and hence V_m . The two mechanisms both allow a switch of V_m between the same two approximate values (~ 0.12 V and ~ 0.5 V), but predict opposite qualitative changes in the conductance. This is in agreement with our observation that V_m is not correlated with G .

Similar effects has been seen theoretically for a conjugated, thiol-tethered molecule attached to Au; Li and Kosov[71] calculated $T(E)$ for several possible geometries of the Au-benzenedithiol-Au junction and found three configurations that were almost equally energetically favourable, but with distinctly different transmission, Figure 6.25. By integrating $T(E)$ from ref. [71] we find the shape of the I-V characteristic (assuming the zero bias transmission up to ± 1.5 V) and see weak minima in the F-N plot at different bias depending on the geometry.

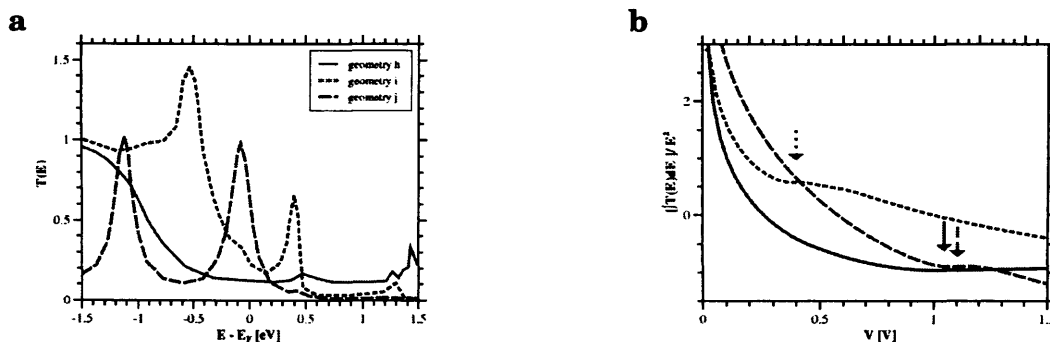


Figure 6.25. (a) $T(E)$ for three different geometries of the Au-Benzenedithiol-Au junction, reproduced from Li and Kosov [71]. (b) $[\int T(E)dE]/E^2$ versus V with local minima marked by the arrows.

We also note that the geometry labelled “j” has a significant peak in $T(E)$ very close to E_F , but this does *not* manifest as a minimum in the F-N plot at low voltage. An interesting observation in our own data is that some I-V curves with relatively high

conductance, and showing signs of resonant features, nevertheless do not show a V_m in the measurable current range (Figure 6.26). It may be that the minimum is outside the bias range probed, or that for these particular barriers/molecular configurations there is no minimum point defined. This can occur if the level broadening is particularly large (i.e. of the order of 1 eV or greater), but the resultant curves would *not* show the molecular resonance features.

An alternative explanation that should be considered is the case of very close Fermi-level alignment of the molecular energy level (cf. geometry “j” in Figure 6.25). As shown in the ML model results in Figure 6.27 when the offset ($E_F - \epsilon$) is sufficiently small there is no observable minimum and $\ln(I/V^2)$ still decreases with increasing bias. Thus the expected Fowler-Nordheim regime, with characteristic increase in $\ln(I/V^2)$ with bias, would not be observed for a well aligned single molecular energy level, and thus the TVS technique is not necessarily sensitive to such molecular orbitals.

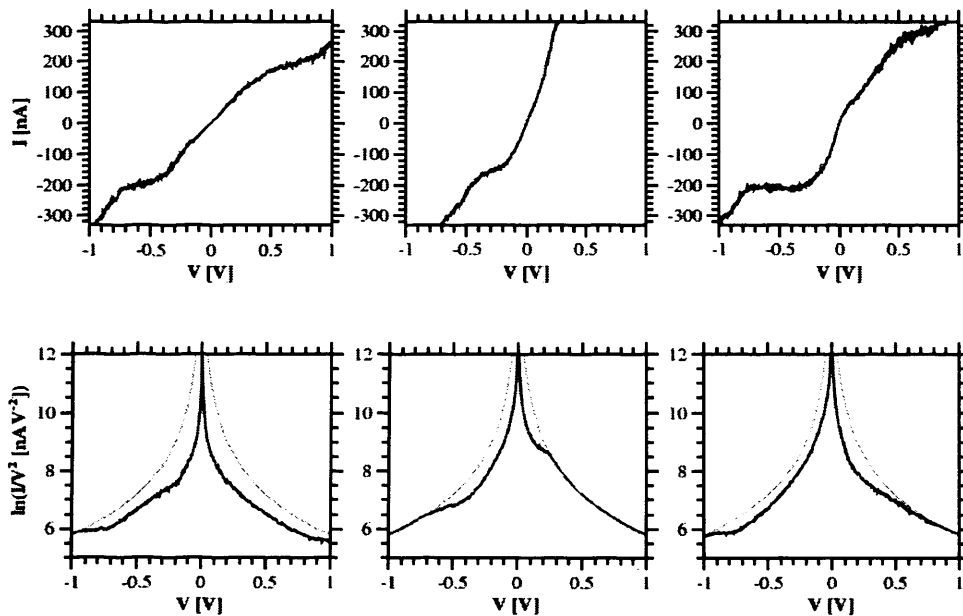


Figure 6.26. I-V curves with high conductance, showing resonant features, but no V_m within the measurable current range.

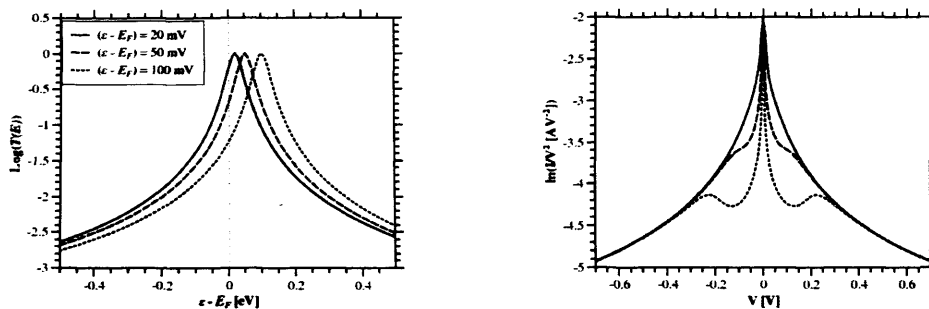


Figure 6.27. ML model: very close Fermi level alignment ($\Gamma = 0.05$ eV, $\eta = 0.5$).

Low temperature results

The behaviour of the molecular junctions at ~ 57 K was similar to that at room temperature, although extra care was taken to stabilise the temperature before measurements to keep drift to a minimum. Jumps in the current were seen and histograms of conductance values show a similar spread and appearance of peaks as previously illustrated for the room temperature data (Figure 6.17).

The analysis of V_m gives similar results to the room temperature data. The frequency distribution of V_m^+ , V_m^- and V_m^{sym} for the low temperature curves is shown in Figure 6.28 as well as the extracted η parameter. The distribution of V_m^{sym} gives peaks at 0.127 ± 0.001 ($\sigma = 0.033$) V, 0.264 ± 0.012 ($\sigma = 0.100$) V and 0.704 ± 0.042 ($\sigma = 0.0261$) V and the distribution of η is approximately Lorentzian with mode at 0.49 and half width at half maximum of 0.20.

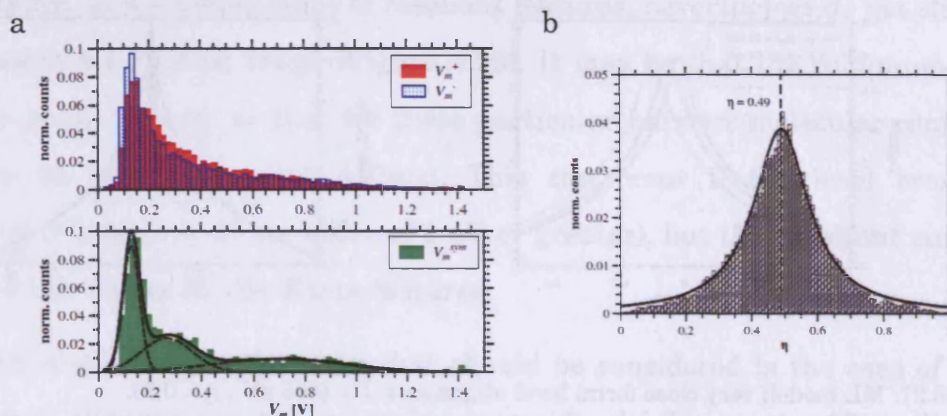


Figure 6.28. (a) Frequency distribution of V_m^+ , V_m^- and V_m^{sym} for all I-V curves at ~57 K. (b) distribution of η

Thus from this analysis there is no conclusive difference between the room temperature and low temperature data, but this is unsurprising for two reasons. Firstly, if we attribute charge transport in the porphyrin molecules to tunnelling through molecular orbitals (as in the ML model) we expect only a weak temperature dependence arising from the increased broadening of the Fermi functions at higher temperature, as well as any broadening of the molecular orbitals themselves (see Appendix A). While this may add up to a small but appreciable effect, we must secondly consider in parallel what the actually effective temperature is in the junction. Tsutsui et al [112] cooled a benzenedithiol single molecule junction to 77 K to perform $I(z)$ measurements at a range of bias values. The authors found that, due to local heating at high bias, the effective temperature at 0.85 V was as high as ~400K, thus we cannot rule out the idea of significant local heating in our I-V measurements where the bias is ramped up to ± 1.5 V.

The results presented in this chapter are similar to those of Noguchi et al [86] [28] who measured I-V for thiol-tethered porphyrin molecules in an electromigrated break-junction experiment at low temperature. They also report the appearance of symmetric, asymmetric and staircase type I-V curves, although the different

characteristics are not due to temporal fluctuations, but rather junction-to-junction differences upon repeated formation of the nanogaps. They report $V_m \sim 0.19$ V for porphyrins with Cu centred macrocycle, but $V_m \sim 0.34$ V for a non-metallised porphyrin. The authors suggest that the lower value for the Cu porphyrin is due to effective barrier height lowering caused by the presence of the d_z^2 orbital of the Cu atom, i.e. in the ML model the central metallisation may introduce a transmissive channel at lower energy offset than any of the other molecular energy levels. Interestingly Qian et al [113] observed a two-state conductance behaviour in Zn-centred porphyrins which they attributed to conformational changes of the molecule, specifically a displacement of the Zn atom out of the porphyrin plane. Similar measurements on the non-metallised porphyrin showed only one conductance value.

The most significant difference in our measurements at low temperature is the relative number of curves exhibiting NDR behaviour ($\sim 0.8\%$ of curves at 57K, compared to $\sim 0.2\%$ at room temperature). The observation of NDR was also made by Noguchi et al and could be accounted for by the presence of adsorbates on the electrodes, giving the contacts a local density of states different from the quasi-continuum often assumed for the metallic leads. At low temperature the probability of an incident adsorbate molecule sticking to the surface is close to unity[64] therefore, even if the local junction effective temperature is relatively high, the low temperature experiment may suffer from an increased rate of adsorbate contamination, and hence more frequent occurrence of the NDR feature.

We can illustrate this adsorbate induced NDR in the ML model by assuming an extra transmission term for the contact(s). Thus far the transmission model, as outlined in chapter 2, assumes a continuous density of states of the metallic contacts, thus the transmission through the metallic contacts can be regarded as $T(E) = 1$. We could more generally regard the transmission through the molecular junction as the product of the molecular transmission and the transmission of the contacts, i.e. $T(E) = T(E)_1 \times T(E)_{mol} \times T(E)_2$. If one or more of the contacts has a non-continuous local density of states this can have a notable impact on the calculated I-V characteristics.

Figure 6.24 illustrates this with a toy example. We model a molecular energy level at $\varepsilon - E_F = 0.4$ eV, $\Gamma = 50$ meV and $\eta = 0.5$, but in addition we assume that the surface contact has a transmission described by another energy level also at $\varepsilon - E_F = 0.4$ eV, $\Gamma = 50$ meV, but necessarily pinned to the Fermi level (i.e. the energy level does not shift with respect to E_F under an applied bias). The shape of the total transmission ($T(E) = T(E)_{\text{contact}} \times T(E)_{\text{mol}}$) in this example can be seen in Figure 6.24 at zero bias and at 0.5 V, as well as the molecular and contact components. The resultant I-V curve shows a decrease in current with increasing negative bias below ~ -0.5 V. So, if the overlap of the molecular level with the localised contact states is reduced, as the bias increases, the conductance may fall.

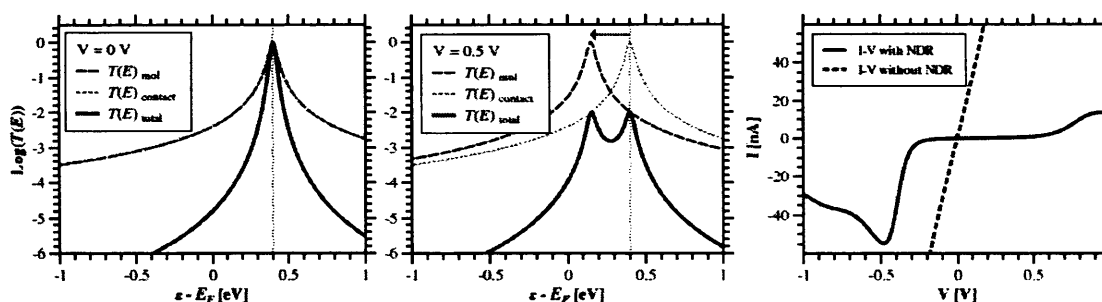


Figure 6.29. Negative differential resistance in the ML model assuming a local density of states at the surface electrode (see text)

This is not the only possible explanation for the appearance of NDR in molecular junctions, for example a bias dependent coupling $\Gamma \equiv \Gamma(V)$ could lead to a similar effect. However, other proposed mechanisms are generally an explicit function of the molecular electronic properties, such as the chemically controlled localisation of atomic orbitals[114], or orbital symmetry matching with the metallic electrodes[115], or indeed bias dependent changes in molecular orbital symmetry leading to a non-linear change in the coupling[116]. If this were the case for the porphyrin molecules we would

expect to see the feature more frequently, although it may be that in some rarely encountered molecular configuration one of these type of mechanisms is realised.

In summary we have performed I-V measurements on the sample of porphyrin dimers at low coverage, without feedback, hence maintaining a constant tip-sample separation throughout a series of repeat measurements. Stochastic fluctuations in the molecular configuration or contact geometry manifest both as jumps in the equilibrium conductance and as changes in the voltage minimum from the transition voltage spectroscopy analysis. We found no correlation between the conductance and V_m and several examples were given to illustrate the complex nature of the changes. Using an extended version of the ML model we proposed realistic mechanisms to account for the observations, allowing an increase in conductance to be accompanied by either an increase *or* a decrease in the value of V_m (or no change in V_m at all).

7 Summary and Conclusions

We now present a summary of the results presented in chapters 4, 5 and 6 and discuss the direction of possible future work. In chapter 4 we performed low bias single molecule conductance (SMC) measurements on the simple alkanedithiol system under ultra high vacuum conditions. Plateaus in the current versus distance, $I(z)$, curves were seen, corresponding to molecular attachment events, and subsequent analysis of the statistical distribution of current values showed a broad peak indicating some preferred values. In all the experiments the main peak in the histograms is in approximate agreement with reported values for the Medium (B) and High (C) conductance groups for nonanedithiol in air and solution. Other low current plateaus were relatively infrequent except in the case of the low coverage sample. However, roughening of the sample at low coverage reduces the occurrence of the low current plateaus again, in agreement with known effects of surface roughness on the SMC.

The magnitude of the lower current plateaus are lower still than the published values for the Low (A) group, by about an order of magnitude. However this is in qualitative agreement with published data for hexanedithiol in UHV, suggesting that the lower current values may be a vacuum effect. The mechanism for this change is unknown, but it is commonly interpreted that the A group is the result of conduction through various gauche conformations of the alkanedithiols, thus the peak conductance value depends on the distribution of molecular conformers that may be explored in the junction. This distribution is known to be affected by temperature[76] and tip-sample separation[34], but perhaps the most obvious difference in the UHV experiment is the lack of surface water or other solvent molecules. If adsorbed water/solvent molecules are responsible for the difference it is still unclear whether the water/solvent molecules actually enhance the conductance by mediating the charge transport itself, or if they simply affect the distribution of the gauche conformers.

In chapter 5 we explained the motivation for studying conjugated porphyrin oligomers and presented results of I-V measurements on porphyrin molecules isolated in an alkanethiol matrix. The concept of transition voltage spectroscopy was introduced and it was argued that the voltage minimum V_m is a good indication of the molecular energy level alignment of the nearest molecular orbital to the electrode Fermi energy (the HOMO or LUMO). From the I-V results we were able to provide estimates of the molecular energy level alignment and degree of contact asymmetry in the Au-porphyrin-Au junctions. The porphyrin molecules are seen to have an energy level at $\sim 0.3 - 0.4$ eV below E_F (assuming HOMO), similar for the monomer and dimer in the oligomer series. However repeated I-V measurements on the isolated molecules showed evidence of fluctuations in the molecular contacts and in some configurations the molecular energy level alignment is at greater offset, possibly ~ 0.6 eV below E_F or greater.

These results were supported by experiments on porphyrin single molecules in chapter 6. Similar to the results for nonanedithiol, current plateaus were found in the $I(z)$ curves for the porphyrin monomer and dimer, and evidence of multiple distinct conductance groups was presented. The porphyrin molecules were found to exhibit well defined contact states with conductance values spanning the range $< 10^{-6} G_0$ up to $\sim 10^{-2} G_0$ and there appears to be up to seven distinct peaks in this range. Thus it is impossible to identify a unique SMC from these measurements, but instead the results suggest a rich variety of different contact/configuration states of the Au-porphyrin-Au junction.

We performed novel measurements in which the STM tip was held static for extended periods of time, allowing the molecules to stochastically change and maintain different contact/configuration states while the I-V characteristics were probed. Similar to the $I(z)$ measurements jumps in the current magnitude covered a broad range of conductance values. The molecular energy level alignment as judged by V_m was seen to fluctuate and often changed simultaneously with a jump in the conductance. The statistical analysis of V_m gave a similar low valued estimate for the

molecular level alignment with E_F at $\sim 0.13 - 0.16$ eV and again with some configurations at greater offsets ~ 0.3 eV or ~ 0.6 eV below E_F . However careful examination of the temporal evolution of these changes, and cross-correlation to changes in the equilibrium conductance, show that the interpretation of the fluctuations is non-trivial.

The spectral weighting of any given molecular energy level in the transmission model of molecular conductance depends on the precise details of the molecular configuration and contact geometry. We have referred to several examples where this is demonstrated theoretically and the appearance of multiple conductance groups in $I(z)$ experiments (published examples and our own data) adds some indirect experimental evidence to this argument. But it is the results of the I-V curve analysis that clearly demonstrate a contact or configuration dependent change in the molecular electronic states relevant to conduction.

It is now clear that the analysis of the I-V curves by transition voltage spectroscopy must be treated with caution. Moreover the experimental results and toy examples based on the ML model also demonstrate that V_m need not necessarily give a good indication of the *closest* molecular energy level to E_F . In cases where molecular orbitals are, or become, sufficiently broadened and have some spectral overlap with other nearby orbitals the voltage minimum may not manifest at all. Most strikingly the case of very close Fermi-level alignment has also been shown to produce no minimum (in the toy example at least) and does not show the Fowler-Nordheim trend, despite the near optimum alignment.

In future work it would be more informative to compare the I-V characteristics to the results of full theoretical calculations of the porphyrin molecule electronic properties. This is currently beyond the scope of this work and the author's expertise. However we anticipate that the results of such calculations would confirm that different molecular contact geometries or configurations give different transport properties and would elucidate the nature of these different states. A number of

experimental avenues could also be explored to further our understanding of these results.

A careful study of the temperature dependence of conductance by $I(z)$ is needed to clarify the dominant conduction mechanism in the porphyrin molecules, i.e. temperature independent behaviour would rule out a thermally assisted hopping mechanism, although longer molecules such as a porphyrin trimer (or longer) may exhibit significant hopping transport nonetheless. It would be instructive to change the molecular end-group, affecting the nature of the binding to the metal electrodes. For example pyridyl or amine end groups can still provide chemical attachment to Au electrodes and we could see if this affects the number or range of the conductance groups in $I(z)$ or affects the measured V_m . Other chemical modifications of the porphyrin molecule could also be considered, such as changing the central metallisation of the porphyrin macrocycle, or modification of the oligomeric structure – e.g. triply linked porphyrins (Figure 7.1) would have significantly different properties compared to the butadiyne linked porphyrins studied here[80]. Changing the metal of the contacts could also have a significant effect on the transport properties.

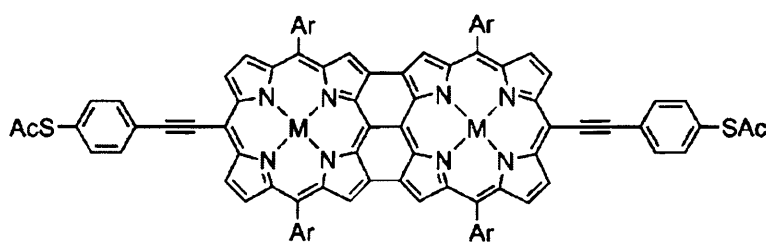


Figure 7.1. Triply linked porphyrin dimer

8 References

- [1] G. Kamarinos, P. Felix. (1996). *J. Phys. D App. Phys.*, **29**, 487-500.
- [2] A. Aviram, M. A. Ratner. (1974). *Chem. Phys. Lett.*, **29**, 277-283.
- [3] M. A. Reed, J. M. Tour. (2000). *Sci. Am.*, **282**, 86-93.
- [4] B. Bhushan (2004). *Springer handbook of nanotechnology*. Springer-Verlag.
- [5] R. F. Service. (2003). *Science*, **302**, 556-+.
- [6] H. Ishii, K. Sugiyama, E. Ito, K. Seki. (1999). *Adv. Mater.*, **11**, 972-972.
- [7] B. Kim, J. M. Beebe, Y. Jun, X. Y. Zhu, C. D. Frisbie. (2006). *J. Am. Chem. Soc.*, **128**, 4970-4971.
- [8] F. Chen, N. Tao. (2009). *Acc. Chem. Res.*, **42**, 429-438.
- [9] C. Li, I. Pobelov, T. Wandlowski, A. Bagrets, A. Arnold, F. Evers. (2008). *J. Am. Chem. Soc.*, **130**, 318-326.
- [10] L. Venkataraman, J. E. Klare, I. W. Tam, C. Nuckolls, M. S. Hybertsen, M. L. Steigerwald. (2006). *Nano Lett.*, **6**, 458-462.
- [11] A. Vilan. (2007). *J. Phys. Chem. C*, **111**, 4431-4444.
- [12] R. Landauer. (1992). *Phys. Scr.*, **T42**, 110-114.
- [13] J. G. Simmons. (1963). *J. App. Phys.*, **34**, 1793.
- [14] J. M. Beebe, B. Kim, J. W. Gadzuk, C. D. Frisbie, J. G. Kushmerick. (2006). *Phys. Rev. Lett.*, **97**, 026801(1-4).
- [15] M. Araidai, M. Tsukada. (2010). *Phys. Rev. B*, **81**, .
- [16] G. Sedghi, K. Sawada, L. J. Esdaile, M. Hoffmann, H. L. Anderson, D. Bethell, W. Haiss, S. J. Higgins, R. J. Nichols. (2008). *J. Am. Chem. Soc.*, **130**, 8582.
- [17] J. M. Beebe, B. Kim, C. D. Frisbie, J. G. Kushmerick. (2008). *ACS Nano*, **2**, 827-832.
- [18] E. H. Huisman, C. M. Guédon, B. J. van Wees, S. J. van der Molen. (2009). *Nano Lett.*, **9**, 3909-3919.
- [19] J. Chen, T. Markussen, K. S. Thygesen. (2010). *arXiv1005.3937*, , .

- [20] S. H. Choi, B. Kim, C. D. Frisbie. (2008). *Science*, **320**, 1482-1486.
- [21] A. V. Pakoulev, V. Burtman. (2009). *J. Phys. Chem. C*, **113**, 21413-21421.
- [22] W. Haiss, S. Martin, L. E. Scullion, L. Bouffier, S. J. Higgins, R. J. Nichols. (2009). *Phys. Chem. Chem. Phys.*, **11**, 10831-10838.
- [23] J. K. Tomfohr, O. F. Sankey. (2002). *Phys. Rev. B*, **65**, .
- [24] S. Datta (2005). *Quantum Transport: Atom to Transistor*. Cambridge University Press.
- [25] J. P. Perdew, A. Ruzsinszky. (2010). *Int. J. Quantum Chem.*, **110**, 2801-2807.
- [26] Y. Q. Xue, M. A. Ratner. (2005). *Int. J. Quantum Chem.*, **102**, 911-924.
- [27] A. Danilov, S. Kubatkin, S. Kafanov, P. Hedegard, N. Stuhr-Hansen, K. Moth-Poulsen, T. Bjornholm. (2008). *Nano Lett.*, **8**, 1-5.
- [28] Y. Noguchi, R. Ueda, T. Kubota, T. Kamikado, S. Yokoyama, T. Nagase. (2008). *Thin Solid Films*, **516**, 2762-2766.
- [29] G. D. Scott, D. Natelson. (2010). *ACS Nano*, **4**, 3560-3579.
- [30] VT-AFM; Omicron NanoTechnology GmbH; <http://www.omicron.de/>
- [31] G. Binning, H. Rohrer, C. Gerber, E. Weibel. (1982). *Phys. Rev. Lett.*, **49**, 57.
- [32] Multimode III SPM; <http://www.veeco.com>. Bias is applied to the STM tip, the sample is grounded. The microscope is kept in a glovebox under a constant flow of nitrogen to reduce the ambient humidity.
- [33] Y. S. Park, A. C. Whalley, M. Kamenetska, M. L. Steigerwald, M. S. Hybertsen, C. Nuckolls, L. Venkataraman. (2007). *J. Am. Chem. Soc.*, **129**, 15768-+.
- [34] W. Haiss, C. S. Wang, I. Grace, A. S. Batsanov, D. J. Schiffrin, S. J. Higgins, M. R. Bryce, C. J. Lambert, R. J. Nichols. (2006). *Nat. Mater*, **5**, 995-1002.
- [35] H. Ishii, K. Seki. (1997). *IEEE Trans. Electron Devices*, **44**, 1295-1301.
- [36] D. M. Alloway, M. Hofmann, D. L. Smith, N. E. Gruhn, A. L. Graham, R. Colorado, V. H. Wysocki, T. R. Lee, P. A. Lee, N. R. Armstrong. (2003). *J. Phys. Chem. B*, **107**, 11690-11699.
- [37] D. M. Alloway, A. L. Graham, X. Yang, A. Mudalige, R. Colorado, V. H. Wysocki, J.

- E. Pemberton, T. R. Lee, R. J. Wysocki, N. R. Armstrong. (2009). *J. Phys. Chem. C*, **113**, 20328-20334.
- [38] E. Ito, T. Arai, M. Hara, J. Noh. (2009). *Bulletin of the Korean Chem. Soc.*, **30**, 1309-1312.
- [39] C. D. Zangmeister, J. M. Beebe, J. Naciri, J. G. Kushmerick, R. D. van Zee. (2008). *Small*, **4**, 1143-1147.
- [40] Y. Li, J. Huang, R. T. McIver, J. C. Hemminger. (1992). *J. Am. Chem. Soc.*, **114**, 2428-2432.
- [41] J. A. M. Sondag-Huethorst, C. Schonenberger, L. G. J. Fokkink. (1994). *J. Phys. Chem.*, **98**, 6826-6834.
- [42] G. E. Poirier, E. D. Pylant. (1996). *Science*, **272**, 1145-1148.
- [43] M. Brust, M. Walker, D. Bethell, D. J. Schiffrin, R. Whyman. (1994). *J. Am. Chem. Soc. Chem. Comms.*, , 801-802.
- [44] M. J. Hostetler, S. J. Green, J. J. Stokes, R. W. Murray. (1996). *J. Am. Chem. Soc.*, **118**, 4212-4213.
- [45] M. T. Cygan, T. D. Dunbar, J. J. Arnold, L. A. Bumm, N. F. Shedlock, T. P. Burgin, L. Jones, D. L. Allara, J. M. Tour, P. S. Weiss. (1998). *J. Am. Chem. Soc.*, **120**, 2721-2732.
- [46] C. D. Bain, J. Evall, G. M. Whitesides. (1989). *J. Am. Chem. Soc.*, **111**, 7155-7164.
- [47] L. Motte, F. Billoudet, M. P. Pileni. (1995). *J. Phys. Chem.*, **99**, 16425-16429.
- [48] W. Y. Wang, T. Lee, M. A. Reed. (2003). *Phys. Rev. B*, **68**, 035416.
- [49] H. B. Akkerman, R. C. G. Naber, B. Jongbloed, P. A. van Hal, P. W. M. Blom, D. M. de Leeuw, B. de Boer. (2007). *Proc. Nat. Acad. Sci. USA*, **104**, 11161-11166.
- [50] S. Martín, W. Haiss, S. Higgins, P. Cea, M. C. López, R. J. Nichols. (2008). *J. Phys. Chem. C*, **112**, 3941-3948.
- [51] B. Q. Xu, N. J. J. Tao. (2003). *Science*, **301**, 1221-1223.
- [52] W. Haiss, H. van Zalinge, S. J. Higgins, D. Bethell, H. Hobenreich, D. J. Schiffrin, R. J. Nichols. (2003). *J. Am. Chem. Soc.*, **125**, 15294-15295.

- [53] W. Haiss, R. Nichols, H. van Zalinge, S. Higgins, D. Bethell, D. Schiffrin. (2004). *Phys. Chem. Chem. Phys.*, **6**, 4330-4337.
- [54] X. L. Li, J. He, J. Hihath, B. Q. Xu, S. M. Lindsay, N. J. Tao. (2006). *J. Am. Chem. Soc.*, **128**, 2135-2141.
- [55] J. Ulrich, D. Esrail, W. Pontius, L. Venkataraman, D. Millar, L. H. Doerrer. (2006). *J. Phys. Chem. B*, **110**, 2462-2466.
- [56] W. Haiss, S. Martin, E. Leary, H. van Zalinge, S. Higgins, L. Bouffier, R. Nichols. (2009). *J. Phys. Chem. C*, **113**, 5823-5833.
- [57] W. Haiss, D. Lackey, J. K. Sass, K. H. Besocke. (1991). *J. Chem. Phys.*, **95**, 2193-2196.
- [58] A. Mangin, A. Anthore, M. L. Della Rocca, E. Boulat, P. Lafarge. (2009). *Phys. Rev. B*, **80**, .
- [59] M. Hugelmann, W. Schindler. (2003). *SURFACE SCIENCE*, **541**, L643-L648.
- [60] S. C. Meepagala, F. Real. (1994). *Phys. Rev. B*, **49**, 10761-10763.
- [61] D. H. Woo, E. M. Choi, Y. H. Yoon, K. J. Kim, I. C. Jeon, H. Kang. (2007). *SURFACE SCIENCE*, **601**, 1554-1559.
- [62] O. Y. Kolesnychenko, O. I. Shklyarevakii, H. van Kempen. (1999). *Phys. Rev. Lett.*, **83**, 2242-2245.
- [63] L. Olesen, M. Brandbyge, M. R. Sorensen, K. W. Jacobsen, E. Laegsgaard, I. Stensgaard, F. Besenbacher. (1996). *Phys. Rev. Lett.*, **76**, 1485-1488.
- [64] K. Jousten (2008). *Handbook of Vacuum Technology*. Wiley-VCH.
- [65] B. Ren, G. Picardi, B. Pettinger. (2004). *Rev. Sci. Instrum.*, **75**, 837-841.
- [66] A. Savitzky, M. J. E. Golay. (1964). *Ana. Chem.* , **36**, 1627-1639.
- [67] M. Fujihira, M. Suzuki, S. Fujii, A. Nishikawa. (2006). *Phys. Chem. Chem. Phys.*, **8**, 3876-3884.
- [68] A. Nishikawa, J. Tobita, Y. Kato, S. Fujii, M. Suzuki, M. Fujihira. (2007). *Nanotech.*, **18**, .
- [69] K. Kobayashi, H. Yamada, T. Horiuchi, K. Matsushige. (1999). *App. Surf. Sci.*,

144-45, 435-438.

- [70] R. L. McCarley, D. J. Dunaway, R. J. Willicut. (1993). *Langmuir*, **9**, 2775-2777.
- [71] Z. Li, D. S. Kosov. (2007). *Phys. Rev. B*, **76**, 035415(1-7).
- [72] C. C. Kaun, T. Seideman. (2008). *Phys. Rev. B*, **77**, .
- [73] Z. F. Huang, F. Chen, P. A. Bennett, N. J. Tao. (2007). *J. Am. Chem. Soc.*, **129**, 13225-13231.
- [74] T. Morita, S. Lindsay. (2007). *J. Am. Chem. Soc.*, **129**, 7262-+.
- [75] X. D. Cui, A. Primak, X. Zarate, J. Tomfohr, O. F. Sankey, A. L. Moore, T. A. Moore, D. Gust, L. A. Nagahara, S. M. Lindsay. (2002). *J. Phys. Chem. B*, **106**, 8609-8614.
- [76] W. Haiss, H. van Zalinge, D. Bethell, J. Ulstrup, D. J. Schiffrin, R. J. Nichols. (2006). *Faraday Discussions*, **131**, 253-264.
- [77] M. Biesaga, K. Pyrzynska, M. Trojanowicz. (2000). *Talanta*, **51**, 209-224.
- [78] M. Calvete, G. Y. Yang, M. Hanack. (2004). *Synth. Met.*, **141**, 231-243.
- [79] T. H. Lee, W. Y. Wang, M. A. Reed. (2003). *Ann. N. Y. Acad. Sci.*, **1006**, .
- [80] K. Tagami, M. Tsukada. (2003). *Jpn. J. Appl. Phys. Part 1*, **42**, 3606-3610.
- [81] K. Liu, X. H. Wang, F. S. Wang. (2008). *ACS Nano*, **2**, 2315-2323.
- [82] L. Müller-Meskamp, S. Karthäuser, H. J. W. Zandvliet, M. Homberger, U. Simon, R. Waser. (2009). *Small*, **5**, 496-502.
- [83] G. Wang, T. Kim, G. Jo, T. Lee. (2009). *J. Am. Chem. Soc.*, **131**, 5980-5985.
- [84] H. Song, T. Lee, N. J. Choi, H. Lee. (2007). *App. Phys. Lett.*, **91**, .
- [85] H. Song, Y. Kim, Y. H. Jang, H. Jeong, M. A. Reed, T. Lee. (2009). *Nature*, **462**, 1039-1043.
- [86] Y. Noguchi, T. Nagase, R. Ueda, T. Kamikado, T. Kubota, S. Mashiko. (2007). *Jpn. J. Appl. Phys. Part 1*, **46**, 2683-2686.
- [87] This is confirmed independently by tracking features over a series of STM images and using this to estimate the lateral drift. For this we get an approximate value of ~ 1.22 nm/min. At 14Hz we can measure 500 I-V curves in ~ 35 seconds during which

time the tip should suffer a lateral drift ~ 0.6 nm.

- [88] H. Aghaie, M. R. Gholmi, M. D. Ganji, M. M. Taghavi. (2009). *Curr. App. Phys.* , **9**, 367-373.
- [89] A. Grigoriev, J. Skoldberg, G. Wendin, Z. Crljen. (2006). *Phys. Rev. B*, **74**, .
- [90] X. J. Wu, Q. X. Li, J. Huang, J. L. Yang. (2005). *J. Chem. Phys.*, **123**, .
- [91] Y. H. Qi, D. R. Guan, C. B. Liu. (2006). *Chinese. J. Chem.*, **24**, 326-330.
- [92] L. Venkataraman, J. E. Klare, C. Nuckolls, M. S. Hybertsen, M. L. Steigerwald. (2006). *Nature*, **442**, 904-907.
- [93] P. Zhao, Z. Zhang, P. J. Wang, D. S. Liu. (2009). *Physica B Cond. Matt.*, **404**, 3462-3465.
- [94] T. Frederiksen, C. Munuera, C. Ocal, M. Brandbyge, M. Paulsson, D. Sanchez-Portal, A. Arnau. (2009). *ACS Nano*, **3**, 2073-2080.
- [95] Y. H. Kim, S. S. Jang, W. A. Goddard. (2005). *J. Chem. Phys*, **122**, 244703.
- [96] J. A. Malen, P. Doak, K. Baheti, T. D. Tilley, A. Majumdar, R. A. Segalman. (2009). *Nano Lett.*, **9**, 3406-3412.
- [97] F. Zahid, A. W. Ghosh, M. Paulsson, E. Polizzi, S. Datta. (2004). *Phys. Rev. B*, **70**, 245317.
- [98] T. W. Kim, G. N. Wang, T. Lee. (2008). *IEEE Trans. Nanotechnol*, **7**, 140-144.
- [99] A. Salomon, T. Boecking, O. Seitz, T. Markus, F. Amy, C. Chan, W. Zhao, D. Cahen, A. Kahn. (2007). *Adv. Mater.*, **19**, 445.
- [100] J. K. Tomfohr, O. F. Sankey. (2002). *Physica Status Solidi B-Basic Research*, **233**, 59-69.
- [101] A. S. Duwez, G. Pfister-Guillouzo, J. Delhalle, J. Riga. (2000). *J. Phys. Chem. B*, **104**, 9029-9037.
- [102] A. A. Kocherzhenko, S. Patwardhan, F. C. Grozema, H. L. Anderson, L. D. A. Siebbeles. (2009). *J. Am. Chem. Soc.*, **131**, 5522-5529.
- [103] W. R. R. Yang, M. W. Jones, X. L. Li, P. K. Eggers, N. J. Tao, J. J. Gooding, M. N. Paddon-Row. (2008). *J. Phys. Chem. C*, **112**, 9072-9080.

-
- [104] S. H. Choi, C. Risko, M. C. R. Delgado, B. Kim, J. L. Bredas, C. D. Frisbie. (2010). *J. Am. Chem. Soc.*, **132**, 4358-4368.
- [105] L. Luo, C. D. Frisbie. (2010). *J. Am. Chem. Soc.*, **132**, 8854-+.
- [106] S. Fujii, U. Akiba, M. Fujihira. (2008). *Chem. Lett.*, **37**, 408-409.
- [107] K. Horiguchi, M. Tsutsui, S. Kurokawa, A. Sakai. (2009). *Nanotech.*, **20**, .
- [108] M. Tsutsui, Y. Teramae, S. Kurokawa, A. Sakai. (2006). *App. Phys. Lett.*, **89**, .
- [109] X. Y. Xiao, B. Q. Xu, N. J. Tao. (2004). *Nano Lett.*, **4**, 267-271.
- [110] H. van Zalinge, D. J. Schiffrin, A. D. Bates, W. Haiss, J. Ulstrup, R. J. Nichols. (2006). *Chem. Phys. Chem*, **7**, 94-98.
- [111] W. Haiss, C. Wang, R. Jitchati, I. Grace, S. Martin, A. Batsanov, S. Higgins, M. Bryce, C. Lambert, P. Jensen, R. Nichols. (2008). *J. Phys. Cond. Matt.*, **20**, .
- [112] M. Tsutsui, M. Taniguchi, K. Yokota, T. Kawai. (2010). *App. Phys. Lett.*, **96**, .
- [113] G. G. Qian, S. Saha, K. M. Lewis. (2010). *App. Phys. Lett.*, **96**, .
- [114] Z. Q. Fan, K. Q. Chen. (2010). *Physica E-Low-Dimensional Systems & Nanostructures*, **42**, 1492-1496.
- [115] S. A. Pan, A. D. Zhao, B. Wang, J. L. Yang, J. G. Hou. (2010). *Adv. Mater.*, **22**, 1967-1971.
- [116] R. Pati, M. McClain, A. Bandyopadhyay. (2008). *Phys. Rev. Lett.*, **100**, .
- [117] Python programming language. <http://www.python.org/>; <http://www.scipy.org/>.
- [118] T. M. Kalotas, A. R. Lee. (1991). *Am. J. Phys.*, **59**, 48-52.

9 Appendix A. Results of numerical calculations

In this appendix we give details of the methods used to perform numerical calculations based on the models outlined in chapter 2. The calculations are performed using a version of a program originally written by Dr Martin Elliott; Extension and modifications I have made are indicated in the text below (**bold text**), where appropriate. The I-V characteristics are calculated for different models by first calculating the transmission function, $T(E)$, and then using the Landauer scattering formalism to calculate the current. The results of the numerical calculations focus on the behaviour of the transition voltage V_m as a function of the barrier parameters. We also present the trends for the low conductance G and the relationship between V_m and G . Below is a comprehensive set of results for the molecular energy level and rectangular barrier (Simmons) models, illustrating the key trends.

The calculations are done using the python programming language[117] and excerpts of the code are included here to illustrate the method.

9.1 Molecular energy level model

Model parameters:

- Energy level position ϵ in eV
- Level broadening (coupling) Γ in eV
- coupling asymmetry η

The transmission is defined using the code below, originally written by Dr Martin Elliott. The original code has been modified to include the asymmetric bias shift of the energy level in the case of asymmetric coupling.

```
def tau_Huisman(E, bias=0.0, mu=6.0, epsilon=10.0, gammal=1.0, gamma2=1.0):
    """
    Finds transmission T(E) at an energy E for a resonant
    tunnelling model of a molecular level.
    a is barrier width in nm
    mu is position of Fermi energy
    epsilon is position of molecular energy level
    beta is decay parameter per nm
    eta is coupling symmetry (0.5 is symmetric)

    Note: energies all in eV here
    """

    gamma = gammal+gamma2          #total broadening
    eta = gammal/gamma

    E=E+(1-eta)*bias              #energy level shift with bias
```

```

term1=eta*(1-eta)*gamma*gamma
term2=gamma*gamma/4 + scipy.square(E-epsilon)
T=term1/term2

return T

```

To included the effects of finite (non-zero) temperature I add the Fermi function to the code:

$$f(E, T) = \left[1 + \exp\left(\frac{E - \mu}{k_b T}\right) \right]^{-1}, \quad (9.1)$$

```

def fermi(E, bias=0.0, mu=6.0, T=1.0):
    '''
    fermi function f(E,T) at an energy E, temperature T
    Note: energies all in eV here
    '''
    Kb = 8.61734315e-5 #Boltzmans constant in eV.K^-1

    term = 1 + exp((E-mu)/(Kb*T))
    F=1/term

    return F

```

The transmission is then effectively weighted by the difference between the the Fermi function at the left and right electrodes, i.e. $T(E) \Rightarrow |f_1(E, T) - f_2(E, T)| \times T(E)$. The model parameters are defined and the I-V curve is calculated:

```

# model parameters ...
mu=5.5 # Fermi level from band bottom 5.5 for Au
epsilon=mu - 0.5
gamma=0.001 # total coupling/broadening
eta=0.5 # degree of asymmetry, eta = gammal/gamma

gammal=eta*gamma
gamma2=gamma-gammal

#finite temperature
Temp= 300.0

# Applied bias range ...
V_start=-2.0; V_end=2.0 # bias range
nsteps=401 # voltage steps

for i in range (0, nsteps):

    muL=mu; muR=mu-V[i] # mu in eV since tau takes energy input in eV
    # choose energy E
    Esteps=400; Emin=min(muL, muR); Emin=Emin-1.0;
    Emax=max(muL, muR); Emax=Emax+1.0; dE=(Emax-Emin)/(Esteps-1);
    E=scipy.linspace(Emin, Emax, Esteps)

```

```
#initialise the arrays
transmission=scipy.zeros(Esteps, dtype='Float64')
fermi_1=scipy.zeros(Esteps, dtype='Float64')
fermi_2=scipy.zeros(Esteps, dtype='Float64')

for j in range (0, Esteps):
    fermi_1[j]=fermi(E[j], bias=V[i], mu=muL ,T=Temp)
    fermi_2[j]=fermi(E[j], bias=V[i], mu=muR ,T=Temp)

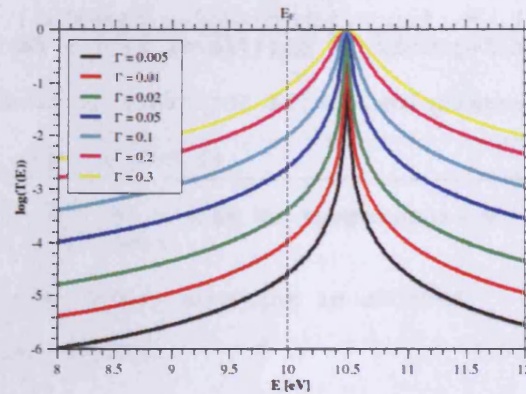
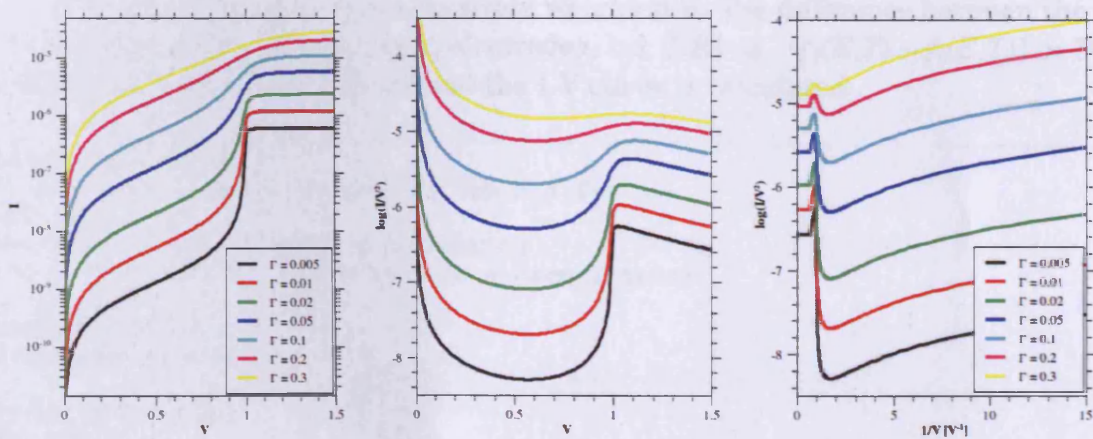
    transmission[j] = tau_Huisman(E[j], bias=V[i], mu=mu, epsilon=epsilon,
gamma1=gamma1, gamma2=gamma2) * abs((fermi_2[j] - fermi_1[j]))

    I[i]=q_e*dE*transmission.sum()# Integrate to find current in units of 2e/h

I=I*2*q_e/h
```

9.1.1 Results - Varying coupling (energy level broadening) Γ

- Γ varied
- $\varepsilon = E_F + 0.5$ eV, $\eta = 0.5$, $E_F = 10$ eV
- Due to increased energy level broadening the value of $T(E)$ at the Fermi energy increases, hence conductance increases.

Figure 9.1. Transmission for various Γ Figure 9.2. Calculated I-V curves; $\ln(I/V^2)$ versus V and $\ln(I/V^2)$ versus $1/V$

Remarks:

- V_m is invariant with increasing level broadening (Γ) for low values of Γ (Figure 9.3).
- As Γ increases further V_m begins to increase
- $\log(G)$ scales linearly with $\log(\Gamma)$
- Hence V_m is also invariant with increasing conductance for low values of the conductance (corresponding directly to the low values of the level broadening)

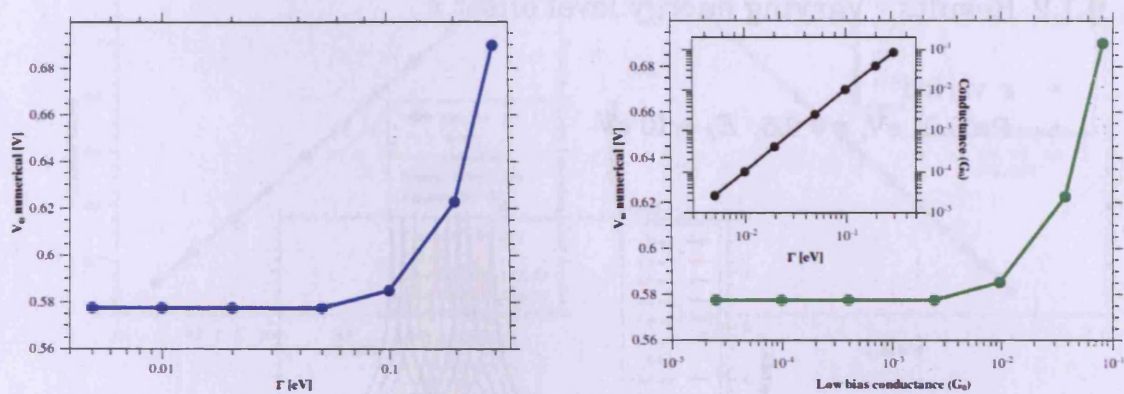
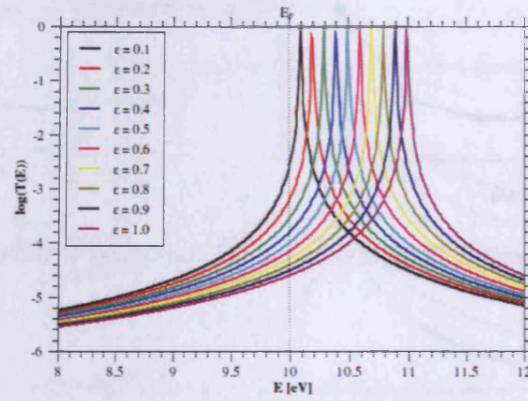
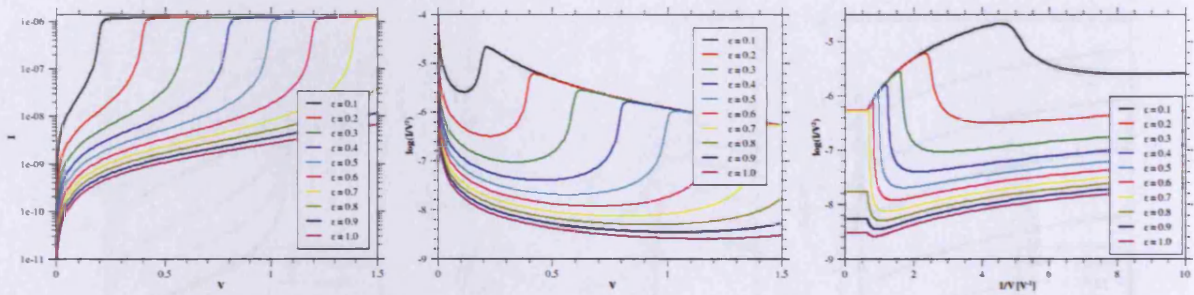


Figure 9.3. (Left) V_m versus Γ . (Right) V_m versus G and (inset) G versus Γ .

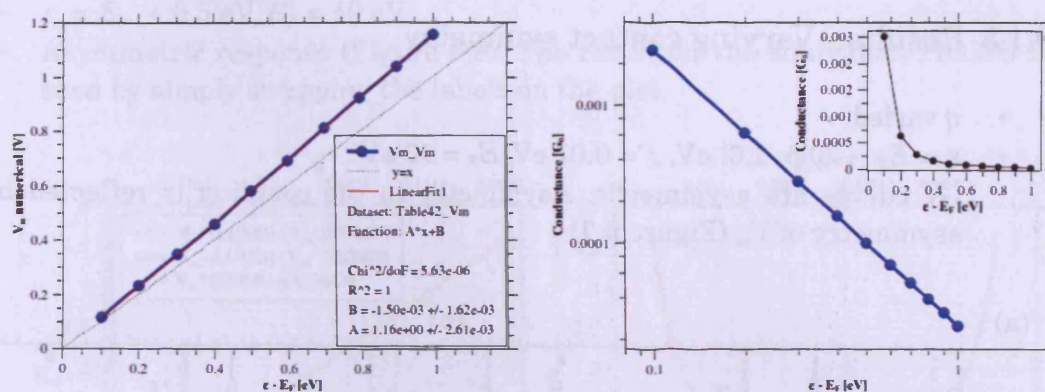
9.1.2 Results - Varying energy level offset ε

- ε varied
- $\Gamma = 0.01$ eV, $\eta = 0.5$, $E_F = 10$ eV

Figure 9.4. Transmission for various ε Figure 9.5. Calculated I-V curves; $\ln(I/V^2)$ versus V and $\ln(I/V^2)$ versus $1/V$

Remarks:

- V_m scales linearly with $\varepsilon - E_F$ (Figure 9.6)
- $\log(G)$ scales linearly with $\log(\varepsilon - E_F)$ (fit to the data gives $G \propto (\varepsilon - E_F)^{-2}$)

Figure 9.6. (Left) V_m versus Γ . (Right) V_m versus G and (inset) G versus Γ .

9.1.3 Results - Varying contact symmetry

- η varied
- $\varepsilon = E_F + \{0.5, 1.0\}$ eV, $\Gamma = 0.01$ eV, $E_F = 10$ eV
- I-V curves are asymmetric. Asymmetry in the coupling is reflected by a bias asymmetry of V_m (Figure 9.7)

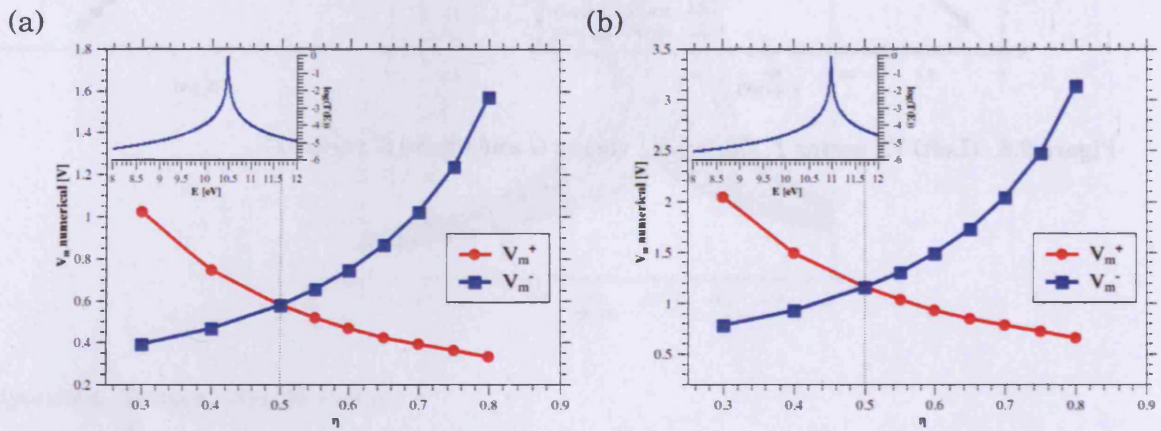


Figure 9.7. V_m versus η . $\varepsilon = E_F + \{(a) 0.5 \text{ or } (b) 1.0\}$ eV, $\Gamma = 0.01$ eV, $E_F = 10$ eV

Remarks

- The exact value of V_m depends on the energy level offset as well as the asymmetry, but the relative asymmetry in V_m is the same, e.g.:
- for $(\varepsilon - E_F) = 0.5$ eV
 - $V_m^-(\eta=0.8)/V_m^-(\eta=0.5) = 2.72$
- for $(\varepsilon - E_F) = 1.0$ eV
 - $V_m^-(\eta=0.8)/V_m^-(\eta=0.5) = 2.72$

However this is not realistic – we have taken the total broadening to be constant whilst independently varying η . A more realistic model would be to fix the contribution to the broadening from one electrode whilst varying the other (i.e. a fluctuating contact); thus the total broadening term is not independent of η . The total broadening is the sum of the broadening terms from each electrode: $\Gamma = \Gamma_1 + \Gamma_2$ and the asymmetry parameter: $\eta = \Gamma_1/\Gamma = 1 - \Gamma_2/\Gamma$ or equivalently $\Gamma_1 = \eta\Gamma$ and $\Gamma_2 = (1 - \eta)\Gamma$. Hence we fix Γ_1 and observe the effect of varying Γ_2 and hence η

- Γ_2 varied, $\Gamma_1 = 0.005$ eV (half the total Γ used in the previous examples)
- hence η varies

- $\varepsilon = E_F + 0.5$ eV, $E_F = 10$ eV
- Asymmetric response (Figure 9.8). The result for the equivalent HOMO level is seen by simply swapping the labels on the plot.

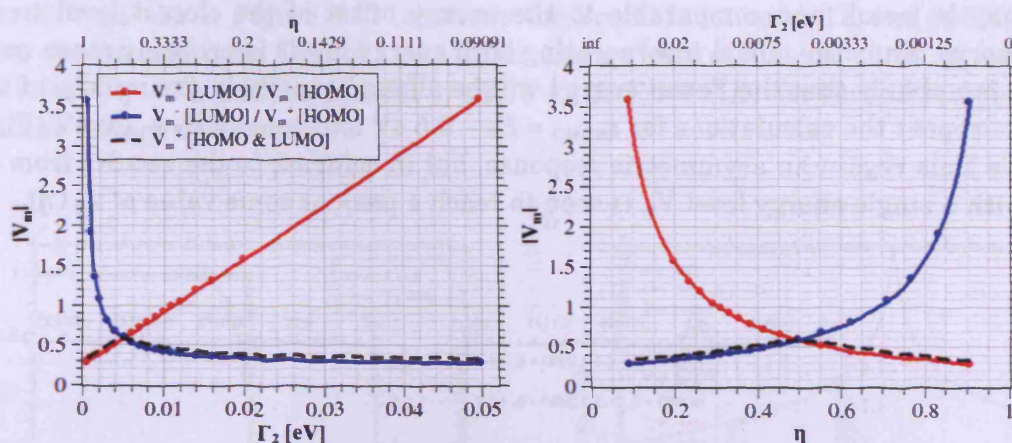


Figure 9.8. (left) V_m versus tip coupling strength, Γ_2 . (right) V_m versus the asymmetry parameter $\eta = (1 - \Gamma_2/T)$. The red curve shows V_m^+ (V_m^-) and the blue curve V_m^- (V_m^+) for a model LUMO (HOMO) level, $\varepsilon_{\text{LUMO}} = E_F + 0.5$ eV ($\varepsilon_{\text{HOMO}} = E_F - 0.5$ eV). (black dashed curve) HOMO and LUMO level $\varepsilon_{\text{HOMO}} = E_F - 0.5$ eV and $\varepsilon_{\text{LUMO}} = E_F + 0.5$ eV (V_m^+ is equal to V_m^-).

Also included in Figure 9.8 is the result of calculations based on a model with a HOMO and LUMO level, both offset by 0.5 eV from E_F . In this case there is no asymmetry, but V_m is still seen to vary with the coupling strength, reaching a maximum value at the point of symmetric coupling and is equal to the V_m value obtained from the single level model. The value of $\log(V_m^+/V_m^-)$ is directly proportional to η (Figure 9.9).

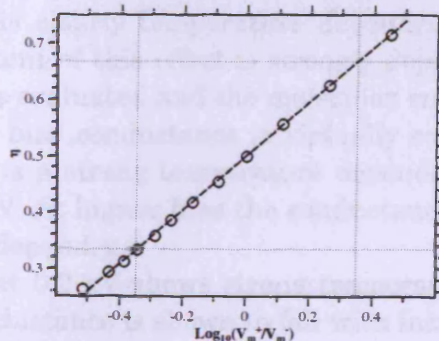


Figure 9.9. η versus $\log(V_m^+/V_m^-)$

The calculations involving a single energy level would only reflect the experimental results in molecular systems if the Fermi energy is closely aligned to either the HOMO or LUMO level and the HOMO-LUMO gap is large enough that the single closest channel dominates. For a conjugated molecule the HOMO – LUMO gap may be small and comparable to the energy offset of the closest level to the Fermi energy. Thus the model incorporating both energy levels is probably more realistic, but it is unlikely that the Fermi energy will be aligned exactly in the middle of the gap, so we repeat the calculations for $\epsilon_{HOMO} = E_F - 0.5$ eV and $\epsilon_{LUMO} = E_F + 1.0$ eV (Figure 9.10). We thus regain an asymmetric response, but in contrast to the results from the model with a single energy level V_m is seen to reach a peak at some value of Γ_2 (η).

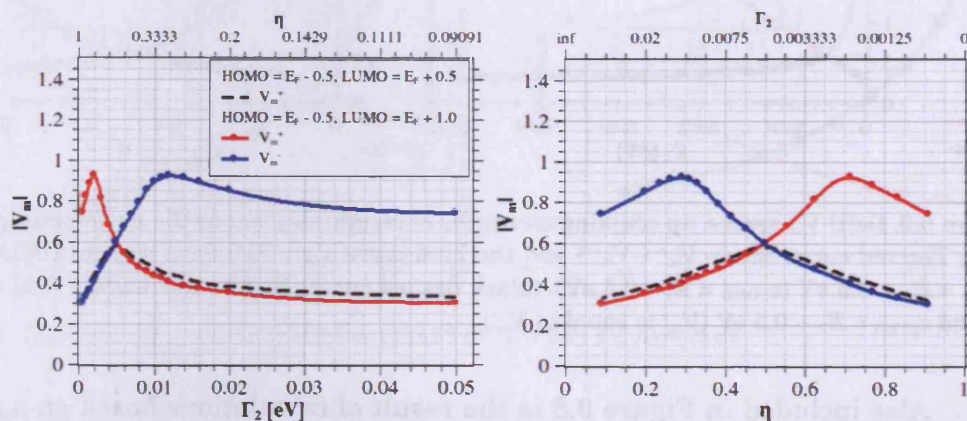


Figure 9.10. (left) V_m versus tip coupling strength, Γ_2 . (right) V_m versus the asymmetry parameter $\eta = (1 - \Gamma_2/\Gamma)$. HOMO and LUMO level, $\epsilon_{HOMO} = E_F - 0.5$ eV, $\epsilon_{LUMO} = E_F + 1.0$ eV (red curve V_m^+ , blue curve V_m^-). (black dashed curve shows previous result for $\epsilon_{HOMO} = E_F - 0.5$ eV, $\epsilon_{LUMO} = E_F + 0.5$ eV, $V_m^+ = V_m^-$).

9.1.4 Results – Varying temperature

The effect of finite temperature is included in the Fermi function of the electrodes, as above. Figure 9.11 (a) shows the Fermi function at 1K and 300K and (b) shows the transmission $T(E)$ of a molecular energy level $\varepsilon = E_F + 0.5$ eV, $\Gamma = 0.02$ eV, $E_F = 5.5$ eV, $\eta = 0.5$ and the product $|f_1(E,T) - f_2(E,T)| \times T(E)$ for several temperatures at a bias voltage of 0.5 V.

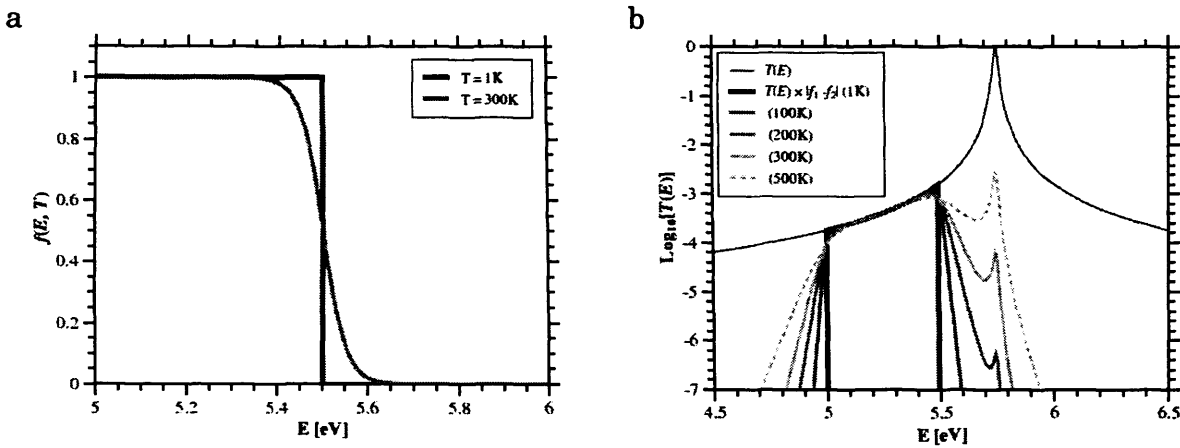


Figure 9.11. (a) Fermi function $f(E, T)$ at 1K and 300K (b) transmission $T(E)$ for an energy level $\varepsilon = E_F + 0.5$ eV, $\Gamma = 0.02$ eV, $E_F = 5.5$ eV, $\eta = 0.5$ and the product of $T(E)$ and $f(E, T)$ for different temperatures at a bias voltage of 0.5 V.

Figure 9.12, Figure 9.13 and Figure 9.14 show I/V versus V , at 200K and 400K, and I/V versus temperature for a molecular level at (9.12) $\varepsilon = E_F + 0.5$ eV, (9.13) $\varepsilon = E_F + 1.0$ eV and (9.14) $\varepsilon = E_F + 0.2$ eV ($\Gamma = 0.02$ eV, $E_F = 5.5$ eV, $\eta = 0.5$).

The conductance is clearly temperature dependent, generally increasing with temperature, but the extent of this effect is strongly dependent on the bias voltage at which the conductance is evaluated and the molecular energetics. For the energy level at 0.5 or 1.0 eV the low bias conductance is virtually constant with temperature. At intermediate bias there is a strong temperature dependence for the 0.5 eV level, but not for the level at 1.0 eV. At higher bias the conductance of the 0.5 eV level is again virtually temperature independent.

The energy level at 0.2 eV shows strong temperature dependence at low bias, but interestingly the conductance is shown to fall with increasing temperature at 0.5 V bias. At higher bias the conductance is temperature independent. Thus we can predict that a measurable temperature dependence of conduction may be seen in molecular junctions dominated by coherently tunnelling, *if* the energetic offset of the molecular orbital is relatively close to the Fermi energy and a suitable bias voltage chosen. In

addition, as the temperature dependence derives from the Fermi function the effect is applicable in any scattering model.

Figure 9.15 shows the temperature dependence of V_m for each of these molecular levels. The room temperature V_m values are lower in all cases than the value at 1K, although the relative decrease depends on the energy level with $\sim 2\%$ decrease for $\varepsilon = E_F + 1.0$ eV, $\sim 10\%$ for $\varepsilon = E_F + 0.5$ eV and $\sim 30\%$ for $\varepsilon = E_F + 0.2$ eV. Above room temperature V_m for the lowest level increases again, while the other levels continue to decrease.

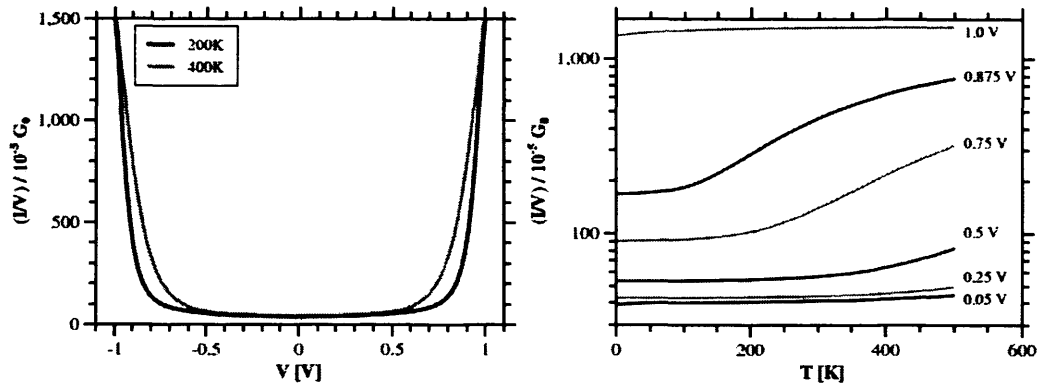


Figure 9.12. (left) I/V versus V at 200 K and 400 K for an energy level $\varepsilon = E_F + 0.5$ eV, $\Gamma = 0.02$ eV (right) I/V versus temperature

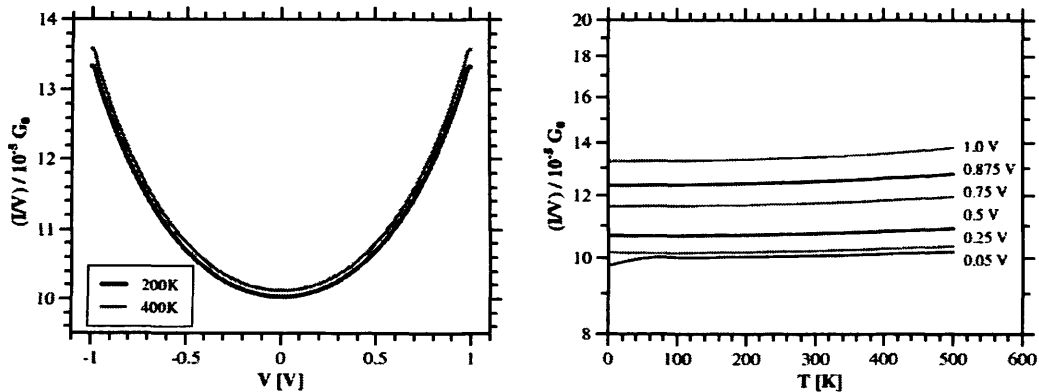


Figure 9.13. (left) I/V versus V at 200 K and 400 K for an energy level $\varepsilon = E_F + 1.0$ eV, $\Gamma = 0.02$ eV (right) I/V versus temperature

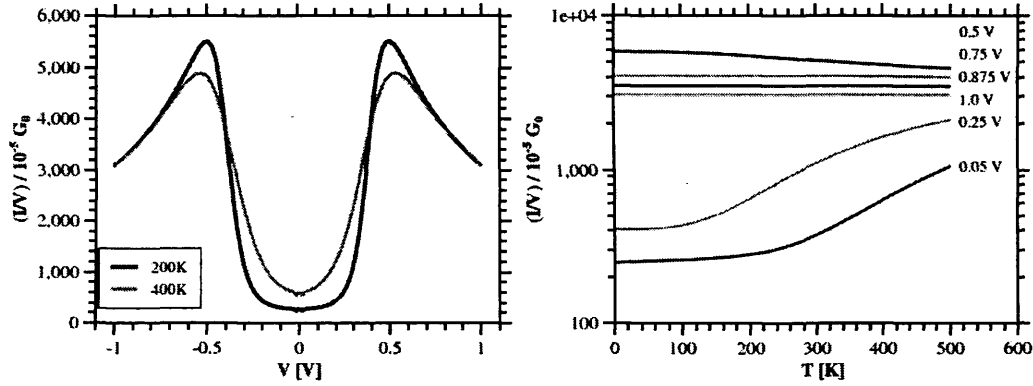


Figure 9.14. (left) I/V versus V at 200 K and 400 K for an energy level $\varepsilon = E_F + 0.2$ eV, $\Gamma = 0.02$ eV (right) I/V versus temperature

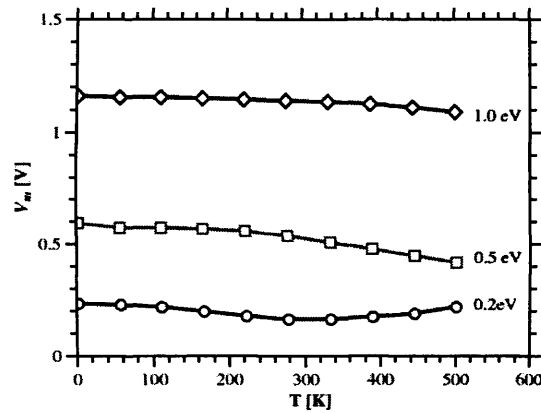


Figure 9.15. V_m versus temperature for three different molecular levels $\varepsilon = E_F + 0.5$ eV, $\varepsilon = E_F + 1.0$ eV and $\varepsilon = E_F + 0.2$ eV ($\Gamma = 0.02$ eV, $E_F = 5.5$ eV, $\eta = 0.5$).

9.1.5 V_m for Alkanes

When we consider the large HOMO-LUMO gap of the alkane chain (~ 8 eV), we might expect that $E_F - E_{HOMO}$ would be around several electron-volts. Thus in published studies, as in this thesis, the value of V_m for alkanethiols (at ~ 1.2 eV) seems very low. Li et al [9] performed DFT calculations of $T(E)$ for a range of alkanedithiols bonded to gold electrodes. The molecular states of the alkane backbone give a HOMO* level at ~ 2.14 eV with a total HOMO*-LUMO gap ~ 7.5 eV. This suggests that a $V_m \sim 2$ V would be measured for an alkane. However, the sulphur of the thiol contacts introduces evanescent gap states, thus the true HOMO of the alkanedithiol is ~ 1.4 eV.

We take $T(E)$ for nonanedithiol and integrate to find the shape of the I-V curve and hence determine the expected V_m based on the calculations (Figure 9.5). This gives $V_m \sim 1.2$ V, in good agreement with experimental evidence. This coincides approximately with the peak in $T(E)$ corresponding to the Sulphur end groups (HOMO) *not* the peak corresponding to the highest orbital of the alkane chain (HOMO*).

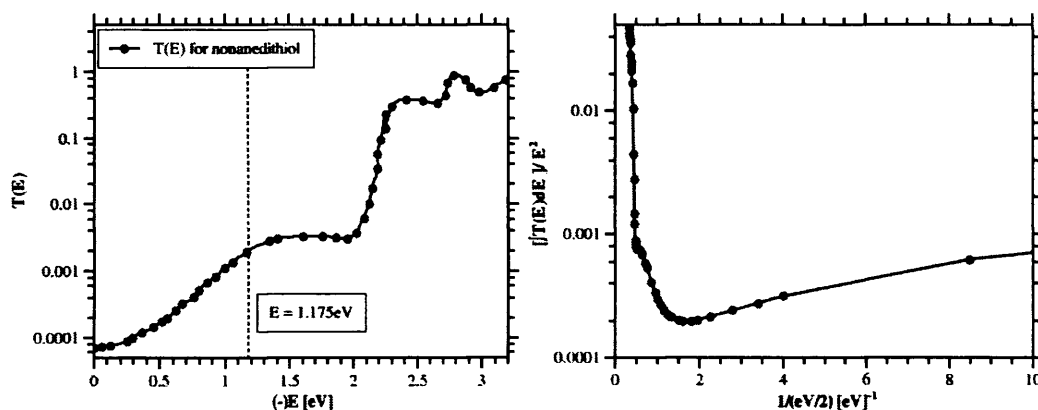


Figure 9.16. (left) $T(E)$ for nonanedithiol from Li et al [9]. Integrated $(\int T(E)dE)/E^2$ versus $1/E$

9.1.6 Fitting to experimental data

In order to use the molecular model to fit experimental data we necessarily make several assumptions about $T(E)$: we assume the single, closest energy level to E_F dominates the transport, furthermore we assume that this is HOMO mediated transport; we assume that the transmission due to this energy level is well approximated by a Lorentzian profile, that the energetic offset scales linearly with bias and the broadening is energy independent. However, we cannot make the assumption that the magnitude of the transmission (unity at $E \equiv \epsilon$) is scaled correctly. As already

seen for alkanedithiols (Figure 9.5) the I-V characteristics, over the experimentally relevant bias range, are dominated by the sulphur gap state with a transmission peak several orders of magnitude below 1. Therefore, for the purpose of fitting, we allow a self-consistent scaling factor into the model; this is explained further below.

At low temperature the differential conductance in the molecular model is:

$$\frac{dI}{dV} = \frac{2e^2}{h} T(E) = \frac{2e^2}{h} \frac{\eta(1-\eta)\Gamma^2}{\Gamma^2/4 + (E-\varepsilon)^2} \quad , \quad (9.2)$$

which in the limit of perfect Fermi level alignment reduces to :

$$\frac{dI}{dV}_{\lim E \rightarrow \varepsilon} = \frac{2e^2}{h} = 2G_0 \quad . \quad (9.3)$$

We assume, in the case of all the molecules studied, and given perfect Fermi level alignment, that the conductance would in fact be something less than G_0 if the transmission peak is less than unity. In the general case (i.e. $\varepsilon \neq E_F$) $dI/dV(E=E_F) = G_0 \times T(E=E_F)$, and given the known low bias conductance G_S (dictated by the setpoint current), we scale the current by a factor of $G_S / (G_0 \times T(E=E_F))$. As this scaling depends on the model parameters itself the initial fitting is done manually and iteratively (with the scaling re-calculated based on the new model parameters) to get a self-consistent solution.

We finally make the assumption that any background contribution from through-space tunnelling is negligible or sufficiently low that the molecular contribution is dominant; thus we do not model a parallel tunnelling process through a rectangular barrier. The validity of this assumption depends strongly on the barrier characteristics of the through-space tunnelling barrier. However, for a barrier width of the order of the molecular length and barrier height of a few eV this assumption seems reasonable; the molecular contribution is dominant.

The fitting is implemented using the addition code below and examples of the fits appear in the results chapter:

```
...
...
scale = (G_s/G0) / tau_Huisman(mu+V_s, bias=V_s, mu=mu, epsilon=mu-eps, gamma1 =
gamma*eta, gamma2 = gamma*(1-eta))
...
...
I=scale*I*2*q_e/h
...
...
#-----
# Curve fitting
#-----
errfunc = lambda c, x, y: IV_calc(eps = map(float,c)[0], gamma = map(float,c)
[1], eta = map(float,c)[2], V_start=V[0], V_end=V[-1], scale=scale,
op_status=op_status)[2] - y # Distance to the target function
```

```
c0 = [eps,gamma,eta] # Initial guess for the parameters
coeffst, errst,infodict, mesg, success = optimize.leastsq(errfunc, c0[:],
args=(V,data_TVS),full_output=1,maxfev=10)

# output the fitting parameters
eps = map(float,coeffst)[0]
gamma = map(float,coeffst)[1]
eta = map(float,coeffst)[2]
...
```

9.2 Simmons model

Model parameters:

- barrier height, ε in eV
- barrier width, z in nm
- effective mass, m^* (fraction of the electron rest mass)

The following code defines the rectangular potential barrier (originally written by Dr Martin Elliott):

```
def SetRectPotential(bias=0.0, height=0.3, nl=10, nc=100, nr=10, dx=1.0):
    """
    Sets potential profile.
    Defaults to 0.3eV barrier 10nm thick with no bias across it.
    nl, nc and nr are number of points in left, right and centre regions.
    dx is step size in nm

    Note: +ve bias lowers right-hand (drain) Fermi level wrt left-hand (source)
    side.
    Energy E of carrier must give real wavevector k in the flat (left and
    right)
    regions for the calculation to be valid.
    See Kalotas: "Assuming particles to be incident
    (from the left) with energy E > 0, we see that Schrodinger's
    equation in the j r h segment reduces to the simple form..."
    """
    nl=max(nl,1); nr=max(nr,1) # use at least one padding point
    N=nl+nc+nr
    x=scipy.zeros(N, dtype='Float64')
    s=nc*dx # barrier width
    eps=2.1*eps0 # dielectric constant

    # Calculate x-range ...
    for i in range (0, N):
        x[i]=i*dx*1e-9 # convert units to SI here
    # make potential profile ...
    V0=scipy.zeros(N, dtype='Float64') # bare potential V_0(x)
    Vb=scipy.zeros(N, dtype='Float64') # applied bias potential V_b(x)
    for i in range (0, nl):
        V0[i]=0.0;
    for i in range (nl, nl+nc):
        V0[i] = height
    for i in range (nl+nc, nl+nc+nr):
        V0[i]=0.0

    if bias<>0.0:
        dVb=bias/(nc-1) # bias dropped across central region only
        for i in range (0, nl):
            Vb[i]=0.0; # define zero of applied bias
        for i in range (nl, nl+nc):
            Vb[i]=-(i-nl)*dVb;
        for i in range (nl+nc, nl+nc+nr):
            Vb[i]=-bias # recall +ve bias lowers potential on the right
```

```
return x, V0+Vb
```

The effect that image forces have on the potential barrier can be included by a slight modification of the above. From Simmons the image force modifies the potential, at a position z in the barrier of classical width s and dielectric constant ϵ , as:

$$\phi(z) = \phi_0 - eV \frac{z}{s} - 1.15\lambda \frac{s^2}{z(s-z)}, \text{ where } \lambda = \frac{e^2 \ln 2}{8\pi \epsilon s}. \quad (9.4)$$

```
def SetRectPotential(bias=0.0, height=0.3, nl=10, nc=100, nr=10, dx=1.0):
    ...
    ...
    lam = q_e*log(2.0)/(8.0*pi*eps*s*1e-9) # term for image force correction
    ...
    ...
    for i in range (nl, nl+nc):
        # image potential approx. from Simmons
        xtemp=(i-nl+1)*dx * (nc-1)/nc
        V0[i] = height - 1.15*lam*s*s/(xtemp*(s-xtemp))
    ...
    ...
```

The transmission is calculated using the code below written as a Fortran module imported in to the python program. This is based on the approach of Kalotas et al [118] in which the actual potential profile is replaced by a series of flat barriers or wells. This can then be solved exactly and the transmission obtained via multiplication of a string of 2x2 matrices. The current is then calculated, as in the molecular model, using the Landauer formalism.

```
module mod
contains
function KK(alpha2, w)
    !Called as K(alpha2, w) where w is the step size
    !and alpha2 (can be negative) is 2*mu*(V-E)/hbar**2. (Both in SI).
    !Returns a (real) array - see equation (12)a of Kalotas et al.
    real (kind=8) :: alpha2, w, alpha, alphaw, beta, betaw, KK(2,2)

    if (alpha2>=0.0) then ! decaying solution ...
        alpha=sqrt(alpha2); alphaw=alpha*w
        KK(1,1)=cosh(alphaw)
        if (abs(alpha)<1e-20) then
            KK(1,2)=-1.0*w*(1-(alphaw**2)/6);
        else
            KK(1,2)=-sinh(alphaw)/alpha
```

```

        endif
        KK(2,1)=alpha2*KK(1,2); KK(2,2)=KK(1,1)
    else ! propagating solution ...
        beta=sqrt(-alpha2); betaw=beta*w
        KK(1,1)=cos(betaw)
        if (abs(beta)<1e-20) then
            KK(1,2)=-1.0*w!*(1-(betaw**2)/6)
        else
            KK(1,2)=-sin(betaw)/beta
        endif
        KK(2,1)=alpha2*KK(1,2); KK(2,2)=KK(1,1)
    endif
end function KK

function tau(n, E, V, x, mu)
    ! Physical constants
    real (kind=8), parameter:: m_e=9.1093826e-31 ! kg
    real (kind=8), parameter:: q_e=1.60217653e-19 ! coulomb
    real (kind=8), parameter:: hbar=1.05457168e-34 ! Js

    real (kind=8) :: tau, E, V(n), x(n), mu, dx, k1, k2, alpha2(n), Pi(2,2)
    dx=(x(n)-x(1))/(n-1)
    ! We assume here that E>V in the incoming and outgoing regions, so we
have
    ! travelling wave solutions there.
    ! The incoming wavevector ...
    k1=sqrt(2*mu*(E-V(1))*(m_e*q_e/hbar**2)) ! in SI units here
    ! The outgoing wavevector ...
    k2=sqrt(2*mu*(E-V(n))*(m_e*q_e/hbar**2)) ! in SI units here
    !print *, k1, k2
    !f2py intent(in) :: E, V, x, mu
    !f2py intent(out) :: tau
    !do i=1,n
    !    alpha2(i)=(2*mu*(V(i)-E)*(m_e*q_e/hbar**2))
    !end do
    alpha2=(2*mu*(V-E)*(m_e*q_e/hbar**2)) !will also work
    Pi(1,1)=1.0; Pi(1,2)=0.0
    Pi(2,1)=0.0; Pi(2,2)=1.0 ! start with identity matrix
    do i=1,n
        Pi=matmul(Pi, KK(alpha2(i), dx))
    end do
    !print *, k1
    tau=4/((Pi(1,1)+Pi(2,2)*(k2/k1))**2 + (Pi(1,2)*k2-Pi(2,1)/k1)**2)
end function tau

end module mod

```


9.2.1 Characteristics as a function of barrier height, ε

- $\varepsilon = (E_F + \text{varied offset}) \text{ eV}$
- $z = 0.7, 1 \text{ and } 2 \text{ nm}, \quad E_F = 10 \text{ V}, \quad m^* = 1.0$

Remarks:

- V_m scales with $(\varepsilon - E_F)$, but is also strongly dependent on the barrier width (Figure 9.2).
- V_m scales with the logarithm of the conductance for a fixed barrier width.

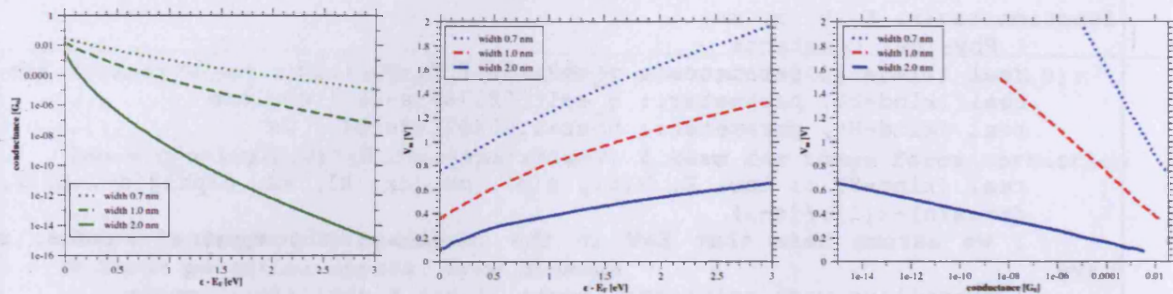


Figure 9.17. Characteristics as a function of barrier height, $\varepsilon = (E_F + \text{varied offset}) \text{ eV}$, Width $z = 0.7, 1$ and 2 nm , $E_F = 10 \text{ V}$, $m^* = 1.0$

9.2.2 Characteristics as a function of barrier width, z

- z varied
- $\varepsilon = E_F + \{0, 0.5, 1.0, 2.0 \text{ and } 4.0\} \text{ eV}$, $E_F = 10 \text{ V}$, $m^* = 1.0$

Remarks:

- V_m scales with barrier width at fixed barrier height (Figure 9.4), but V_m does *not* scale *linearly* with $1/\text{width}$ as suggested in [18].
- V_m scales with the logarithm of the conductance for a fixed barrier height, but the dependence is non-linear and markedly different from the previous trend upon varying barrier height at fixed width (Figure 9.2).

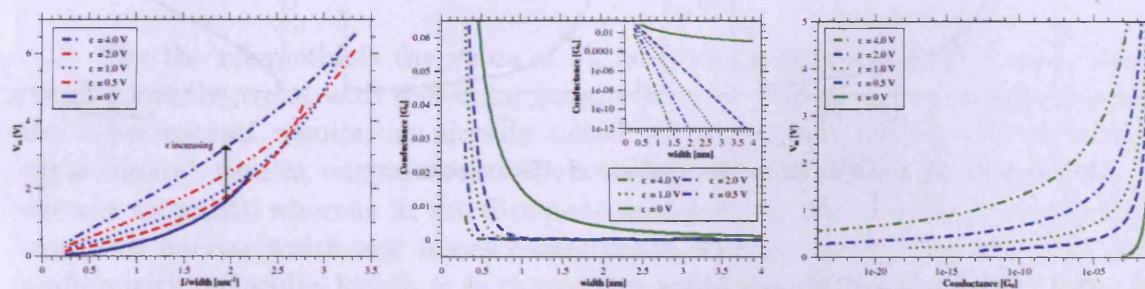


Figure 9.18. Characteristics as a function of barrier width, z . $\varepsilon = E_F + \{0, 0.5, 1.0, 2.0 \text{ and } 4.0\} \text{ eV}$, $E_F = 10 \text{ V}$, $m^* = 1.0$.

9.2.3 Versus effective mass

- m^* varied
- $\varepsilon = E_F + 0.5$ eV, $z = 1$ nm, $E_F = 10$ eV

Remarks:

- V_m is strongly dependent on the effective mass of the charge carrier (Figure 9.1) as is the conductance.

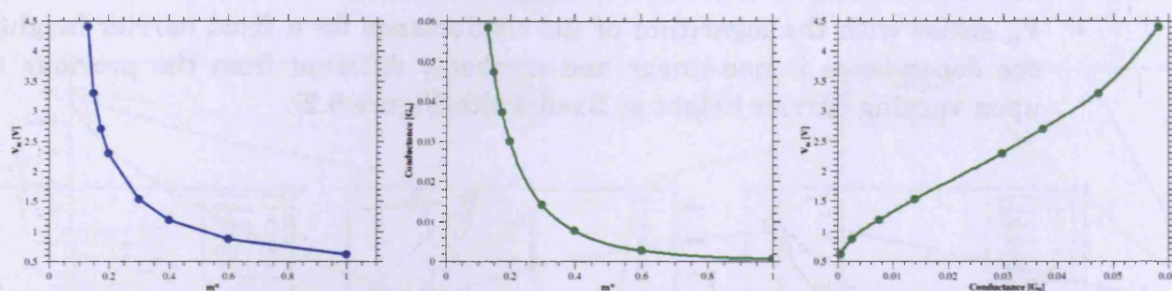


Figure 9.19. V_m and G as a function of electron effective mass m^*

9.3 Summary/Discussion

The qualitative findings of the calculations based on the molecular model are in agreement with reported experimental findings of Beebe et al [14][17] and similar calculations by Huisman *et al*[18]. V_m is invariant with increasing level broadening (Γ) for low values of Γ and hence is also independent of conductance over a wide range. V_m scales linearly with $\varepsilon - E_F$, hence it is a direct probe of the closest molecular energy level, assuming the model $T(E)$ is a reasonable approximation to the real transmission. Asymmetric coupling produces asymmetric I-V characteristics and the value of $\log(V_m^+/V_m^-)$ is directly proportional to η . However, at the extremes of asymmetry contributions from a second energy level may have an influence on V_m , so it is not necessarily enough to consider only the single closest energy level.

The V_m behaviour in the Simmons model is altogether more complicated and, as discussed by Huisman, the model is not consistent with published experimental results on molecular systems. The most important point to note is that V_m is *not* equal to the barrier height to tunnelling. For completeness we calculate V_m in the Simmons model, based on the known/estimated physical parameters of the molecules we have studied, and compare this to the experimental results (Table 5). The barrier height for each molecule is assumed to be equal to the molecular HOMO level offset from E_F , as measured by UPS for the porphyrins, or from DFT calculations of the alkane chain for the alkanethiols [9].

Molecule	$\varepsilon - E_F$ [eV]	z [nm]	m^*	V_m (numerical) [V]	V_m (experimental) [V]	Conductance [G_0]
Dodecanethiol	2.14 [9]	$1.774 \times \cos(30)$	0.28^b	1.38	1.13	1.08×10^{-5}
Hexadecanethiol	2.14 [9]	$2.282 \times \cos(30)$	0.28^b	1.05	1.27	2.90×10^{-7}
Porphyrin Monomer	1.12^a	2.47	1.00^c 0.28^c	0.32 0.63	0.39	5.26×10^{-12} 1.58×10^{-6}
Porphyrin Dimer	1.08^a	3.82	1.00^c 0.28^c	0.20 0.39	0.34	4.75×10^{-18} 9.87×10^{-10}

Table 5. Results of numerical calculations based on the rectangular barrier (Simmons) model, using the parameters listed, relevant to the molecules studied. ^a Results of UPS measurements. ^b The value of m^* for alkanes is taken from [23]; ^c m^* for the porphyrins is unknown.

For the alkanethiols the value of V_m is in rough agreement with experimental results, but the trend with molecular length (barrier width) is in contradistinction to the experimental results, as already noted by Huisman *et al*[18]. In addition the experimental results suggest that V_m is independent of the conductance (i.e. the current setpoint), whereas in the Simmons model V_m is seen to scale in a non-trivial way with barrier width and hence conductance. For the porphyrins the trend of V_m scaling with molecular length is in the correct sense, but the Simmons result predicts a larger change than experimentally observed (a factor of ~ 1.6 compared to ~ 1.1 respectively). More importantly the predicted conductance difference between monomer and dimer, more than 5 orders of magnitude, is in extreme disagreement with experimental results[16]. Thus the Simmons model does not provide a good description for the experimental results of this thesis.

10 Appendix B. Sample preparation

Outline for preparation of sample of:

- Porphyrin monolayers with piperidine ligands
 - and mixed monolayers of porphyrin in an alkanethiol matrix,
- on substrates of**
- Au on mica
 - or Au single crystal.

10.1 Au substrates

Au substrates are sputtered and annealed in UHV before use. We use a sputtering pressure of 4.5×10^{-6} mbar and the ion gun is set to energy 1000 V, extractor 466 V and focus 859 V with emission current of 10 mA. The substrate is positioned to maximise the current ($\sim 3 \mu\text{A}$ for these settings) and is sputtered for ~ 15 minutes. The substrate is subsequently annealed; for Au on mica we use 350°C for ~ 1 hour; for the Au single crystal ~ 10 minutes at 650°C followed by ~ 1 hour at 450°C . When using the Au single crystal we repeat the sputter and anneal treatment several times. Afterwards the substrates are kept in UHV until needed.

10.2 Molecular solutions

- Fresh solutions of molecules are prepared for each experiment.
- For the alkanethiols, alkanedithiols and piperidine ligands we make large stock solutions at 1×10^{-2} M in toluene, which may be stored for several months.

10.2.1 Alkanethiols/dithiols

- Fresh solutions of alkanethiols/dithiols at 5×10^{-5} M are prepared from the concentrated stock solutions by diluting 200 times with toluene.
- A freshly sputtered and annealed Au substrate is removed from vacuum and immersed in the solution for ~ 15 s to achieve a low coverage phase of the molecules. The sample is subsequently rinsed for ~ 1 minute in toluene and dried under flowing nitrogen.

10.2.2 Porphyrins

- The porphyrins (Oxford) are received in powder form in separate vials containing ~0.5 mg each. Solutions at 5×10^{-5} M in toluene are simply prepared by dissolving the powder in the solvent. An example is outlined below:
- 0.48 mg of porphyrin dimer (actyl-protected thiol end-group with octyloxy side-chains), with molecular weight 2472.04 g mole⁻¹, is equal to 1.942×10^{-7} moles.
- This is diluted in 800 μ L of toluene to make an initial solution at 2.427×10^{-4} M.
- The target concentration is 5×10^{-5} M, so we must dilute by a factor of $2.427/0.5 = 4.854$.
- We transfer the solution to a larger container and add toluene to achieve the target concentration, i.e. the total volume should be $4.854 \times 800 \mu\text{L} = 3.88$ mL, so we add 3.08 mL of toluene to the previous solution.
- If we wish to add piperidine as a ligand for the porphyrin molecules we must add enough to have an excess of piperidine molecules relative to the number of porphyrin molecules, e.g. we add 200 μ L of piperidine at 1×10^{-2} M, which is 2×10^{-6} moles, giving a porphyrin to piperidine ratio of ~ 1:10.
- A freshly sputtered and annealed Au substrate is removed from vacuum and immersed in the solution for ~ 15 s to achieve a low coverage phase of the molecules. The sample is subsequently rinsed for ~ 1 minute in toluene and dried under flowing nitrogen.
- A higher coverage can be achieved by leaving the substrate in the solution overnight or up to several days.

10.2.3 Mixed monolayers

- Porphyrin molecules were isolated in an alkanethiol matrix using the one-step matrix insertion method[45] for mixed monolayer samples.
- We prepare fresh solutions of alkanethiol and porphyrin both at 5×10^{-5} M in toluene, as above.
- The solutions are then mixed together at a ratio of 100:1 (alkanethiol to porphyrin) by volume.
- The mixed solution is then placed in a nitrogen filled glovebox (<0.05% oxygen, and less than 5% humidity).
- A freshly sputtered and annealed Au/Mica substrate is removed from UHV and immediately immersed in the mixed solution.
- The sample was left to incubate in the solution overnight then rinsed in toluene for 1 minute, to remove any unbound/physisorbed molecules, and dried in flowing nitrogen for about 1 minute.

- We prepare the molecular layers on Au/mica substrates, purchased from Phasis Sàrl, Switzerland and sputtered and annealed in UHV before use.
- Electrical contact to the sample was made using a small amount of conductive silver paint.

10.3 STM tips

- STM tips were made from Au wire by electrochemical etching in HCl/ethanol (1:1)[65].
- The counter electrode is made from thick (1 mm) Au wire formed into a ring and placed at the surface of the etching solution. The 0.25 mm wire for the tip is suspended in the centre of the ring with ~2 mm submerged below the liquid surface.
- The electrodes are connected to a d.c. power supply and a bias of +2.4 V is applied to the tip electrode. Etching proceeds until the submerged portion of the wire falls off. At this point the power supply is manually switched off to prevent over-etching at the tip apex.

11 Appendix C.

11.1 UPS results

Ultraviolet photoelectron spectroscopy measurements were performed on the Au single crystal sample and samples of dodecanethiol monolayer and porphyrin monolayer on Au. Modification of the Au surface with the molecular monolayers shows a significant attenuation of the Au(111) valence spectra peaks, as expected [101].

Using either the HE I (21.21 eV) or HE II (40.8 eV) resonance we see a peak in the spectrum of the porphyrin molecule 1.12 ± 0.005 eV below E_F (Figure 11.1). This peak is absent in the spectrum of Au or dodecanethiol and represents the molecular HOMO level of the porphyrin molecule. Similarly for the porphyrin dimer we measure $E_{HOMO} - E_F = 1.080 \pm 0.005$ eV.

We also estimate the vacuum level shift upon adsorption of the molecular layers from the shift in the low energy cut-off. For both the porphyrin monomer and dodecanethiol the effective work-function change induced by the molecules is ~ 0.85 eV and from these measurements it suggests that the metal-molecule interface energetics are similar for both molecules.

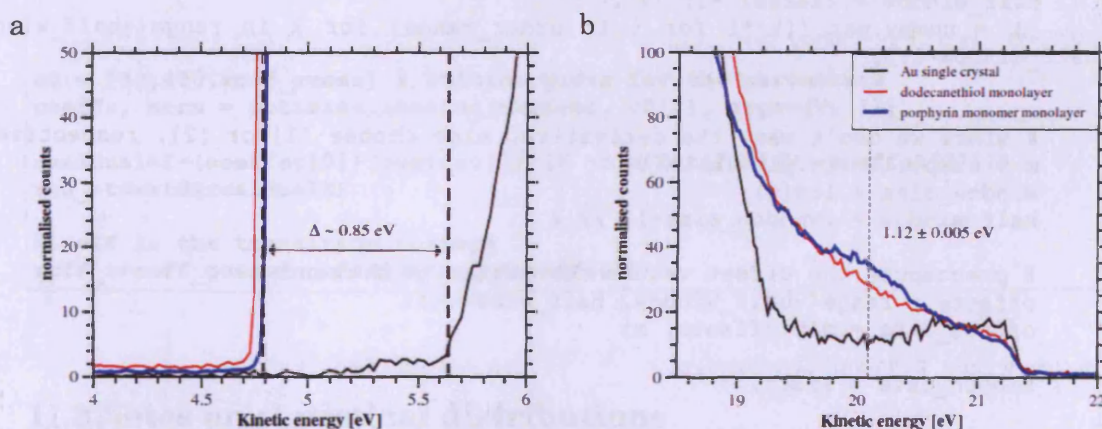


Figure 11.1. UPS results for the bare Au single crystal and Au with dodecanethiol or porphyrin monolayers (a) low energy cut-off (b) high energy range.

11.2 Voltage minimum analysis

The voltage minimum in the plot of $\log(I/V^2)$ versus $1/V$ is determined by a simple automated algorithm in three stages. The data is smoothed using the Savitsky-Golay algorithm to reduce the noise inherent in each individual curve.:

```

def savitzky_golay(data, kernel = 61, order = 3):
    """
    http://www.scipy.org/Cookbook/SavitzkyGolay
    applies a Savitzky-Golay filter
    input parameters:
    - data => data as a 1D numpy array
    - kernel => a positive integer > 2*order giving the kernel size
    - order => order of the polynomial
    returns smoothed data as a numpy array

    invoke like:
    smoothed = savitzky_golay(<rough>, [kernel = value], [order = value])
    """
    try:
        kernel = abs(int(kernel))
        order = abs(int(order))
    except ValueError, msg:
        raise ValueError("kernel and order have to be of type int (floats will
        be converted).")
    if kernel % 2 != 1 or kernel < 1:
        raise TypeError("kernel size must be a positive odd number, was: %d" %
        kernel)
    if kernel < order + 2:
        raise TypeError("kernel is too small for the polynomials\nshould be >
        order + 2")

    # a second order polynomial has 3 coefficients
    order_range = range(order+1)
    half_window = (kernel - 1) // 2
    b = numpy.mat([[k**i for i in order_range] for k in range(-half_window,
    half_window+1)])

    # since we don't want the derivative, else choose [1] or [2], respectively
    m = numpy.linalg.pinv(b).A[0]
    window_size = len(m)
    half_window = (window_size-1) // 2

    # precompute the offset values for better performance
    offsets = range(-half_window, half_window+1)
    offset_data = zip(offsets, m)

    smooth_data = list()

    # temporary data, with padded zeros (since we want the same length after
    smoothing)
    data = numpy.concatenate((numpy.zeros(half_window), data,
    numpy.zeros(half_window)))
    for i in range(half_window, len(data) - half_window):
        value = 0.0
        for offset, weight in offset_data:
            value += weight * data[i + offset]
        smooth_data.append(value)
    return numpy.array(smooth_data)

```

The positions of local minima are found using the function below, being careful to avoid the extreme ends of the data set where spurious minima could be found close

to 0 V (due to smoothing artefacts), or at high bias, due to saturation of the current amplifier.

```
def local_minima_fancy(fits, window=51):
    """
    http://old.nabble.com/Finding-local-minima-of-greater-than-a-given-depth-
    td18988309.html
    """
    from scipy.ndimage import minimum_filter
    import numpy
    fits = numpy.asarray(fits)
    minfits = minimum_filter(fits, size=window, mode="wrap")
    minima_mask = fits == minfits
    good_indices = numpy.arange(len(fits))[minima_mask]
    good_fits = fits[minima_mask]
    order = good_indices.argsort()
    return good_indices[order], good_fits[order]
```

To robustly determine the position of the minimum point a parabola is fitted over a small range centred on the previously determined minimum point:

```
#-----
# Curve fitting
#-----
fitfunc = lambda c, x: c[0]+(c[1]*(x-c[2])*(x-c[2])) # Target function
errfunc = lambda c, x, y: fitfunc(c, x) - y # Distance to the target function
...

c0 = [50,400,xoff_guess] # Initial guess for the parameters
coeffs, errs = optimize.leastsq(errfunc, c0[:], args=(V, I))

residual=I-(coeffst[0]+(coeffst[1]*(V -coeffst[2])*(V -coeffst[2])))
res_std=std(residualt)

# xoff is the transition voltage
xoff_t=xoff_guess#coeffs[2]*sign(coeffs[1])
```

11.3 Notes on statistical distributions

The statistical data gathered from many of the experiments can be described by fitting a suitable distribution to the histogram of a measured parameter, e.g. the voltage minimum from I-V curve analysis or conductance from $I(z)$ curves. Where a peak in the histogram distribution occurs at a given value it is common to attempt to characterise that peak by fitting a Gaussian (normal) distribution. This is suitable for values centred around a particular value, with a spread that is symmetric about the peak position and where there are few outliers at extreme values.

The probability density function for the Gaussian distribution is:

$$P(x) = \frac{1}{\sqrt{2\pi\sigma^2}} \exp\left(-\frac{(x-\mu)^2}{2\sigma^2}\right) . \quad (11.1)$$

The expected distribution of a measured parameter is often unknown, but the advantage of approximating any given data set to a normal distribution is that the mean (μ) and standard deviation (σ) are both well defined and directly accessible as the fitting parameters. Therefore fitting of a Gaussian distributions is often used even when the absolute goodness-of-fit is less than for a more complicated distribution function. It has been assumed herein that Gaussian peak fitting is appropriate for describing the distribution of $\log(\text{Current})$ and has also been used to determine peak positions in histograms with multiple peaks. In the latter case the tails of each peak cannot be resolved above the background, or peaks are too close together to determine their exact shape clearly. Hence, and in lieu of a proposed or expected alternative distribution, the use of multiple Gaussian peaks is justified by the simplicity of the interpretation.

For data that is asymmetrically distributed about a single peak value a distribution that has non-zero skewness is more appropriate. This may, for example, be useful where a parameter is restricted to always be greater than zero, but may take any positive value and will hence be skewed to the right by infrequent, large, positive outliers. An example of this type of distribution, and the type used to fit some of the voltage minimum histograms, is the so-called extreme, or Gumbel, distribution. The probability density function for the Gumbel distribution is:

$$P(x) = \frac{1}{\beta} \exp\left[\frac{x-x_0}{\beta} - \exp\left(\frac{x-x_0}{\beta}\right) + 1\right] . \quad (11.2)$$

The peak (mode) is at x_0 , the mean = $x_0 + \beta\gamma$ (γ is the Euler-Mascheroni constant), and $\sigma^2 = 1/6\pi^2\beta^2$ (i.e. $\sigma = 1.283\beta$). This has been used where the fit to the data histogram seems more reasonable than the Gaussian fit.

Finally, an alternative to the normal distribution may be considered where the data is symmetrically distributed, but with high kurtosis (that is a distribution with a sharp peak and long, fat tails either side of the peak). An example of this is the Cauchy or Lorentz distribution. While the median and mode are defined for the Lorentz distribution (the peak position in both cases), the mean and standard deviation are not.

The probability density function is:

$$P(x) = \frac{1}{\pi \gamma \left[1 + \left(\frac{x - x_0}{\gamma} \right)^2 \right]} , \quad (11.3)$$

where x_0 is the peak centre (median and mode). The Lorentz distribution is actually the distribution expected for the ratio of two parameters X and Y which are both normally distributed, with zero mean.

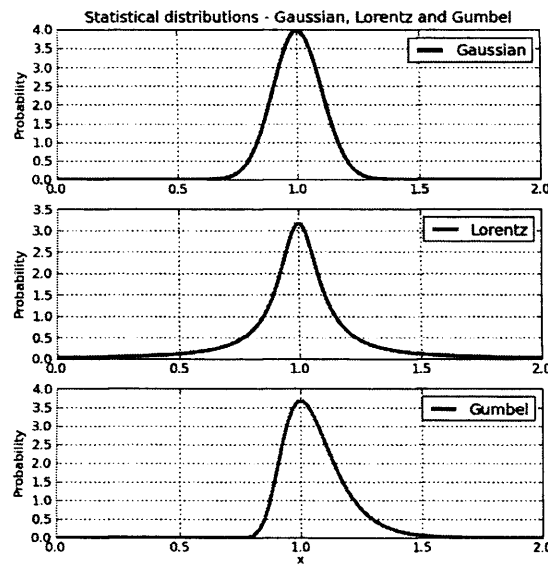


Figure 11.2. Statistical distributions of the Gaussian, Lorentzian and Gumbel type, with the same peak position and standard deviation

12Appendix D. Example I-V data set

